Study of Steel Structural Systems Subjected to Fire

Mian Zhou

A dissertation submitted in partial fulfillment
of the requirements for the degree of
Doctor of Philosophy
of
Brunel University London.

Department of Civil Engineering
Brunel University London

October 25, 2019

I, Mian Zhou, confirm that the work presented in this thesis is my own. Where information has been derived from other sources, I confirm that this has been indicated in the work.

Abstract

Performance-based engineering design aims to improve codified, rule-based practice by allowing a more flexible, and performance focused approach. In structural fire design, it enables more complex fire loading scenarios to be considered, ranging from fire following earthquakes to a localised fire travelling through a large compartment space, or a combination of both. However, the tools used for performance-based structural fire design rely on accurate material models to capture the structural response to complicated fire loading.

One critical limitation in the current generation of performance-based tools is that thermo-mechanical analysis with fire has been frequently performed using material models which do not take strain reversals into account. The assumption of "no strain reversals" in the building materials at elevated temperatures was established because the fire loading is traditionally simplified to a temperature time curve only considering heating stage, and the structural components are usually considered subjected to uniform heating. However this assumption is no longer valid when complex fire loading is applied.

A new rate-independent combined isotropic-kinematic hardening plasticity model was developed in this research for the thermo-mechanical analysis of steel materials in fire. This model is capable of modelling: strain reversals, the Bauschinger effect with its associated transient hardening behaviour and material non-linearity at elevated temperatures. Its accuracy is demonstrated through five validation studies of the proposed material model against experimental data.

The engineering value of the proposed material model is demonstrated in this work through three case studies. The new material model was adopted for: (1)

evaluating the remaining structural fire resistance after a moderate earthquake, (2) investigating stainless steel structural systems in fire, and (3) studying the fire performance of a single steel beam subjected to travelling fires. These studies demonstrated that the new material model produces a more accurate analysis of the structural fire resistance than can be achieved using existing methods.

This research proposes an improved computational tool for evaluating structural fire resistance of complex steel structures. It therefore represents a contribution to the improvement and adoption of performance-based engineering for structural fire design, and can be used for various engineering applications.

Publications

Journal Papers

M. Zhou, R. Cardoso, and H. Bahai, “A new material model for thermo-mechanical analysis of steels in fire”, *International Journal of Mechanical Sciences*, vol. 159, pp. 467 – 486, 2019

M. Zhou, L. Jiang, S. Chen, A. Usmani and R. Cardoso, “Remaining fire resistance of steel frames following a moderate earthquake —A case study”, *Journal of Constructional Steel Research*, accepted, 2019

M. Zhou, R. Cardoso, H. Bahai, and A. Usmani, “A thermo-mechanical analysis of stainless steel structures in fire”, *Engineering Structures*, under review, 2019

Conference Papers

M. Zhou, L. Jiang, Y. Wang, S. Chen, A. Usmani, “Case study of residual fire resistance of multi-story steel frames following moderate earthquakes”, in The 8th International Conference on Steel and Aluminium Structures, 2016

M. Zhou, L. Jiang, Y. Wang, S. Chen, A. Usmani, “Case study of residual fire resistance of multi-story steel frames following moderate earthquakes”, in The 1st European Conference on OpenSEES, 2017

M. Zhou, R. Cardoso, H. Bahai, and A. Usmani, “Thermo-mechanical behaviour of structural stainless steel frames in fire”, in The 10th International Conference on Structures in Fire, 2018

M. Zhou, R. Cardoso, H. Bahai, and A. Usmani, “A novel steel material model for structural thermo-mechanical analysis in fire ”, in The 1^{st} Eurasia Conference on OpenSEES, 2019

Acknowledgements

Mother says I am a lucky kid, not the smart kid but the lucky one. I have turned up at the right place at the right time for so many times. Like that mundane Aberdeen afternoon 4 years ago when I emailed Prof. Asif Usmani then in Edinburgh asking whether he had a PhD position for me. I would like to express my sincere gratitude to Prof. Usmani for having faith in me and offering me this PhD position, and for all the advice and support he has provided me with over the years.

There is the chinese saying that for a good story you can guess the start but never the ending. Being the not smart kid, I only had the location of my PhD story right. Being the lucky kid, I am grateful for Prof. Hamid Bahai being a great listener and facilitator, and to Dr. Giulio Alfano whose open mindedness and dedication to students I admire greatly. I would also like to thank Dr. Rui Cardoso. For the patience, guidance and advice he showed me, I could not have asked for a better first supervisor. He taught me the great lesson of sticking with the principles of the academic life, i.e., zero tolerance for any violations of Newton's laws. My PhD is a good story after all, owing to all the brilliant academics and wonderful friends who helped me along the way.

I think I am indeed a lucky kid because I have always had the best support from my dear mum and dad. I thank them for always being my rock. Last but certainly not least, I would like to thank my Dr. wind turbine soon to be himself indoors, who has been there for me through the peaks and troughs of the whole journey.

Contents

1 Introduction **22**

1.1 Motivation and aims . . . 22

1.2 Research scope and approach . . . 26

2 Literature Review **28**

2.1 History of structural fire resistance design . . . 28

2.2 Performance-based structural fire resistance design framework . . . 33

2.2.1 Estimate of fire demand . . . 33

2.2.1.1 Analytical fire models . . . 34

2.2.1.2 Computational fire dynamics models . . . 37

2.2.1.3 Design fires and fire scenarios . . . 38

2.2.2 Heat transfer for structures in fire . . . 38

2.2.3 Estimate of structural fire resistance . . . 40

2.2.3.1 Material softening at elevated temperatures . . . 41

2.2.3.2 Global structural mechanisms in fire . . . 44

2.2.4 Damage of Passive Fire Protection coatings . . . 48

2.3 Stainless steel structures in fire . . . 50

2.3.1 Thermal expansion . . . 51

2.3.2 Thermal properties . . . 54

2.3.3 Existing research on stainless steel structures in fire . . . 56

2.4 Material models for thermo-mechanical analysis with fire . . . 57

2.4.1 Material non-linearity . . . 57

2.4.2 Existing non-linear material models . . . 59

2.4.3 Bauschinger effect . . . 64

2.4.4 Strain rate dependency for structural fire analysis . . . 65

2.4.5 Existing kinematic hardening plasticity models at room temperature . . . 67

2.4.5.1 Mroz's multi-surface model . . . 67

2.4.5.2 Two yield-surface models . . . 68

2.4.5.3 Non-linear kinematic hardening models . . . 69

3 A New Material Model for Thermo-mechanical Analysis of Steels in Fire 72

3.1 Temperature effects on plasticity models . . . 72

3.1.1 Parametric dependency on temperature . . . 74

3.1.2 Temperature rate dependency for internal variables . . . 74

3.2 Decoupling thermal and mechanical step . . . 75

3.2.1 Elastic modulus at elevated temperatures . . . 77

3.2.2 Yield surfaces at elevated temperatures . . . 77

3.2.3 Plastic flow potential at elevated temperatures . . . 78

3.2.4 Internal state variables' evolution at elevated temperatures . 80

3.3 A new plasticity model for thermo-mechanical analysis with fire . . 81

3.3.1 Thermal step . . . 81

3.3.2 Mechanical step . . . 85

3.3.2.1 First kinematic hardening variable $\dot{\boldsymbol{\beta}}_1$ . . . 86

3.3.2.2 Second kinematic hardening variable $\dot{\boldsymbol{\beta}}_2$ . . . 88

3.3.3 Thermal step during reverse loading . . . 90

3.3.4 Elastoplastic consistent tangent modulus $\boldsymbol{D}^{ep}$ . . . 91

3.3.5 Summary of the new model . . . 92

3.4 Validation of isotropic & kinematic hardening during monotonic loading . . . 96

3.4.1 Bauschinger effect determination at elevated temperatures . 97

3.4.2 FE model descriptions . . . 97

3.4.3 Results and discussion . . . 99

3.5 Validation of Bauschinger effect and transient hardening 101
3.6 Validation of thermal unloading algorithm 105
3.7 Validation for multi-axial loadings 106
  3.7.1 Experiments in literature review 106
    3.7.1.1 Room temperature 107
    3.7.1.2 Elevated temperature 650 °C 108
  3.7.2 Validation model in Abaqus 108
    3.7.2.1 Model descriptions 108
    3.7.2.2 Material properties 109
  3.7.3 Validation results 109
    3.7.3.1 Initial yield surfaces 109
    3.7.3.2 Subsequent yield surface after radial pre-loading at room temperature 111
    3.7.3.3 Subsequent yield surface after pure torsion pre-loading at 650 °C 111
3.8 Validation for transient loadings during heating and cooling 112
  3.8.1 Experimental model 112
  3.8.2 Validation model 113
  3.8.3 Validation of isothermal thermo-mechanical experiments . . 114
  3.8.4 Validation of transient (anisothermal) thermo-mechanical experiments 116
    3.8.4.1 Comparison with isotropic hardening model . . . 118
3.9 Uniaxial material model 119
3.10 Summary and conclusions 119

4 Remaining Fire Resistance of PFP Coated Steel Frames Subjected to A Moderate Earthquake 121
4.1 Introduction 121
4.2 Cementitious PFP damage indicator 123
4.3 Impact of seismic steel frame designs on PFP damage 126
  4.3.1 FE Model geometry 127

4.3.2 FE model Loadings 129

4.3.2.1 Gravity loads 129

4.3.2.2 Earthquake load 130

4.3.3 FE model Materials 130

4.3.4 FE models for seismic analysis 130

4.3.5 Earthquake response 131

4.3.6 Damage to cementitious PFP 132

4.3.7 Comparison study of strain results 133

4.3.7.1 Moment resisting frame 133

4.3.7.2 Concentrically braced frame 133

4.3.7.3 Discussion 135

4.3.8 Sensitivity study of modelling assumptions of MRF 135

4.3.8.1 Effect of floor slabs on strain distributions 148

4.3.9 Conclusions of sensitivity study 151

4.4 Remaining fire resistance assessment of MRF 152

4.4.1 PFP damage area identification 152

4.4.2 Heat transfer analysis 155

4.4.2.1 Fire loading 155

4.4.2.2 Fire protection required 155

4.4.2.3 Coefficients for heat transfer analysis 155

4.4.2.4 Heat transfer analysis results 156

4.4.3 Thermo-mechanical analysis 157

4.4.3.1 FE model 157

4.4.3.2 Thermo-mechanical analysis results 158

4.5 Discussion and conclusions 160

5 A Thermo-mechanical Analysis of Stainless Steel Structures in Fire 163

5.1 Introduction 163

5.2 Temperature development in stainless steel I sections 164

5.2.1 Heat transfer model validation 164

5.2.2 Heat transfer parametric study 166

5.3 Stainless steel structural behaviour in fire 167

5.3.1 Simply supported beams in fire 168

5.3.1.1 FE model validation 168

5.3.1.2 Comparison study 170

5.3.1.3 Discussion 174

5.3.2 Plane frame structures in fire 175

5.3.2.1 FE model validation 175

5.3.2.2 Comparison study 177

5.3.2.3 Effect of axial restraints 181

5.4 Conclusions 189

6 Bauschinger Effect in Steel Beams Subjected to Realistic Building Fire 191

6.1 Introduction 191

6.2 Thermal loading 193

6.3 Numerical analysis in 3D 194

6.3.1 FE model 194

6.3.2 Stress/Deformation analysis —Case 1 197

6.3.3 Stress/Deformation analysis —Case 2 199

6.3.4 Comparison study 200

6.4 Numerical analysis in 2D 202

6.4.1 Stress deformation analysis 202

6.5 Summary 205

7 Conclusions and Future Work 206

7.1 Summary and conclusions 206

7.1.1 Application to remaining structural fire resistance 207

7.1.2 Application for novel construction materials 208

7.1.3 Application for advanced structural design 209

7.2 Limitations and future work 209

Appendices 211

A Numerical Algorithm for Combined Isotropic and Kinematic Hardening Model 211

B Implementation for Plane Stress Material Model 214

C Derivation of Elastoplastic Consistent Tangent Modulus D^{ep} 217

D Tables of Parameters 221

Bibliography 224

List of Figures

1.1 Performance based engineering design framework for structures in fire 22

2.1 Stiffness reduction of carbon steel and stainless steel at elevated temperatures [1,2] 42
2.2 2% Strength reduction of stainless steel and carbon steel at elevated temperatures 43
2.3 Thermal elongation 53
2.4 Thermal conductivity 54
2.5 Specific heat 55
2.6 Material model construction illustrations 60
  a Case A 60
  b Case B 60
2.7 Construction of stress strain path, proposed by Bailey et al. [3] 63
2.8 A schematic view of two surface model 68

3.1 Stiffness reduction factors 77
3.2 EC3 stress-strain curves vs Least square fitting 79
3.3 Stress-strain curves at elevated temperatures, Nominal vs Curve fitting 80
  a Austenitic group III 80
  b Duplex group II 80
3.4 Combined isotropic/kinematic hardening yield surfaces with temperature changes in the deviatoric stress space 82
3.5 Re-positioning of yield surface due to changing temperatures 84

3.6 Reverse loading criterion 86

3.7 Proposed model during loading –reverse loading in the deviatoric stress space 87

  a Loading 87

  b Reverse loading 87

3.8 Typical Bauschinger ratio and Reverse loading ratio evolution . . . 89

3.9 Proposed model during reverse loading in the deviatoric stress space 90

3.10 Yield surface evolution, T_0 to T_2 94

  a Initial yield surface at T_0 and T_1 94

  b Yield surface T_1 94

  c Thermal step, T_1 to T_2 94

  d Mechanical step, T_1 to T_2 94

3.11 Bauschinger ratio, least square fitting 98

3.12 Reverse yield test specimen (all dimensions in mm) [4] 98

3.13 Hardening variables comparison 100

  a Isotropic 100

  b Kinematic 100

3.14 Stress-strain curves comparison 102

  a T= 300°C 102

  b T= 700°C 102

3.15 Hardening models comparison 104

  a T= 300°C 104

  b T= 700°C 104

3.16 Thermal unloading validation 106

3.17 Abaqus plate model 109

3.18 Initial yield surfaces comparison 110

  a Room temperature 110

  b 650 °C 110

3.19 Subsequent yield surfaces comparison 112

  a Room temperature 112

b 650 °C 112

3.20 Thermo-mechanical test specimen (all dimensions in mm) [5] . . . 114

3.21 Stress strain curves comparison, Isothermal thermo-mechanical experiments 115

a T =150 °C 115

b T =350 °C 115

c T =600 °C 115

d T =850 °C 115

e T =1000 °C 115

3.22 Stress strain curves comparison, Transient thermo-mechanical experiments 116

a Tmax =350 °C 116

b Tmax =600 °C 116

c Tmax =850 °C 116

d Tmax =1000 °C 116

4.1 $\varepsilon_{critical}$ vs. Stress reversal Number 126

4.2 Acceleration history of 1994 Northridge earthquake 127

4.3 Moment resisting frame in N-S direction (penthouse not shown) . . 128

4.4 Concentrically braced frame in N-S direction (Typical) 129

4.5 Max. tensile strain diagram, MRF 135

a Strain distribution in Pier 1 135

b Strain distribution in Pier 2 135

c Strain distribution in Pier 3 135

d Strain distribution in Floor beams 135

4.6 Max. tensile strain diagram, Concentrically braced frame 137

a Strain distribution in Pier 1 137

b Strain distribution in Pier 2 137

c Strain distribution in Pier 3 137

d Strain distribution in Floor Beams 137

4.7 Model 1, Schematic illustration 140

4.8 Model 2, Schematic illustration 140
4.9 Panel zone, Schematic representation 141
4.10 Model 3, Schematic illustration 141
4.11 Model 4, Schematic illustration 142
4.12 Leaning column system, Schematic representation 142
4.13 Strain distribution in Pier 3, MRF 145
  a Model 2 145
  b Model 3 145
  c Model 4 145
  d Model 5 145
4.14 Strain distribution in floor beams, MRF 147
  a Model 2 147
  b Model 3 147
  c Model 4 147
  d Model 5 147
4.15 Bending moment diagram of floor beams, Gravity load 149
  a Model 1 149
  b Model 2 149
  c Model 3 149
4.16 Pier 3 moment diagram, Gravity load 150
4.17 Pier 3 Max. moment diagram, Seismic load 150
4.18 Max. negative &positive moments in floor beams, Seismic load . . . 151
  a Model 2 151
  b Model 3 151
4.19 Schematic view of the cementitious PFP damage identified in MRF, Model 4 153
4.20 Strain distribution in Pier 1 & 2, Model 4 154
  a Pier 1 154
  b Pier 2 154
4.21 Temperature history results 157

4.22 Schematic illustration of thermal loading application 157
4.23 Pier 3 joint displacement comparison 159
4.24 Vertical reaction development, with PFP damage 160

5.1 I section subjected to 4 sides heating 165
5.2 Temperature development within sections 165
5.3 Temperature difference in bottom flange, 4 sides heated 167
5.4 Temperature difference in web, 4 sides heated 167
5.5 Validation of simply supported beam model 169
  a Four sides heating 169
  b Three sides heating 169
5.6 Deflection comparisons, Simply supported beam 172
  a Series 1 and 2 172
  b Series 3 and 4 172
5.7 Stress strain development, simply supported beam 174
  a Series 1 174
  b Series 2 174
  c Series 3 174
  d Series 4 174
5.8 EHR3 frame configuration 176
5.9 EHR3 frame deflection comparison 177
5.10 Beam midspan deflection V4 179
5.11 Column midspan deflection U2 180
5.12 Stress strain at the beam-column joint 182
  a Stress strain in the beam 182
  b Stress strain in the Column 182
5.13 EHR3 frame with external axial restraints applied 183
5.14 Beam midspan def (V4), Beam L.R.=0.30 184
5.15 Column vertical disp, Column L.R.=0.15 184
5.16 Beam axial force vs. temp., Beam L.R.=0.30 185
5.17 Beam midspan def vs. temp, Beam L.R.=0.60 187

5.18 Column vertical disp vs. temp, Column L.R.=0.30 187
5.19 Stress strain developments at beam-column joint 188
  a Stress strain in the column, $0.05K_\beta$ 188
  b Stress strain in the column, $0.15K_\beta$ 188
  c Stress strain in the beam, $0.05K_\beta$ 188
  d Stress strain in the beam, $0.15K_\beta$ 188

6.1 Structural model geometries 193
  a Case study structural plan view with predefined travelling fire trajectory 193
  b Schematic view of the investigated beam cross-section . . . 193
6.2 Temperature history 195
  a Case 1 195
  b Case 2 195
6.3 Single steel beam modelled, half of the model length shown 196
6.4 Midspan cross-section results, Case 1 198
  a Deflection, $\overline{\varepsilon^p}$ vs. temp 198
  b Axial stress (S11) vs. temp 198
6.5 Midspan cross-section results, Case 2 200
  a Deflection, $\overline{\varepsilon^p}$ vs. temp 200
  b Axial stress (S11) vs. temp 200
6.6 Proposed material model vs. Isotropic hardening model 201
  a Endspan S11 vs. Temp 201
  b Midspan S11 vs. Temp 201
6.7 Midspan deflection, 2D compared with 3D 203
6.8 Midspan S11 vs. Temperature, 2D 204
  a Case 1 204
  b Case 2 204

List of Tables

2.1 Simplified grade family at elevated temperatures 43

2.2 Mean coefficient of thermal expansion ($10^{-6}/°C$) 53

2.3 Types of the constitutive equations 58

3.1 Model parameters, Isothermal experiments 114

3.2 Model parameters, Transient experiments 117

4.1 Gravity loads 129

4.2 Fundamental building periods 131

4.3 Inter-story drift ratios, Moment frame model 132

4.4 Inter-story Drift Ratios, Braced Frame Model 132

4.5 Number of cycles in Pier 3, Moment frame model 132

4.6 MFR inter-story drift ratios (%), Pier 3 143

4.7 Cementitious PFP thickness 155

5.1 Section dimensions and Section factors 166

5.2 Material properties 171

5.3 Comparison study series, Simply supported beams 171

5.4 Test parameters used in Validation 177

5.5 Comparison study series, EHR3 frame 178

A.1 Numerical algorithm for the proposed combined isotropic- kinematic hardening model 211

B.1 Numerical algorithm for plane stress material 215

D.1 Least square fitting results for hardening law, EC3 carbon steel . . . 221

D.2 Least square fitting results for hardening law, Austenitic III 221

D.3 Least square fitting results for hardening law, Duplex II 222

D.4 Least square fitting results, 304L stainless steel in Section 3.4 222

D.5 Least square fitting results, Low carbon steel in Section 3.5 222

D.6 Least square fitting results, 316 stainless steel in Section 3.7 222

D.7 Least square fitting results for hardening law, St 37.2 carbon steel in [6] 222

D.8 Least square fitting results, 304 Stainless Steel 223

D.9 Bauschinger ratio calibration results, based on Fig.8 in [5] 223

Chapter 1

Introduction

1.1 Motivation and aims

This project aims to improve the performance-based structural fire design, and subsequently apply it to a range of parametric studies to gain valuable engineering insights into realistic steel structural behaviour in building fires.

The most important advantage of performance-based engineering for structural fire design is that the structural resistance or capacity is gauged accurately against realistic representations of demand, in this case, fire loading. Figure 1.1 illustrates the performance-based engineering design framework for structures in fire [1,7]. It brings together demand (fire modelling), propagation (heat transfer analysis), structural capacity design (thermo-mechanical analysis) and re-evaluation. The integration of this framework has been greatly facilitated by the continuous development of computational tools, for instance computation fluid dynamic (CFD) method and finite element analysis (FEA) method.

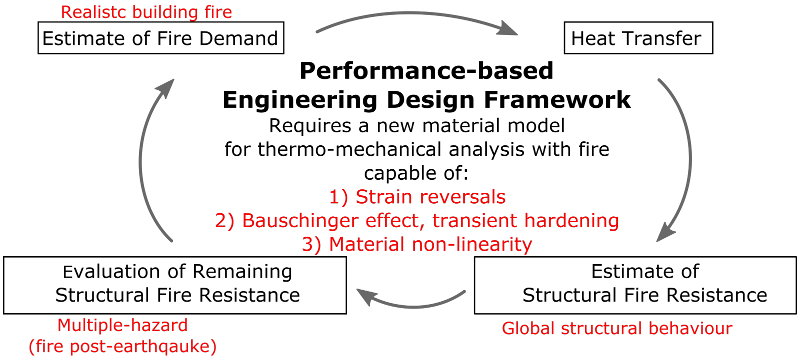

Figure 1.1: Performance based engineering design framework for structures in fire

Performance-based design allows engineers to take advantage of computational tools in novel design cases where a traditional prescriptive approach becomes unsuitable. The computational tools have also allowed engineers to explore structural behaviour in realistic building fire scenarios, unbound from the limitations of experiments, to embrace innovations in building design. As computational tools are being applied to an increasingly wide range of design scenarios, the fundamental assumptions adopted at the early stage of structural fire design have to be revisited and reviewed, because their applicability in new design scenarios might become inappropriate.

For decades, the fire demand on structures was estimated by using sets of simplified temperature time curves encompassing only heating stage, assuming uniform gas temperatures within building compartments. This fundamental assumption has allowed thermo-mechanical analysis to use simple material models that did not consider strain reversals during fire.

In modern architectural designs where large open spaces prevail, the 'uniform gas' assumption has been criticised for being unrealistic. A statistical survey [8] carried out on the Informatic Forum Building at the University of Edinburgh, opened in 2009, with a modern open-plan design, indicated that the fundamental assumptions made for traditional fire safety design methods in Eurocode 1 [9], e.g., opening factor <0.2, compartment height $<4m$, compartment size <500 m^2, are applicable to only 8% of the total volume of the building. With the continuous development of travelling fire methodology framework [10–12], which accounts for the spatial development of building fires, Dai et al. [13] have demonstrated that structures will experience cross-sectional temperature gradient reversals and 'cyclic' heating and cooling during the course of a fire development. Consequently, when performing structural analysis subjected to realistic building fire, the "no (mechanical) strain reversals in the material during fire" simplification can no longer be assumed valid.

For estimating the structural fire resistance, the global structural behaviour has not always been taken into consideration. The traditional structural design has been component based, with fire protection applied as an ad hoc solution. Investigations into how buildings actually respond to a fire as a structural system only started after the observation during the Broadgate fire incident [14] in London in 1990. During the Broadgate fire, the partly completed 14 story office block exhibited no collapse despite the passive fire protection to the steelwork being incomplete. The backbone of the performance-based structural fire design is taking global structural behaviour into account. It allows for load redistributions between the hot and the cold part of the structures, and structural redundancies to be taken advantages of.

The importance of selecting a realistic design fire scenario; the significance of taking global structure behaviour into account are further acknowledged and reinforced by the numerous research [15–19] carried out investigating the global collapse mechanism of tall buildings after the collapse of the World Trade Centre buildings on September 11, 2001. As a result, the "no (mechanical) strain reversals in the material during fire" simplification becomes unsuitable for estimating structural fire resistance.

Another field where the performance-based structural fire design is gaining growing attention and research interests is its application to multi-hazard analysis frameworks, whether adopting it as a design tool to consider fire following earthquake, or using it to evaluate remaining fire resistance of structures post-earthquakes. For this type of applications, strain history from seismic loadings has to be taken into account for the structural behaviour in fire. Therefore, for multi-hazard analysis frameworks, it is inappropriate to use material models that are not able to handle strain reversals during fire.

The post-earthquake structural fire resistance can be undermined by the damage to the passive fire protection (PFP) systems caused by earthquakes. New construction materials that are able to survive building fires without any PFP provide a potential solution to mitigate this safety hazard. Additionally, economical and environmental benefits can be achieved by eliminating the application of PFP to steel frame structures.

Recent experimental research [20–22] on structural stainless steel materials has suggested that structural stainless steel has potentially superior performance in fire, compared to normal carbon steel. However, there is little experimental data on large fire tests for stainless steel structures, because testing the behaviour of steel sub-assemblies and frame structures in a fire is extremely expensive and one single test provides only a limited amount of data. The current research gap in understanding stainless steel structural systems in fire can be approached economically and efficiently by using the FEA. One of the distinctive material characteristics of stainless steel when compared to carbon steel is its higher material non-linearity. The non-linear stress-strain behaviour of the steel materials have to be represented properly by the material models. The material non-linearity is regarded as a norm in other engineering fields. But it is not commonly modelled in structural engineering design, largely owing to the elastic perfectly plastic behaviour that carbon steel exhibits favourably at room temperature.

Reviewing the present development of the performance-based framework of structural design in fire, it has revealed that the assumption "no (mechanical) strain reversals in the material during fire", made in the early days of structural in fire design is no longer suitable for today's engineering requirements. When considering a global structure subjected to a simple uniform heating compartment fire, mechanical strains develop as thermal strains being converted into mechanical strains due to restrained thermal expansions. The mechanical stress re-distributions between the cold and hot part of the structure can therefore lead to non-monotonic loading at certain parts of the structure. Furthermore, complex building fires, such as travelling fires that bring about simultaneous heating and cooling within one large compartment, can cause non-monotonic mechanical strain development in the structural components within the compartment due to their complicated thermal loading history. Additionally, mechanical strain reversals are likely to develop during the heating stage of a fire in structures where high initial strains already exist due to historically experienced earthquakes.

Therefore, the performance-based structural fire design framework requires a sophisticated material model for thermo-mechanical analysis with fire that can model the following material behaviour at elevated temperatures:

1. Handle non-monotonic loading paths;
2. Include the Bauschinger effect and transient hardening behaviour associated with strain reversals at elevated temperatures;
3. Model material non-linearity at elevated temperatures.

1.2 Research scope and approach

This research aims to develop a plasticity material model for the purpose of thermo-mechanical analysis of steel structures in fire. A combined isotropic and kinematic hardening model is developed to account for the Bauschinger effect and the transient hardening behaviour of steels at elevated temperatures. The numerical algorithm developed for the new material model is firstly implemented in the Abaqus Umat subroutine [23] and validated using experimental data from a literature review. The work is presented in Chapter 3.

The new multi-axial material model is also adapted to a 1D plasticity model and implemented in the open source software OpenSEES [24] as a uniaxial material model. It is adopted to investigate the remaining structural fire resistance of steel frame structures with damaged PFP resulted from a moderated earthquake. An integrated multi-hazard framework for assessing the post-earthquake remaining fire resistance of steel frames protected by cementitious PFP is proposed in Chapter 4.

Chapter 5 investigates the structural behaviour of stainless steel in fire using the FEA method with the new material model, focusing on the behavioural differences between carbon steel and stainless steel structures. The impact of stainless steel's high material non-linearity and high thermal expansion on its structural fire performance is analysed and discussed.

In Chapter 6, the proposed material model is adopted to investigate the structural behaviour of a steel I-section beam subjected to realistic building fires simulated using the extended travelling fire framework (ETFM) model [12]. The FEA investigation is performed using a 3D model in Abaqus with the proposed multi-axial material model implemented in Umat, and also using a 2D model in OpenSEES with the new material model implemented as a uniaxial model.

Chapter 2

Literature Review

2.1 History of structural fire resistance design

The structural fire resistance design philosophy can be generally divided into the prescriptive-based and performance-based approaches. The prescriptive approach can be considered an application of a general set of rules or well-known solutions, that provides a previously accepted level of safety. The performance-based approach focuses on the aims of protecting and crafting solutions to meet the aims. In prescriptive codes, the safety solutions are prescribed without explicitly stating the intent of the requirement. Whereas in performance-based design procedures, desired objectives are presented and the engineers are given the freedom of selecting the solution that will meet the targets.

Yet the actual boundary of prescriptive and performance-based design principles is always evolving. It's commonly said that "yesterday's performance is today's prescription". Matured solutions of today will become the standards of tomorrow.

Historically, fire resistance design of structures has been based on upon single element behaviour in standard fire resistance test. It can be said that fire resistance testing methods relate to the behaviour of components and structures in the post-flashover fire stage. This method enables elements of construction such as walls, floor, columns and beams to be assessed according to their ability to remain stable, resist the passage of flame and hot gases and provide resistance to heat transmission.

The origin of the standard fire curve was the work conducted by Robinson in

1917 [25]. Robinson took temperature data from a number of furnace tests and specified a standard curve that fitted the data most closely. This temperature time curve has been incorporated into a number of national and international standards, for example ISO 834 [26], Eurocode 1 [9], ASTM E-119 [27], with essentially no changes since its development. The standard temperature time curve is defined as:

$$T = 20 + 354log(8t+1) \tag{2.1}$$

where T is the fire temperature and t is time.

Because this fire curve is derived based on the test data from furnaces, it naturally does not represent accurately the realities of a building fire. As a result, the validity of this curve has always been a subject of criticism. However, due to the urgent need to develop a reliable test method to achieve world-wide harmonisation of fire test results, the adoption of an internationally uniform standard fire curve was pursued at the turn of the 20^{th} century, so that a result obtained in one laboratory will be equally valid in all other test centres. As indicated by Ira Woolson [28], then Chairman of the National Fire Protection Association's (NFPA) Committee on Fire Resistive Construction, the overarching goal of those efforts was to adopt one single standard for all fire tests and remove an immense amount of confusion within the fire testing community.

In 1928, based on the recognition that the standard time temperature curve was not a 'real' fire, Simon Ingberg [29] presented a method for quantifying a fire's 'severity' resulting from burnout of all the combustible contents in a compartment. Ingberg's method assumes that if the area under the temperature time curves of two fires are equal then the severity of the fires is also equal. Using this argument, Ingberg suggested that the standard fire curve could represent real fires since the area under it and the area under the curves from real fires tended to be about equal. However, in reality, the equal area hypothesis was proved to be false according to the work done by Drysdale [30] and by Thomas [31]. Drysdale pointed out that the radiative heat flux from fire is proportional to T^4 (T in K), so simple scaling is impossible as heat transfer is dominated by radiation, e.g., 10 minutes at 900 °C will not have the same effect as 20 minutes at 450 °C.

Despite it not being obvious at the time, Ingberg's publications on this topic fundamentally (and unfortunately) linked the concept of 'time' to the performance objectives used to define the 'fire resistance' of structural elements. In the decades that followed, alternative severity metrics were introduced, and in some cases adopted, by the structural fire engineering community. These included: the 'Maximum Temperature Concept', the 'Minimum Load Capacity Concept', and the 'Time Equivalent' Formulae; however, all of these were fundamentally linked to results from isolated elements tested under the 'standard' time temperature curve [32].

Apart from criticisms of the standard temperature time curve, the reliability of standard fire tests has also always been a matter of concern. Harmathy [33] pointed out that tests in different furnaces were unlikely to give the same results.

In short, the problem of measuring temperature in furnaces stems from the fact that the furnace gas temperature is not the same as the corresponding black body heat radiation level. The difference between the two is generally greater in shallow (often gas fuelled) furnaces than in deeper (often oil fuelled) furnaces. UK fire resistance testing furnaces are mostly powered by natural gas while many European test furnaces are fuelled by oil.According to the current ISO 834 [26] and corresponding national standards, the furnace temperature is controlled and obtained by rather thin thermocouples. They give, in principle, the gas temperature. The specimens, however, are more sensitive to the radiation level, particularly in shallow furnaces, depends very much on the furnace wall temperature. The wall temperature is much lower than the gas temperature and therefore the specimen will be exposed to less onerous tests in shallow furnaces than in deep ones.

There have been continuous efforts to develop a method to achieve reliable fire resistance testing results. Harmathy [33] proposed the normalised heat concept, on the basis that the severity of the fire can be expressed as the overall heat penetrating into the enclosure, which provides an approach to compare testing results obtained in unlike furnaces. More recently, Maluk [32] proposed a novel test method —the Heat-Transfer Rate Inducing System (H-TRIS). H-TRIS directly controls the thermal exposure by time history of incident heat flux instead of temperature, consequently is capable of produce testing results of higher repeatability.

Closely linked to the standard fire resistance test is the application of fire protection materials. The fire protections can be designed in accordance with the prescription provided by the 'yellow book' (ASFP, 2000) [34] or the BSI PD 7974-3 [35], or determined using EC 3 Part 1-2 [1]. All the approved fire protection materials have been tested according to the standard fire test procedures, as specified in BS 476 Part 21 [36].

The adoption of fire protection materials approved by standard fire testing caused the separation of fire safety engineering design from structural engineering design. From the separation point onward, it has become a common practice that structural engineers design a structure for a room temperature environment, with fire protection requirement being left as an add-on design after the structural design process.

Unfortunately the repercussions of this separation are profound. To an extent it has allowed structural engineers to focus on structural analysis and optimisation, freed from fears of losing structural capacity due to elevating temperatures within structural components. Meanwhile it left fire safety engineers to focus their research on fire dynamics and fire prevention systems. However for decades, this led to an unawareness of how building structures actually behave in fire within the structural engineering community.

The realisation that building resists fire in a far more complex manner than standard fire tests suggest was brought home forcibly in June 1990 during the fire incident in a partly completed 14 story office block on the Broadgate development in London [14]. Despite the passive fire protection to the steelwork was incomplete at the time of fire, no structural failure occurred and the integrity of the floor slab was maintained during the fire.

The observations from real building fire events provoked pondering about how buildings can be designed to resist fire. In order to better understand the global structural behaviour of multi-story steel frame building, Building Research Establishment (BRE) conducted large scale tests in an eight-story steel frame structure, which was designed and constructed to resemble a typical modern city centre office structure, at the Cardington Large Building Test Facility. The Cardington frame fire tests provided researchers a wealthy amount of testing data to investigate and understand the behaviour of the whole frame composite steel concrete structures in response to fire [37–39].

Since the Cardington tests, and the later 9/11 World Trade Centre events, the importance of selecting a realistic design fire scenario; the significance of taking global structure behaviour into account have been acknowledged in present design codes and standards. Structural Eurocode 1-4 gives guidance on design procedures following both prescriptive rules and performance-based codes. Both design approaches allow for using advanced calculation models for analysing mechanical behaviour of individual structural members, part of the structure or the entire structure.

One of the major differences between the prescriptive approach and the performance-based approach proposed by the current Eurocodes lies in the selection of fire load, with prescriptive approach using nominal fire curves while performance-based approach allowing for fire models defined by designers based on physical and chemical parameters.

In order to define a fire model according to the performance-based approach, it requires expertise in both structural mechanics and fire dynamics. Consequently there is a present need to 'reunite' the fire safety engineers and structural engineers. Buchanan [40] in 2008 expressed his view that "fire engineers and structural engineers need to talk to each other much more than they do now, and each group needs to learn as much as possible of the other discipline". This viewpoint is recently strengthened again by Dai et al. [12] when discussing the current advancement in 'travelling fire' research.

2.2 Performance-based structural fire resistance design framework

As the performance-based engineering design framework enables the determination of structural resistance against realistic fire demand, it requires a much higher level of understanding of the available capacity of the analytical and computational tools that aid the design framework. These state of the art tools are able to provide reliable estimate of demand and capacity meanwhile taking into account, in some reasonable way, the uncertainties inherent in these estimations. This section reviews the tools developed for the four cornerstones of the performance-based structural in design framework, namely estimate of fire demand; heat transfer; estimate of structural fire resistance and evaluation of remaining structural fire resistance.

2.2.1 Estimate of fire demand

A performance-based approach to fire safety evaluation and building design is an elaborate process consisting of many steps and requires the use of decision making tools based on analytical and computational models. The selection of a suitable fire of assumed characteristics, which is referred to as the "design fire", is one of the most important steps in this process [41]. A design fire is generally considered to be a quantitative description of the main time-varying properties of a fire based on reasonable assumptions about the type and quantity of combustibles, ignition method, growth of the fire and its spread from the first item ignited to subsequent items, and the decay and extinction of the fire [42].

Following ignition, the evolution of a fire within a building generally consists of three stages: growth or pre-flashover period; fully-developed or post flashover period, and decay period. The flashover marks the beginning of a fully developed fire and is generally associated with enclosed spaces [30], and can be defined as the transition from a localised fire to the general conflagration within the compartment when all fuel surfaces are burning [43]. The occurrence of the flashover is generally believed to be promoted by hot-gas temperature between 500 and 600 °C, and heat flux levels of about 15-20 kW/m^2 at the floor level of the enclosure [30].

Each component of a holistic fire safety design is related to a different stage of the fire development. The life safety of occupants is particularly important during the pre-flashover stage since toxic products of combustion can quickly give rise to untenable conditions. Therefore, the fire growth rate critically influences the egress design, while the smoke production largely determines the smoke ventilation system design. The most common method to describe fire growth is using the t-square model, which gives the Heat Release Rate (HRR) by [30]:

$$\dot{Q} = \alpha t^2 \tag{2.2}$$

where $\dot{Q}$ is HRR (kW); α is the fire growth coefficient (kW/s^2); t is the time after effective ignition (s).

The structural integrity of the building and the safety of fire rescue personnel are the main concerns during the post-flashover, i.e., the fully developed fire stage. When addressing structural behaviour, the growth and flashover within time scales that are much smaller than those required to significantly affect the mechanical strength of structural systems, consequently the focus of estimating fire demand for structural fire resistance design has been on fully developed fires. Therefore, the fire demand for structural fire resistance design is usually quantified as a simplified time temperature relationship.

When quantifying the fire in a building environment for structural fire resistance design, the concept of compartment fire has permeated through most of prescriptive codes, acted as a pre-requisition for some fire models. Compartmentalisation was initially exploited as a means of reducing the rate of fire spread in buildings to enable safe evacuation and a more effective intervention by fire service. Later, it was adopted by engineers as a basis for establishing, under certain specific circumstances, temperatures and thermal loads imposed by a fire to the building structure.

2.2.1.1 Analytical fire models

One of the first formal attempts to account for fire action on building structures emerged in 1918, when the American Society for Testing and Materials (ASTM) standardised a time temperature relationship, called the fire curve, which subsequently became the 'Standard Fire Curve', as in Equation 2.1. It can be said that the Standard Fire Curve can represent the fire demand of a fully developed compartment fire.

Kawagoe [44] questioned the physical basis of the Standard Fire Curve and established the concept of the compartment fire. Through experimental observations, he defined the link between ventilation, gas phase temperature and burning rate. Numerous research [45–49] published during 1960-1990 provided refinements and extensions to the fundamental concept initiated by Kawagoe [44]. Lie [45] proposed a time temperature curve to represent a fire in a lightweight construction building; Pettersson et al. [46] emphasised the time evolution of fire and proposed the Swedish parametric fire curves; Ma and Makelainen [47] developed a parametric time temperature curve to represent small to medium post-flashover fire temperatures; Barnett [48, 49] developed an empirical model for compartment fire temperatures by curve fitting 142 natural fire tests using a single log normal equation to represent both growth and decay phase.

The basic principle behind the compartment fire is that the characteristic time scales for pre-flashover stage are very short. As a consequence, energy is assumed to be released as a function of reactant supply, i.e., oxygen in the case of 'ventilation-controlled' fire and fuel in the case of a 'fuel-controlled' fire.

On the basis of compartment fire concept, assuming uniform temperature distribution within the compartment, Eurocode 1 [9] provides a parametric fire model, allowing a time temperature relationship to be obtained by a function of compartment size, fuel load, ventilation openings and the thermal properties of wall lining materials. In general, parametric curves include a non-linear heating phase, followed by a linear cooling phase. The Eurocode parametric fire model is applicable to compartments with mainly cellulosic type of fuel loads, floor areas up to 500 m^2, thermal inertia of the wall lining between 100 and 2200 $J/m^2s^{1/2}K$ and opening factors between 0.02 and 0.2 $m^{1/2}$.

Eurocode parametric fire curves are the most popular approach to estimate the fire demand in a post-flashover building fire environment. The limitation of its validity roots in the fact that our knowledge of the behaviour of compartment fires comes from experiments with near cubical compartments, with characteristic dimensions ranging from $0.5m$ to $3m$ [30].

In circumstances where fuel distribution is localised, a fuel-controlled fire can remain in pre-flashover stage. Such fire scenarios are likely to be found in parking buildings [50], airports, metro stations, atriums and bridges [51], and are discovered displaying significant spatial variation of heat flux or temperature. For estimating fire demand of localised fires, the localised fire model of Eurocode 1 [9] can be used provided that the fire plume impinges on the ceiling. The 'plume impingement' is the pre-requisition to its application as Eurocode 1 localised fire model is based on Hasemi localised fire tests [52, 53]. For smaller localised fires that produce no plume impingement or in cases of fire in open air, Eurocode 1 [9] suggests that the Heskestad method [54] may be adopted.

With contemporary structures becoming open and spacious, the validity of compartment fire concept in modern structural design has been challenged in recent years, based on the ground that in large building enclosures fire naturally evolves in the scale of both time and space. The spatial and temporal distribution of temperature have been observed in recent large compartment fire tests [55–57]. In addition, after reviewing various compartment fire tests conducted before 2010, Dai et al. [12] concluded there had always been a fire spreading nature recorded in those early fire tests despite the size of the tested compartments were smaller than 200 m^2.

The spreading nature of fire presents a challenge to the estimate of fire demand for large building compartments. In 2007, Rein et al. [58] firstly introduced the terminology "travelling fire" to describe the spreading nature of fire observed in large enclosures. Sten-Gottfried and Rein [10, 11] later proposed a travelling fire model, which uses Alpert's ceiling jet model [59] to calculate far field temperature and assumes a uniform temperature (800-1200 °C) for near field.

Recently, Dai et al. [12] proposed a new travelling fire framework, which is constructed based on a 'mobile' version of Hasemi's localised fire model combined with a simple smoke calculation for the areas away from the fire. Implemented in open source finite element software OpenSEES [24], Dai's fire model enables the analysis of temperature development accounting for the existence of a smoke layer and the varying surface fuel distribution which are ignored in Sten-Gottfried and Rein's model.

This section has reviewed various analytical fire models, providing engineers with approaches to estimate the fire demand of a building fire for structural fire resistance design. In order to select a suitable fire model for structural resistance fire design, structural engineers have to be fully aware of each model's limitations and applicabilities.

2.2.1.2 Computational fire dynamics models

Fire behaviour in a building environment is complex, influenced by the building's geometry, ventilation and type of occupancy. Computational fluid dynamic (CFD) models allow the simulation of complex physical phenomena for any combination of geometry, ventilation condition and fuel density. CFD analyses systems solving fluid flow, heat transfer and associated phenomena, comply with the following conservation laws of physics:

1. the mass of a fluid is conserved;
2. the rate of change of momentum equal the sum of the forces on a fluid particle (Newton's second law)
3. the rate of change of energy is equal to the sum of the rate of heat increase and the rate of work done on a fluid particle (first law of thermodynamics)

There are many CFD tools now available, for example, Fire Dynamics Simulator (FDS), OpenForm, Ansys Fluent, and Smartfire. Due to its complex nature, it's long been commented that the results of CFD models often show high inconsistency between various users, and high error margin when compared with testing results as observed in Dalmarock fire experiments [60,61]. There has been an enormous amount of effort put into model validations within FDS community with the aim of building a broad database of validation studies which can help assess the inconsistency of the simulation results between models and their users [62]. Nevertheless, for building environment that sits outwith the applicability of analytical fire models, CFD equips engineers with a scientifically sound approach for fire demand estimate.

2.2.1.3 Design fires and fire scenarios

The magnitude of fire demand is predominantly decided by the selection of design fire. Analytical fire models and CFD models provide an engineering with description of a design fire scenarios in terms of a temperature time relationship or a HRR time relationship.

Considering fire being a future event means that there is an endless number of possible fire scenarios. The final choice of design fire can be one specific fire scenario that is considered the worst case scenario, or a combination of a series of fire scenarios. ISO [42] recommends risk assessment and introduced a method based on the event tree analysis for ensuring that all relevant fire scenarios are accounted for, and to make the design fire selection process clearer and more consistent. Baker et al. [63] proposed to use probabilistic analysis to determine design fires, based on the Monte Carlo technique in combination with a zone fire model.

To conclude, establishing a design fire requires detailed analysis within the framework of performance-based engineering.

2.2.2 Heat transfer for structures in fire

Once the fire demand is established, the next step is to propagate this demand to the structure through heat transfer analysis.

There are three basic mechanisms of heat transfer, which are conduction, convection and radiation. Inside structural components, heat conduction occurs as a flow of heat from high temperature regions to low temperature regions [30]. The basic equation is the Fourier's law, representing a one-dimensional heat conduction, which is given by:

$$q\text{''} = -k\frac{dT}{dx} \tag{2.3}$$

where dT represents the temperature difference across an infinitesimal distance dx, and q” is the rate of heat transfer across the distance. k is the thermal conductivity, which is temperature-dependent for most building materials.

The heat exchanges between a structural member and fire or ambient air are primarily through convection and radiation. Convection occurs when a solid is surrounded by a dynamic fluid, with an empirical relationship known as the Newton’s law:

$$q” = h\Delta T \tag{2.4}$$

where h is the convective heat transfer coefficient, and ΔT is the temperature difference between the solid surface and surrounding fluid. h is highly dependent on the characteristics of the thermal system, which can be determined through a comprehensive study. Eurocode 1 [9] provides some typical coefficients of convection for the commonly accepted fire models.

For perfect given conditions, the rate (E) at which energy is radiated from a body is proportional to the fourth power of its absolute temperature:

$$E = \varepsilon \sigma T^4 \tag{2.5}$$

where σ is the Stefan-Boltzmann constant, T is the absolute temperature (K), ε is the emissivity, which is largely a function of surface finishes. ε is equal to its absorptivity according to Kirchhoff’s Law [30]. For black body $\varepsilon = 1.0$.

The resulting heat flow by radiation between flame and a structural member can be given by:

$$q” = \Phi \varepsilon_r \sigma (T_f^4 - T_m^4) \tag{2.6}$$

where T_f is the absolute temperature of the fire flame, and T_m is the absolute temperature of the structural member. Φ is known as the configuration factor and usually is given a value of 1.0 if the member is completely surrounded by flames. ε_r represents the resultant emissivity when considering reflectivity, which is given by:

$$\varepsilon_r = \frac{1}{1/\varepsilon_f + 1/\varepsilon_m - 1} \tag{2.7}$$

where ε_f is the emissivity of the fire flame and ε_m is the emissivity of the structural member.

Heat absorption of the material itself is taken into account in the transient form of the heat conduction equation, which is governed by the following second order diffusion equation:

$$\rho c_p \frac{\partial T}{\partial t} = \nabla(k \nabla T) \tag{2.8}$$

where ρ is the density of the structural member, c_p is the specific heat capacity, and k is the thermal conductivity.

The solution of this transient heat conduction requires the specification of initial condition and boundary conditions, which are given as:
Initial condition for the domain:

$$T(t_0) = T_0, \quad in \quad \Omega \tag{2.9}$$

Natural boundary condition:

$$T(t) = T_b, \quad on \quad \Gamma_T \tag{2.10}$$

Essential boundary condition:

$$-k \triangledown T = \bar{q}, \quad on \quad \Gamma_q \tag{2.11}$$

where $\bar{q}$ is the heat flux on the boundary, which consists of convective heat flux (q_c), radiant heat flux (q_r), and prescribed heat flux (q_{pr}),

$$\bar{q} = q_c + q_r + q_{pr} \tag{2.12}$$

2.2.3 Estimate of structural fire resistance

Thermo-mechanical analysis is commonly used for analysing structures in fire for estimating their structural fire resistance.

In a fully coupled thermo-mechanical analysis, the structure deformation affects heat transfer as a result of plastic work while the heat transfer in turn affects the structural deformation due to material thermal softening. The flame edge temperature has been observed at about 550 °C in small-scale compartment fires and the maximum temperature in a post-flashover building fire can reach 1200 °C [30]. As a result, for most structures in fire, the internal heat accumulation generated from plastic work during fire is commonly considered negligible when compared to the heat received from the external fire source.

The thermo-mechanical interaction considered in structural fire analysis is a one-way coupling thermo-mechanical analysis in which an uncoupled heat transfer simulation drives a stress analysis through thermal expansion. The fire loading is introduced to the structure as a temperature time history produced by the heat transfer analysis. The temperature effects on the constitutive material model are result of external fire heating only.

2.2.3.1 Material softening at elevated temperatures

The primary cause to the loss of structural fire resistance is the material softening at elevated temperature which can be presented in two forms: reduction in the tangent modulus and the yielding value.

Carbon steel, usually simply referred as the steel in construction industry. The material properties of steel at high temperatures are very different to those at room temperature. The characteristic form of the steel stress-strain curve at ambient temperature is rapidly lost as temperature increases. At 200 °C there is no longer a clear yield point and the stress-strain curve becomes increasingly non-linear at higher temperatures. To obtain an alternative to a yield stress the proof stress concept is often adopted [64, 65]. Typically the proof stress is defined as the stress required to produce a plastic strain of 0.2%. Considering deformation under fire conditions is less critical than at room temperature, Eurocode adopts the strength at 2% strain as the yield strength for structural fire resistance analysis.

There are a number of means by which the stress-strain behaviour of steel at elevated temperatures may be obtained. The two most common methods are the isothermal and anisothermal methods. In the anisothermal method a sample is subject to a known load then heated at a uniform rate; whereas in the isothermal method a sample is heated to a uniform temperature and then loaded. It has been noted that the data derived from any type of high temperature test is very variable even for identical steels [64].

The ability of a material to retain stiffness at elevated temperature is crucial for achieving fire resistant structures. The material stiffness can be measured by the modulus of elasticity, also know as Young's modulus. Figure 2.1 presents the stiffness reduction factors provided by the Eurocode 3 [1] for carbon steel and by the Design Manual for Structural Stainless Steels (DMSSS) [2] for stainless steels. A generic set of stiffness reduction factors is proposed for all stainless steel grades. The comparison shows that stainless steels offer better retention of stiffness than the carbon steel at temperatures higher than 200 °C.

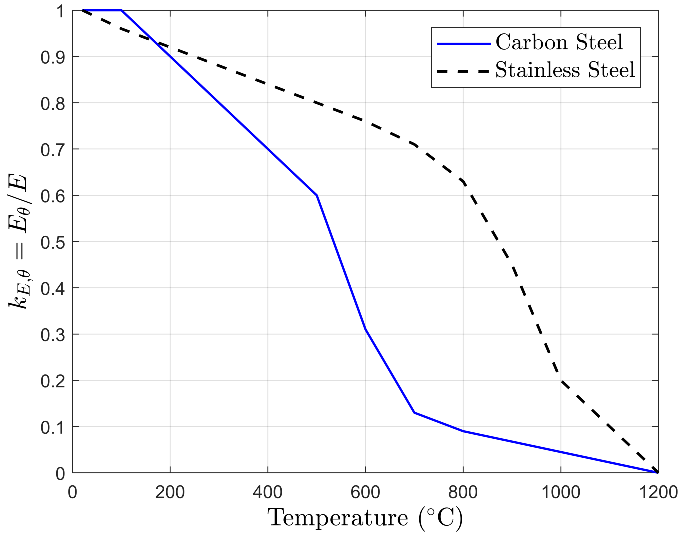

Figure 2.1: Stiffness reduction of carbon steel and stainless steel at elevated temperatures [1, 2]

It is worth noting that, the k_E reduction factors are for the initial modulus of elasticity. At room temperature, unlike carbon steel showing an elastic perfectly plastic behaviour, stainless steel already exhibits a non-linear stress-strain relationship, which means its tangent modulus quickly deviates from its initial elastic modulus as stress approaching the yield strength. Such behaviour can give rise to earlier and faster stiffness reduction for stainless steel structures in fire when the stress

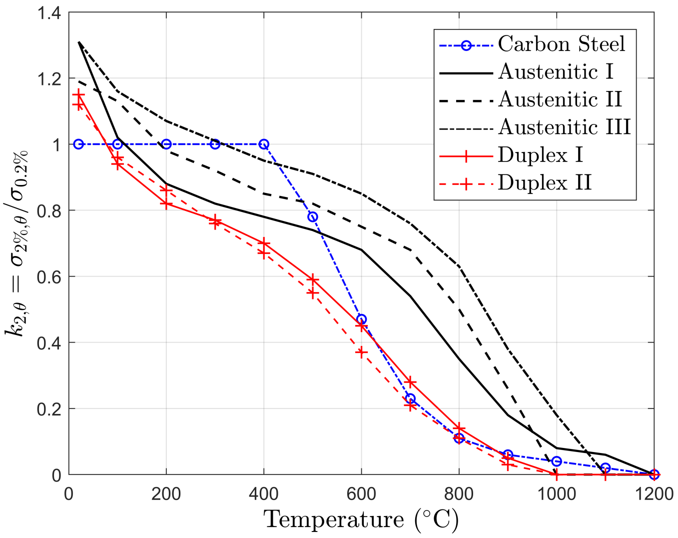

Figure 2.2: 2% Strength reduction of stainless steel and carbon steel at elevated temperatures

quickly reaches the material's yielding value due to strength reduction combined with increased loading induced by restrained thermal expansion. Therefore, the values of k_E in Figure 2.1 cannot provide a reliable comparison of the stiffness retention capability between carbon steel and stainless steel structures in fire.

Eurocode 3 [1] provides a total of eight sets of strength reduction factors for different grades of stainless steel, and a single set for carbon steel. The Design Manual for Structural Stainless Steel (DMSSS) [2] proposes to apply one set of generic reduction factors to groups of grades that exhibit similar properties. The DMSSS simplifies all the grades of austenitic and duplex stainless steels into three austenitic groups and two duplex groups, as summarised in Table 2.1.

Table 2.1: Simplified grade family at elevated temperatures

Group	Grades
Austenitic I	1.4301;1.4307;1.4318
Austenitic II	1.4401;1.4404;1.4541
Austenitic III	1.4571
Duplex I	1.4362;1.4062;1.4482
Duplex II	1.4462,1.4162,1.4662

Figure 2.2 shows the strength reduction factor $k_{2,\theta}$ at elevated temperature for carbon steel, austenitic groups, and duplex groups. Strength reduction factor $k_{2,\theta}$

is the 2% strength at temperature θ, normalised by the 0.2% proof strength $\sigma_{0.2\%}$ at 20 °C. At lower temperatures, stainless steels have a reduction factor $k_{2,\theta}$ of greater than unity because of the 2% strain limit at elevated temperatures and the use of 0.2% strain limit at room temperature. Unlike the elastic perfectly plastic carbon steel whose $\sigma_{0.2\%}$ is equivalent to $\sigma_{2\%}$ at room temperature, stainless steels exhibit substantial strain hardening and possess a greater strength at 2% strain than that at 0.2% plastic strain at room temperature. As shown in Figure 2.2, generally, austenitic grades shows a better $\sigma_{2\%}$ retention than carbon steel at temperature above 500 °C. Overall, duplex grades offer poor strength retention with over 60% $\sigma_{2\%}$ lost at 500 °C. Austenitic III offers the best $\sigma_{2\%}$ retention among all stainless steel grades. Austenitic III also exhibits an overall better retention capability than the carbon steel, with only a slight lower reduction factor between approximately 360 °C and 420 °C.

2.2.3.2 Global structural mechanisms in fire

Taking global structural behaviour into account for the estimate of structural fire capacity is essential to the performance-based engineering design. A real-life building structure is a redundant/indeterminate structure in which the pattern of forces and stresses cannot be determined by equilibrium alone, but also depend on the relative stiffness of parts of the structure. Consequently, the pattern of forces and stresses in a building structure are determined based on both equilibrium and compatibility consideration. Conversely, the isolated members tested in fire furnaces are mostly determinate structures, in which the pattern of internal forces and stresses can be determined using equilibrium considerations alone.

Under collapse conditions, redundant and determinate structures are more sharply differentiated. Provided it has adequate ductility and does not suffer from instability, the redundant structure is capable of finding different load paths and mechanisms to continue supporting additional load when its yield strength has been reached at a single location. The determinate structure collapses when the most highly stressed region reaches the local strength.

Due to the historical adoption of furnace fire testing on simply supported single element for structural fire resistance design, the behaviour of structures in fire has since been understood to be dominated by the material degradation under constant loading at high temperatures, which leads to high deflections or ‘run-away’ mechanisms as observed in furnaces.

However, during Cardington investigation, it was discovered that this typical ‘run-away’ mechanism did not occur in the steel beams in the building, even though the temperature of the bottom flange had exceeded 800 °C. This indicates that a steel beam in a framed structure, with the aid of restraints from surrounding members, has better fire resistant capability than individual steel beams [66].

Fire tests conducted on axially restrained steel beams by Li and Guo [67], and Liu et al. [68], showed that the behaviour of the restrained beams were very different from that of isolated beams. The most interesting finding from their experiments is the observance of catenary action. Catenary action in a beam is the ability of the beam to support itself by means of axial tension when the beam undergoes a large deflection. When subjected to fire, catenary action develops in the beam as a result of the deflected shape caused by thermal expansion and thermal bowing [69].

Heating induces thermal expansion strains (ε_T) in most structural materials, as given by Equation 2.13:

$$\varepsilon_T = \alpha \Delta T \tag{2.13}$$

where α is the thermal expansion coefficient and ΔT is the temperature increment.

The temperature distribution within structural components is usually not uniform. The cross-sectional thermal gradient of structural members causes the bottom surface to expand more than the top surface, inducing bending in the member. This effect is called thermal bowing.

Modelling and investigation of the full-scale Cardington frame fire tests show that it is the axial forces induced by thermal expansion and large displacements resulted from thermal bowing, and not material degradation that govern the structural response in fire. Based on the study of Cardington tests, Usmani et al. [39] stated that material degradation, such as steel yielding and buckling, can even be beneficial in developing the catenary action prior to the final failure when material degradation and loads begin to dominate the behaviour once again. Kodur and Dwaikat [70] shared a similar viewpoint and suggested that the statement by Usmani et al. [39] summarised well the behaviour of a beam in a real redundant structure for a real event of fire. Dwaikat and Kodur [71] presented a detailed interpretation of the structural behaviour of a translationally and rotationally restrained beam exposed to fire, dividing the behaviour into three distinctive stages, namely 'Elastic', 'Elasto-plastic' and 'Catenary action'.

It is well understood that if an axially restrained beam is slender it will buckle before the material reaches its yield stress. The classic Euler buckling Load P_{cr} for a beam column is given by

$$P_{cr} = \frac{\pi^2 EI}{l^2} \tag{2.14}$$

where E is the elastic modulus of the material, I is area of moment of inertia, and l is effective length.

Equating P_{cr} to the thermal expansion induced compression ($EA\alpha\Delta T$), the critical buckling temperature is then given by

$$\Delta T_{cr} = \frac{\pi^2}{\alpha}(\frac{r}{l})^2 = \frac{\pi^2}{\alpha\lambda^2} \tag{2.15}$$

where r is the radius of gyration, λ is slenderness ratio, l/r.

Equation 2.15 is based on the ideal assumption that the axial restraint is perfectly rigid. While in practice the restraint stiffness is of a finite value. Assuming the axial restraint is of a stiffness k_t, the critical buckling temperature can be calculated by

$$\Delta T_{cr} = \frac{\pi^2}{\alpha\lambda^2}(1 + \frac{EA}{k_t l}) \tag{2.16}$$

where λ is the slenderness ratio.

The EA/lk_t term in Equation 2.16 is the 'relative stiffness' ratio of the beam to its restraints provided by end connections and surrounding structures.

The failure of the beam, either by yielding or buckling, causes a sudden change in the deflection, leading to the subsequent catenary action. Consequently, the behaviour of a beam in a real redundant structure in a real event of fire undergoes four distinct stages.

In Stage 1, elastic response dominates the behaviour wherein beam expands as a result of continuous heating, compressive axial force and bending moment develop in the beam due to the effect of end restraints.

Stage 2 sees a sudden increase in deflection, as a result of either yielding or buckling failure of the beam, which leads to reduction of the compressive axial force that's induced by constrained thermal expansion.

Stage 3 begins when the axial force in the beam reverses from compression to tension. Thus the fire induced compressive axial force completely vanished and the tensile forces start to develop in the beam. The load bearing mechanism gradually changes from flexural to catenary action.

In the final stage, the beam starts to 'runaway' when the material degradation and loading becomes unbearable for the catenary mechanism to continue.

Recognising the beneficial role of catenary action plays at carrying large displacement in fire, there has been an ongoing research interest to achieve an efficient method for structural fire resistance design by taking advantage of the catenary action in a rational and reliable manner. Wang and Yin [72,73] developed an analytical method for predicting the fire behaviour of restrained beams based on a parametric study of finite element models. Wang and Yin's method is only suitable for cases of a specific deflection profile and neglects the additional bending moment generated in the beam due to the shift of effective section centroid [71].

Kodur and Dwaikat [70] investigated the response of steel beam-columns exposed to fire based on a set of numerical studies using finite element software ANSYS, and subsequently proposed a performance-based methodology for fire design of restrained beams. Kodur and Dwaikat's method assumes both the translational and rotational restraints continue to perform elastically during the entire course of the design fire. This assumption seems unrealistic because it has been demonstrated that the stiffness of rotational restraints available to beams at the beginning can reduce substantially early at around 200 °C [74].

2.2.4 Damage of Passive Fire Protection coatings

The fire resistance of steel structural components in composite steel frame buildings is commonly provided by passive fire protection (PFP) coatings. Current standards [9, 27] measure the fire resistance of structural components using the concept of time. For instance, a 2 hr fire-resistance rating means the PFP protected structural components can withstand a standard fire of 2 hours. There are two popular categories of PFP: cementitious coating and intumescent coating.

Cementitious PFP has been and still is a popular choice due to its advantages of being cost effective, ease of application and lightweight when compared with the itumescent fireproof coatings [75]. The fireproof coatings are generally spray or hand applied. The spray-applied cementitious coating is commonly referred to as spray-applied fire resistive material (SFRM). Being specifically designed to be lightweight, cementitious PFP are naturally fragile and brittle hence prone to damage under deformation or vibration. Numerous research [76–91] have been carried out to investigate the damage mechanisms in cementitious PFP, in order to investigate the fragility of it when the structures are subjected to large deformations in earthquake, impact or blast.

At material level, Chen et al. [76] carried out tests to evaluate the mechanical and inter-facial properties of cementitious coatings, including compressive and tensile strength, normal bonding strength and shear bonding strength. However, they did not measure the load-displacement response at the coating-steel interface and reported only the maximum strength attained at fracture.

Braxtan and Pessiki [77] evaluated the bond strength of SFRM through tests on small scale steel coupons, investigated the effect of mixing methods (wet mix or dry mix) and the steel surface finish on bond performance. They reported that the bond strength was three times higher for the wet mix than that for the dry mix, and mill finish of steel can considerably degrade the adhesion strength. When strains become large and strain compatibility at the interface becomes difficult to maintain, the cementitious wet mix tends to crack in order to accommodate large deformations. However they did not provide any load-displacement response at the SFRM-steel interface.

Arablouei and Kodour [78] carried out Drop Mass Impact tests in conjunction with numerical modelling to determine the Dynamic Increase Factor (DIF) of fracture properties for SFRMs. Tan et al. [79] used single cantilever beam specimens to measure the fracture energy of SFRMs under pure normal stress. Direct shear tests were carried out by Arablouei and Kodur [80] to measure the stress-displacement response under pure shear stress at the interface between the SFRM and the steel plate.

At structural level, Keller and Pessiki [83, 84] investigated the damage of cementitious PFP at bolted connections of gravity beam-column frames subjected to cyclic loading. Braxtan and Pessiki [81, 82] also carried out experiments to study the damage pattern of SFRM that was applied on steel moment frame beam-column assemblies under quasi-static cyclic loadings, representing strong seismic events. The SFRM debonding was observed first to occur at the location where the steel had yielded at the drift ratio of 1%. The large detachment of SFRM occurred at the plastic hinge when the drift ratio exceeded 3%. In addition, delamination occurred at places where the flange buckling occurred.

Chen et al. [76, 85] undertook an extensive testing programme of testing to study the damage mechanisms in cementitious coatings applied on steel plates subjected to monotonic axial loading and bending. They concluded that the plate curvature had the most significant influence on the damage mechanism. They found thicker insulation led to an earlier inter-facial damage.

Further experiments [86, 87] have also been carried out to study damage patterns in cementitious coatings that are applied on structural columns subjected to both monotonic and cyclic loadings, which found that the cracking initiated at a lower load level and the complete delamination/peel-off failure occurred at a lower strain level under cyclic loading than that under monotonic loading.

In order to develop an understanding on the process of the delamination between SFRM insulation and steel surface , Arablouei and Kodur [80, 88–91] have been focusing on developing constitutive material models and employed the Cohesive Zone Model (CZM) to simulate initiation and propagation of cracks at SFRM-steel interface under various types of loadings. They associated the SFRM delamination with plastic hinge formation and proposed a damage index factor based on the material fracture energy.

Damage in cementitious coating caused by loading events such as windstorms, fires or earthquakes can result in potential reductions in its structural fire resistance. This fire safety concern is further compounded by the fact that cementitious PFP is usually concealed by architectural claddings and finishes, which hinders any regular monitoring and post-earthquake inspections. As a result, the fire resistance of structures using cementitious PFP system could suffer significant reductions after a period of use due to unaccounted for PFP damage. Especially if this period consisted multiple small/moderate earthquakes.

It is worthy noting that the term ‘performance’ in performance-based design not only refers to a building’s behaviour during the outbreak of a natural hazard, but it also relates to a building’s survivability after a disaster. The performance-based design offers a process or methodology to evaluate the reductions in buildings’ structural fire resistance as a result of post-earthquake damage in PFP system. The functionality and the continued availability of services of building structures can be effectively and efficiently protected from fire hazards using the performance-based engineering framework for the structures in fire design.

2.3 Stainless steel structures in fire

The development of structural design codes, standards and specifications for stainless steel has been under increasing interest of the academics and the industry since early 1960s. Several European research projects have been carried out to analyse the performance of structural stainless steel, resulting in the publication of the Design Manual for Structural Stainless Steel (DMSSS). The latest (fourth) edition of the DMSSS [2] was published in 2017.

Recent experimental research [20–22] on stainless steel material behaviour at elevated temperatures suggested that stainless steel exhibits superior stiffness and strength retention capabilities, and a lower emissivity when compared with the carbon steel. The findings motivated further research on stainless steel structural behaviour in fire, as is the case of the European Coal and Steel Community (ECSC) project ‘Development of the use of stainless steel in construction’ and the ECSC project ‘Stainless steel in fire’.

The superior material behaviour of stainless steel at elevated temperatures offers potential economical gains through savings on fire protection systems. A comparison of the strength and stiffness retention capability between carbon steel and stainless steel has been presented in Section 2.2.3.1. Besides the material’s strength and stiffness retention capability, thermal expansion induced compression also plays a crucial role in the steel structural behaviour in fire.

2.3.1 Thermal expansion

For thermo-mechanical analysis, in addition to the mechanical strain induced by general external loading or geometry non-linearity due to deformation, thermal strain caused by temperature increments through thermal expansion also needs to be considered. The fundamental principal relationship that governs the behaviour of structures in fire is [39]:

$$\varepsilon_{total} = \varepsilon_{mechanical} + \varepsilon_{thermal} \tag{2.17}$$

The total strain (ε_{total}) governs the deformed shape of the structure through kinematic or compatibility considerations, whereas, the stress state σ in the structure, elastic or plastic, depends only on the mechanical strain.

If the thermal expansion is free to develop in an unrestricted manner, axial expansion or thermal bowing will result from thermal expansion while leading to no additional stress:

$$\begin{gathered} \Delta\varepsilon_{total} = \Delta\varepsilon_{thermal} \\ \Delta\varepsilon_{mech} = 0 \qquad \Delta\sigma = 0 \end{gathered} \tag{2.18}$$

In contrast, if the thermal strains are fully restrained, stresses (σ) in structural members will result from the $\varepsilon_{mechanical}$:

$$\begin{gathered}\Delta\varepsilon_{total} = 0 \\ \Delta\varepsilon_{total} = \Delta\varepsilon_{mech} + \Delta\varepsilon_{thermal} \Rightarrow \Delta\varepsilon_{mech} + \Delta\varepsilon_{thermal} = 0 \\ \Rightarrow \Delta\varepsilon_{mech} = -\Delta\varepsilon_{thermal} \\ \Delta\sigma \neq 0\end{gathered} \tag{2.19}$$

In real structures under fire, rigid connections between structural components will result in high stresses being developed in structural members, which might lead to structural plastification, even though the deflection might be small. Alternatively, where less restraints are in place, larger deflections may develop but accompanied with lower stress levels. Therefore, the structural behaviour due to material thermal expansion in real structures is a complicated issue which depends strongly on the structural restrains.

Eurocode 3 [1] suggests the thermal elongation $\Delta L/L$ of austenitic stainless steel could be determined using the equation:

$$\Delta L/L = (16 + 4.79 \times 10^{-3}\theta_a - 1.243 \times 10^{-6}\theta_a^2) \times (\theta_a - 20) \times 10^{-6} \tag{2.20}$$

where L is the length at 20 °C, ΔL is the temperature induced expansion and θ_a is the temperature.

The mean coefficients of thermal expansion for typical types of stainless steel specified in DMSSS [2] are summarised in Table 2.2. The available results suggest that austenitic grade exhibits the greatest thermal expansion while ferritic grade expands the least amongst the three.

In analogy to the thermal elongation equation proposed by the Eurocode 3 [1] for austenitic grade, an elongation equation as in Equation 2.21 is proposed for the duplex grade. Equation 2.21 was determined by least square fitting the thermal expansion coefficient vs. temperature relationship of the duplex grade as presented

Table 2.2: Mean coefficient of thermal expansion ($10^{-6}/°C$)

Steel Temperature range(°C)	Duplex	Austenitic	Ferritic
100	13.2	16.7	10.3
200	13.9	17.2	10.7
300	14.3	17.7	11.1
400	14.7	18.1	11.5
500	15.1	18.4	11.8
600	15.4	18.8	12.0
700	15.9	19.1	12.4
800	16.3	19.4	12.9
900	16.7	19.4	13.4
1000	17.1	19.7	14.0
1100	17.5	20.0	-

in Table 2.2.

$$\Delta L/L = (12.88 + 4.6e^{-3}\theta_a - 4e^{-7}\theta_a^2) \times (\theta_a - 20) \times 10^{-6} \tag{2.21}$$

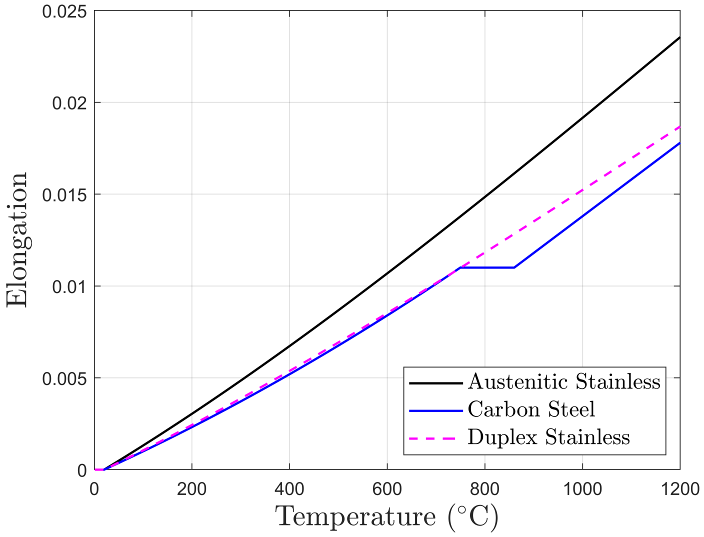

Figure 2.3: Thermal elongation

Overall, stainless steel grades show higher thermal elongation in comparison with carbon steel, as shown in Figure 2.3, with the austenitic grade being the highest.

2.3.2 Thermal properties

Stainless steel exhibits different thermal properties that makes it behave differently in heat transfer analysis when compared to carbon steel. According to EC 3 Annex C [1], the thermal conductivity (λ_a) of stainless steel could be determined using the following equation:

$$\lambda_a = 14.6 + 1.27 \times 10^{-2} \theta_a \qquad W/mK \tag{2.22}$$

where θ_a is the temperature.

Figure 2.4 shows the thermal conductivity temperature curve of stainless steel in conjunction with that of carbon steel. The thermal conductivity of carbon steel reduces from 53 W/mK at room temperature to 27 W/mK at 800 °C and beyond. In contrast, the conductivity of the stainless steel grows with rising temperature, increasing from 15 W/mK at room temperature to about 30W/mK at 1200 °C. In general, for temperature below 1000 °C, the stainless steel displays a lower thermal conductivity than carbon steel.

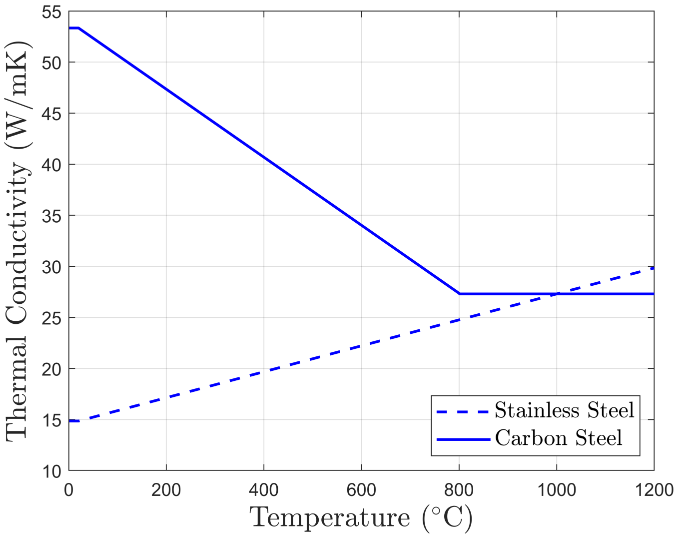

Figure 2.4: Thermal conductivity

Eurocode 3 Annex C [1] provides the following equation from which the specific heat (c_a) of stainless steel could be determined:

$$c_a = 450 + 0.28 \times \theta_a - 2.91 \times 10^{-4} \theta_a^2 + 1.34 \times 10^{-7} \theta_a^3 \qquad J/kgK \tag{2.23}$$

where θ_a is the temperature.

Figure 2.5 compares the evolution of specific heat of stainless steel and carbon steel over increasing temperatures. On average, the specific heat of stainless steel is about 550 J/kgK, as compared with the approximately 600 J/kgK of carbon steel. One significant difference is that the austenitic stainless steel shows no phase change when subjected to heating up to 1200 °C, whereas the carbon steel exhibits a phase change in the region of 723 °C.

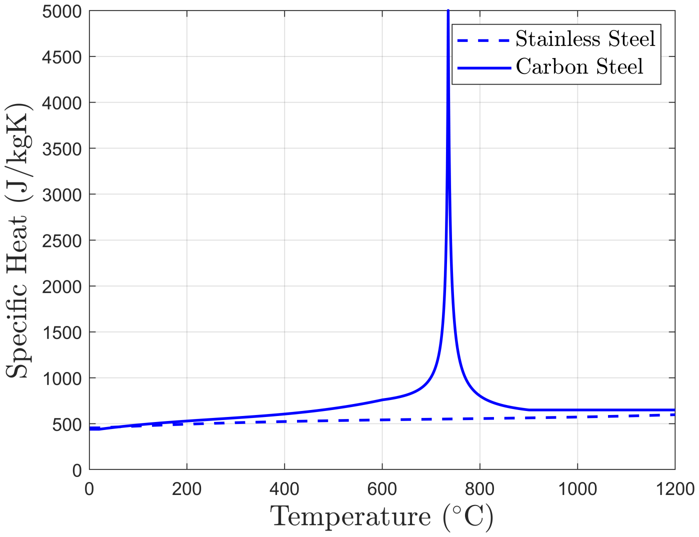

Figure 2.5: Specific heat

Enthalpy formulation is the method commonly adopted in numerical solution to tackle phase change problems in materials. The method enables the heat capacity to be defined as a smooth function of temperature. Cheng and Usmani [92] proposed that the enthalpy (H) within a temperature range could be defined as in Equation 2.24. This method has been implemented in the heat transfer module in OpenSEES [93].

$$H = \int_{T_r}^{T} \rho c_p dT \tag{2.24}$$

where Tr is the reference temperature, c_p is the specific heat, ρ is the density.

Eurocode 3 [1] stated that the unit mass of both carbon steel and stainless steel could be considered independent of temperature and taken as 7850 kg/m^3. In addition, a lower emissivity of 0.4 can be adopted for stainless steel due to its polished finish surface, in comparison to the 0.7 for carbon steel.

2.3.3 Existing research on stainless steel structures in fire

European Coal and Steel Community (ECSC) project 'Development of the use of stainless steel in construction' and the ECSC project 'Stainless steel in fire' , co-ordinated with the British Steel Construction Institution, has studied the behaviour in fire of a range of structural stainless steel grades. Numerous experimental research [21, 94–96, 96–98] has been carried out to obtain the material's mechanical properties at elevated temperatures and the property data has been included in the latest DMSSS [2].

In addition, a range of research activities [99–101] have been conducted to study the structural behaviour of stainless steel in fire. Available experimental data [21, 102, 103] suggest that austenitic stainless steel columns and beams can retain their load-carrying capacity for a longer period of time than carbon steel structural members, due to their superior strength and stiffness retention capacity. However, existing experimental data have been limited to the behaviour of individual stainless steel structural components in fire.

Numerical investigations using finite element analysis has been employed to study the stainless square hollow column behaviour in fire [104], and the lateral-torsional buckling behaviour of beam column members in fire [101, 105]. The testing of steel members, sub-assemblies and frame structures in a fire is extremely expensive and any one test only provides limited useful data. In view of the richly diversified grades of stainless steel family, numerical investigation can be considered as an economical and efficient approach to study stainless steel structural systems in fire.

2.4 Material models for thermo-mechanical analysis with fire

The Cardington tests [106], together with advances in computing power and modelling techniques, have propelled for a generation of numerical models for heated structures. Many programs have been specifically developed for structural analysis under fire conditions, with early development focused on geometric non-linearity resulted from large deflection due to thermal bowing and expansion. Most of these programs belong to individual researchers or research groups, and most of them have seen their development stalled after a while. Today, only some of them are still being developed and probably used by other researchers, most notably are, SAFIRE (University of Liege) and VULCAN (University of Sheffield).

The accuracy of finite element (FE) models is strongly dependent on the material model adopted. Carbon steel and stainless steel exhibit non-linear stress- strain relationships at elevated temperatures, hence require material non-linear analysis.

2.4.1 Material non-linearity

Ramberg and Osgood [107] proposed the expression in Equation 2.25 to describe the non-linear relationship between stress and strain:

$$\varepsilon = \frac{\sigma}{E} + K(\frac{\sigma}{E})^n \tag{2.25}$$

where ε is the strain, σ is the stress, K and n are material constants.

Saab [108] proposed to use the Ramberg-Osgood equation to better represent the non-linearity exhibited by carbon steel at elevated temperatures. Saab adopted a modified version of the Ramberg-Osgood equation for stress-strain relationships at high temperatures, given as:

$$\begin{aligned} \varepsilon &= \frac{\sigma}{E_{20}} + \frac{3}{7}(\frac{\sigma_{y20}}{E_{20}})(\frac{\sigma}{\sigma_{y20}})^{50} \qquad 0 < \theta \leq 80 \ \ ^\circ\mathrm{C} \\ \varepsilon &= \frac{\sigma}{E_\theta} + 0.01(\frac{\sigma}{\sigma_{y\theta}})^{\eta_\theta} \qquad 80 < \theta \leq 800 \ \ ^\circ\mathrm{C} \end{aligned} \tag{2.26}$$

where E_{20} is the elastic modulus at ambient temperature; σ_{y20} is the yield strength at ambient temperature; ε is the mechanical strain; σ is the mechanical stress; E_θ is the elastic modulus at temperature θ; $\sigma_{y\theta}$ is the yield strength at temperature θ; η_θ is the material constant at elevated temperatures. Saab also proposed methods to calculate η_θ based on curving fitting.

The major drawback of a Ramberg-Osgood type stress strain equation is that there is no closed-form inversion of the relation to describe stress in terms of strains, hindering its application in strain-based finite element analysis. Graphic iteration technique can be adopted to bypass this difficulty however it is very computationally expensive. An explicit stress formulation will considerably improve the computation efficiency.

Mostaghel and Byrd [109] derived an approximated inversion of the typical Ramberg-Osgood equation using a power law $\varepsilon = E\varepsilon - \alpha\varepsilon^\beta$ to represent the σ in the elastic strain dominated region and using a binomial series expansion up to fourth order to obtain the stress-strain relation for the plastic dominated region. Abdella [110] proposed an approximate inversion formula $\sigma = \frac{E\varepsilon}{1+c\varepsilon^p}$, specifically for stainless steel stress-strain curves represented using Ramberg-Osgood type equations.

Various strain-based constitutive equations, summarised in Table 2.3, offer the capability to describe the non-linear stress strain behaviour. The Holloman law [111] is a power law based equation. The parameter n is the strain hardening exponent. In addition to the power law, the Ludwik law [112] introduces a third material constant, initial yield stress (σ_0), and the Swift law [113] accounts for the prestrain (ε_1). The Voce law [114] is exponential function based, and suitable for materials exhibiting a saturation stress (σ_s).

Table 2.3: Types of the constitutive equations

Author(s)	Equation	Parameters
Holloman	$\sigma = K\varepsilon^n$	K,n=constants
Ludwik	$\sigma = \sigma_0 + K\varepsilon^n$	σ_0,K,n=constants
Swift	$\sigma = K(\varepsilon_1 + \varepsilon)^n$	K, n=constants, ε_1=prestrain
Voce	$\sigma = \sigma_0 + (\sigma_s - \sigma_0)exp(-n\varepsilon)$	σ_0, σ_s, n=constants

2.4.2 Existing non-linear material models

Franssen [115] proposed that the constitutive material model for steels at elevated temperatures could be constructed by using a set of temperature-dependent stress-strain curves and the plastic strain to track the complete strain history at varying temperatures; the transient hardening associated with the Bauschinger effect could be modelled using the Masing's rule [116].

This approach has been implemented in the finite element software SAFIR [117] for Eurocode 3 [1] steel materials with an elliptical curve adopted for the non-linear isotropic hardening behaviour [118]; and in OpenSEES as the uniaxial material model Steel01Thermal for Eurocode 3 carbon steel [119], where a simplified tri-linear stress-strain relationship was adopted to represent the non-linear stress strain relationship. Franssen's approach has also been used by Bailey et al. [120], Lu et al. [121] and Lien et al. [122] to study the cooling behaviour of steel structures.

Franssen's approach can handle the stress reversals at increasing temperatures caused by high initial strain or the stress reversals experienced during cooling. Figure 2.6a illustrates the tracing of the stress-strain path under heating using the Franssen's model for the case where the strain reversal at increasing temperatures is caused by high initial strain, denoted here as Case A. A set of temperature-dependent stress-strain curves are constructed from the origin, with increasing non-linear hardening at higher temperatures. Having reached equilibrium at the time step (i), Point A on the stress-strain curve of temperature $T(i)$, the plastic strain $\varepsilon_R(i)$ is calculated by unloading material state from Point A following the slope E(i) to the intercept with the strain axis. At time step $(i+1)$, temperature is increased, resulting in a reduction in the elastic range which is represented by the yield strength of proportional limit $\sigma_p(i+1)$, and a reduction in the elastic modulus $E(i+1)$. The new stress-strain path at $T(i+1)$ is constructed following the steps:

1. Reload from the strain axis interception Point O' via the slope $E(i+1)$, join the original stress-strain curve of $T(i+1)$ at the interception Point D.

2. Extend the line DO', which is parallel to the tangent of the original stress-strain curve, to Point C. Point C is defined by assuming the size of the elastic

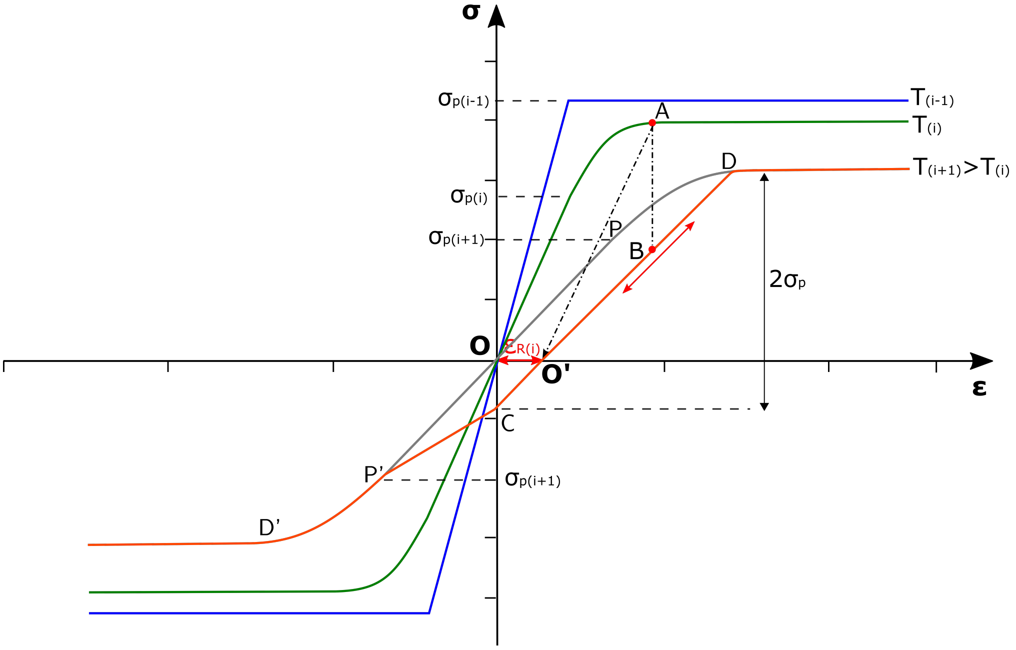

(a) Case A

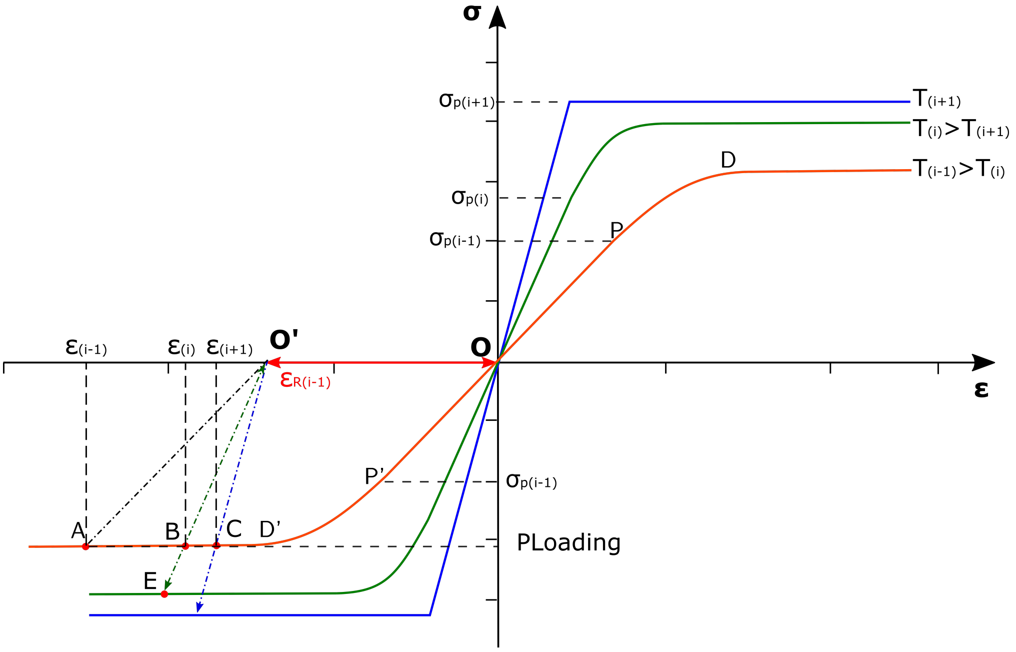

(b) Case B

Figure 2.6: Material model construction illustrations

zone is $2\sigma_p(i+1)$, considering the Bauschinger. Thus Point C defines the new elastic limit on this path.

3. Join Point C and Point P', assuming a linear relationship. The new stress-strain curve at $T(i+1)$ is now defined by the orange curve DO'CP'D', replacing the original curve DPOP'.

The stress state at $T(i+1)$ can therefore be determined using the new stress-strain curve DO'CPD'. Point B at $T(i+1)$ is the equivalent stress state of Point A at $T(i)$, which is determined by preserving the mechanical strain of Point A prior to the first iteration at step $T(i+1)$. At Point B, the material can be either further loaded in tension or unloaded/loaded into compression.

The same principle applies in the case where the strain reversal is experienced during cooling, denoted herein as Case B. Similar to the Case A, a set of temperature-dependent stress-strain curves are constructed from the origin, assuming the material regains its original properties when being cooled from the higher temperature $T(i-1)$ to $T(i+1)$. Figure 2.6b depicts the tracing of the stress and strain during cooling using the Franssen's approach. For simpler demonstration purpose, a constant loading $P_{loading}$ is considered, presenting a statically determinate structures. High initial compressive mechanical strain (Point A) resulted from heating is assumed. During cooling, the plastic strain $\varepsilon_R(i-1)$ remains unaffected by the temperature. The final equilibrium at $T(i+1)$ is obtained at Point C. For global structure analysis, member forces can increase at step $T(i)$ as some part of the structure regains its stiffness under cooling. If the loading at $T(i)$ goes beyond Point E, the $\varepsilon_R(i)$ will change. Therefore the reference Point O' should be computed and updated at the end of each temperature step during the analysis, which then is used to define the stress-strain relationship for the next temperature step.

Franssen's approach always starts with a set of original stress-strain curves, based on which the modified stress-strain relationship at elevated temperature is determined. This procedure limits its application in scenario where multiple strain reversals are expected. For example, in the event of fire immediately following an earthquake, a series of localised fires are likely occur within buildings. As a result, combinations of Case A and Case B will prevail in the building materials since simultaneous heating and cooling is expected for the structure.

Figure 2.6 schematically shows the elastic perfectly plastic behaviour of carbon steel at the lower temperature, and the non-linear stress strain behaviour at elevated temperatures. The elastic-plastic stress-strain relationship of carbon steel at room temperature transforms into a non-linear relationship when the temperature exceeds 100 °C. For stainless steel, its stress-strain curves exhibits a non-linear relationship in general.

Bailey et al. [3] used a Ramberg-Osgood relation to present the non-linear stress-strain relationships, with Masing's rule [116] implemented for defining hysteresis loop in unloading. Masing's [116] rule offers that the unloading curve can be uniquely defined based on the loading curve using polar scaling with a factor of two. When the loading curve is defined by an equation $\sigma = f(\varepsilon)$, if a new coordinate system (σ', ε'), with the origin at the strain reversal point used, the unloading curve can be represented by a relation $\sigma'/2 = f(\varepsilon'/2)$ [123]. The main procedures proposed by Bailey et al. [3] for the stress strain paths construction, as illustrated in Figure 2.7, can be summarised as follows:

1. The uniaxial stress-strain relationship is defined by a Ramberg-Osgood type of equation: $\varepsilon_T = \frac{\sigma_{(T)}}{E_{(T)}} + k(\frac{\sigma_T}{\sigma_{yT}})^{n_T}$. Where $E_{(T)}$ and σ_{yT} are temperature-dependent elastic modulus and yield stress. K is a material constant.

2. Once the strain reversal Point A $(\varepsilon_{A1}, \sigma_{A1})$ is identified at temperature T1, the unloading path can be constructed by $\varepsilon_{T1} = \varepsilon_{A1} - 2(\frac{\sigma_{(A1)}-\sigma_{(T1)}}{2E_{(T1)}} + 0.01\frac{\sigma_{(A1)}-\sigma_{(T1)}}{2\sigma_{(T1)}}^{n_{T1}})$, using Masing's Rule.

3. Calculate the Reference Point $O_2(\varepsilon_R, 0)$. ε_R is the unrecoverable plastic strain, $\varepsilon_R = \varepsilon_A - \frac{\sigma_A}{E_{T1}} - 0.02(\frac{\sigma_A}{2\sigma_{yT1}})^{n_{T1}}$.

4. The stress-strain path for the next temperature T2 is constructed by positioning the unloading curve for T2 so it intersects the Reference Point O_2. The interception Point C $(\varepsilon_{A2}, \sigma_{A2})$ is obtained by solving the following equation: $0.02(\frac{\sigma_{A2}}{2\sigma_{yT2}})^{n_{T2}} - 0.01(\frac{\sigma_{A2}}{\sigma_{yT2}})^{n_{T2}} + \varepsilon_R = 0$.

5. Repeat calculation for Reference Point O_2 at Temperature T2 for the new stress, which will be used to define the stress-strain relationship for the next temperature step.

As shown in Figure 2.7, the assumed strain reversal Point A ($\varepsilon_{A1}, \sigma_{A1}$) at temperature T1 is beyond the elastic limit. Prior to iteration at Temperature T2, by preserving the mechanical strain from previous temperature step, Point B is located on the new stress strain path of T2, highlighted in dashed orange line. The dashed orange line represents the new elastic region on the stress strain path of T2. At temperature T2, if the strain is increased to a point beyond Point C, then the original stress-strain curve of T2 is used and a new reference point will have to be formed. If the strain value is between $-\varepsilon_{A2}$ and ε_{A2}, the path of dashed orange line is followed.

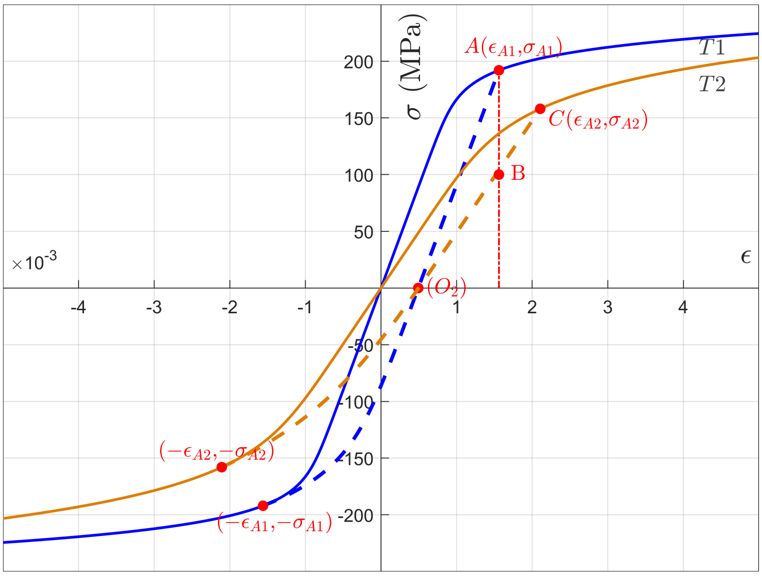

Figure 2.7: Construction of stress strain path, proposed by Bailey et al. [3]

The mathematical process involved in this constitutive material model presents three challenges for computational implementation:

1. The same Ramberg-Osgood type of equation is assumed for both tensile and compressive stress-strain relationship. This means the exponent parameter n has to be an odd integer.

2. Iteration method is required when solving the non-linear equation to deter-

mine the new strain reversal point (Point C in the Step 4) for the next temperature step. This considerably increases the computing time.

3. The nature of Ramberg-Osgood equation presents a challenge for displacement based finite element modelling because there are no closed-from solutions expressing the stress as an explicit function of the stress. As a result, graphical or iterative numerical procedures have to be employed to compute the stress corresponding to a given strain.

In conclusion, models using Franssen's approach are only valid provided that either only one unloading phase follows the loading phase or cyclic loading occurs with always increasing stress level. In other words, they cannot reliably account for multiple strain reversals (> 2) because the set of stress-strain curves are constructed always starting from the origin. Furthermore, the Bauschinger effect and the transient hardening captured by the Masing's rule is only an approximated representation of the material's behaviour.

2.4.3 Bauschinger effect

At room temperature, Silvestre et.al [124] experimentally evaluated the Bauschinger ratio (B.R.) of Austenitic 316L and ferritic 430 BA stainless steel. The Bauschinger ratio (ϑ) is defined as in Equation 2.27. They observed that Austenitic 316L showed a considerable Bauschinger effect (B.R.=0.81), while 430 BA showed a tendency toward isotropic behaviour (B.R.=0.92). Olsson [125] conducted biaxial tests on the Austenitic 1.4301, 1.4436 and Duplex 1.4462 stainless steel and determined their B.R. as 0.75, 0.70 and 0.60 respectively. Following the same testing procedures, Gozzi [126] further determined the Bauschinger ratio of Austenitic 1.4318 stainless steel, and obtained B.R.=0.65. In light of the experimental results, the stainless steels show a more pronounced Bauschinger effect.

$$\vartheta = \frac{Y_{iso}}{Y_{1D}} \tag{2.27}$$

where Y_{iso} is the proportion of isotropic hardening, and Y_{1D} is the total hardening. At the starting point, there is only isotropic hardening, $Y_{iso} = Y_{1D} \Rightarrow \vartheta = 1.0$.

For various metal materials it has been observed that the Bauschinger effect is temperature-dependent [5, 127–129]. Phillips et al. [127] observed that the Bauschinger ratio of the aluminium decreased as the temperature increased. Harvey et al. [128] investigated the evolution of the isotropic hardening variable and kinematic hardening variable of 304L stainless steel at elevated temperatures (20 °C, 200 °C, 600 °C, 800 °C and 1000 °C) using reverse yield experiments, and demonstrated the temperature-dependent nature of the Bauschinger effect. When investigating material's kinematic hardening behaviour under cyclic loading at high temperatures, Maciejewski et al. [129] and Ohno et al. [5] observed different degrees of the Bauschinger effect and transient hardening at varying temperatures for low carbon steel and 304 stainless steel, respectively.

2.4.4 Strain rate dependency for structural fire analysis

Material models for representing steel behaviour at elevated temperatures are based on a set of temperature-dependent stress-strain curves. The mathematical representation of these curves is usually determined by fitting the test data obtained from stress or strain rate controlled testing of coupons heated under quasi-static conditions. The strain rate range used for testing is usually restricted to approximately 0.00025 –0.0025 s^{-1}, and the codified stress rate range is between 6 and 60 MPa s^{-1} [130]. When strain rate is above 0.0001 s^{-1}, structural steel material starts to exhibit notable strain rate sensitivity, defined as the increase in yield strength with increasing strain rate, [131]. The strain rate sensitivity increases with increasing temperature [132]. The strain rate of 1.0 s^{-1} can be considered as an initial starting point for evaluating dynamic load effect as related to material strain rate sensitivity [133]. When subjected to building fire, structural loading is generally static and moderate to high strain rate levels are not expected to occur until the structure approaches its collapse state [134]. Steady state analysis is the common approach for structural fire analysis, dynamic analysis has been adopted in various research [135–137] for investigating the behaviour of fire-induced structural collapse.

Heating rate has a great effect on the strain rate when the structure is under transient (anisothermal) loading conditions, where the structure is stressed to a specific level and then exposed to uniform heating [138]. This is the opposite of the steady (isothermal) loading condition, in which the structure is heated up to a specific temperature, which is then held constant while the loading is applied. The transient loading condition is generally considered to be more representative of actual fire scenarios, where an already stressed structure experiences increasing temperatures. The heating rate of steel members under fire conditions depends on the nature of the fire, the geometry of the structure and the section properties as well as any fire insulation which has been applied. For a typical beam, with 2 hour fire rated protection, the heating rate of steel generally varies between 3 and 7 °C/min, while for unprotected steel sections, the heating rate can vary between 25 and 40 °C/min [138].

Creep is defined as the time-dependent plastic strain under constant stress and temperature. At room temperature and under service load levels, creep deformations of steel are insignificant. Generally, the influence of creep in the steel strain evolution becomes noticeable at temperatures above 450 °C [139].

The Eurocode 3 [1] temperature-dependent stress-strain curves for steel were derived based on data from transient loading tests under a heating rate of 10 °C/min [140]. This code specifies that a material model constructed based on the Eurocode 3 stress-strain curves is applicable for heating rates between 2 and 50 °C/min, and states that “the effects of transient thermal creep need not be to given explicit consideration”. In other words, a material model developed based on Eurocode 3 stress-strain curves takes creep at high temperatures into account implicitly.

The ASCE manual [141] states that high temperature creep should be accounted for in fire resistance analysis through the use of temperature-dependent stress-strain curves derived from transient-state tests at relevant heating and strain rates; or adopting specific creep models developed for structural steel at high temperatures. Therefore it is left to the engineers to decide which model to use.

2.4.5 Existing kinematic hardening plasticity models at room temperature

It is well known that the theory of plasticity provides the framework for the continuum constitutive descriptions of the behaviour of solids that experience permanent plastic deformations. The rate-independent plasticity theory is restricted to the conditions for which the permanent deformations do not depend on the rate of the loading applied. Several rate-independent plasticity models have been developed using the rate-independent plasticity framework with internal variable concept to model the non-linear strain hardening, and the complex material behaviour under non-monotonous loading such as the Bauschinger effect and transient hardening.

Isotropic hardening models are adequate for proportional loading conditions where the loading increases monotonically and no unloading occurs. In order to properly represent material's response under complex non-monotonous deformation paths, it has been common to adopt kinematic hardening models. In this section, three main types of kinematic hardening models are briefly reviewed and discussed.

2.4.5.1 Mroz's multi-surface model

Mroz's model [142] uses a series of linear segments to model the non-linear stress-strain behaviour, i.e., instead of using a single hardening modulus for the entire stress-strain curve, each discretised segment of the stress-strain curve has one constant hardening modulus. In three dimensional stress space, Mroz's model can be represented by several hypersurfaces f_0,f_1,...f_n, where f_0 is the initial yield surface, and f_1 to f_n define regions of constant hardening moduli.

On one hand, to produce a smooth non-linear curve, a large number of yield surfaces are necessary, requiring high computational power. On the other hand, the plastic moduli (E^p) under uniaxial loading of Mroz's model can be determined straightforwardly from the stress-plastic strain curve generated from uniaxial tensile tests.

2.4.5.2 Two yield-surface models

The two-surface model concept was proposed by Krieg [143] and Dafalias & Popov [144] independently in the 70s. They introduced the concept of a bounding (outer) surface and a loading (inner) surface. A schematic view of the two yield surface model is illustrated in Figure 2.8. The current stress state (Point a) is defined on the loading surface while a corresponding stress state is defined on the bounding surface (Point A). The $\boldsymbol{\sigma}$ and $\boldsymbol{\Sigma}$ are the Cauchy stress tensor of the loading surface and bounding surface respectively, $\boldsymbol{\beta}$ is the backstress tensor that defines the centre position of the loading surface and $\boldsymbol{B}$ is the backstress tensor that defines the centre of the bounding surface.

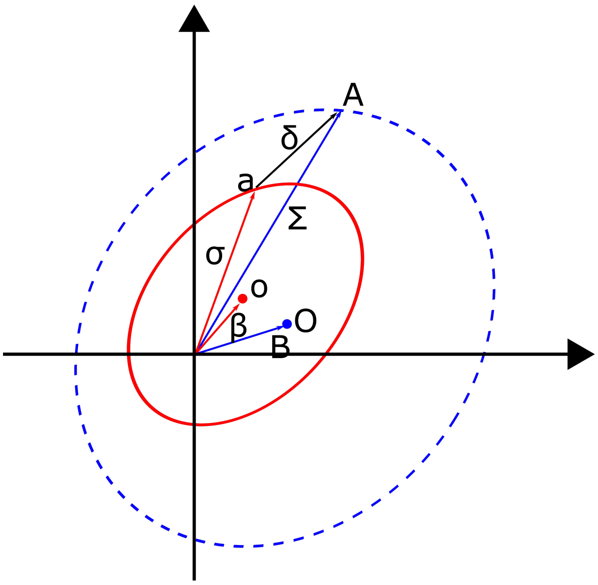

Figure 2.8: A schematic view of two surface model

Compared with the Mroz's multi-surface model that defines a set of piecewise plastic moduli, the two surface model defines a continuous variation of the plastic modulus between the bounding surface and the loading surface. The nonlinear hardening behaviour —smooth transition between elastic and plastic region, is realised through the relative movement of the two surfaces. The main difference between Krieg's model, and Dafalias & Popov's model is the approach adopted for incorporating the Bauschinger effect. Krieg [143] prescribes kinematic-isotropic proportioning factors to decompose the total hardening into isotropic and kinematic hardening parts for the loading surface and the bounding surface respectively. In Dafalias & Popov's model [144], the Bauschinger effect is realised by defining the plastic hardening modulus as a function of the gap (δ in Figure 2.8) between the bounding and the loading surface.

Lee et al. [145] resolved the issue of 'overshooting', the unrealistic transient behaviour of the two-surface model which may occur when the material is unloaded before being reloaded to its original stress state, by only updating the hardening behaviour when reverse loading occurs for plastic deformation.

Recently, Cardoso & Yoon [146] explicitly incorporated the Bauschinger ratio in the constitutive equation of the two surface model by defining it as an exponential function of the accumulated plastic strain ($\overline{\varepsilon^p}$).

2.4.5.3 Non-linear kinematic hardening models

The non-linear kinematic hardening model commonly used is a generalisation of Prager's [147] and Ziegler's [148] linear kinematic hardening models. The Prager's linear kinematic hardening rule [147] assumes the yield surface translates in the direction of plastic strain increment. Ziegler [148] modified Prager's rule by assuming yield surface translates along the direction of the relative stress tensor $\boldsymbol{\eta}$:

$$\boldsymbol{\eta} = \boldsymbol{\sigma} - \boldsymbol{\beta} \tag{2.28}$$

where $\boldsymbol{\sigma}$ is Cauchy stress tensor and $\boldsymbol{\beta}$ is the backstress tensor.

The evolution equation for the kinematic hardening variable $\boldsymbol{\beta}$ can be expressed as:

$$\boldsymbol{\beta} = \frac{2}{3} H \boldsymbol{\varepsilon^p} \qquad \text{and} \qquad \dot{\boldsymbol{\beta}} = \frac{2}{3} H \dot{\boldsymbol{\varepsilon}}^{\boldsymbol{p}} \tag{2.29}$$

the material constant H is the hardening modulus and $\boldsymbol{\varepsilon^p}$ is the plastic strain tensor.

For modelling material behaviour under cyclic loading, Chaboche [149, 150] proposed a non-linear kinematic hardening model as expressed in Equation 2.30. The backstress ($\dot{\boldsymbol{\beta}}$) is modelled using multiple (M) terms of non-linear kinematic hardening, with different material constants γ_i assigned for each term to allow for a more extensive strain domain and a better description of the soft transition between elasticity and the onset of plastic flow [151].

$$\dot{\boldsymbol{\beta}} = \sum_{i=1}^{M} \dot{\boldsymbol{\beta}}_i \qquad \dot{\boldsymbol{\beta}}_i = \frac{2}{3} H_i \dot{\boldsymbol{\varepsilon}^{\boldsymbol{p}}} - \gamma_i \boldsymbol{\beta}_i \dot{\overline{\varepsilon^p}} \tag{2.30}$$

with:

$$\dot{\overline{\varepsilon^p}} = \sqrt{\frac{2}{3} \dot{\boldsymbol{\varepsilon}^{\boldsymbol{p}}} : \dot{\boldsymbol{\varepsilon}^{\boldsymbol{p}}}} \tag{2.31}$$

The variable $\dot{\overline{\varepsilon^p}}$ is the accumulated plastic strain rate and γ is a material constant. The term $-\gamma \boldsymbol{\beta} \dot{\overline{\varepsilon^p}}$, called the dynamic recovery term, includes the effect of saturation in the kinematic hardening model.

Chaboche's model is developed based on the non-linear kinematic hardening model firstly proposed by Armstrong & Frederick [152] in 1966. Armstrong & Frederick's model can be considered as a particular case of Chaboche's model where $M = 1$, i.e., only one dynamic recovery term is used.

Another possible improvement upon Prager's linear kinematic hardening rule is introducing non-linearity by replacing the constant kinematic hardening modulus H with a generic function of the accumulated plastic strain, $\overline{\varepsilon^p}$ [153].

$$\dot{\boldsymbol{\beta}} = \frac{2}{3} H(\overline{\varepsilon^p}) \dot{\boldsymbol{\varepsilon}}_{\boldsymbol{p}} \tag{2.32}$$

in this case, a scalar function,

$$\overline{\beta} \equiv \overline{\beta}(\overline{\varepsilon^p}) \tag{2.33}$$

must be defined such that

$$H(\overline{\varepsilon^p}) = \frac{d\overline{\beta}}{d\overline{\varepsilon^p}} \tag{2.34}$$

defines the kinematic hardening curve. This curve can be obtained from simple uniaxial tests in a manner analogous to the determination of the hardening curve for the purely isotropic hardening model.

The models reviewed in this section are presented within the framework of small strains and applicable to the scheme of rate-independent plasticity. The three types of plasticity models are not completely independent from each other [154].

Chaboche and Rousselier [149] demonstrated mathematically that the non-linear kinematic hardening rule can be considered as a particular case of two-surface theory where the bounding surface can only expand isotropically but cannot translate.

Chapter 3

A New Material Model for Thermo-mechanical Analysis of Steels in Fire

Adapted from M. Zhou, R. Cardoso, and H. Bahai, “A new material model for thermo-mechanical analysis of steels in fire”, *International Journal of Mechanical Sciences*, vol. 159, pp. 467 – 486, 2019

All of the existing kinematic hardening models reviewed in Section 2.4.5 focus on the mechanical aspect of the material behaviour under isothermal conditions, without explicitly stating the effects of temperature and temperature changes. Thus the three objectives identified in the Introduction (Chapter1) have been answered to some degree by the existing models for isothermal conditions. In order to develop an appropriate plasticity model for thermo-mechanical analysis of steel materials subjected to fire, the effects of temperature and temperature changes have to be addressed, which is discussed in the following sections.

3.1 Temperature effects on plasticity models

Within the framework of thermodynamics, temperature changes in the material can result from internal heat generation and external heat source. The flame edge temperature has been observed at about 550 °C in small-scale compartment fires and the maximum temperature in a post-flashover building fire can reach 1200°C [30].

Therefore for general structural fire analysis, the heat transfer between the material and the external fire is believed to predominate the temperature changes within the material. Thus in this work the temperature rise in the material due to plastic work is assumed negligible in comparison to that caused by external fires. Consequently, it's considered appropriate to decouple the heat transfer analysis from the thermo-mechanical analysis for structural analysis with fire. Strictly referring to the effects induced by external fire loading, the temperature effects on the parameters and variables in the constitutive equations and the evolution laws of a plasticity model is the main focus of this chapter.

The influence of elevated temperatures on elastic/inelastic material response, can be treated within the framework of theories of creep [123], or using the viscoplasitc theory [155–157], where material response is treated as time-dependent. For general structural fire analysis, not considering the stage of fire-induced collapse, the structural loading is generally static. Experimental evidence [158] has shown that different loading rates have no significant influence on the initial yield surfaces at elevated temperatures. Sun et al. [159] and Maciejewski et al. [129] examined strain-rate sensitivity of carbon steel beams and steel-framed structures subjected to elevated temperatures using the Chaboche and Rousselier's viscoplastic model [149]. Both [129, 159] concluded that the strain rate dependency only becomes noticeable when the temperature goes beyond material's transitional temperature, about 700 °C for low carbon steel.

For steel structural fire design, EC 3 [1] implicitly includes the effects of transient thermal creep in its prescribed stress-strain curves. Material models constructed based on the EC3 stress-strain curves are applicable for heating rates between 2 and 50 °C/min, without the need to explicitly consider transient thermal creep [1].

Hence a time-independent/rate-independent plasticity model is assumed to be adequate for the structural fire analysis, as the strain rate has been shown insignificant, and the thermal creep can be taken into account implicitly through stress-strain curves. The influence of temperature and temperature changes within the framework of rate-independent plasticity model is investigated and discussed in the following sections.

3.1.1 Parametric dependency on temperature

The material parameters in the constitutive equations are considered to be temperature-dependent. For structural steel materials, e.g., carbon steel and stainless steel, EC3 [1] defines reduction factors of elastic modulus, yield stress (proportional limit stress) and 0.2% proof stress at elevated temperatures 20-1200 °C, with 100 °C intervals. The plastic modulus can be determined using the uniaxial stress-strain curves at elevated temperatures which can be found in design standards and literature. For example, EC3 [1] provides formulas for determining the stress-strain relationships of structural steels using its corresponding reduction factors.

3.1.2 Temperature rate dependency for internal variables

The most commonly adopted two internal state variables to be considered are the accumulated plastic strain $\overline{\varepsilon^p}$ and the backstress tensor $\boldsymbol{\beta}$. The scalar $\overline{\varepsilon^p}$ defines the isotropic hardening of the von Mises yield surface, while the tensor $\boldsymbol{\beta}$ defines the translation of the yield surface centre in the deviatoric stress space.

The evolution of $\boldsymbol{\beta}$ at elevated temperatures has been a subject of discussion for decades and the inclusion of a temperature rate is considered necessary for obtaining stable conditions [151]. Using the framework of thermodynamics with decoupled heat transfer, considering only the kinematic hardening of the material, the thermodynamic potential, or the Helmholtz free energy (ψ) can be defined as in Equation 3.1. The ψ can be split into a sum of an elastic contribution, ψ_e, which is dependent on the elastic strain (ε^e) and the temperature (T), and a contribution of hardening, ψ_p.

$$\psi = \psi_e(\boldsymbol{\varepsilon^e}, T) + \psi_p(\boldsymbol{\alpha}, T) \tag{3.1}$$

Where the $\boldsymbol{\alpha}$ is the back-strain tensor. As the internal heat generation due to plastic work is not considered in this work, the ψ_p in Equation 3.1 does not contribute to the heat transfer analysis in the material model proposed in this chapter.

If the part ψ_p of the Helmholtz free energy is expressed in a quadratic form as:

$$\psi_p(\boldsymbol{\alpha}) = \frac{1}{3}H(T)\boldsymbol{\alpha} : \boldsymbol{\alpha} \tag{3.2}$$

where the hardening modulus (H) is now a function of temperature. Then the corresponding backstress is given by:

$$\boldsymbol{\beta} = \frac{\partial \psi}{\partial \boldsymbol{\alpha}} = \frac{2}{3}H(T)\boldsymbol{\alpha} \tag{3.3}$$

Differentiating Equation 3.3 over temperature gives:

$$\frac{\partial \boldsymbol{\beta}}{\partial T} = \frac{2}{3}H(T)\frac{\partial \boldsymbol{\alpha}}{\partial T} + \frac{2}{3}\frac{\partial H(T)}{\partial T}\boldsymbol{\alpha} \tag{3.4}$$

The evolution of the internal variable backstress $\boldsymbol{\beta}$ over changing temperatures can therefore be determined using Equation 3.4.

3.2 Decoupling thermal and mechanical step

For isotropic materials, the thermal expansion caused by a change in temperature is uniform in all directions. It is an experimentally observed fact that a stress free material body will experience relative elongations but no angular changes as results of an increase or a decrease in temperature. This thermally induced strain can be imposed on the stress induced strains (mechanical strains), provided there is no change in the temperature due to the deformation of the material. Thus the total strain, which is a measure of the deformation of the material, consists of a mechanical part and a thermal part, as expressed in Equation 2.17.

The stress state (σ) for the structural material (elastic or plastic) depends only on the mechanical strains, which means thermal expansion does not directly contribute to plastic yielding if there is no boundary restraint. Where there is no boundary restraint and no external loading, the material is free to expand resulting in changes in the deformation such as axial expansion or thermal bowing. However there is no mechanical strain developed in the material in this case, hence no change of the stress state, as summarised in Equation 2.18. By contrast, where there is still no external loading but there exist boundary restraints that fully prevent any thermal expansion, the deformation of the structural material remains unchanged. As seen in Equation 2.19, in this case, the mechanical strains are developed, subsequently cause changes in the stress state.

The above two scenarios represent two opposite boundary conditions in real structures under fire. It can be clearly shown that any changes in the stress state that would cause material yielding are direct results of mechanical strain development. Therefore, rate-independent plasticity models developed for isothermal conditions are appropriate for modelling the mechanical aspect of the thermo-mechanical analysis of structural materials subjected to fire.

A thermo-mechanical analysis of structural materials in fire can be viewed as a series of isothermal mechanical analyses, each one corresponding to a thermostatic state. At each state, the isothermal mechanical analysis is carried out at the temperature related to that state. The temperature difference between two neighbouring states affects the evolution of internal variables as discussed in Section 3.1. By adding a thermal step upon the established isothermal mechanical analysis to incorporate the temperature effects, a new material model developed within the framework of rate-independent plasticity will become capable of thermo-mechanical analysis with fire.

The main objective of the thermal step is to implement temperature effects into the material parameters for the constitutive equations and the evolution equations of the internal variables, thereby enabling the subsequent mechanical analysis to be performed in an isothermal state. By isolating the mechanical aspect of the analysis from any thermal effects, it allows us to take advantages of sophisticated stress integration methods developed for existing plasticity models, such as forward-Euler method incorporating sub-incrementation [160–163], midpoint method [164, 165], radial return method [166–168], and backward-Euler method [169–171], in order to achieve higher computing efficiency.

The material parameters that are temperature-dependent and have to be updated at the thermal step are the following:

1. Elastic modulus
2. Yield stress, defined as occurring at proportional limit
3. Parameters in the constitutive equation for $\boldsymbol{\varepsilon^p}$, or flow rule
4. Parameters in the evolution equations for internal variables

3.2.1 Elastic modulus at elevated temperatures

Figure 3.1 presents the reduction factors (k_E) of initial elastic modulus provided by EC3 [1] for carbon steel and Design Manual of Structural Stainless Steel (DMSSS) [2] for stainless steel. Both steel materials exhibit reduction of stiffness at increasing temperatures.

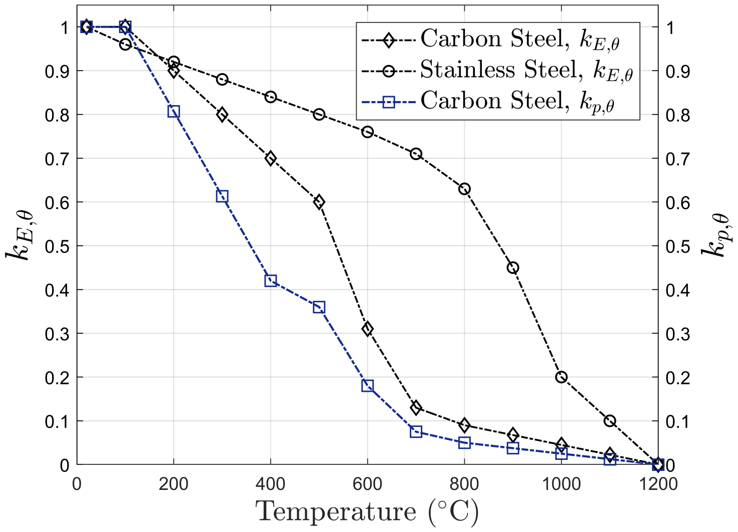

Figure 3.1: Stiffness reduction factors

3.2.2 Yield surfaces at elevated temperatures

The yielding, defined as occurring at the proportional limit, is temperature-dependent. The initial yield surfaces at elevated temperatures shrink as temperature rises. Figure 3.1 shows the reduction factors of yield stress (k_p) for carbon steel according to EC 3 [1].

At room temperature, the von Mises yield criterion has been shown to be in excellent agreement with experiments for many ductile metals [172]. It predicts the initial yield surface to be a circle in the deviatoric stress space. At elevated temperatures, Phillips et al. [127] experimentally determined yield surfaces of pure aluminium at 66 °C, 108 °C and 152 °C; Lissenden et al. [158] experimentally investigated the initial yield surface of type 316 stainless steel at 650 °C; Inoue and Tanaka [173] obtained the initial yield surfaces of low carbon steel at 200 °C, 250 °C, 300 °C and 450 °C through a series of experiments. They all found that the size and shape of the experimentally determined initial yield surfaces agreed satisfactorily to that predicted using the von Mises yield criterion. It is therefore reasonable to believe the von Mises yield criterion remains applicable at elevated temperatures.

3.2.3 Plastic flow potential at elevated temperatures

The foundation of the plastic flow potential theory is the normality flow rule of a potential function. At higher temperatures, Lissenden et al. [158] observed that for 316 stainless steel, the directions of the plastic increment pointed in the general direction of the outward normal of the yield locus at 650 °C. It is believed that the normality is still applicable for steels at elevated temperatures. Consequently, the flow potential can be determined by the yield function and hardening law using the associated flow theory [172].

The hardening law of the carbon steel material model can be obtained by least square fitting the EC 3 [1] stress-strain curves at elevated temperatures using the Voce law:

$$\sigma_{y,T} = \sigma_{y_0,T} + v_T(1 - exp(-\delta_T \overline{\varepsilon_p})) \tag{3.5}$$

where $\sigma_{y_0,T}$ is the initial yield stress (yielding stress of proportional limit) at temperature T, which can be calculated using reduction factor (k_p) prescribed by the EC3 or determined through least square fitting the stress-strain curves. The parameter v_T and δ_T are both temperature dependant material constants. It's found that a better least square fitting results, using the Adj-R-square ratio as the indicator, could be achieved by determining $\sigma_{y_0,T}$ through curve fitting. Figure 3.2 presents the carbon steel stress —plastic strain curves at elevated temperatures obtained using least square fitting in conjunction with the nominal EC 3 curves. A general good agreement is achieved. The material parameters obtained are summarised in Table D.1. The linear interpolation technique is employed for obtaining the values for intermediate temperatures.

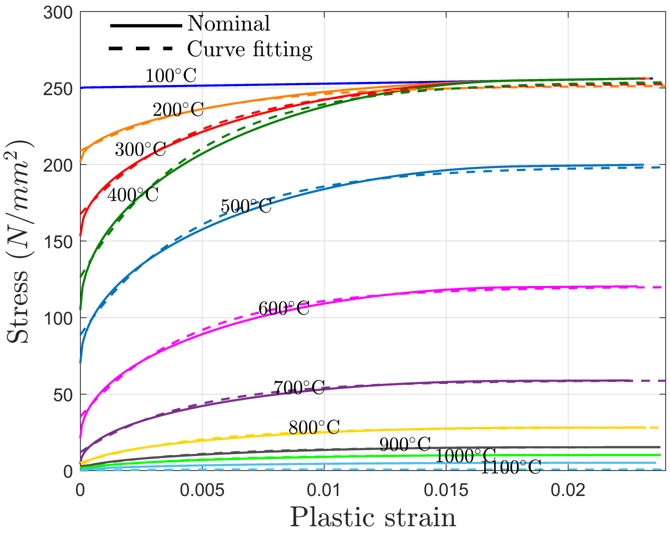

Figure 3.2: EC3 stress-strain curves vs Least square fitting

Unlike carbon steel displaying a saturation stress, stainless steel exhibits a substantial strain hardening effect. Therefore, a modified Ludwik strain hardening law [112] has been adopted for stainless steel:

$$\sigma = \sigma_0 + k(\varepsilon_{p,0} + \varepsilon_p)^n \tag{3.6}$$

where σ_0 is the initial yield stress, and k and n are material parameters. The parameter $\varepsilon_{p,0}$ was introduced as the incipient plastic strain. Because stainless steel does not exhibit a distinct yielding point, in this study the initial yielding point (σ_0) is defined at the stress point where the plastic strain reaches 0.1% of the total strain, i.e., $\varepsilon_{p,0} = 0.001\varepsilon_{total}$.

The advantages of adopting the modified Ludwik law are twofold. Firstly, by keeping the proportion of plastic strain to total strain ($\varepsilon_p/\varepsilon$) constant, the elastic range ($\sigma_{0_T}/\sigma_{0.2\%,T}$) of the stress-strain curves was maintained uniform at elevated temperatures. This approach differs from traditionally adopting one proof strain, e.g., 0.01% as the yield point for all temperatures. Secondly, the numerical instabilities caused by the original Ludwik law were circumvented by the introducing of $\varepsilon_{p,0}$, which had an order of magnitude of 10^{-6} for Austenitic III stainless steel and 10^{-7} for Duplex II stainless steel.

The hardening function parameters determined for the DMSSS Austenitic group III using least square fitting are summarised in Table D.2. At each temperature level, the curve fitting value of σ_{0_T} is about 22% of the 0.2% proof strength ($\sigma_{0.2\%,_T}$). Table D.3 presents the hardening function parameters determined for the DMSSS Duplex group II.

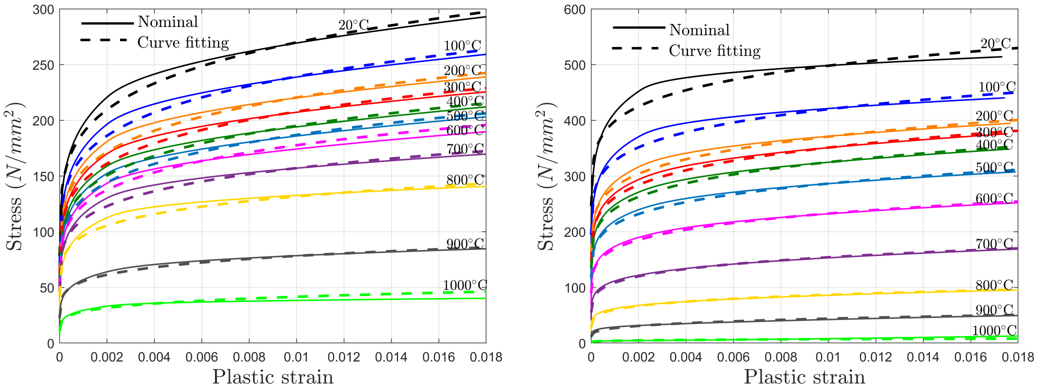

(a) Austenitic group III **(b)** Duplex group II

Figure 3.3: Stress-strain curves at elevated temperatures, Nominal vs Curve fitting

3.2.4 Internal state variables' evolution at elevated temperatures

The accumulated plastic strain $\left(\overline{\varepsilon^p}\right)$ remains constant during the thermal step. The backstress tensor $\boldsymbol{\beta}$ evolves over changing temperatures as expressed in Equation 3.4. At the thermal step where no change in the (mechanical) strain increment considered, $\frac{\partial \boldsymbol{\alpha}}{\partial T} = 0$. Equation 3.4 can be reduced to:

$$\frac{\partial \boldsymbol{\beta}}{\partial T} = \frac{2}{3}\frac{\partial H(T)}{\partial T}\boldsymbol{\alpha} \tag{3.7}$$

Since $\boldsymbol{\beta}$ is deemed temperature rate-independent, its value at a temperature point T can be determined by:

$$\boldsymbol{\beta}_T = (\boldsymbol{\beta})_{T=0} + \frac{\partial \boldsymbol{\beta}}{\partial T} T \tag{3.8}$$

As the tangent hardening modulus H is linearly interpolated between two stress —strain curves at different temperatures, H becomes H_T —the hardnening modulus at the temperature T, and substituting Equation 3.7 into Equation 3.8 gives:

$$\boldsymbol{\beta}_T = (\boldsymbol{\beta})_{T=0} + \frac{2}{3} H_T \boldsymbol{\alpha} \tag{3.9}$$

Equation 3.9 can therefore be used to determine the new position of the yield surface centre due to a temperature change at the thermal step for current material point position.

3.3 A new plasticity model for thermo-mechanical analysis with fire

The new rate-independent plasticity model for thermo-mechanical analysis of steel materials subjected to fire developed is a combined isotropic and kinematic hardening model. It adopts the concept of yield and bounding surfaces of the two-surface plasticity theory in combination with the Bauschinger ratio to model the material's Bauschinger effect. Meanwhile, two kinematic hardening variables are used to model the transient hardening behaviour that material exhibits upon reverse loading. The theoretical details of the proposed new model are described in this section.

3.3.1 Thermal step

During the thermo-mechanical analysis, the thermal step is responsible for updating both the bounding and the yield surface at elevated temperatures. In the proposed material model, the bounding surface at a temperature T is considered to have isotropic hardening only, shown as dashed circles in Figure 3.4. The size of the bounding surface can be obtained using the uniaxial tensile stress —plastic strain relationships combined with von Mises yield criterion, with all the material parameters at the temperature T applied. This gives the bounding surface (F=0):

$$\begin{gathered} F_T = J(\boldsymbol{\sigma}) - \sqrt{\frac{2}{3}} Y_{1D,T}(\overline{\varepsilon^p}) = 0 \\ J(\boldsymbol{\sigma}) = \sqrt{\boldsymbol{s} : \boldsymbol{s}} \end{gathered} \tag{3.10}$$

where J represents the size of the surface in the deviatoric stress space, $\boldsymbol{s}$ is the deviatoric stress tensor, and Y_{1D} is the uniaxial stress-plastic strain relationship.

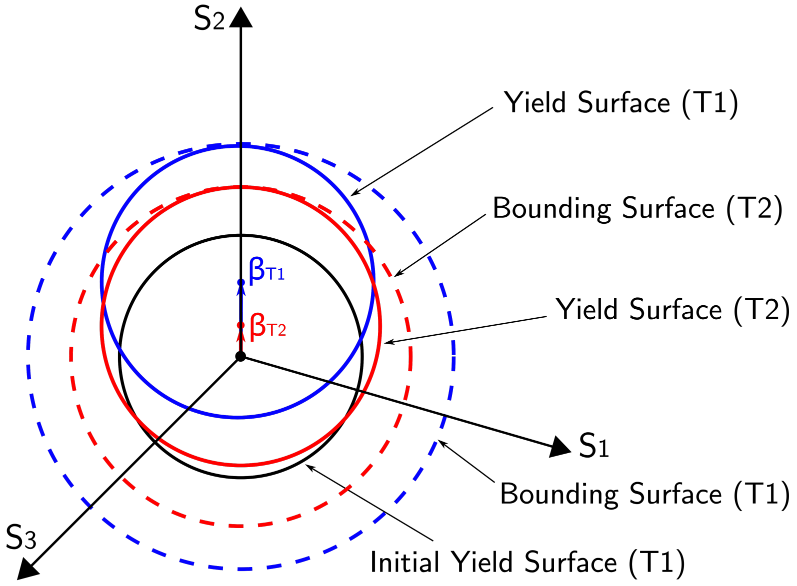

Figure 3.4: Combined isotropic/kinematic hardening yield surfaces with temperature changes in the deviatoric stress space

The (inner) yield surface ($f = 0$) can expand isotropically and move kinematically. The yielding function is defined as in Equation 3.11, incorporating the Bauschinger ratio ϑ_T. With the same uniaxial stress-strain curve adopted, the bounding surface and yielding surface share the same shape, as shown in Figure 3.4.

$$\begin{gathered} f_T = J(\boldsymbol{\sigma} - \boldsymbol{\beta_T}) - \vartheta_T \sqrt{\frac{2}{3}} Y_{1D,T}(\overline{\varepsilon^p}) = 0 \\ J(\boldsymbol{\sigma} - \boldsymbol{\beta_T}) = \sqrt{(\boldsymbol{s} - \boldsymbol{\beta_T}) : (\boldsymbol{s} - \boldsymbol{\beta_T})} \end{gathered} \tag{3.11}$$

The Bauschinger ratio ϑ_T decomposes the size of the bounding surface at the current temperature into the isotropic and the kinematic hardening part of the yield surface, and is defined by Equation 3.12. At the starting point there is only isotropic hardening, $Y_{iso,T} = Y_{1D,T} \Rightarrow \vartheta_T = 1.0$.

$$\begin{gathered} \vartheta_T = \frac{Y_{iso,T}}{Y_{1D,T}} \\ 0 \leq \vartheta_T \leq 1 \end{gathered} \tag{3.12}$$

The evolution of the Bauschinger ratio is evaluated using an exponential function of accumulated plastic strain ($\overline{\varepsilon^p}$):

$$\vartheta_T = a_T exp(-b_T \overline{\varepsilon^p}) + c_T \tag{3.13}$$

where a_T, b_T, c_T are temperature-dependent material coefficients.

During thermo-mechanical analysis, the subsequent yield surfaces shrink due to the reduction in the elastic region at elevated temperatures, meanwhile they also expand and translate due to plastic hardening. As illustrated in Figure 3.4, at temperature T1, the initial yield surface is the black circle, the bounding surface ($F_{T1} = 0$) is the dashed blue circle, and the yield surface ($f_{T1} = 0$) is the solid blue circle. The yield surface sits inside the dashed blue circle and of a larger size than the black circle since it considers both isotropic and kinematic hardening.

For an increasing temperature T2, the bounding surface ($F_{T2} = 0$) is the red circle in dashed line. At the thermal step, since there is no (mechanical) strain increment considered, the yield surface at T2 ($f_{T2} = 0$) should not go beyond the bounding surface. The movement of the yield surface caused by the evolution of backstress due to changing temperatures should be restricted by the bounding surface.

Upon a temperature change, the backstress tensor $\boldsymbol{\beta_T}$ gives a new position of the yield surface centre in the deviatoric stress space, and is determined by Equation 3.14. It is derived from Equation 3.9, by adopting uniaxial tensile stress-plastic strain curves for the determination of hardening modulus and the Bauschinger ratio for decomposing the kinematic hardening from the total hardening.

$$\boldsymbol{\beta_T} = (1.0 - \vartheta_T)\sqrt{\frac{2}{3}} Y_{1D,T}(\overline{\varepsilon^p}) \frac{\boldsymbol{\varepsilon^p}}{\|\boldsymbol{\varepsilon^p}\|} \tag{3.14}$$

The re-positioning of the yielding surfaces resulting from temperature changes is performed at the thermal step, to allow the plastic strain increment to be determined in the subsequent mechanical step following the established algorithms of associative plastic flow rule. As illustrated in Figure 3.4, the yield surface centre has to be re-positioned from $\boldsymbol{\beta}_{T1}$ to $\boldsymbol{\beta}_{T2}$.

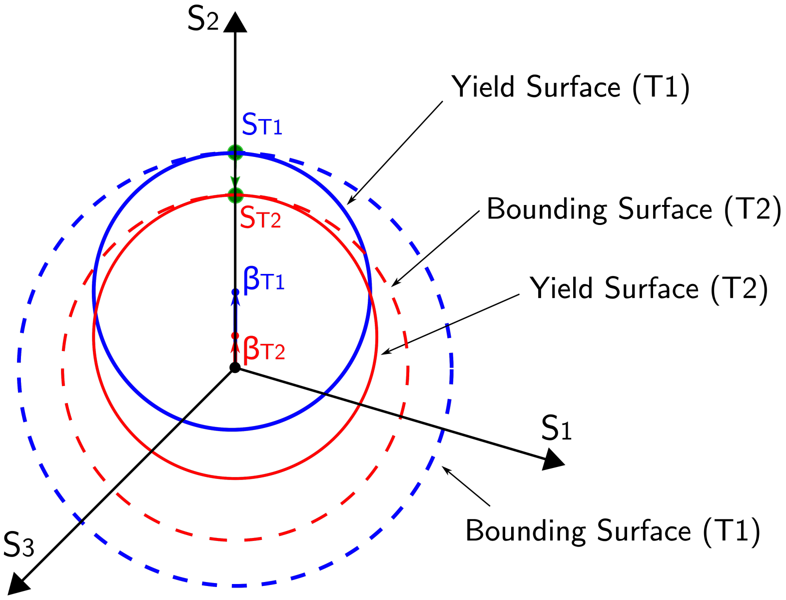

Figure 3.5: Re-positioning of yield surface due to changing temperatures

When temperature increases from T1 to T2, S_{T1} (green dot on the blue circle in Figure 3.5), which is the stress state converged at T1, now sits outside of the bounding surface of T2 (red circle in dashed line). The bounding surface size at T2 (J^*_{T2}) can be determined by Equation 3.15. The Bauschinger ratio at T2 (ϑ_{T2}) determines the size of the yield surface at T2 (J_{T2}) following Equation 3.16 and the backstress $\overline{\beta}_{T2}$ using Equation 3.17. The Bauschinger ratio ensures the yield surface always stays inside the bounding surface.

$$J_{T2}^{*} = \sqrt{\frac{2}{3}} Y_{1D,T2}(\overline{\varepsilon^{p}}) \tag{3.15}$$

$$J_{T2} = \vartheta_{T2} J_{T2}^{*} \tag{3.16}$$

$$\overline{\beta}_{T2} = (1 - \vartheta_{T2}) J_{T2}^{*} \tag{3.17}$$

The direction of the backstress tensor at T2 ($\boldsymbol{\beta}_{T2}$) is in the direction of the plastic strain tensor, hence the $\boldsymbol{\beta}_{T2}$ can be computed following Equation 3.18 :

$$\boldsymbol{\beta_{T2}} = \overline{\beta}_{T2} \frac{\boldsymbol{\varepsilon^{p}}}{||\boldsymbol{\varepsilon^{p}}||} \tag{3.18}$$

The equivalent stress state (S_{T2}) on the yield surface of T2 (green dot on the red circle in Figure 3.5) can therefore be determined following Equation 3.19:

$$\boldsymbol{S_{T2}} = J_{T2} \frac{\boldsymbol{\varepsilon^{p}}}{||\boldsymbol{\varepsilon^{p}}||} - \boldsymbol{\beta_{T2}} \tag{3.19}$$

As can be seen in Equations 3.18 and 3.19, during the thermal re-positioning, the direction of the yield surface centre and the equivalent stress state are determined by the direction of the plastic strain tensor. In the proposed material model, plastic strain tensor is the plastic internal variable at the thermal step.

3.3.2 Mechanical step

At the mechanical step, the stress state is considered isothermal hence the temperature dependence can be deemed “frozen” during the stress integration process. The Bauschinger effect is captured by incorporating Bauschinger ratio ($\vartheta(\overline{\varepsilon^{p}})$) as an internal variable. The evolution function of $\vartheta(\overline{\varepsilon^{p}})$ is an exponential growth function of the accumulated plastic strain ($\overline{\varepsilon^{p}}$), thus $\vartheta(\overline{\varepsilon^{p}})$ is a plastic internal variable as it evolves over plastic hardening. Besides the Bauschinger effect, the material also exhibits transient hardening upon reverse loading. In the proposed model, two non-linear kinematic hardening variables are adopted to capture these two behaviour, defined as in Equation 3.20. The second variable ($\dot{\boldsymbol{\beta}}_{2}$) only gets activated upon

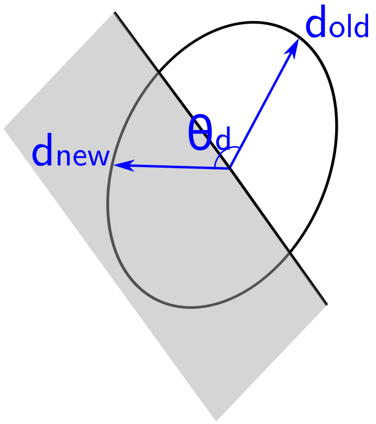

Figure 3.6: Reverse loading criterion

reverse loading.

$$\dot{\boldsymbol{\beta}} = \dot{\boldsymbol{\beta}}_1 + \dot{\boldsymbol{\beta}}_2 l \tag{3.20}$$

The internal variable —reverse loading index (l) is introduced to track any drastic changes in the loading direction. Figure 3.6 shows the reverse loading can be detected by the angle θ_d between the old loading direction and the new loading direction as follows:

$$\begin{gathered} cos(\theta_d) = \frac{\boldsymbol{\eta}_{old} \cdot \boldsymbol{\eta}_{new}}{\|\boldsymbol{\eta}_{old}\| \|\boldsymbol{\eta}_{new}\|}; \qquad \boldsymbol{\eta} = \boldsymbol{s} - \boldsymbol{\beta} \\ cos(\theta_d) \geqslant 0, \quad l = 0; \qquad cos(\theta_d) < 0, \quad l = 1 \end{gathered} \tag{3.21}$$

3.3.2.1 First kinematic hardening variable $\dot{\boldsymbol{\beta}}_1$

During monotonic loading, as illustrated in Figure 3.7a, the first backstress term ($\dot{\boldsymbol{\beta}}_1$) accounting for the movement of the yielding surface (solid blue circle) is determined through the Bauschinger ratio ($\vartheta(\overline{\varepsilon^p})$) as follows:

$$\dot{\boldsymbol{\beta}}_1 = (1 - \dot{\vartheta}(\overline{\varepsilon^p}))\sqrt{\frac{2}{3}}\dot{Y}_{1D}(\overline{\varepsilon^p})\frac{\boldsymbol{\eta}}{\|\boldsymbol{\eta}\|} \tag{3.22}$$

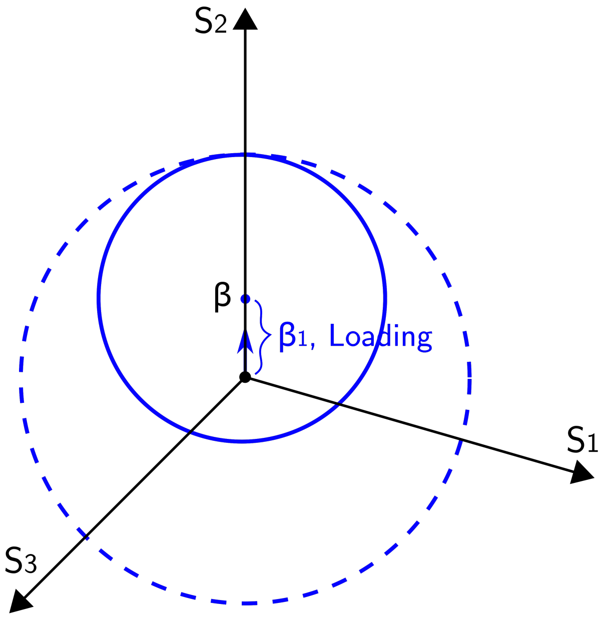

(a) Loading

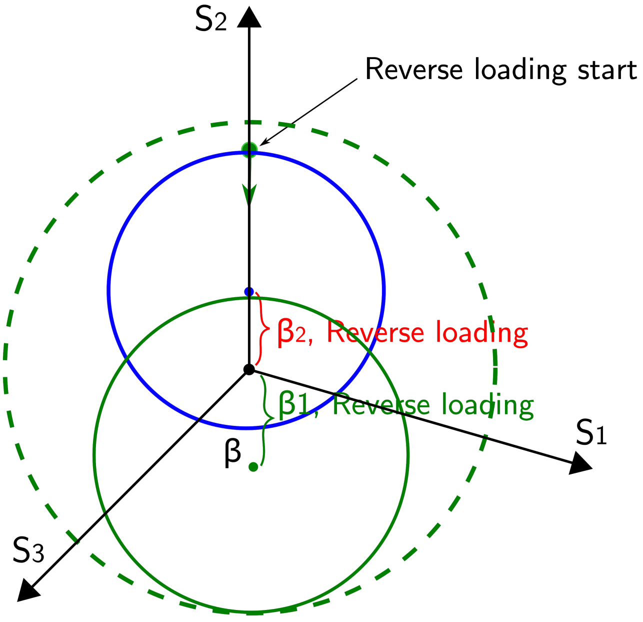

(b) Reverse loading

Figure 3.7: Proposed model during loading –reverse loading in the deviatoric stress space

Upon reverse loading, the $\dot{\boldsymbol{\beta}}_1$ continues to develop in the reverse loading direction as $\overline{\varepsilon^p}$ increases. The $\vartheta(\overline{\varepsilon^p})$ decomposes the kinematic hardening out of the total hardening at the new loading direction, illustrated as the green bracket portion of the radius of the new bounding surface (dashed green circle) in Figure 3.7b.

3.3.2.2 Second kinematic hardening variable $\dot{\boldsymbol{\beta}}_2$

In addition to the $\dot{\boldsymbol{\beta}}_1$, a second kinematic hardening variable is introduced in the proposed model to describe the shifted yield surface centre (blue dot in Figure 3.7) travelling back to the origin of the deviatoric stress space. Acknowledging the evanescent characteristic of kinematic hardening, the second variable $\dot{\boldsymbol{\beta}}_2$ can be viewed as the yield surface exhibits an urgent tendency to move back quickly to the origin upon reversing.

The exponential growth function of Equation 3.13 adopted for Bauschinger ratio evolution indicates that the yield surface moves away from the origin at an exponential speed during initial loading. It is reasonable to postulate that the yield surface exhibits the same tendency upon reversing, shifting back to the origin at an exponential rate, if not following the identical speed to that during the initial loading. Based on this assumption, a reverse loading ratio ($\upsilon(\overline{\varepsilon_l^p})$) is introduced as an exponential decay function of the effective plastic strain of the new reloading branch, denoted $\overline{\varepsilon_l^p}$, as in Equation 3.23. The scalar $\overline{\varepsilon_l^p}$ accounts for the effective plastic strain accumulated during each loading branch, and will be reset to zero whenever reverse loading is detected. The material parameter in Equation 3.23 can be obtained from the testing data of reverse loading curves. Simplifying to assume the same exponential speed for backtracking, the material constant b in the Bauschinger ratio evolution Equation 3.13 can be applied to the parameter V_b.

$$\upsilon = 1.0 - exp(-V_b\overline{\varepsilon_l^p}) \tag{3.23}$$

The typical evolution of reverse loading ratio is compared with that of Bauschinger ratio in Figure 3.8. The Bauschinger ratio starts at 1.0 indicating pure isotropic hardening at the beginning of plastic hardening. It decays and steadies at a value below 1.0 where kinematic hardening has reached its saturation value. Contrarily, the reverse loading ratio starts from 0.0 meaning the backtracking is yet

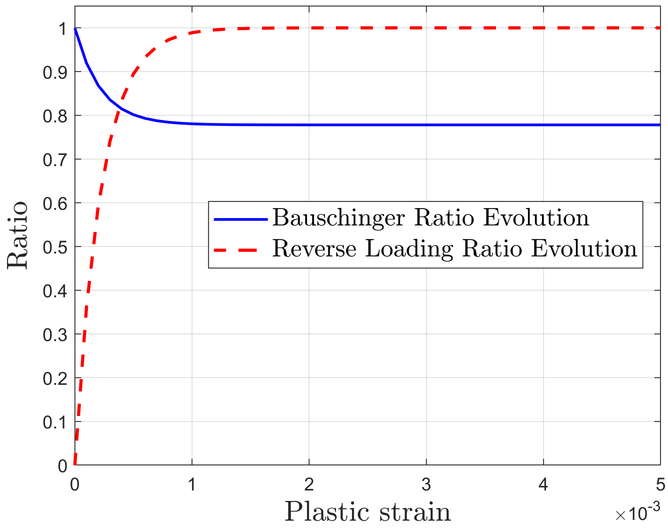

Figure 3.8: Typical Bauschinger ratio and Reverse loading ratio evolution

to start, and plateaus at the value of 1.0, which indicates at this point the entire distance travelled by the yield surface centre in the previous loading branch has been recovered.

The kinematic hardening ($\dot{\boldsymbol{\beta}}_2$) is therefore defined as:

$$\dot{\boldsymbol{\beta}}_2 = \dot{\upsilon}\sqrt{\frac{2}{3}}\dot{\overline{\beta_l}}\frac{\boldsymbol{\eta}}{\|\boldsymbol{\eta}\|} \tag{3.24}$$

The $\overline{\beta_l}$ is a scalar —the distance the yield surface centre travelled during the last loading branch in the uniaxial stress direction, as shown in Figure 3.9, and can be obtained as follows:

$$\dot{\overline{\beta_l}} = V_h\sqrt{\frac{3}{2}\dot{\boldsymbol{\beta}}_{\boldsymbol{n}} : \dot{\boldsymbol{\beta}}_{\boldsymbol{n}}} \tag{3.25}$$

where $\dot{\boldsymbol{\beta}}_{\boldsymbol{n}}$ is the rate of the (total) backstress tensor at the end of last loading branch prior to the start of reserve loading. The material parameter V_h is introduced to account for potential softening/hardening during reverse loading. It can be obtained using experimental reverse stress-strain data.

The second variable $\dot{\boldsymbol{\beta}}_2$ gets activated upon reverse loading, more precisely only when re-yielding starts. Between the reverse loading point and the re-yielding point, shown as the green dots in Figure 3.9, is the unloading range during which plastic internal variables remain unchanged.

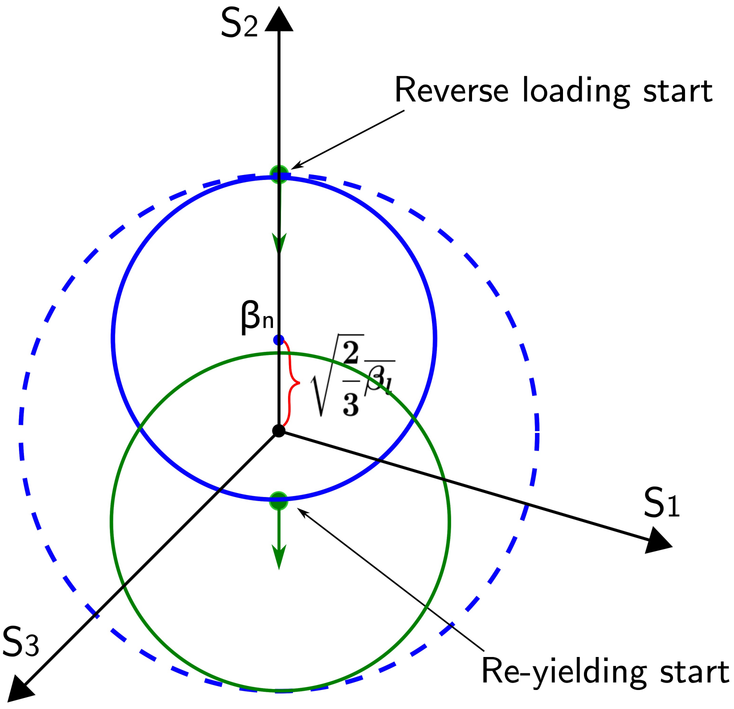

Figure 3.9: Proposed model during reverse loading in the deviatoric stress space

3.3.3 Thermal step during reverse loading

The second kinematic variable $\dot{\boldsymbol{\beta}}_2$ was introduced in Section 3.3.2 to account for material's transient hardening behaviour during reverse loading at the mechanical step. The thermal step described in Section 3.3.1 applies to the temperature changes experienced by the internal variables during initial monotonic loading. For modelling temperature changes that occur during reverse loading, the $\dot{\boldsymbol{\beta}}_2$ has to be appropriately incorporated in the thermal step to ensure the transient behaviour is retained.

The $\dot{\boldsymbol{\beta}}_2$ describes the yield surface backtracking the distance ($\overline{\beta_l}$) that has been travelled in the stress space prior to the reverse loading. Since the distance ($\overline{\beta_l}$) is inherited from the previous loading branch, it remains constant during the reverse loading. As shown in Equation 3.24, the temperature only affects the 'speed' of the $\boldsymbol{\beta}_2$, as the material parameter V_b in the evolution function of the reverse loading ratio (υ), Equation 3.23, is temperature-dependent.

Therefore, the $\dot{\boldsymbol{\beta}}_2$ does not actively contribute during the thermal step. The procedures described in Section 3.3.1 for updating bounding and yield surface resulting from temperature changes, can be viewed as taking place from the yield surface centre that is positioned at $\boldsymbol{\beta}_2$ in the stress space. Thus the algorithm proposed in Section 3.3.1 is still applicable, recognising that the backstress used in the algorithm exclusively refers to the first kinematic hardening variable $\boldsymbol{\beta}_1$. The only modification required is in the last step —calculating the equivalent stress state —to take the $\boldsymbol{\beta}_2$ into account. Equation 3.19 now becomes:

$$\boldsymbol{S}_{\boldsymbol{T2}} = J_{T2}\frac{\boldsymbol{\varepsilon^p}}{||\boldsymbol{\varepsilon^p}||} - \boldsymbol{\beta}_{\boldsymbol{1}_{\boldsymbol{T2}}} - \boldsymbol{\beta}_2 \tag{3.26}$$

3.3.4 Elastoplastic consistent tangent modulus $\boldsymbol{D^{ep}}$

The exact linearisation of the incremental stress updating procedure, rather than to appeal to the rate stress —strain tangential relation, is essential for achieving quadratic rates of convergence in the iterative solution of the finite element equilibrium equations as emphasised by Negtegaal [174], Simo and Taylor [175].

Linearising the incremental constitutive function of stress tensor ($\boldsymbol{\sigma}$) yields the consistent tangent operator ($\boldsymbol{D}$).

$$\boldsymbol{D} = \frac{\partial \Delta \boldsymbol{\sigma}}{\partial \Delta \boldsymbol{\varepsilon}} \tag{3.27}$$

The fully implicit backward-Euler return mapping algorithm has been adopted in the proposed material model to solve the yield condition equation:

$$\Phi(\Delta\gamma) \equiv ||\boldsymbol{\eta}_{n+1}^{trial}|| - 2\mu\Delta\gamma - (\overline{\beta_1}_{n+1} - \overline{\beta_1}_n) - \hat{H}(l)(\overline{\beta_2}_{n+1} - \overline{\beta_2}_n) - \sigma_{y,iso} = 0 \tag{3.28}$$

where $\overline{\beta_1}$ is the first kinematic term contributing to overall hardening and is a function of accumulated plastic strain ($\overline{\varepsilon^p}$) as defined in Equation 3.17. $\overline{\beta_2}$ is the second kinematic hardening term defined in Equation 3.24, l is the reverse loading index, and $\sigma_{y,iso}$ is the radius of the yield surface as defined in Equation 3.16. $\hat{H}$ is the Heaviside step function.

Equation 3.28 states the yield condition equation of full terms, using the Heaviside step function to include the second kinematic hardening term whenever reverse loading is detected. The Heaviside step function is a non-differentiable function, which means the elastoplastic consistent tangent modulus has to be derived for monotonic loading and reverse loading differently.

The elastoplastic consistent tangent during monotonic loading has been obtained as:

$$\boldsymbol{D^{ep}} = \boldsymbol{D^{e}} - 4\mu^2 \frac{1}{\Theta} \boldsymbol{N} \otimes \boldsymbol{N} - \frac{4\mu^2}{\|\boldsymbol{\eta}^{trial}_{n+1}\|} [\boldsymbol{I_{dev}} - \boldsymbol{N} \otimes \boldsymbol{N}] \tag{3.29}$$

$$\Theta = 2\mu + \frac{2}{3} H_{1D}(\overline{\varepsilon^p}_n + \sqrt{\frac{2}{3}} \Delta\gamma) \tag{3.30}$$

During reverse loading, Equation 3.29 is still applicable with the term Θ modified to include the $\boldsymbol{\beta_2}$ term as follows:

$$\Theta = 2\mu + \frac{2}{3} H_{1D}(\overline{\varepsilon^p}_n + \sqrt{\frac{2}{3}} \Delta\gamma) - \frac{2}{3} \overline{\beta_l} exp\big(-V_b(\overline{\varepsilon^p_l}_n + \sqrt{\frac{2}{3}} \Delta\gamma)\big)(-V_b) \tag{3.31}$$

A detailed derivation of the elastoplastic consistent tangent modulus is provided in Appendix C.

3.3.5 Summary of the new model

The proposed material model has been presented in this section, with the material variables introduced and described in details. The new model solves the thermo-mechanical behaviour of a material using two sequential steps, a thermal step followed by a mechanical step. Figure 3.10 schematically summaries the evolution of yield surfaces at changing temperatures. The initial yield surface ($\overline{\varepsilon^p} = 0$) at temperature T_0 is shown as the black solid circle in Figure 3.10a. As temperature increased to T_1, the initial yield surface shrinks into the blue solid circle in Figure 3.10a. At T_1, the material is stressed in the S_2 direction to the stress state S_{T1}, achieving an accumulated plastic strain of $\overline{\varepsilon^p}$. The solid blue circle in Figure 3.10b represents the yield surface at T_1 resulted from the combined isotropic and kinematic plastic hardening of the $\overline{\varepsilon^p}$. The dashed blue circle in Figure 3.10b represents the corresponding bounding surface, which is the yield surface considering only isotropic hardening.

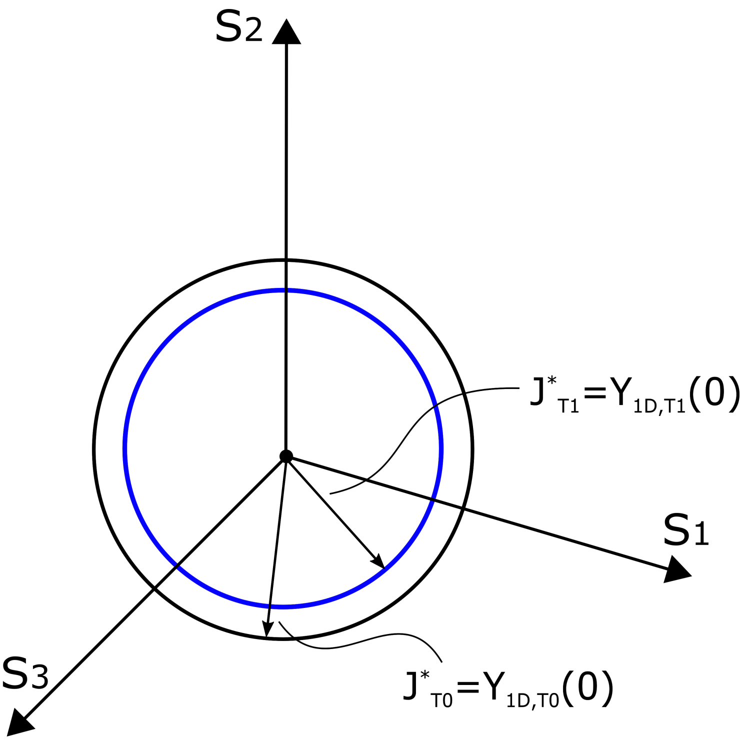

(a) Initial yield surface at T_0 and T_1

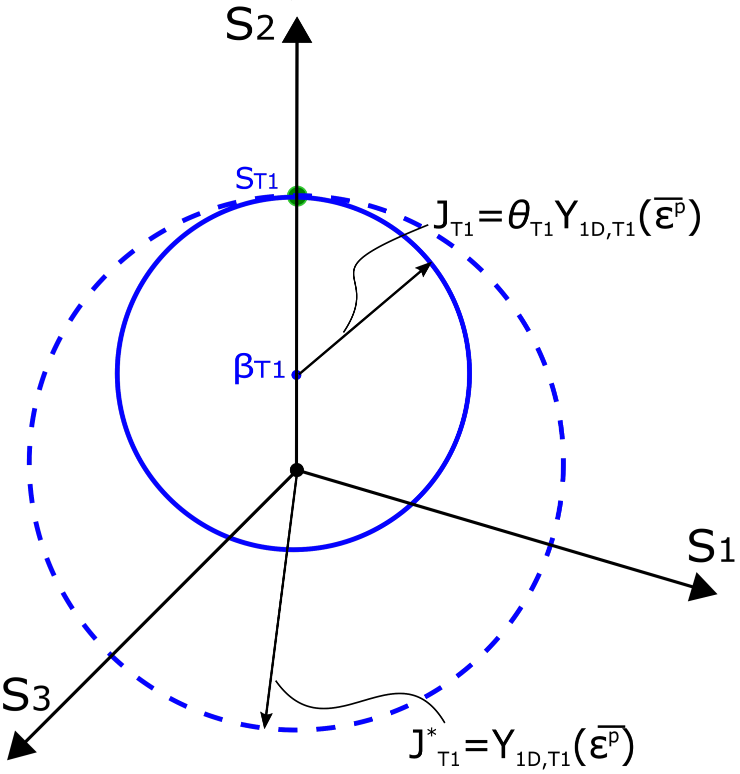

(b) Yield surface T_1

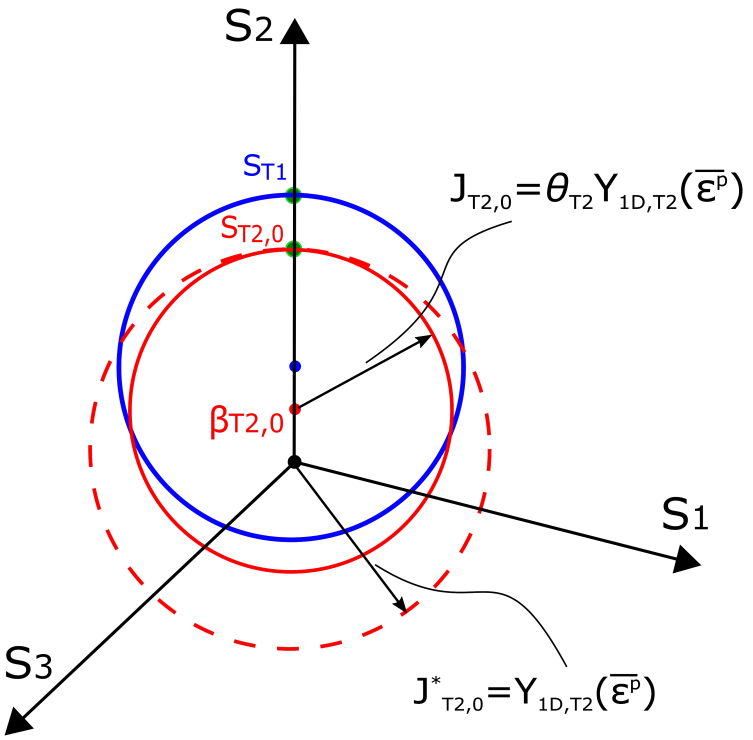

(c) Thermal step, T_1 to T_2

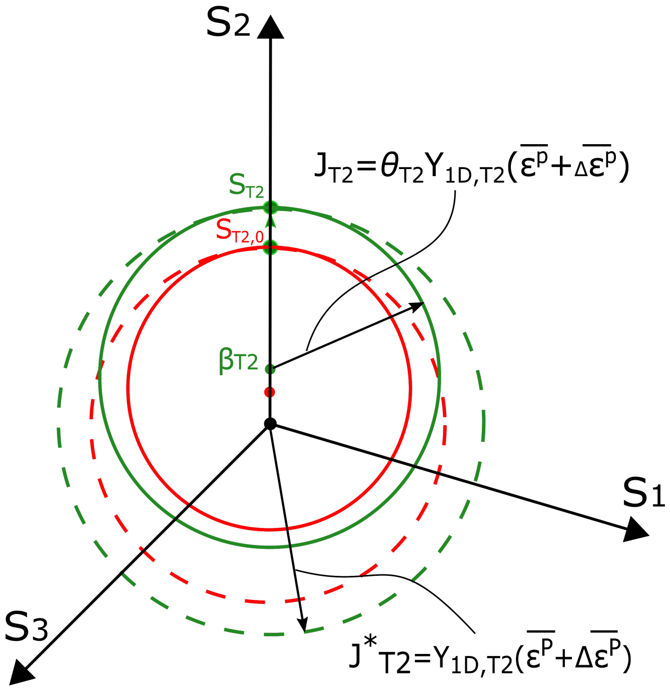

(d) Mechanical step, T_1 to T_2

Figure 3.10: Yield surface evolution, T_0 to T_2

When the yield surface at temperature T1 (the solid blue circle in Figure 3.10b and 3.10c) experiences an increment to a higher temperature T2, the thermal step determines the current state (size and position) of the yield surface at T2 (the solid red circle in Figure 3.10c). For the thermal step, the $\overline{\varepsilon^p}$ remains constant, the solid red circle can therefore be determined by the T2 hardening function ($Y_{1D,T2}(\overline{\varepsilon^p})$) and the Basuchinger ratio ϑ_{T2}. The size of the yield surface ($J_{T2,0}$) and the position of the yield surface centre ($\boldsymbol{\beta_{T2,0}}$) are determined following the Equation 3.15 to Equation 3.19. The dashed red circle represents the bounding surface at T2 which is the yield surface considering only isotropic hardening caused by the $\overline{\varepsilon^p}$. The thermal step finds the equivalent stress state of S_{T1} (the stress point sitting on the yield surface of T1) on the yield surface of T2. The equivalent stress state $S_{T2,0}$ in Figure 3.10c is determined using the Equation 3.26. The decrease in the stress from S_{T1} to $S_{T2,0}$ is caused by the shrinking of the yield surface due to the temperature increase.

The mechanical behaviour (changes in the mechanical strain due to deformation) is handled in the subsequent mechanical step. If plastic hardening occurs at T2, the stress state $S_{T2,0}$ is further stressed in the S_2 direction to the S_{T2}, resulting in an increment of $\Delta\overline{\varepsilon^p}$, then the yield surface at T2 determined at the thermal step (the solid red circle shown in Figure 3.10c and 3.10d) will be updated to the solid green circle in Figure 3.10d , computed following the stress integration process. The size of the yield surface (J_{T2}) is updated to take into account the increased isotropic hardening, and the position of the yield surface centre ($\boldsymbol{\beta_{T2}}$) is updated as a result of increased kinematic hardening, which is determined following the Equation 3.20.

The total material parameters adopted for the new model is summarised as follows:

1. Elastic modulus, E_T.
2. Initial yield strength, σ_{0_T}.
3. Hardening function parameters.
4. Parameters of Bauschinger ratio (ϑ_T) evolution function as shown in Equation 3.13.
5. Parameters of Reverse loading ratio (υ_T) evolution function as shown in Equation 3.23.

It is worth noting that the hardening function parameters are decided by the strain hardening constitutive law selected for the material. In this work, the Voce law adopted for the carbon steel required two function parameters v_T and δ_T; the modified Ludwick law selected for the DMSSS stainless steels required two function parameters k_T and n_T.

3.4 Validation of isotropic & kinematic hardening during monotonic loading

For the thermo-mechanical analysis, the parameters in the evolution function of the Bauschinger ratio becomes temperature dependant. The main objective of this section is to validate the evolution of the Bauschinger ratio in the proposed material model as a function of accumulation plastic strain ($\overline{\varepsilon^p}$) in conjunction with temperature.

Harley et al. [128] conducted a series of reverse yield experiments to measure the evolution of isotropic hardening variable (κ) and kinematic hardening variable ($\overline{\beta}_{11}$) in 304L stainless steel over a range of temperatures. The scalar isotropic hardening variable κ is related to the size of a rate-independent yield surface. The $\overline{\beta}_{11}$ is associated with the translation of the yield surface centre in the uniaxial stress direction. The experimental observations are consistent with the combined isotropic/kinematic hardening framework. Despite their inability to directly capture the initial elastic unloading behaviour in the reverse yield experiments largely due to the inelastic material behaviour of 304L stainless steel, they determined the parameters by correlating the data from additional Large Strain Reverse (LSR) experiments and the tensile segment of the reverse yield experiments. Harley et al.'s [128] data provided us an insight into how the Bauschinger effect evolves at elevated temperatures, particularly into how the two internal variables (κ and $\overline{\beta}_{11}$) of a combined isotropic/kinematic hardening plasticity model evolve at elevated temperatures.

In this validation study, at first, the κ and $\overline{\beta}_{11}$ results of Harley et al.'s experiments were analysed, based on which, a set of temperature-dependent evolution function parameters of the Bauschinger ratio were determined using the least square fitting technique. The parameters determined were implemented in the proposed material model for thermo-mechanical analysis in Abaqus using the Umat subroutine [23]. The validation was performed by comparing the Abaqus results with the experimental data.

3.4.1 Bauschinger effect determination at elevated temperatures

Based on the uniaxial stress state of the reverse yield experiment conducted in [128], neglecting the term for rate dependence in yield strength, the Bauschinger ratio (ϑ) can be determined following:

$$\sigma_{11} = \kappa + \beta_{11}; \qquad \vartheta = \frac{\kappa}{\sigma_{11}} \tag{3.32}$$

The Bauschinger ratios were calculated using Equation 3.32 at temperature 20 °C, 200 °C, 600 °C, 800 °C and 1000°C, respectively, and are presented in Figure 3.11. At each temperature level, Bauschinger ratios saw a general decreasing trend except at 1000°C. The initial plummeting of ϑ_{1000} indicated a drastic shrink of the yield surface. When considering the strain is kept constant, Figure 3.11 suggests the Bauschinger ratios experienced a reduction from 20°C to 200°C followed by a rise to 800°C, then a drop again as temperature raised to 1000°C.

The evolution function parameters of the Bauschinger ratios at each temperature level can be obtained using the least square fitting method, adopting the exponential law as in Equation 3.13. The parameters were determined at each temperature level individually and are summarised in Table D.4. They were subsequently implemented in the Umat subroutine [23] for this validation study. The fitted curves are plotted in Figure 3.11 along with the experimental values.

3.4.2 FE model descriptions

The experiments were conducted using specimens of 304L stainless steel rod, following the same reverse yield testing procedures Miller et al. [4] adopted for testing OFHC copper. The specimen is illustrated schematically in Figure 3.12.

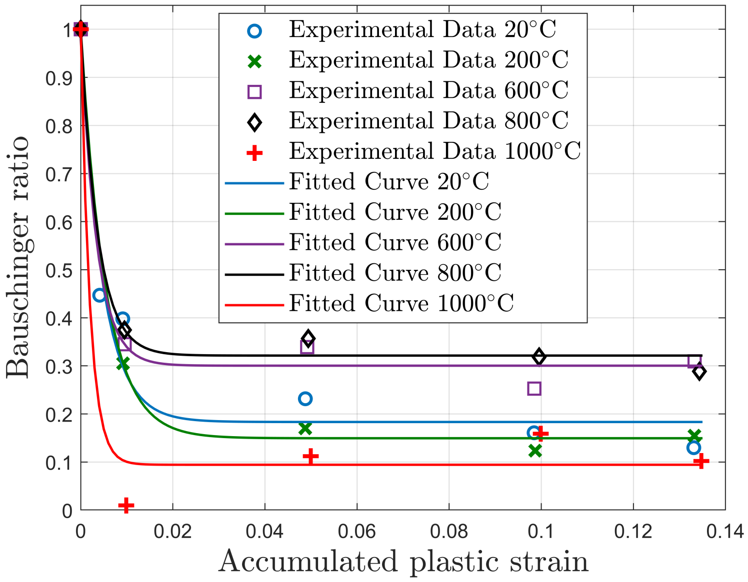

Figure 3.11: Bauschinger ratio, least square fitting

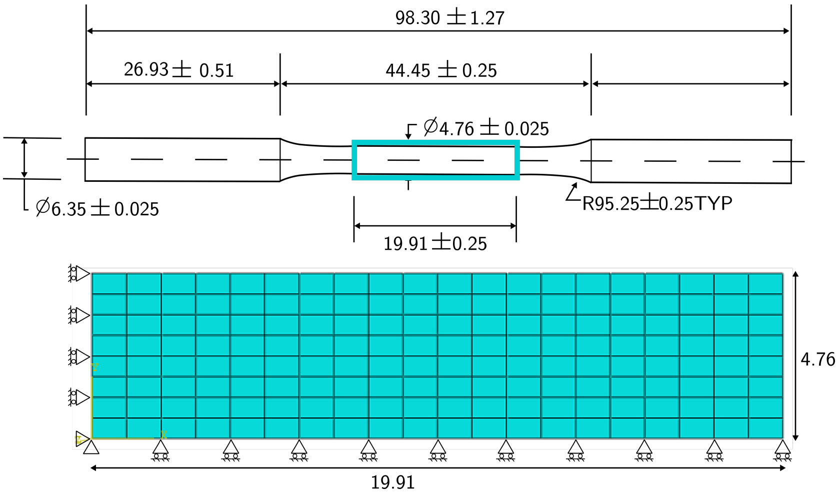

Figure 3.12: Reverse yield test specimen (all dimensions in mm) [4]

The cross-section of the gauge (outlined in Figure 3.12) was modelled using the 4-node plane stress elements in Abaqus/CAE, shown as in Figure 3.12. The model was restrained in axial direction at one end. The uniform temperature was applied in the first step. In the second step, a horizontal monotonic tensile load was applied at the other end to a maximum 5.0% axial strain.

The stress-strain curves of the 304L stainless steel used in the experiments were applied in the material model for this validation. Thus the parameters of the hardening function were obtained by least square fitting the stress-strain curves following the same approach adopted for EC3 carbon steel in Section 3.2.3, and are summarised in Table D.4 . The Young's modulus were applied following the reported values : 195.3 GPa (20 °C), 182.8 GPa (200 °C), 153.8 GPa (600 °C), 125.7 GPa (800 °C), and 94.3 GPa (1000 °C).

3.4.3 Results and discussion

In the proposed material model, the isotropic hardening variable is computed following Equation 3.33.

$$\kappa = \vartheta_T Y_T(\overline{\varepsilon^p}) \tag{3.33}$$

where Y_T is the isotropic hardening function and $\overline{\varepsilon^p}$ is the accumulated plastic strain.

The kinematic hardening variable in uniaxial stress state, $\overline{\beta}_{11}$, is calculated as follows:

$$\overline{\beta}_{11} = \sqrt{\frac{3}{2}} \|\boldsymbol{\beta}\| \tag{3.34}$$

where $\boldsymbol{\beta}$ is the total backstresses.

The Abaqus results for isotropic hardening (κ) and kinematic hardening ($\overline{\beta}_{11}$) are presented and compared with the experimental data in Figure 3.13a and Figure 3.13b, respectively. A generally good agreement is observed. The comparison has demonstrated that the evolution of Bauschinger ratio has been successfully implemented in the proposed material model as a function of temperature and accumulated plastic strain.

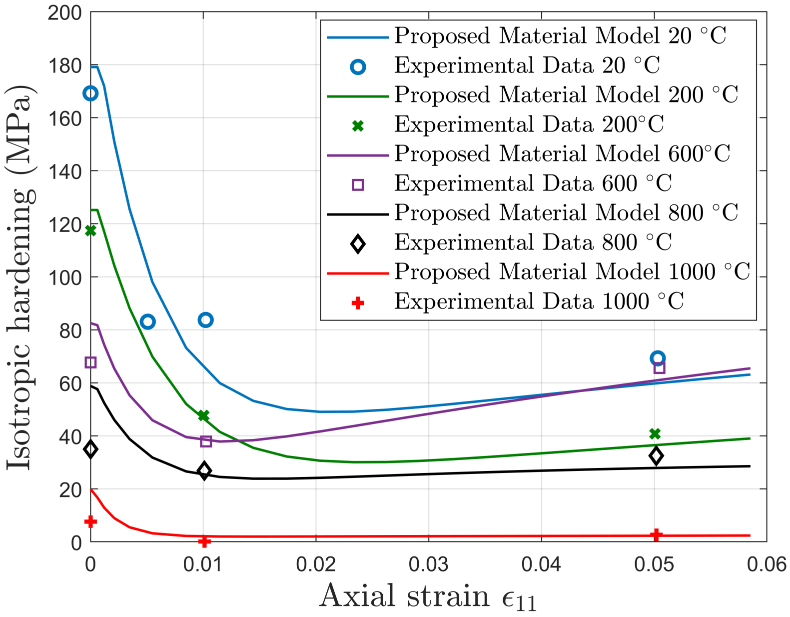

(a) Isotropic

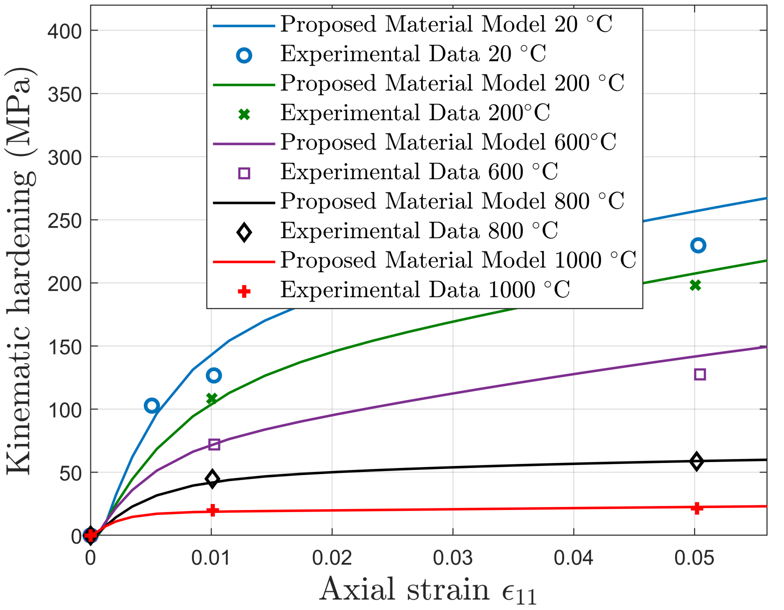

(b) Kinematic

Figure 3.13: Hardening variables comparison

3.5 Validation of Bauschinger effect and transient hardening

The Bauschinger effect and the transient hardening behaviour typically observed during reverse loading at room temperature also occur at elevated temperatures. In this section, the capability of the proposed material model to capture the Bauschinger effect and the transient hardening behaviour is validated using the experimental data obtained by Maciejewski et al. [129], who conducted a series of monotonic and cyclic loading tests on low carbon steel material (A572 Grade) at high temperatures. For the validation purpose, the experimental data of the reversed stress-strain relationship of the very first loading loop associated with the monotonic stress-strain curve has been used thereby the cyclic hardening/softening effect was excluded.

The testing was performed on cylindrical specimens with an overall length of 114 *mm*, a gauge length of 25 *mm*, and a gauge diameter of 11 *mm*. The same finite element modelling approach as in the previous validation was adopted. The proposed material model was employed for the tested low carbon steel material. The hardening function parameters were obtained by least square fitting the experimental stress-strain curves at 300 °C and 700 °C. The material properties of the Young's modulus and the initial yield stress were also calibrated from the experimental data.

The stress-strain curve (in red) at 300 °C and 700 °C obtained using least square fitting is compared with the experimental data (blue circle) in Figure 3.14a and Figure 3.14b respectively. The good agreement observed demonstrated that the Voce hardening law successfully captured the non-linear stress-strain relationship of the tested low carbon steel materials at elevated temperatures.

The hardening function parameters obtained, as summarised in Table D.5, were subsequently implemented in the Abaqus Umat code. Three reverse loading tests with varying prestrain levels were simulated in Abaqus to examine the hardening behaviour during reverse loading at 300 °C and 700 °C. The Abaqus stress-strain relationship results of monotonic loading range are compared with the curve fitting stress-strain curves in Figure 3.14a and Figure 3.14b, the good agreement suggests the hardening functions have been successfully implemented in Umat. Varying degrees of transient hardening were predicted by the proposed material model at different prestrain levels. The Bauschinger effect and the transient hardening predicted by the proposed material at the prestrain level experienced in the experiments has been investigated for the validation in the following.

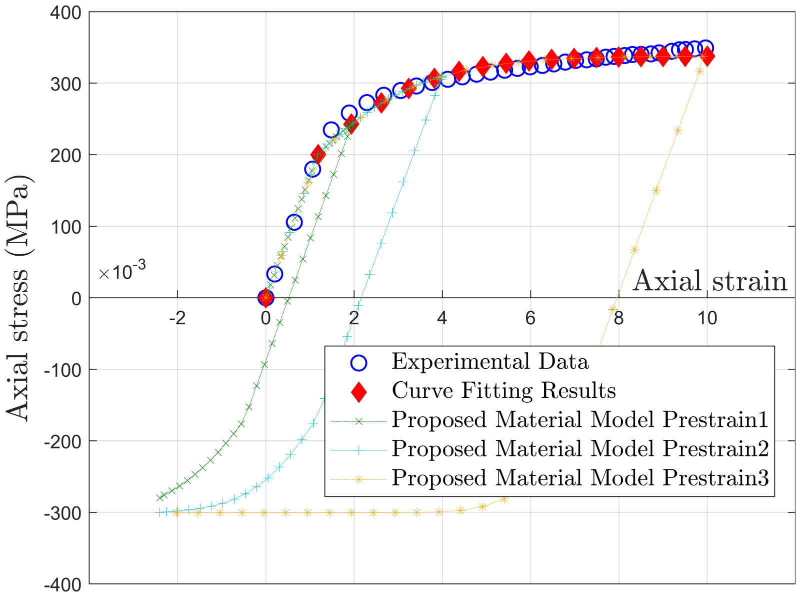

(a) T= 300°C

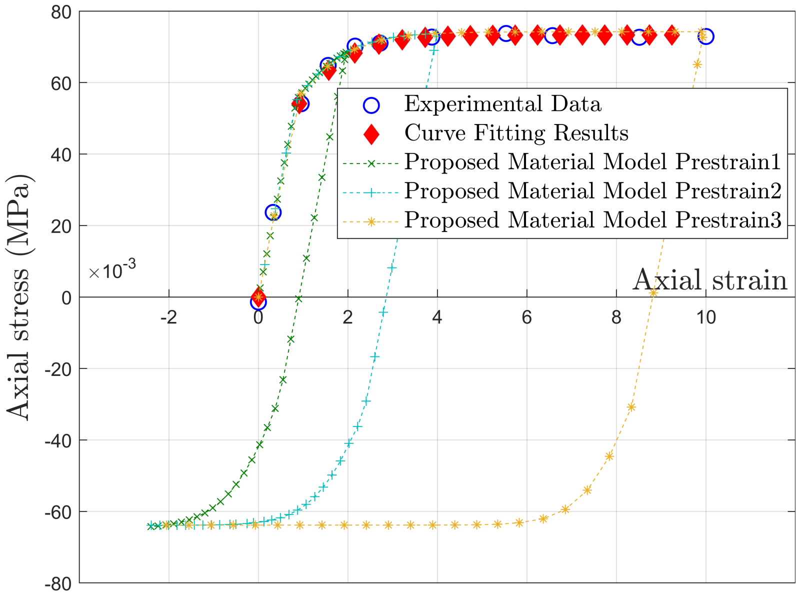

(b) T= 700°C

Figure 3.14: Stress-strain curves comparison

The Bauschinger ratio (ϑ) was determined using Equation 3.35, based on the experimental data of the reversed stress-strain curves of the very first loading loop at 300 °C and 700 °C respectively, as plotted in Figure 3.15a and Figure 3.15b. The S11L is the highest stress point during monotonic loading, and S11U is the lowest stress point before the material yields upon reverse loading, which is the transitional point form the solid blue line to the dashed blue line in the two Figures. The solid blue line presents the loading-unloading range of the stress-strain development while the dashed blue line starts from the re-yielding point of the reverse loading range.

$$\kappa_{11} = \frac{S11L - S11U}{2}; \qquad \alpha_{11} = \frac{S11L + S11U}{2}; \qquad \vartheta = \frac{\kappa_{11}}{\kappa_{11} + \alpha_{11}} \tag{3.35}$$

where κ_{11} and α_{11} represents the amount of isotropic and the amount of kinematic hardening respectively.

The Bauschinger ratio was therefore 0.597 at 20°C, 0.790 at 300 °C and 0.724 at 700 °C. The Equation 3.13 was adopted in least square fitting to describe the Bauschinger ratio evolution, assuming it would achieve stabilisation shortly after the first strain reversal. The determined evolution function parameters are summarised in Table D.5. The value of b_T in Equation 3.13 was adopted for the reverse loading ratio evolution function —Equation 3.23, as discussed in Section 3.3.2.2.

Figure 3.15a and Figure 3.15b compares the stress-strain development during the loading-unloading-reverse loading predicted using isotropic hardening model and the proposed material model with the experimental data at 300 °C and 700°C respectively. The proposed material model predicted the re-yielding point very well, properly captured the Bauschinger effect. Beyond the yielding point, the proposed material model also predicted the material's transient hardening behaviour to a degree of satisfactory at both temperature levels. On the other hand, the isotropic hardening model was not able to capture the Bauschinger effect and the transient hardening behaviour.

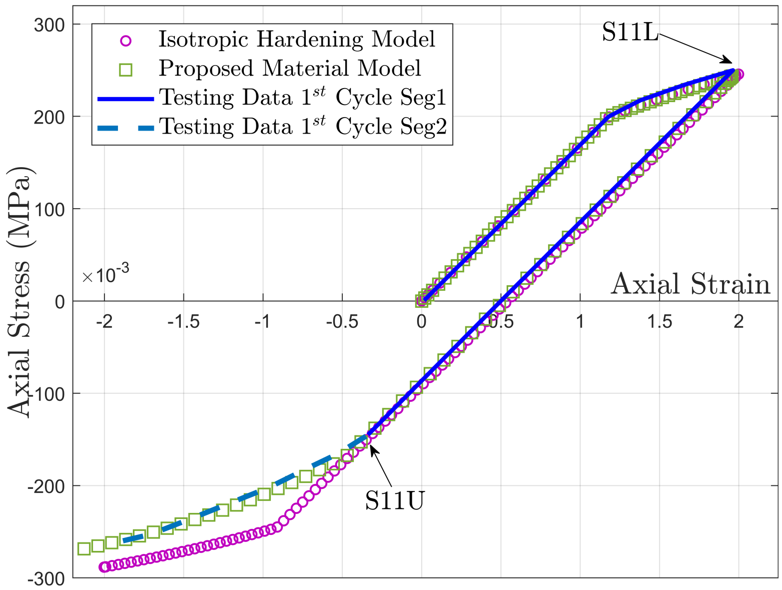

(a) T= 300°C

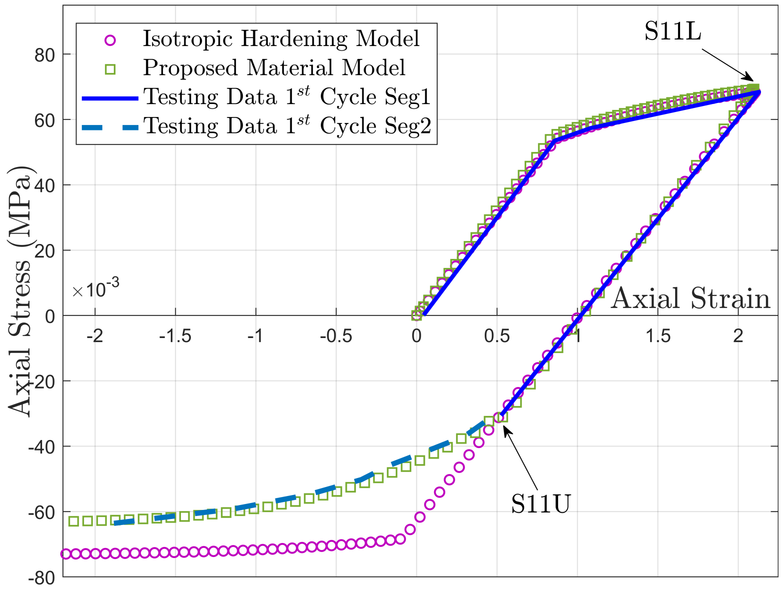

(b) T= 700°C

Figure 3.15: Hardening models comparison

3.6 Validation of thermal unloading algorithm

This section focuses on validating the implementation of the algorithm, developed for the yield surface re-positioning due to changing temperatures, in the Abaqus Umat code. At the thermal step, the new size of the yield surface is determined by Equation 3.16 and the new position of the yield surface centre is computed using Equation 3.18. The new position and size of the yield surface induces a reduction in the stress state, a phenomenon commonly referred to as thermal unloading. While the re-positioning of yield surfaces is an invisible internal process, the thermal unloading manifests itself in the changing of mechanical stress, hence can be examined numerically. The validation was therefore performed by comparing the thermal unloading result predicted by the proposed material model to its analytical solution.

The model geometry and the material properties of the low carbon steel at elevated temperatures from previous validation in Section 3.5 were utilised. A loading scenario has been designed specifically in the following way to accommodate a clear examination of the mechanical behaviour resulted from the yield surface re-positioning at the thermal step:

1. Pre-strain the material to a mechanical strain level of 0.002, into the plastic region at 300°C.

2. Increase temperature to 700°C while keeping mechanical strain constant. In this manner any changes in the stress observed at the end of the thermo-mechanical analysis is a result of the yield surface re-positioning due to temperature changes. This was achieved by applying displacement controlled boundary conditions.

3. The thermal expansion coefficient was set to zero so the observed strain results were entirely mechanical strains.

Figure 3.16 shows the stress-strain path during the designed loading process. The prestrain at 300 °C produced an accumulated plastic strain of 5.481×10^{-4}.

At 700 °C, the new yield stress =64.05 MPa (red point) is determined by Equation 3.16. For the mechanical strain =0.002, since $0.002 \times E_{700} < 64.05$, the stress state $(0.002, 48.91)$ (green cross) now sits within the yield surface. E_{700} is the elastic modulus at 700 °C. The unloading stress-strain development predicted by the proposed material model is shown in blue square, and the final stress state $=(0.002, 48.89)$, was computed by the algorithm developed based on Equation 3.26. As the thermal unloading behaviour has been successfully captured, it is believed that the algorithm for the re-positioning of the yield surface due to changing temperatures, has been correctly implemented in the Umat code.

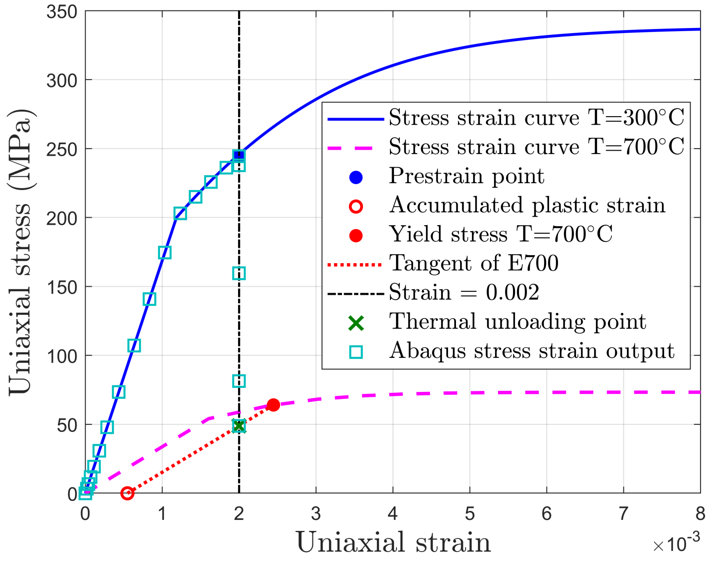

Figure 3.16: Thermal unloading validation

3.7 Validation for multi-axial loadings

In the previous three validations, the models were subjected to uniaxial loading only. In this section, the proposed material model is further tested under multi-axial loading conditions.

3.7.1 Experiments in literature review

Lissenden et al. [158] carried out experiments to determine the initial yield surface of 316 stainless steel at room temperature and its subsequent yield surface at elevated temperature 650 °C, with the impact of pre-loading on the subsequent yield surface also investigated. Tubular specimens fabricated from AISI type 316 stainless steel were used to determine the yield surfaces in the axial –shear (σ_{11}—σ_{12}) stress space. This particular stress space was used for the experiments because tubular specimens can be relatively easily subjected to combined axial-torsional loading. A small offset strain definition of yield, $10\mu\varepsilon = 10 \times 10^{-6} m/m$, was adopted by Lissenden et al. [158] to allow multiple probes in various directions to be conducted on a single specimen for the yield surface determination. This process eliminated the specimen-to-specimen variation in the test results and ensured negligible change in the material state. The extensometer was used to achieve the decoupled measurements of axial and shear strain due plasitc hardening. For each surface determination, 16 unique probes at different angles in the axial-shear (σ_{11}—σ_{12}) stress space were performed to find the shape and size of the surface. The testing results were plotted in the modified stress space ($\sigma_{11}/\sqrt{3}$—σ_{12}) where a von Mises yield surface was shown as a circle.

The experimental data obtained by Lissenden et al. [158] were employed for the validation in the section. A brief description of the loading procedure and the findings of the experiments at room temperature and at 650 °C is provided in the following sections.

3.7.1.1 Room temperature

The testing results suggested the initial yield surface could be represented using a circle of radius 82 MPa predicted by the von Mises yield criterion in the modified stress space, with the centre located at (-8 MPa, -4 Mpa) rather than at the origin, possibly due to initial residual stresses caused during the fabrication. The impact of pre-stress on the subsequent yield surfaces was investigated by applying a radial pre-loading, defined by $\sigma_{12} = \sigma_{11}/\sqrt{3}$, until 50% beyond the initial yield to a maximum stress point (160 MPa, 84 MPa), followed by subsequent unloading to half of the maximum stress level. The subsequent yield surface determined after pre-stressing showed the distortion typically found for radial pre-loading which consists mainly of contraction of the yield surface in the pre-loading direction with a particular flattening on the side nearest origin [176].

3.7.1.2 Elevated temperature 650 °C

The experiments found that the initial yield surface at 650 °C was a von Mises circle in the modified stress space ($\sigma_{12} = \sigma_{11}/\sqrt{3}$) of a radius of 54 MPa, with its centre located at (-4 MPa, -2 MPa).

Pre-loading was applied as pure torsion in the elevated temperature case. Maximum tensorial shear strain of 2500 $\mu\varepsilon$ was applied, followed by unloading. Three subsequent yield surface determination tests were made for the specimen 316SS22 and 316SS16 respectively, showing translation and elongation in the direction of the pre-loading (positive torsion).

3.7.2 Validation model in Abaqus

3.7.2.1 Model descriptions

The model geometry of Abaqus benchmark example 3.2.1 [177], a uniformly loaded elastic-plastic plate, was utilised in this validation study. Since the main objective was to validate the proposed material model algorithm implemented in the Abaqus Umat subroutine, instead of constructing the entire tubular specimen, the simple plate model was used. It allows for a clearer assessment of the accuracy of the integration of the plasticity equations, provided the same loading effect from the experiments can be reproduced in the finite element model.

The key aspect of the chosen loading process in the experiments, i.e., axial loading in combination with torsion, was to ensure the applied axial stress and shear stress were decoupled. The same loading effect was realised in the Abaqus plate model by applying carefully designed boundary conditions as illustrated in Figure 3.17. The boundary conditions were constructed to ensure pure shear force and pure axial force applied in a decoupled manner to the plate of examination, outlined in red. Kinematic coupling was adopted for the nodal constraints.

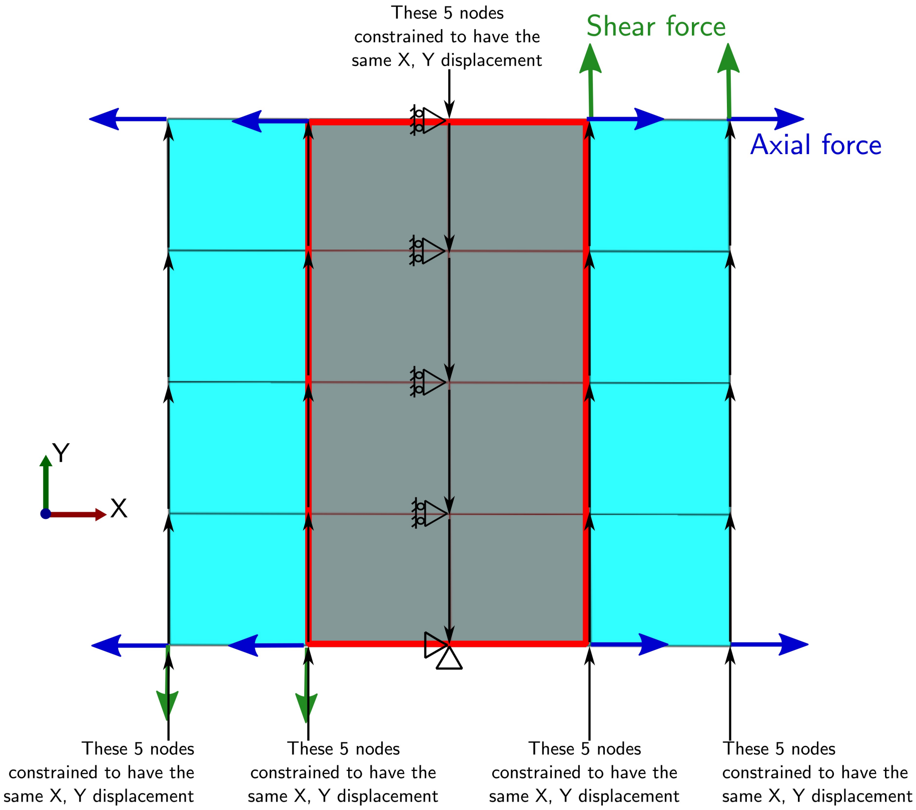

Figure 3.17: Abaqus plate model

3.7.2.2 Material properties

Initial yield stress of the 316SS material at room temperature (147 MPa) and at 650 °C (94 MPa) were calibrated from the experimental results. The elastic modulus is approximately 194 GPa at room temperature, and 106 GPa at 650 °C. The hardening parameters of the material were determined using the experimental stress-strain results and are summarised in Table D.6. The Bauschinger ratio was calculated using the maximum positive and negative stress point in the pre-loading direction of the yield surface results. The parameters of the Bauschinger ratio evolution function are presented in Table D.6.

3.7.3 Validation results

3.7.3.1 Initial yield surfaces

Figure 3.18a compares the initial yield surfaces of 316SS at room temperature determined by the experimental results with that predicted by the proposed material model. The predicted yield surface is an ideal circle in the modified stress space as von Mises yield function is adopted. The experimental data suggests the initial yield surface of 316SS is close to a circle with a degree of anisotropy in compressive yield strength.

At elevated temperature 650 °C, the yield surface determined by the experiments is closer to a von Mises circle than it was at room temperature. The comparison between experimental results and predictions is shown in Figure 3.18b.

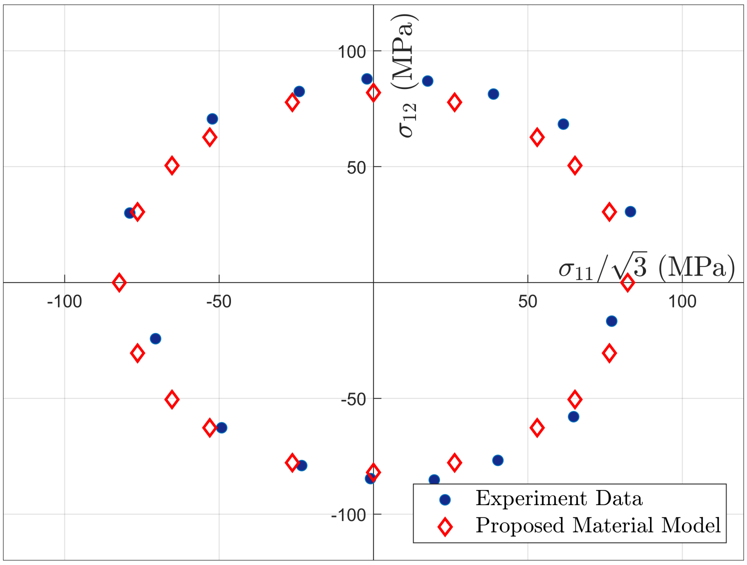

(a) Room temperature

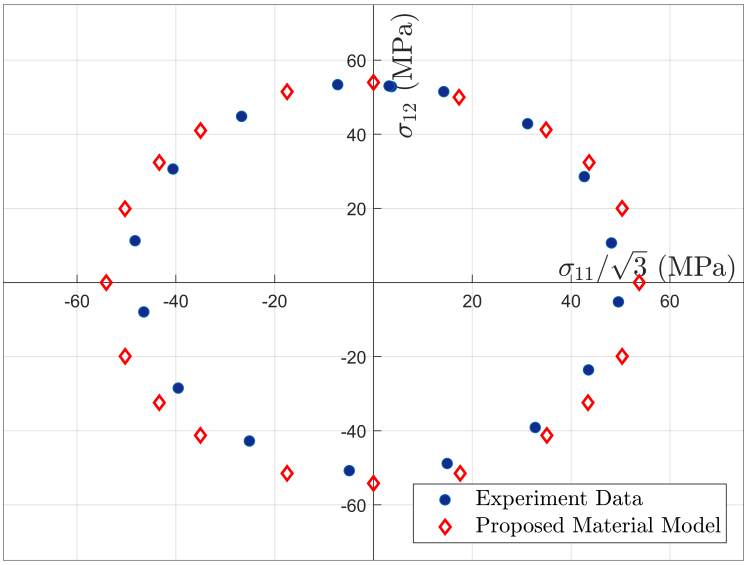

(b) 650 °C

Figure 3.18: Initial yield surfaces comparison

3.7.3.2 Subsequent yield surface after radial pre-loading at room temperature

Figure 3.19a compares the subsequent yield surface of 316SS after radial pre-stressing, determined by the experiments and the proposed material model. The prediction of the proposed material model is an ideal von Mises circle being translated and expanded in the direction of the pre-loading. The distortion of the subsequent yield surface due to radial pre-loading was not included. Nevertheless, the translation and expansion of the subsequent yield surface in the direction of the pre-loading has been clearly captured by the proposed material model.

3.7.3.3 Subsequent yield surface after pure torsion pre-loading at 650 °C

At the elevated temperature, pre-loading was applied as pure torsion resulting in no noticeable distortion of the subsequent yield surface, as shown in Figure 3.19b. Consequently, the experimental results suggest the subsequent yield surface is an nearly ideal von Mises circle with slight anisotropy in compressive yield strength. As a result, a highly satisfactory agreement has been observed between the experimental results and the predictions. The translation and elongation of the subsequent yield surface in the direction of pre-loading has been successfully captured by the proposed material model.

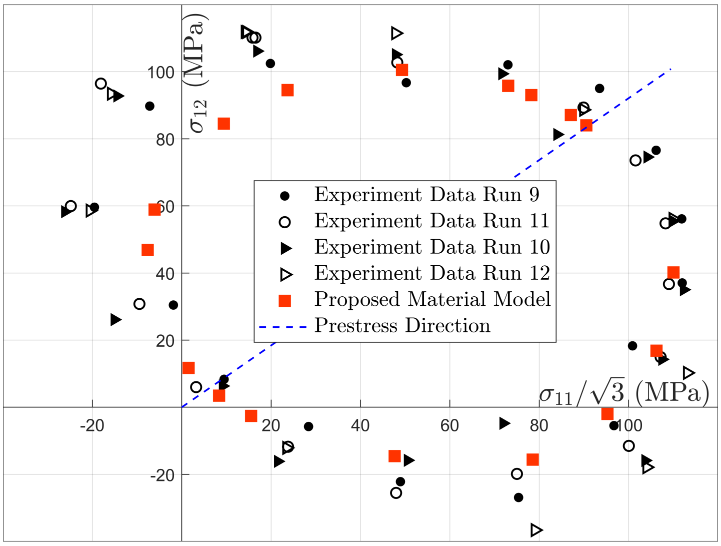

(a) Room temperature

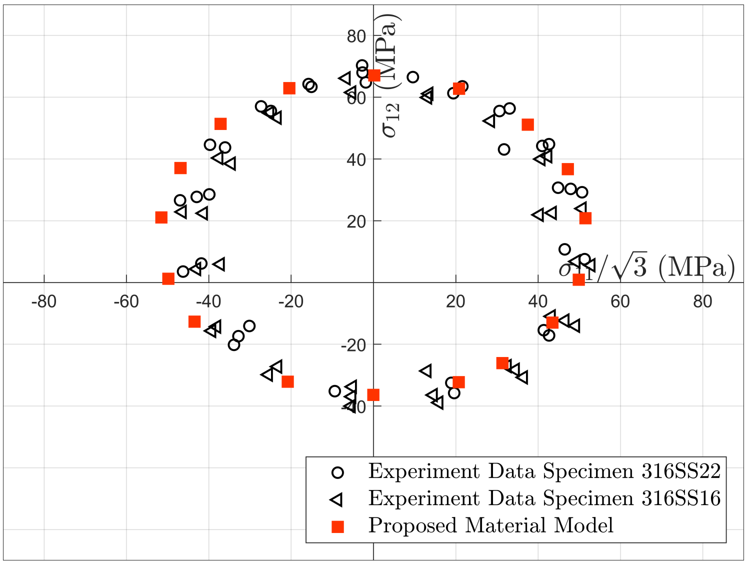

(b) 650 °C

Figure 3.19: Subsequent yield surfaces comparison

3.8 Validation for transient loadings during heating and cooling

The capability of the proposed material model in capturing the evolution of the Bauschinger effect and transient hardening in steel materials has been validated at elevated temperatures for isothermal loading conditions in previous sections. In real fire, the structures experience simultaneous loading and temperature changes, similar to a transient (anisothermal) loading condition.

In this section, the proposed material model is validated against the experimental data obtained by Ohno et al. [5], who conducted a series of thermo-mechanical cyclic experiments on the 304 stainless steel, under both isothermal and anisothermal loading conditions.

3.8.1 Experimental model

In this section, a brief description of the experiments conducted by Ohno et al. [5] is provided. The testing was conducted using a solid 160 *mm* long bar specimens with a gauge of 20 *mm* long and of 10 *mm* diameter, as illustrated schematically in Figure 3.20.

The isothermal thermo-mechanical experiments were carried out at temperature levels of 150 °C, 350 °C, 600 °C, 850 °C and 1000 °C. With a strain rate of $10^{-4}s^{-1}$ the specimen was first strained to a maximum tensile strain of 0.005, followed by compressively strained to a strain of -0.005 while the temperature was kept constant. The transient thermo-mechanical experiments were performed for four temperature ranges of [Tmin,Tmax]. The Tmin is 150 °C for all the four ranges whereas the Tmax varies from 350 °C, 600 °C, 850 °C to 1000 °C. Whilst being heated from Tmin to Tmax, the specimen was loaded in compression at a strain rate of $4.17^{-5}s^{-1}$ to a maximum compressive strain of -0.01. In the subsequent cooling from Tmax to Tmin, the specimen was subjected to tension at a strain rate of $8.33^{-5}s^{-1}$ until it reached the final strain of 0.0. For the validation of the proposed material model, the experimental stress-strain results of the very first loading loop of the cyclic tests were used in this study.

3.8.2 Validation model

The cross-section of the gauge was modelled using 4-node plane stress elements in Abaqus/CAE. The model was restrained in axial direction at one end, and is presented in Figure 3.20. The proposed material model implemented in the Abaqus Umat subroutine was used for testing the 304 stainless steel. The hardening function parameters were obtained by least square fitting the experimental tensile stress-strain curves from isothermal experiments using the modified Ludwik law of Equation 3.6. Table D.8 summarises the hardening function parameters obtained.

The Bauschinger ratio was determined based on the first loop of the stress-strain results of the cyclic isothermal experiments reported in [5], using Equation 3.35. The obtained Bauschinger ratios are presented in Table D.9. The Bauschinger ratios suggest that a substantial Bauschinger effect occurred in the tested 304 stainless steel at elevated temperatures, similar to what was observed in [128]. The exponential function of Equation 3.13 was adopted in least square fitting to describe the Bauschinger ratio evolution. The obtained function parameters are presented in Table D.8.

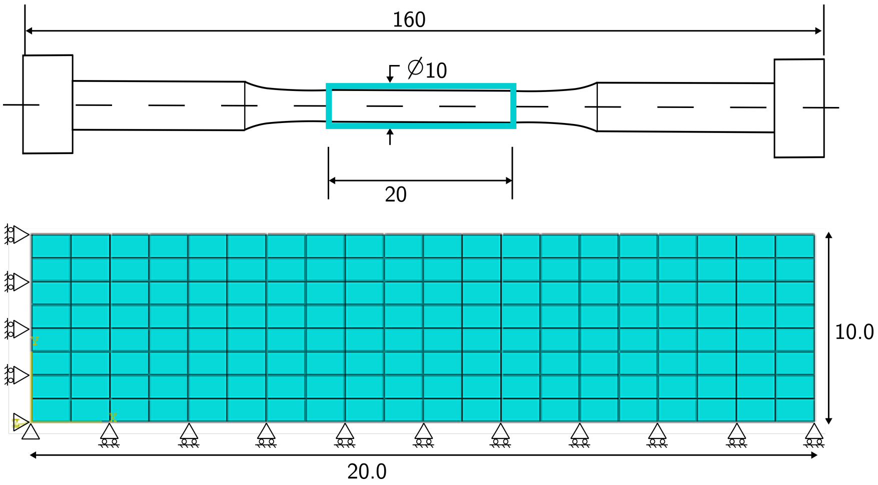

Figure 3.20: Thermo-mechanical test specimen (all dimensions in mm) [5]

3.8.3 Validation of isothermal thermo-mechanical experiments

Figure 3.21 compares the stress-strain development during the loading-reverse loading predicted by the new material model and the experimental data of the isothermal thermo-mechanical experiments at five varying temperatures. An overall good agreements have been observed, which suggests that the new material model is capable of capturing the Bauschinger effect and transient hardening behaviour very well under isothermal loading conditions. The model parameters of the new material model, namely the parameter V_b of the reverse loading ratio υ evolution function from Equation (3.23), and the parameter V_h of the second kinematic hardening term from Equation (3.25) were set to obtain the best possible overall curve fitting. The parameters used are summarised in Table 3.1.

Table 3.1: Model parameters, Isothermal experiments

Temperature	V_b	V_h
150 °C	1100	1.80
350 °C	1300	1.88
600 °C	1600	1.86
850 °C	2250	2.00
1000 °C	2000	1.70

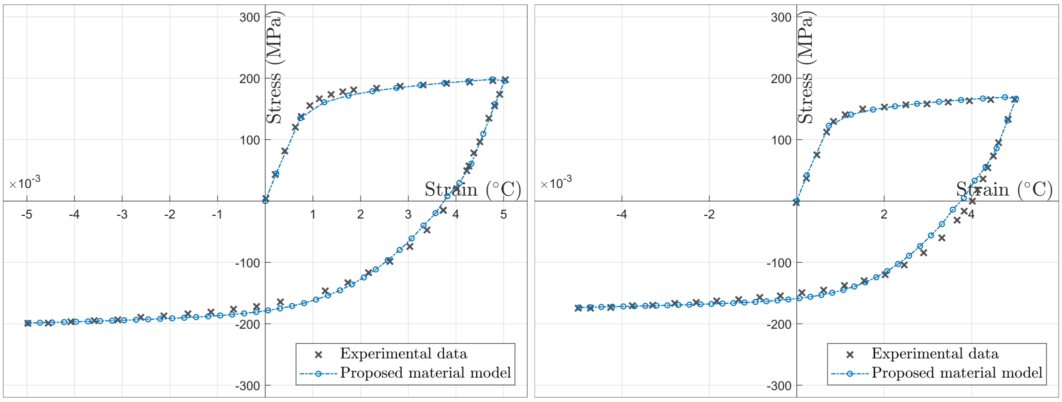

(a) T =150 °C **(b)** T =350 °C

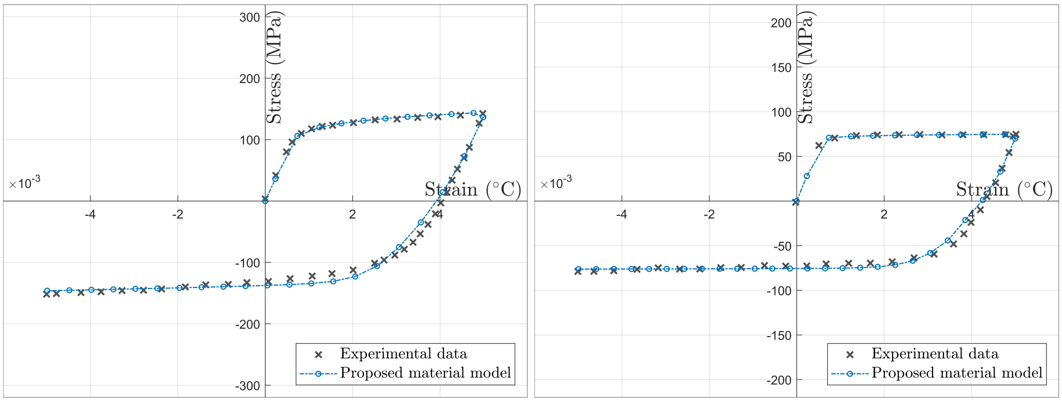

(c) T =600 °C **(d)** T =850 °C

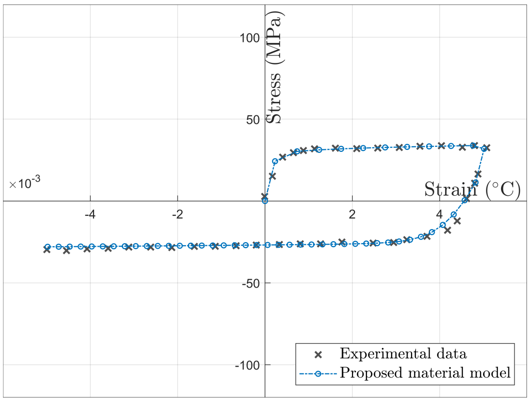

(e) T =1000 °C

Figure 3.21: Stress strain curves comparison, Isothermal thermo-mechanical experiments

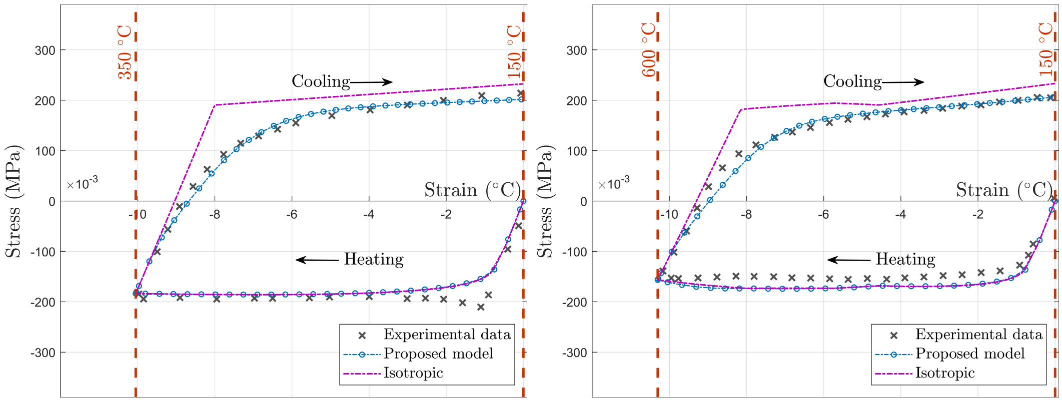

(a) Tmax =350 °C **(b)** Tmax =600 °C

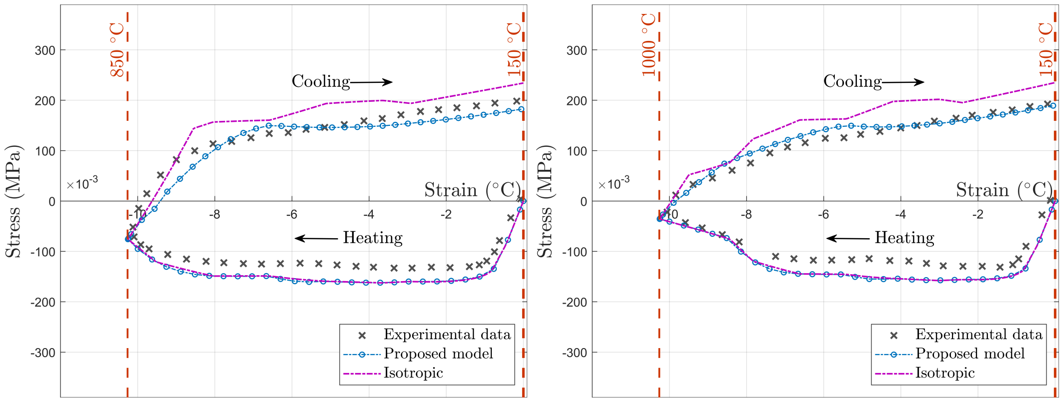

(c) Tmax =850 °C **(d)** Tmax =1000 °C

Figure 3.22: Stress strain curves comparison, Transient thermo-mechanical experiments

3.8.4 Validation of transient (anisothermal) thermo-mechanical experiments

Figure 3.22 compares the stress-strain development during the loading-reverse loading predicted by the proposed material model and the experimental data of the four transient thermo-mechanical experiments. During initial compressive loading, small deviation between the predicted stresses and the experimental data were observed, particularity at higher temperatures. This is believed to be caused by the different constitutive behaviour in tensile and compressive loading of stainless steel material [178] as the hardening functions have been obtained based on the isothermal tensile stress-strain curves. The transient (anisothermal) state of loading could also be a source for the deviation. Nevertheless, it can be seen that the varying hardening modulus of the stress-strain curve during the heating has been captured well by the proposed material model.

Table 3.2: Model parameters, Transient experiments

Temperature	V_b	V_h
850 °C	2250	3.40
1000 °C	800	10.50

For the reverse loading curve during cooling, the predictions of the proposed material model using the model parameters from Table 3.1 are in good agreement with the experimental data at 350 °C and 600 °C. For 850 °C and 1000 °C, higher values of V_h have to be adopted to achieve a satisfactory fit of the reverse stress-strain relationship. It's also noted that the material model parameter V_b ceased to be temperature-dependent during cooling from 1000 °C, a value of 800 was adopted for the entire cooling process. The model parameters used for at 850 °C and 1000 °C are presented in Table 3.2.

The mechanical behaviour of steel materials are a phenomenological manifestation of their microstructure. The effect of very high temperatures on the microstructure determines the material's mechanical behaviour when being cooled from the high temperature. Various experimental research [179–186] have discovered that steel materials only display different mechanical behaviour after being cooled from a critical maximum temperature (Tcr) or above, i.e., little change in mechanical behaviour can be found if the materials are cooled down from a temperature that's lower than Tcr. Qiang et al. [179, 180] identified a Tcr of 600 °C for high strength structural steels S460, S690 and S960. Wang et al. [181] found that the high strength structural steel Q460 could recover its original tensile stress-strain behaviour after experiencing temperatures up to 700 °C. Azhari et al. [182] proposed a Tcr of 600 °C for the ultra-high strength steel (Grade 1200) based on their experimental findings. For austenitic stainless steel (1.4307), Wang et al. [183] and Tao et al. [184] found different behaviour in stress-strain curves when the maximum temperature exceeded 500 °C. Huang and Young [185, 186] observed that the ferritic stainless steel and lean duplex stainless steel can generally regain its mechanical properties after being cooled from a temperature up to 600 °C.

Sufficiently high temperature exposure that causes phase changes in the microstructure inevitably gives rise to different mechanical behaviour. It has been discovered that the transition of ferrite to austenite phase at high temperatures causes the change in the material's mechanical behaviour, which occurs above 650 °C in ultra-high strength steel [187] and around 800 °C in lean duplex stainless steel [186]. The transition of ferrite to martensite above 800 °C causes change in the mechanical behaviour in the ferritic stainless steel after being cooled from 800 °C [185]. Additionally, when exposed to a temperature higher than its Tcr, the material's post-fire mechanical behaviour becomes strongly influenced by the cooling rate [182, 185, 186].

The existing literature provide a sound explanation why different model parameters had to be deployed for the validation of the stress-strain relationship during cooling phase in the case of Tmax =850 °C and 1000 °C. Figure 3.22c and 3.22d demonstrate the new material model offered good predictions of the reverse stress-strain behaviour for transient thermo-mechanical experiments.

3.8.4.1 Comparison with isotropic hardening model

In Figure 3.22, the results of the new material model are also compared with the isotropic hardening model of Abaqus. The new combined isotropic-kinematic hardening material model works the same as the isotropic hardening model during the initial loading during heating. For the reverse loading during cooling, the isotropic hardening model overestimates the stress response and cannot capture the transient hardening behaviour and the variation in the hardening modulus satisfactorily.

The material model presented has been shown to have the capability of describing accurately the experimentally observed phenomena, which traditional models are not capable to capture, e.g., the Bauschinger effect and the transient hardening and their consequences on the mechanical response to subsequent loadings during heating and cooling. Comparisons and experimental results in general showed good agreement with respect to initial and subsequent yield stress as well as stress-strain response, and the qualitative improvement compared to the simulations obtained using isotropic hardening model is quite evident.

3.9 Uniaxial material model

The proposed multi-axial material model has also been adapted to a one-dimensional J_2 plasticity model, and implemented as uniaxial material models in OpenSEES [24]. The uniaxial material "SteelEC02Thermal" has been implemented for the carbon steel, "Stainless01Thermal" for the duplex stainless steel and "Stainless02Thermal" for the austenitic stainless steel.

3.10 Summary and conclusions

In this chapter, a new rate-independent combined isotropic-kinematic hardening model has been developed for assessing steel materials for thermo-mechanical analysis with fire.

Harley et al. [128] observed substantial development of $\bar{\beta}_{11}$ and swift drop of κ within the first 1.0% of straining at elevated temperatures in 304L stainless steel. Different steel materials will exhibit different degrees of Bauschinger effects [188]. Due to limited available testing data on the evolution of isotropic and kinematic hardening variables at elevated temperatures, it was not possible to carry out more validations than those presented. However, it should be noted that the validation was conducted to demonstrate the capability of the proposed material model to capture the temperature-dependent Bauschinger effects, not to justify for any particular materials. Thus different sets of temperature-dependent function parameters should be adopted for different materials accordingly.

By adopting two non-linear kinematic hardening variables, the proposed material model is capable of modelling the Bauschinger effect and transient hardening behaviour at elevated temperatures efficiently.

Due to the lack of experimental data on the re-positioning of yield surface centre at elevated temperatures, the corresponding algorithms was validated by comparing the thermal unloading stress result of the proposed material model to its analytical solution.

The multi-axial validation results demonstrated that the proposed material model has been successfully implemented for three dimensional analysis. It is capable of capturing the expansion and translation of the yield surfaces, presenting the yield surface as a von Mises circle.

The capability of the new material model has also been validated for transient loading conditions during both heating and cooling. This demonstrated that the proposed model is suitable for post-fire structural assessment..

In conclusion, the capability of the new material model proposed in this chapter for capturing the Bauschinger effect and transient hardening behaviour at elevated temperatures has been demonstrated. The algorithm for the proposed material model in multi-axial state is presented in Appendix A, and has been successfully implemented in the Abaqus Umat subroutine. The multi-axial material model has also been adapted to a 1D plasticity model and implemented as a uniaxial material model in the open source software OpenSEES [24].

Chapter 4

Remaining Fire Resistance of PFP Coated Steel Frames Subjected to A Moderate Earthquake

Adapted from M. Zhou, L. Jiang, S. Chen, A. Usmani and R. Cardoso, “Remaining fire resistance of steel frames following a moderate earthquake —A case study”, *Journal of Constructional Steel Research*, accepted, 2019

4.1 Introduction

The fire resistance of steel structural components in composite steel frame buildings is commonly provided by passive fire protection (PFP) coatings. Current standards [9, 27] measure the fire resistance of structural components using the concept of time. For instance, a 2 hr fire-resistance rating means the PFP protected structural components can withstand a standard fire of 2 hours. There are two popular categories of PFP: cementitious coating and intumescent coating. In USA and Asia, cementitious PFP has been and still is a popular choice for its advantages of being cost effective, ease of application and lightweight when compared with other type of fire insulations [75]. Being specifically designed to be lightweight, Cementitious PFP is naturally fragile and brittle hence prone to damage under deformation or vibration. Damage in the coating caused by loading events such as windstorms, fires or earthquakes can result in potential reductions in the structural fire resistance.

This hazard should be of particular concern for small/moderate earthquakes because modern earthquake design philosophy widely accepts that structures should be designed to resist moderate earthquakes without any structural damage [189]. For instance, ASCE/SEI 7-10 [190] specifies for structures categorized as Seismic Design Category (SDC) C —approximately correlated to a Modified Mercalli Intensity (MMI) VII ground shaking according to FEMA P-750 [191], the damage should be limited to non-structural components. In contrast, there is no equivalent requirement currently in place to ensure the integrity of fire resistant coatings on structural members. This fire safety concern is further compounded by the reality that cementitious PFP is usually concealed by architectural claddings and finishes —hindering any regular monitoring and post-earthquake inspections. As a result, the fire resistance of structures, e.g., structural fire-resistance rating, could suffer significant reductions after a period of use due to unaccounted for PFP damage. Especially if this period consists of multiple small/moderate earthquakes.

An integrated FEA-based multi-hazard framework using the new material model developed by Zhou et al. [192], also presented in Chapter 3, is proposed in this chapter for assessing the remaining fire resistance of cementitious PFP protected steel frame structures subjected to moderate earthquakes. In this chapter, the term 'remaining fire resistance' is employed to refer to the fire resistance capacity of PFP coated structures after being subjected to earthquakes. It provides structural engineers with a practical solution to address the fire safety concern associated with the undetected PFP damage. For significant structures, the proposed framework can be integrated into its structural integrity assessment to provide on-line fire safety monitoring.

This framework adopts a strain-based damage indicator to identify any potential PFP damage. Recent work as reviewed in Section 2.2.4 has offered fundamental insights into the damage mechanisms of cementitious coatings under various loading conditions and provided data for quantifying the damage scale sustained by such coatings under seismic loadings. The development of damage indicator is presented in Section 4.2.

In Section 4.3, the proposed framework is demonstrated by a case study of remaining fire resistance of multi-story steel frames subjected a moderate earthquake loading. This case study uses two equivalent seismic steel frame designs: a steel moment resisting frame (MRF); and the other a steel concentrically braced frame (CBF), based on FEMA P-751, NEHRP Recommended Provisions: Design Examples [193]. Because it is of the greatest interest to analyse a loading scenario where cementitious PFP suffers significant damage while the structure itself experiences only superficial damage, an earthquake loading of mild to moderate intensity was selected for the seismic analysis. A sensitivity study was carried out in Section 4.3.8 to investigate the impact of various design and modelling assumptions on the PFP damage pattern in the MRF. The study results provide a benchmark guideline for selecting an appropriate finite element model for PFP damage assessment.

In Section 4.4, a thermo-mechanical analysis was carried out to quantify the remaining fire resistance of the frames subjected a moderate earthquake loading. A 2-D heat transfer analysis was used to determine the temperature evolution over time in the fully protected and the damaged steel members subjected to the Standard Fire Curve (ISO 834) [26].

All three analyses, namely the time history seismic analysis, the cross-sectional heat transfer analysis and the thermo-mechanical analysis have been performed using the native and developed capabilities in the open source software framework OpenSEES [24].

4.2 Cementitious PFP damage indicator

A number of researchers have investigated damage mechanisms in cementitious PFP. Keller and Pessiki [83, 84] investigated the damage of cementitious PFP at bolted connections of gravity beam-column frame subjected to cyclic loading. Braxtan and Pessiki [77,82] studied the damage pattern of PFP applied on steel moment frame beam-column assemblies under a strong seismic event, and revealed a link between damage and plastic hinge formation. Chen et al. [76,85] undertook an extensive testing programme to study damage mechanisms in cementitious coatings applied to steel plates subjected to monotonic axial loading and bending.

Further experiments [86, 87] have been carried out to study damage patterns in the cementitious coating applied structural columns subjected to both monotonic and cyclic loading. Wang [87] noted that when the tested column was subjected to cyclic loading, the cracking initiated at a lower load level, and the complete delamination/peel-off failure occurred at a lower level of strain than that under monotonic loading. This is believed to be caused by the cyclic loading/unloading process and the frequent stress reversals experienced in the coating. It is also observed that, under cyclic loading, cracks first appeared at the tensile side of the member, and the transverse crack formed under tension resulted in the final complete peel-off failure.

The interpretation of this phenomenon can be straightforward: under cyclic loading cracks will be introduced on both flange surfaces by tensile force because cracks are able to form at a substantially lower tensile strain [85]. Once the cracks opened, they will continue to absorb energy and keep growing until delamination/peel-off failure occur as a result of the cyclic stress reversals. The progression of tensile cracks prevents additional cracks from being generated. Consequently it is essentially the tensile cracks that initiate and lead to the final peel-off/detachment failure. This explanation can be further validated by Wang's observation that the number of cracks remained constant throughout the cyclic loading test. Wang [87] reported that, the strain level at which complete peel-off failure observed in cementitious coatings was 0.00198 on the tension side under monotonic loading and 0.00135 under cyclic loading. Correlating Wang's data to drift ratios, Chen et al. [86] reported the delamination occurred on the cyclic loaded column at a drift ratio of 0.0155 whereas similar delamination observed on the monotonic loaded column at a higher drift ratio of 0.0449.

As demonstrated by the experimental data, the damage strain under monotonic loading ($\varepsilon_{monotonic}$) is higher than that under cyclic loading (ε_{cyclic}). Subjected to realistic loading conditions, a critical damage strain ($\varepsilon_{critical}$) in cementitious coating can be considered of a value in-between the $\varepsilon_{monotonic}$ and the ε_{cyclic}. For damage assessment, simply adopting $\varepsilon_{monotonic}$ can underestimate the damage scale whereas ε_{cyclic} can be conservative. The $\varepsilon_{monotonic}$ can be considered as the upper bound of the critical damage strain while the ε_{cyclic} as the lower bound.

A power law based formula is considered suitable and proposed for estimating the critical damage strain in cementitious coatings. The formula assumes that the critical damage strain moves rapidly from the higher value under monotonic loading to the lower value under cyclic loading with increasing number of stress reversals:

$$\varepsilon_{critical} = \varepsilon_{cyclic} + (\varepsilon_{monotonic} - \varepsilon_{cyclic})exp^{-kn} \tag{4.1}$$

where

$\varepsilon_{critical}$: the critical strain above which the coating is assumed completely lost

$\varepsilon_{monotonic}$: Strain above which the coating delaminated under monotonic tensile loading, obtained from testing results

ε_{cyclic} : Strain above which the coating delaminated under cyclic loading, obtained from testing results

n : Number of stress reversals experienced in the coating

k : Material parameter

The proposed damage formula is a deterministic approach and there exists a need for much greater volume of experimentation for refinement so a statistical and probabilistic approach could be used to account for the uncertainties associated with the damage phenomena in quasi-brittle cementitious materials, and for the determination of the material variable k. The biggest uncertainty probably comes from the cementitious material per se due to the manufacturers/suppliers owned material recipes and application techniques.

For this study, we adopted the experimental values in [87] ($\varepsilon_{monotonic} = 0.0198$ and $\varepsilon_{cyclic} = 0.0135$) as the upper and lower bound damage indicator. The upper and lower bound damage indices provide a guideline for the potential PFP damage assessment, and should not be deemed as definitive failure limits. For any specific cementitious PFP damage assessment, variations in the bound limits are inevitable as a result of the inherent uncertainties in the materials.

Figure 4.1 shows the relationship between the $\varepsilon_{critical}$ and the number of stress reversals experienced in the cementitious coating, based on Equation 4.1. A value of 0.1 was assumed for the material variable k. The critical strain approaches ε_{cyclic} very rapidly and becomes nearly insensitive to the number of stress reveals when $n > 90$. Earthquake loading usually consists of a large number of cycles. For instance, Figure 4.2 presents the acceleration history of the 1994 Northridge earthquake based on Canoga Park record. In cases of earthquake loading, it can be considered reasonable to estimate the damage scale in the cementitious PFP system using ε_{cyclic}.

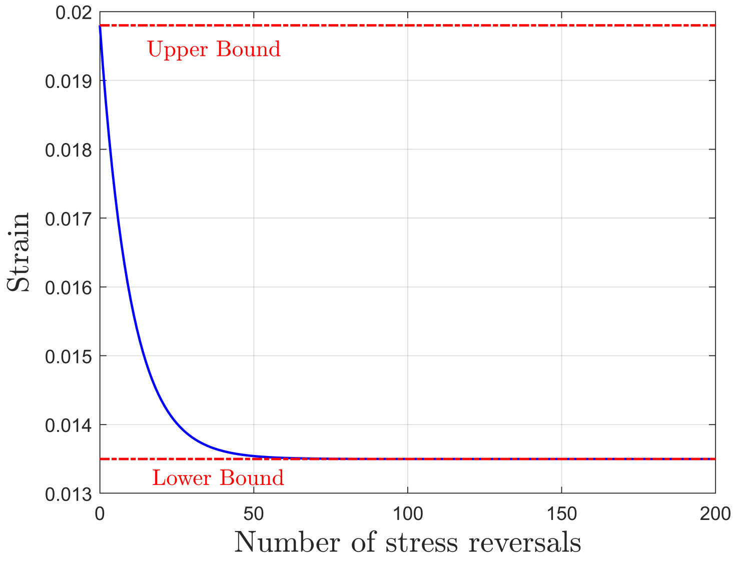

Figure 4.1: $\varepsilon_{critical}$ vs. Stress reversal Number

4.3 Impact of seismic steel frame designs on PFP damage

Design examples and seismic design guidelines from American standards have been adopted in this case study in order to fully take advantage of the analysis techniques and tools offered by the OpenSEES. Since the software is developed as the computational tool for research at the California based Pacific Earthquake Engineering

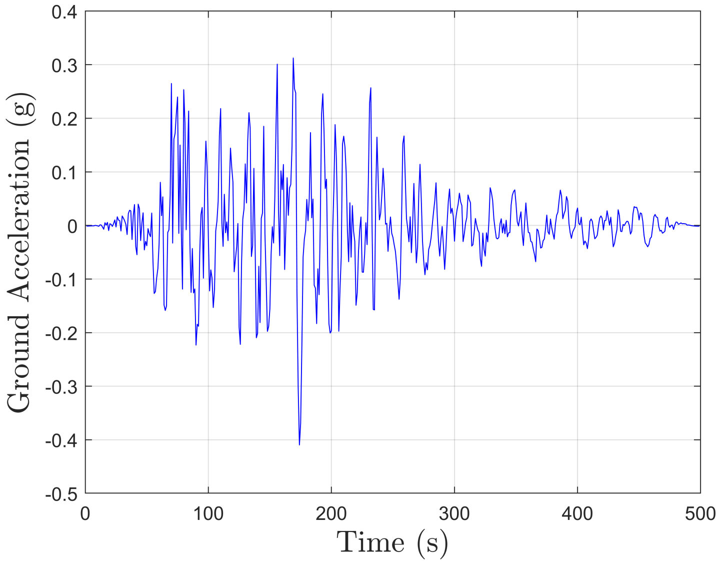

Figure 4.2: Acceleration history of 1994 Northridge earthquake

Research (PEER) Centre, the analysis techniques are mostly developed for structural designs using American standards, especially for seismic steel frame structural designs.

The structural models are based on FEMA P-751 [193], which are two equivalent alternatives —a steel moment resisting frame (MRF) and the other a steel concentrically braced frame (CBF), designed for a seven-story office building in Los Angeles California. The building is of a rectangular plan, which is 177 feet and 4 inches (54.0 m) along in the E-W direction and 127 feet and 4 inches (38.8 m) wide in the N-S direction. It is framed in structural steel with 25 feet (7.6m) bays in each direction. The typical story height is 13 feet and 4 inches (4.1 m) with the exception of the first story which is 22 feet and 4 inches (6.8 m) high. The building has a penthouse, which extends 16 feet (4.9 m) above the roof level and covers the central bay areas.

4.3.1 FE Model geometry

The typical N-S direction frame of the two alternative designs were modelled, the overall geometries are shown in Figure 4.3 and Figure 4.4 respectively, with the member sizes displayed. The braced frames are in a two-story X configuration.

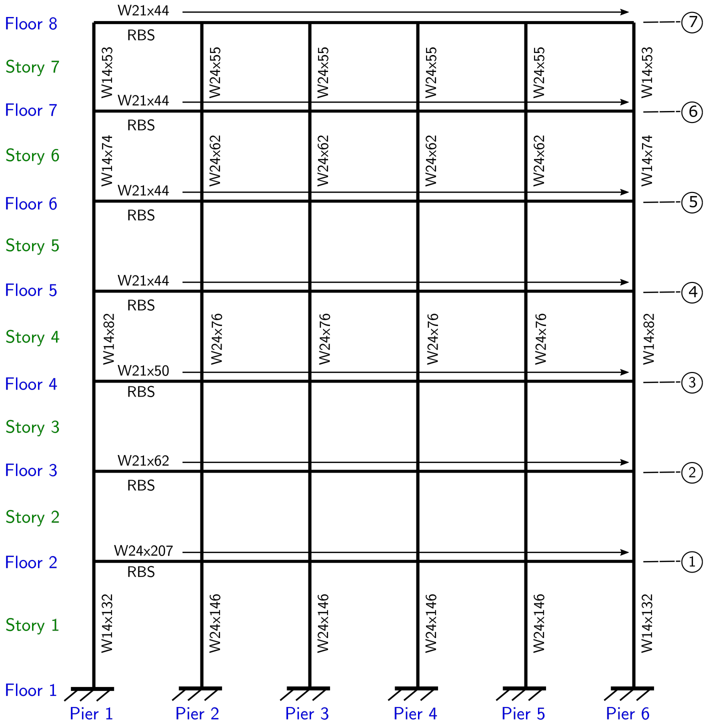

Figure 4.3: Moment resisting frame in N-S direction (penthouse not shown)

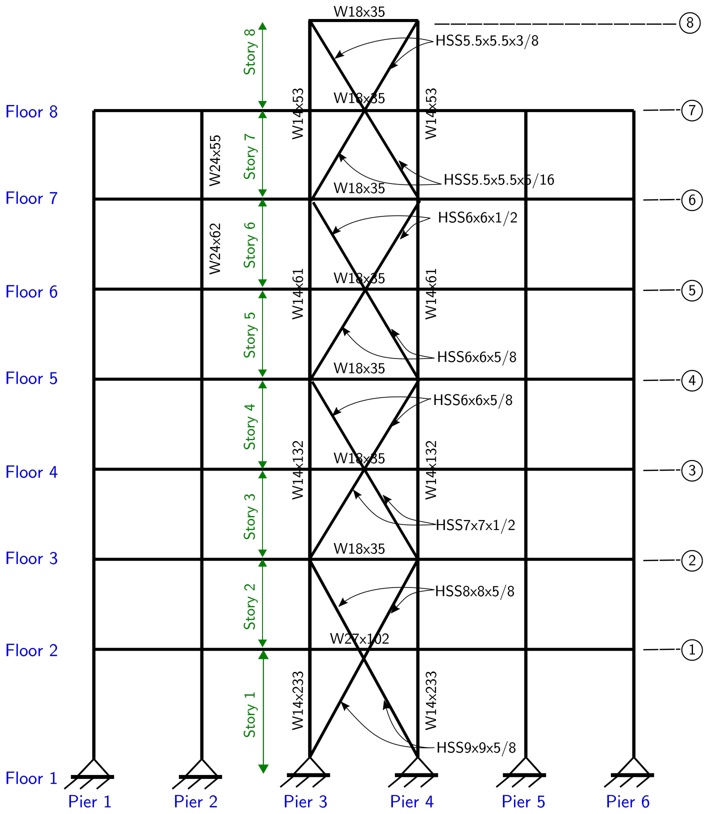

Figure 4.4: Concentrically braced frame in N-S direction (Typical)

4.3.2 FE model Loadings

4.3.2.1 Gravity loads

The gravity loads including structural self-weight, fireproofing, wall cladding and equipment weights were applied as body force to the model in the first step of the analysis. Table 4.1 presents the gravity loads for each floor level.

Table 4.1: Gravity loads

Floor Level	Loads (kips)
Penthouse roof	94
Lower roof	1537
Typical floor	1920

4.3.2.2 Earthquake load

The Canoga Park record from the 1994 Northridge earthquake occurred in Los Angeles, California, from the OpenSEES library, as shown in Figure 4.2 was adopted. The most serious fire safety risk results from a loading scenario where cementitious PFP suffers significant damage while the structure itself experiences only superficial damage. As the unaccounted for PFP damage seriously reduces the structural fire resistance. Therefore, a ground motion reduction factor =0.65 was applied to the Peak Ground Acceleration (PGA) to achieve the desired moderate earthquake level. Under the reduced earthquake load, the global structural behaviour is constrained to remain in the elastic region.

4.3.3 FE model Materials

For all the wide flange sections, ASTM A992, Grade 50 steel (fy= 50 ksi or 345MPa) was used. The ASTM A500 Grade B steel (fy= 46 ksi or 315MPa) was adopted for the HSS sections.

4.3.4 FE models for seismic analysis

For the base model of the MRF and the CBF, the structural members were modelled from centreline to centreline, using 2D Euler-Bernoulli Force-based Beam-Column (FB) element which can account for geometric non-linearity. The strength, stiffness, dimensions and shear distortions of panel zones were neglected in the base models. The uniaxial material Steel02 [194] from OpenSEES library was adopted, which can properly account for steel's isotropic strain hardening when subjected to seismic loading.

The braces of the CBF were modelled using the method proposed by Uriz and Mahin [195] to ensure brace global buckling behaviour is captured, in which each brace was modelled with 10 FB elements using corotational geometric transformation. Additionally, initial out-of-plane imperfection of 0.5% effective length was applied at the middle of the braces that would help trigger lateral buckling in the dynamic analyses. Gusset plate connection was modelled using pinned connection which has been considered appropriate for analysing moderate earthquake response.

Fully fixed boundary conditions were applied to the MRF at the bottom and pinned connections were applied to the CBF.

The implicit transient analysis using Newmark integrator was performed to determine the seismic responses of the steel frames.

4.3.5 Earthquake response

Time history analyses of the two frames were performed. The approximate fundamental natural periods calculated using ASCE/SEI 7-10 Section 12.8.2 [190] and the first mode natural periods from OpenSEES analysis are reported in Table 4.2. It is expected and verified by the recommendations [193] that the modelling natural periods will exceed the Standard's approximation as a result of member selections.

Table 4.2: Fundamental building periods

Frame Type	ASCE 7-10 (s)	OpenSEES Results (s)
Moment resisting frame	1.596	1.617
Concentrically braced frame	0.896	0.946

The inter-story drift ratios (IDR) are presented in Table 4.3 and 4.4 for the MRF and CBF respectively. The corresponding IDRs from FEMA P-751 [193] are included in the tables only as a benchmark reference since different seismic loadings were used. The FEMA P-751 values were determined using the seismic design ground motion specified by ASCE 7-10 [190] for office buildings in the region of seismic design category D, i.e., Los Angeles, whereas the OpenSEES results were obtained using the modified Northridge earthquake ground motion. For the MRF, the FEMA P-751 and OpenSEES IDRs results display similar trends: lower values at the bottom and at the top while higher values around the middle stories. For the CBF, higher IDRs occurred at the upper stories. Lower consistency is found in the OpenSEES CBF model results when compared with the FEMA P-751 values. This is believed to be caused by the modelling methodology adopted for capturing the global buckling behaviour of the braces. Overall, the IDRs in the CBF are lower than that in the MRF, which is as expected.

Table 4.3: Inter-story drift ratios, Moment frame model

Level	FEMA P-751 (%)	OpenSEES (%)	Allowable Drift Ratio (%)
Story7	1.2	0.77	2.0
Story6	1.7	1.25	2.0
Story5	2.0	1.56	2.0
Story4	2.0	1.41	2.0
Story3	1.8	1.02	2.0
Story2	1.2	0.54	2.0
Story1	1.1	0.60	2.0

Table 4.4: Inter-story Drift Ratios, Braced Frame Model

Level	FEMA P-751 (%)	OpenSEES (%)	Allowable Drift Ratio (%)
Story7	0.93	0.57	2.0
Story6	0.94	0.55	2.0
Story5	0.84	0.57	2.0
Story4	0.84	0.46	2.0
Story3	0.71	0.53	2.0
Story2	0.59	0.42	2.0
Story1	0.52	0.55	2.0

4.3.6 Damage to cementitious PFP

Table 4.5 shows the number of stress reversals experienced in the Pier 3 of the MRF model over its full height under the selected earthquake load. The large number of stress reversals observed suggest a reasonable assessment of the PFP damage can be achieved by using the lower bound damage indicator (ε_{cyclic}), as discussed in Section 4.2.

Table 4.5: Number of cycles in Pier 3, Moment frame model

Level	Stress Reversals No. (n)
Story7	100
Story6	83
Story5	93
Story4	42
Story3	29
Story2	55
Story1	62

4.3.7 Comparison study of strain results

The maximum tensile strain of the seismic analysis results in each structural member of the MRF and the CBF are presented in this section. The strain distributions within the columns and floor beams provide an immediate link to the potential PFP damage pattern.

4.3.7.1 Moment resisting frame

The maximum tensile strain values of the seismic analysis results in the Pier 1, Pier 2 and Pier 3 are plotted in Figure 4.5a, 4.5b and 4.5c respectively. The surface strain at the Left Hand Side (LHS) flange and at the Right Hand Side (RHS) flange of the Piers are plotted separately. The strain values in the Pier 4, 5 & 6 are similar to that in the Pier 3, 2 &1 correspondingly owing to the structural symmetry. As shown, high strain values occurred around floor joints. With the indicative lower and upper bound damage limit highlighted on Figure 4.5, any strain values that exceed the ε_{cyclic} are considered an indication for potential damage in the cementitious PFP. No damage in Piers is indicated by the strain results of the base model, as seen in Figure 4.5.

The maximum tensile strain values of all the floor beams are plotted in Figure 4.5d. High strains are observed near beam-column joints. Potential damage were observed at floors 5 and 6, which also ties back to the high IDRs observed at these two floors.

4.3.7.2 Concentrically braced frame

For the concentrically braced frame, the maximum tensile strain values in the Pier 1, 2 and 3 are presented in Figure 4.6a, 4.6b and 4.6c. As shown, the strain levels in the CBF columns are well below the ε_{cyclic}. Similarly, the maximum tensile strain values in the beams are also lower than the ε_{cyclic}, as plotted in Figure 4.6d. High strain values were observed in the braces during the seismic analysis however brace members do not have any bearing on the fire resistance of the frame. As a result, no potential damage in the PFP of the concentrically braced frame has been identified based on the seismic analysis results.

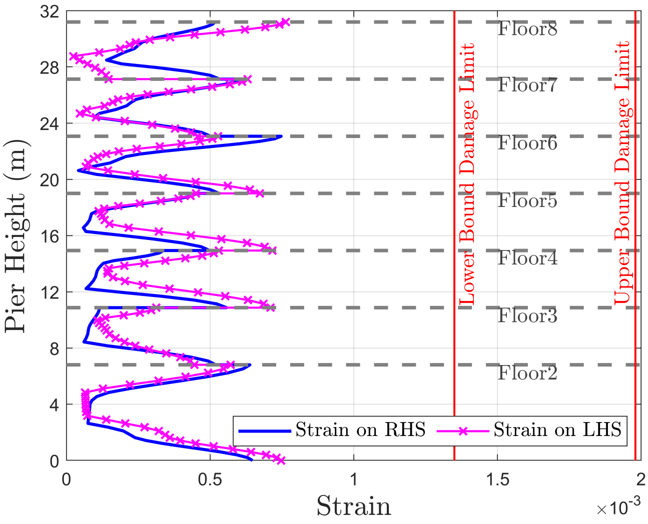

(a) Strain distribution in Pier 1

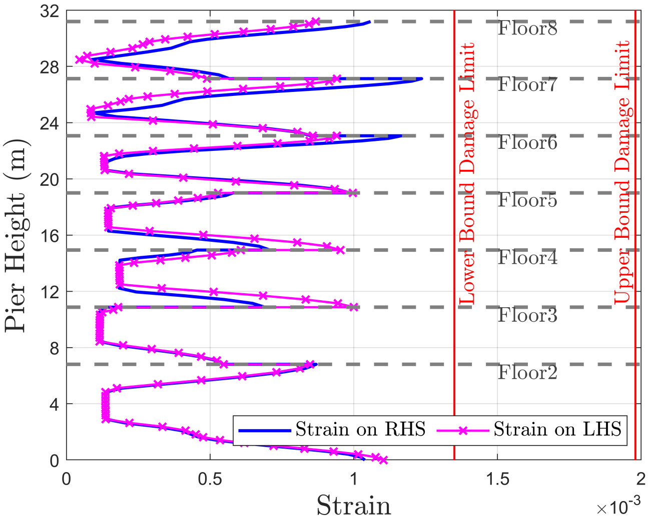

(b) Strain distribution in Pier 2

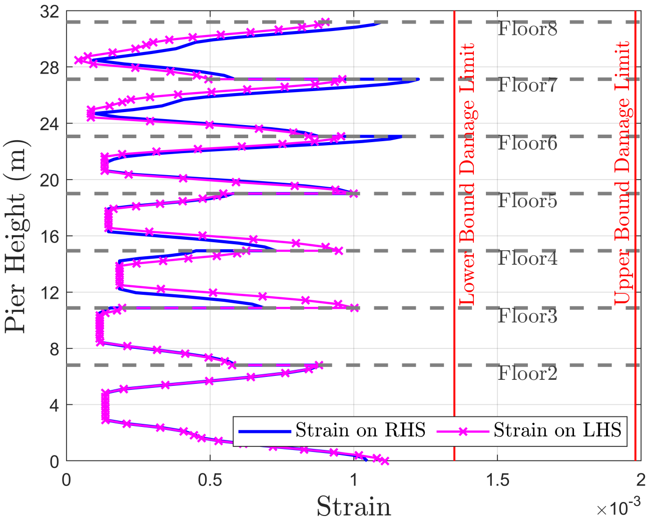

(c) Strain distribution in Pier 3

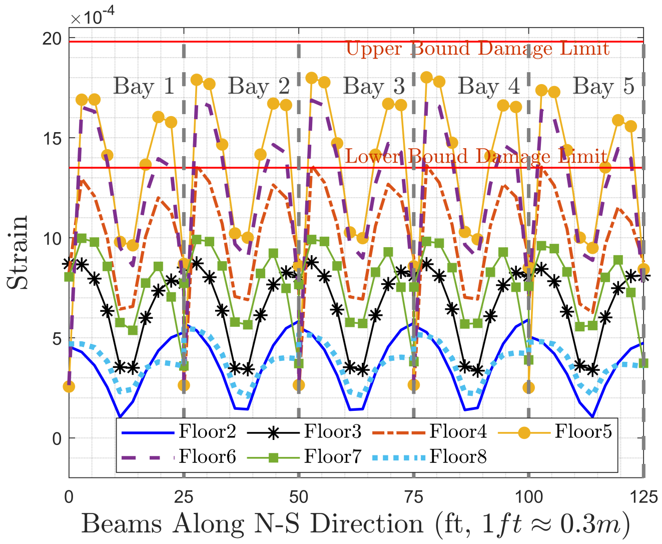

(d) Strain distribution in Floor beams

Figure 4.5: Max. tensile strain diagram, MRF

4.3.7.3 Discussion

For the two equivalent seismic frame designs, the comparison study suggests that the MRF suffers high likelihood of potential PFP damage when compared with the CBF. High strain values were observed especially in the floor beams around beam-column connections in the MRF. Because the elemental strain results have been adopted as the damage indicator, a sensitivity study of the influence of the modelling assumptions was considered necessary and hence carried out for the MRF. The results of the study are presented and discussed in the following section.

4.3.8 Sensitivity study of modelling assumptions of MRF

The base model used in Section 4.3.7, which is a centreline-to-centreline bare frame model, is the most common model for structural engineering analysis. It is believed to be adequate for providing a reasonable approximation of the global response of the structure under seismic loading, for instance the IDRs.

However, for seismic analysis the strain distribution at structural element level, i.e, in beams and columns, can be significantly affected by the relative stiffness of the beams/columns framing into a connection. In this MRF example [193], panel zones and reduced beam sections are adopted to ensure strong column and weak

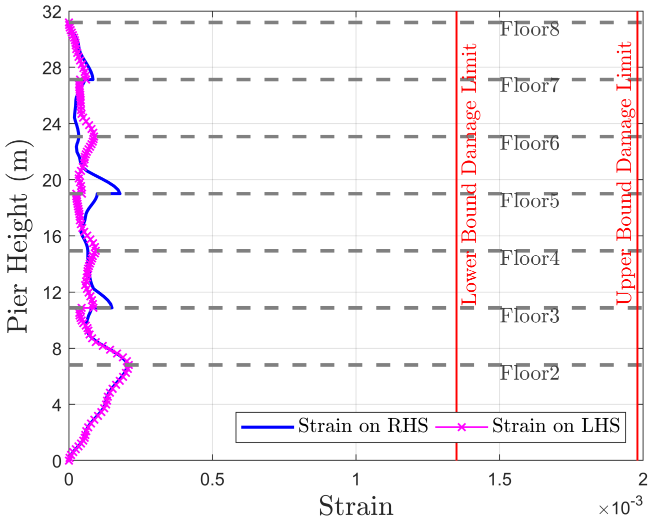

(a) Strain distribution in Pier 1

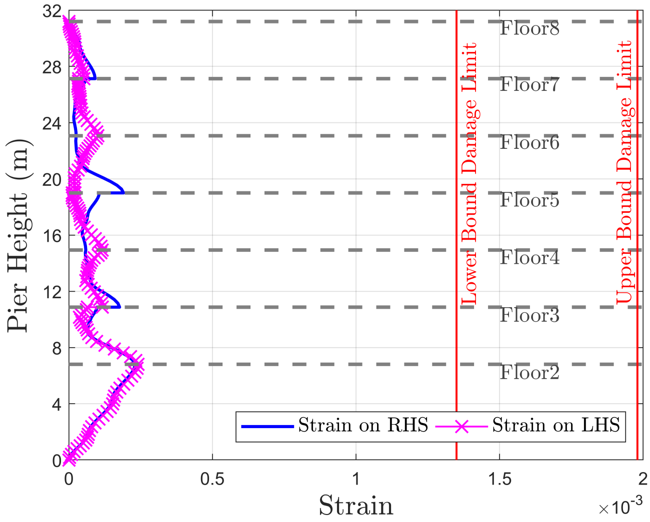

(b) Strain distribution in Pier 2

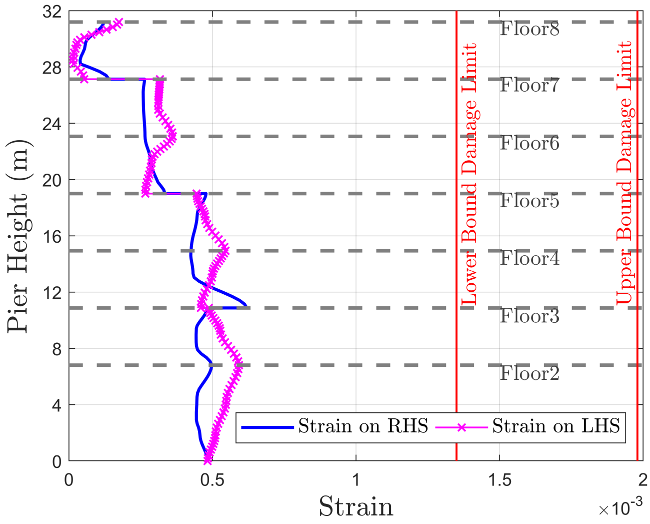

(c) Strain distribution in Pier 3

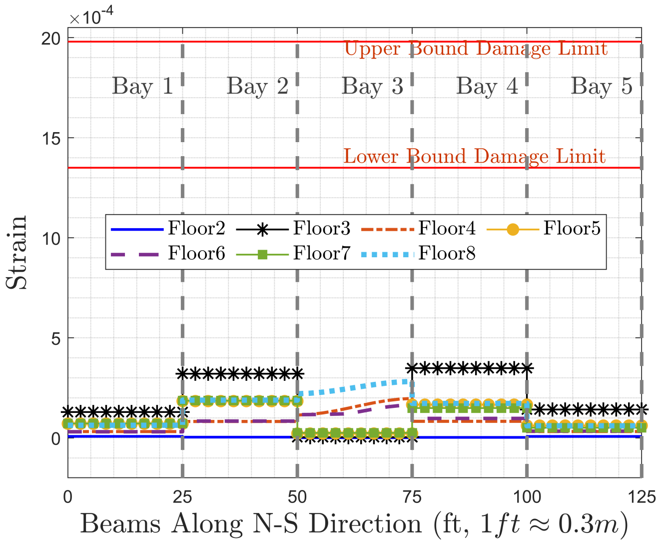

(d) Strain distribution in Floor Beams

Figure 4.6: Max. tensile strain diagram, Concentrically braced frame

beam design of seismic frames. Such design decisions inevitably change the relative stiffness between the beams and columns.

The second factor influencing the relative stiffness ratios is the contribution of floor slabs to the stiffness of floor beams. Yet it is difficult to determine whether the strains in the beams would consequently increase or decrease because the stiffness contribution from the slabs will also attract more loads into the beams for the seismic analysis.

Thirdly, as in most typical steel frame designs, the MRF is located on the perimeter of the structure, with the interior frames designed for gravity loads. The P-delta effect caused by the vertical loads on the interior frames is also worth examining.

The sensitivity study in this section focuses on evaluating the effects of these factors on the PFP damage identification for the MRF. In addition to the base model (Model 1), four more additional models were constructed for the sensitivity study:

1. Model 1: A basic centreline model of bare moment resisting frame, where the beams and columns extend from centreline to centreline, as shown schematically in Figure 4.7. The strength, stiffness, dimensions, and shear distortion of panel zones are neglected.

2. Model 2: Bare frame model (Model 1) with panel zone dimensions (depth of beam by depth of column), strength, stiffness and shear distortions considered. The Model 2 is shown schematically in Figure 4.8. Columns and beams are modelled to have clear span length. The panel zone is explicitly modelled following the approach of Gupta and Krawinkler [196], as illustrated in Figure 4.9. The rectangle composes of eight very stiff beam-column elements representing the rectangular joint area of the column web that lies between the flanges of the connecting beams. The rotational spring at one corner allows the shear distortions in the panel zone where as the other three corners are jointed by a pin connection.

3. Model 3: Model 1 with the contribution of floor slabs to the beams' strength and stiffness considered. The floor slab is modelled as part of the beam using composite beam section. The contributing slab width (B) is calculated following Equation 4.2. The stiffness contribution of slabs is accounted for based on the assumption of isotropic composite action between the slabs and the beams neglecting factors such as shear studs and reinforcements in the slab.

$$\begin{gathered} B = b_f + 0.2L \quad \text{(for interior beam spans)} \\ B = \text{Min}\ \{b_f + 0.1L,\ \ b_f + overhang\} \quad \text{(for exterior beam spans)} \end{gathered} \tag{4.2}$$

   where b_f is the flange width of the steel floor beam and L is the span of the beam.

4. Model 4: Model 2 with the contribution of reduced beam section (RBS) design incorporated. Figure 4.11 shows schematically the Model 4, with the RBSs highlighted in red. The detailing of the RBS is shown in the Section B-B. In the FE model, the reduced beam section was divided into 8 segments and each segment was represented using the averaged flange width size.

5. Model 5: Model 4 with effect of inner gravity columns considered. The P-Delta effect is introduced to the model by modelling an imaginary leaning

column loaded with all the vertical load tributary to the frame at each floor level. A rigid truss element is used to link the leaning column to the main moment frame structure in order to transfer the P-Delta effect. The leaning column is connected to the truss-column joint by a spring element with a very small stiffness to ensure the columns do not attract significant moments. The imaginary leaning column is given very high axial stiffness to represent aggregate effect of all the inner gravity columns. A schematic view of the leaning column system is shown in Figure 4.12.

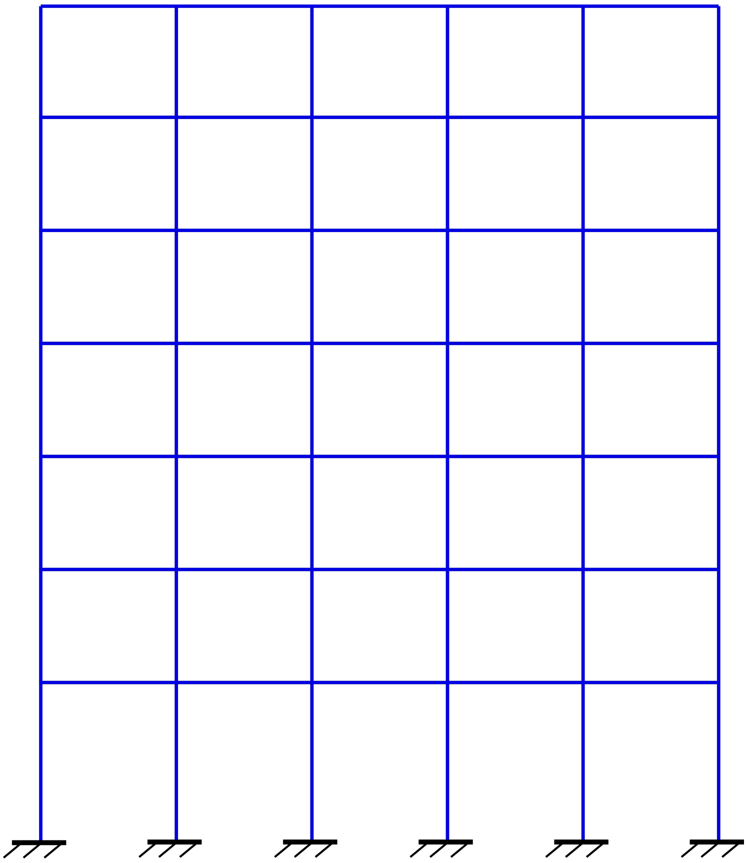

Figure 4.7: Model 1, Schematic illustration

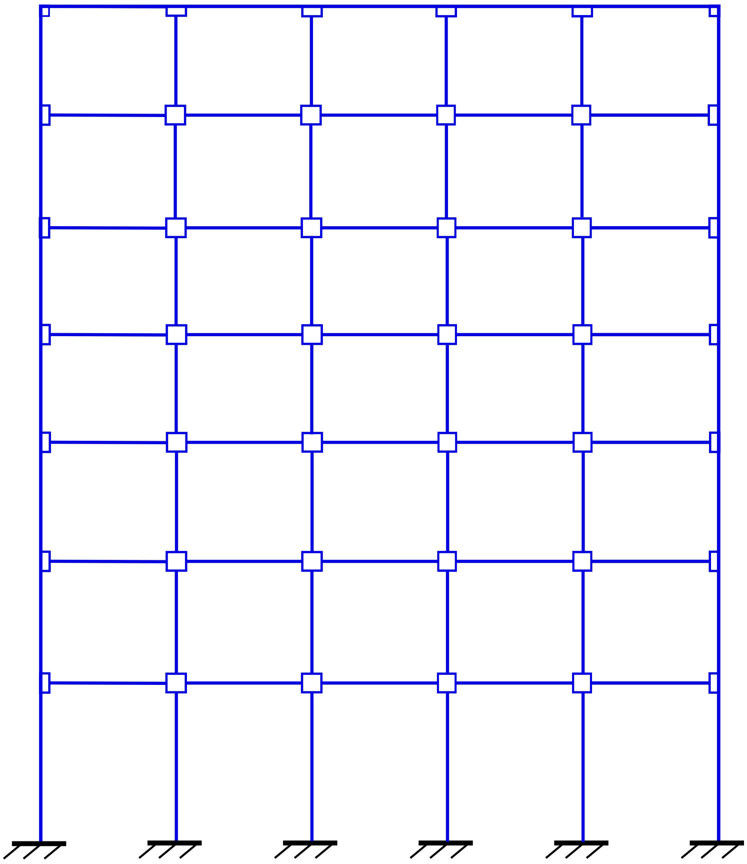

Figure 4.8: Model 2, Schematic illustration

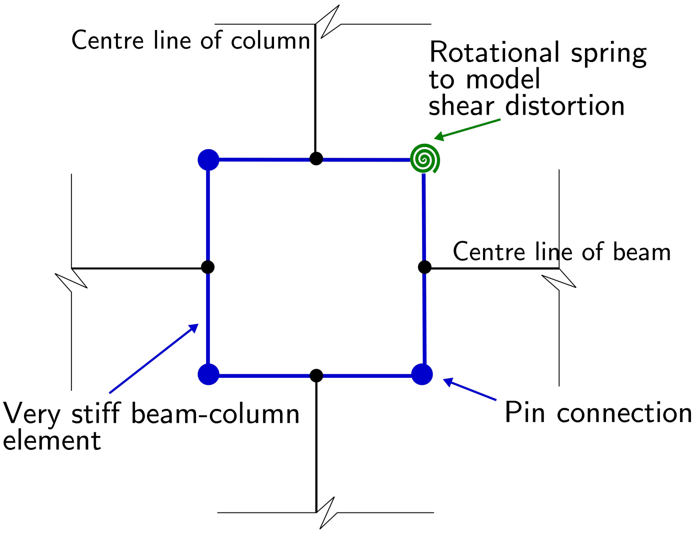

Figure 4.9: Panel zone, Schematic representation

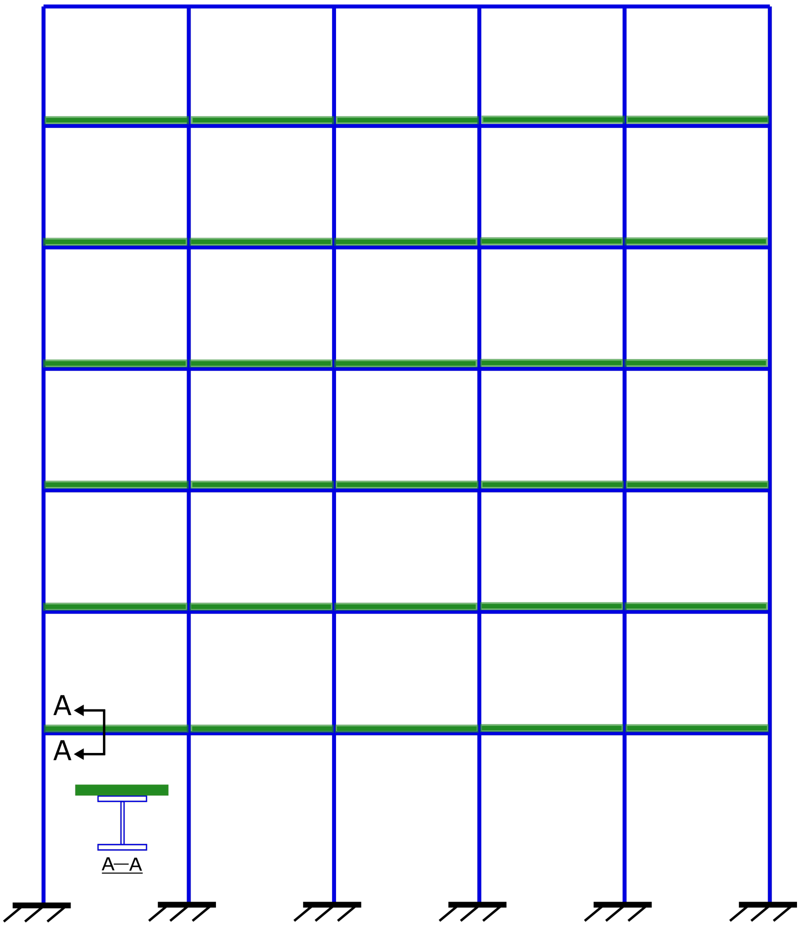

Figure 4.10: Model 3, Schematic illustration

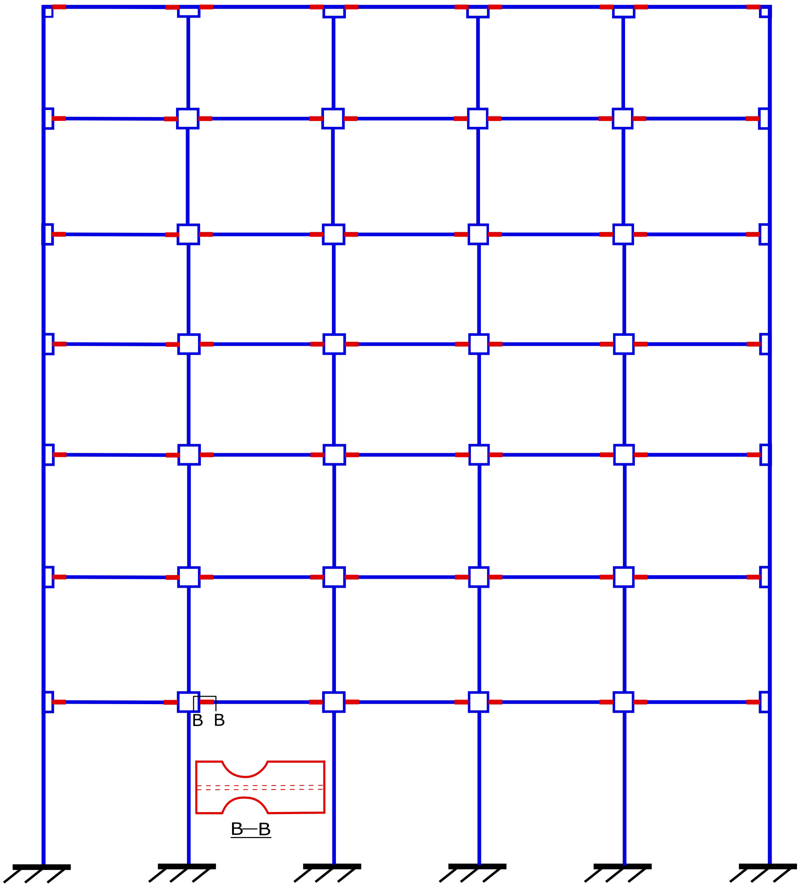

Figure 4.11: Model 4, Schematic illustration

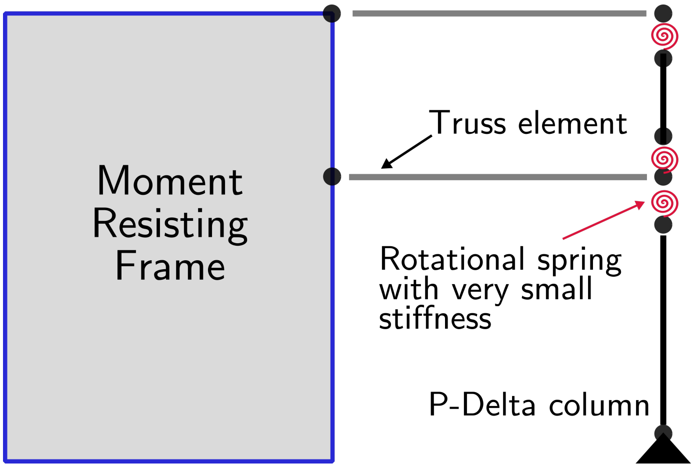

Figure 4.12: Leaning column system, Schematic representation

Table 4.6 presents the IDR of the Model 1 to 5. Comparing the results of Model 2 &4 to that of Model 1, it shows that for the same structural representation, changes in the relative column/beam stiffness ratio could cause notable differences in the IDR results. An overall higher IDRs are observed in the Model 3 and Model 5, indicating that the additional stiffness from floor slabs attracted higher seismic loading to the frame. The rigid truss elements introduced in the Model 5, connecting the frame to the leaning column, largely represented the behaviour of floor slabs during the seismic analysis.

Table 4.6: MFR inter-story drift ratios (%), Pier 3

Level	Model 1	Model 2	Model 3	Model 4	Model 5
Story7	0.77	0.77	1.09	1.10	1.09
Story6	1.25	1.13	1.78	1.79	1.78
Story5	1.56	1.42	2.10	2.08	2.10
Story4	1.41	1.48	1.68	1.64	1.68
Story3	1.02	1.16	1.22	1.22	1.22
Story2	0.54	0.76	1.08	1.05	1.08
Story1	0.60	0.68	0.92	0.91	0.92

Figure 4.13 compares the strain distributions in the Pier 3 produced by the different modelling approaches. Comparing the Model 2 results with that of the base model (Model 1), shown earlier in Figure 4.5c, similar diagram patterns are observed, indicating no significant change in the Pier 3 strain distribution as a result of including panel zones. With further connection detailing of the reduced beam section added, Model 4 sees a similar strain distribution pattern in the Pier 3 to that of Model 2, but catching an overall higher strain level at floor connections particularly at the Pier bottom and at the floor 7. Comparing Figure 4.13d to Figure 4.13c, it is also observed that the Model 5 produces nearly identical strain results in the Pier 3 to that of Model 4, indicating P-Delta effect had minimum impact on the frame column behaviour under the selected seismic loading. On the other hand, noticeable differences in the strain distribution are observed in the Model 3 results, shown as Figure 4.13b, where significantly higher strain values are shown at each floor connection.

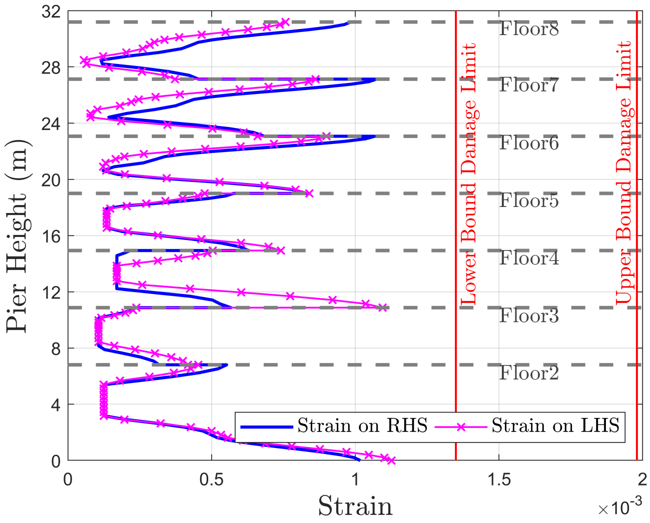

(a) Model 2

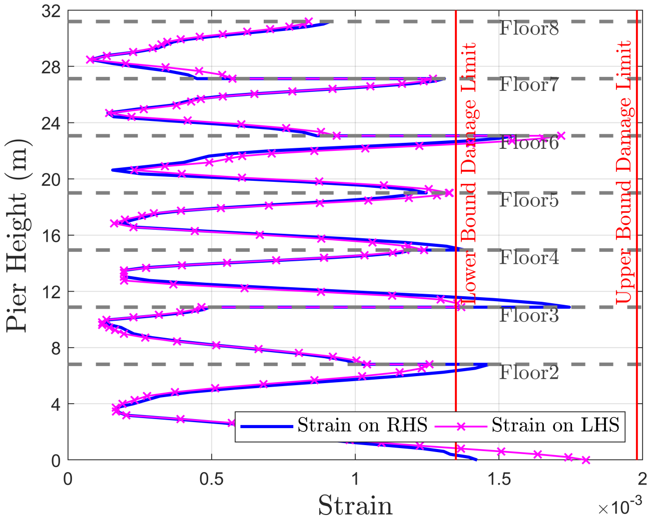

(b) Model 3

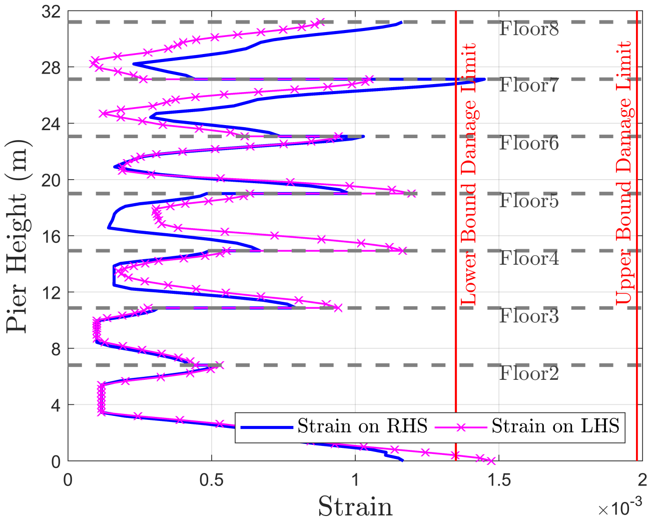

(c) Model 4

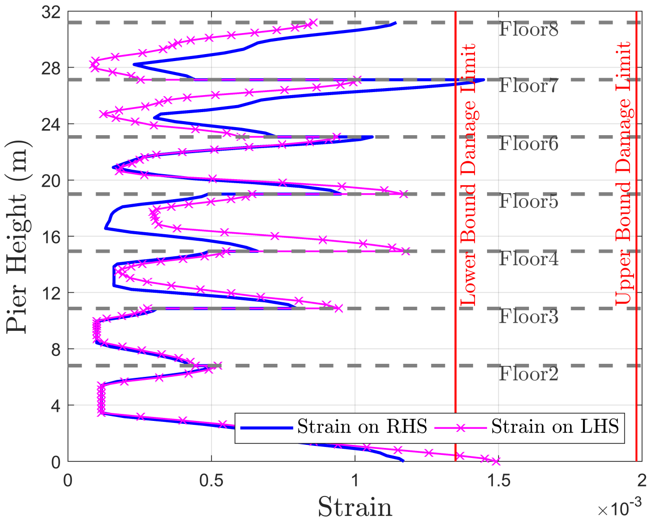

(d) Model 5

Figure 4.13: Strain distribution in Pier 3, MRF

Figure 4.14 presents the strain distributions in the floor beams produced by the Model 2 to Model 5. Compared to the strain distribution in the Model 1, shown earlier in Figure 4.5d, strain levels in Figure 4.14a are generally lower. With the inclusion of panel zone in the Model 2, high strains are now concentrated within the plasticified panel zone area, leading to lower strains in the floor beams. The Model 4 sees an in increase in the strain levels at beam ends where reduced beam section design is included. Similar to what observed in the strain distributions of Pier 3, the Model 5 produces almost identical beam strain results to the Model 4, indicating negligible P-Delta effect in this loading scenario. Irrespective of different strain levels, Model 1,2,4,5 see similar strain distribution patterns in floor beams: non-linear bending moment diagram with maximum positive moment at middle span and high negative bending moment at two ends. In contrast, with stiffness contribution from slabs included, the Model 3 observes a nearly linear moment distribution diagram in floor beams, suggesting substantially stiffer beam behaviour during the seismic analysis.

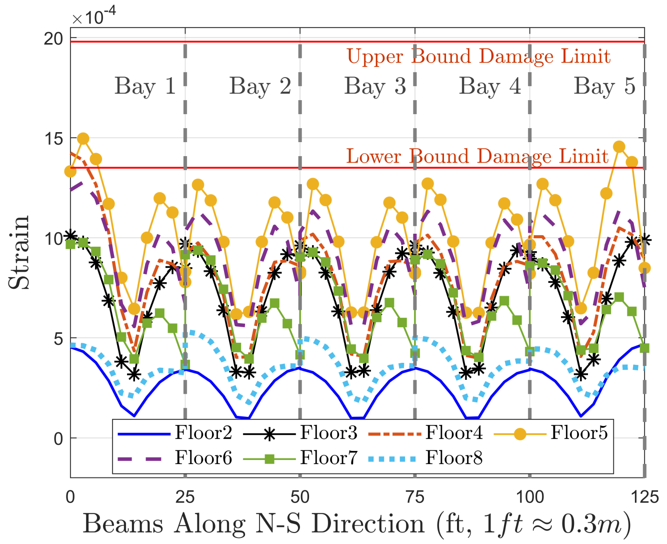

(a) Model 2

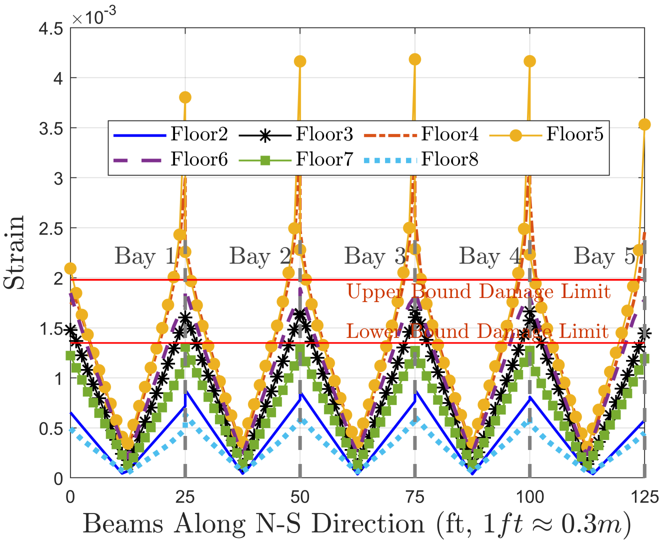

(b) Model 3

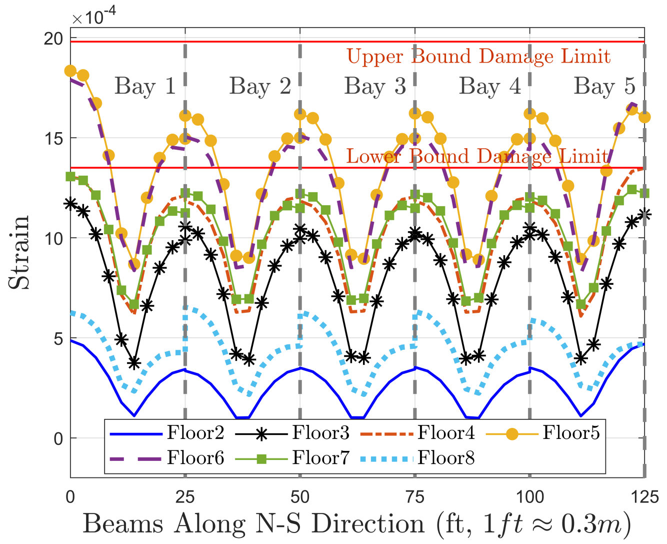

(c) Model 4

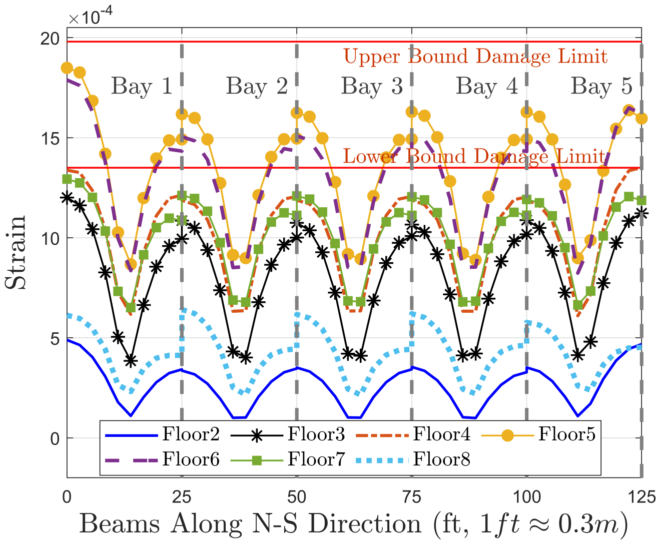

(d) Model 5

Figure 4.14: Strain distribution in floor beams, MRF

The examination of strain distributions in the floor beams and Pier 3 produced by different models suggest Model 2 can reasonably capture the representative strain distribution patterns. It is considered essential for the finite element model to capture the concentrated plastification phenomenon within the panel zone area.

The inclusion of the reduced beam section design in Model 4 increased the strain levels in the Piers, particularly at the bottom and at the floor 7 because of the increased column/beam stiffness ratio.

The comparison between the Model 4 and the Model 5 indicates minimum impact of P-Delta effect in this moderate earthquake loading. It is worth noting that the strains presented in this section are the strain results at the outmost layer of the flanges. Plastic hinge does not form until the whole cross-section reaches the yielding capacity. In spite of a few locations where the strain result exceeded the material's yield strain (0.0016), the global structure behaviour is still predominantly elastic.

The sensitivity analysis found that the inclusion of floor slabs brings about a different structural response in the frame structures, giving rise to higher strains in the piers and floor beams, indicating that the dominating effect of the stiffness contribution of floor slabs is attracting higher seismic loading. This behaviour is investigated further in the following section.

4.3.8.1 Effect of floor slabs on strain distributions

When comparing Figure 4.15a with 4.15b, it is shown that the inclusion of panel zone connection detailing caused no significant changes in the strain distribution pattern in the floor beams for the gravity load case. Lower strain values were observed in the Model 2 as stiffer panel zone connections took upon a larger portion of the loading at the beam ends. Compared with the Model 1, Figure 4.15c shows the inclusion of floor slabs in the Model 3 reduced the negative bending moments at beam ends while raised the positive bending moments at middle span.

Figure 4.16 compares the bending moment diagrams of the gravity loading in the Pier 3 predicted by the Model 1, 2 and 3 respectively. It is evident that changes in the relative column/beam stiffness ratios can lead to different load distribution within the structural frames. The inclusion of floor slabs forms stronger restraints at the column ends, consequently columns experience higher moments at beam-column joints.

Figure 4.17 compares the maximum bending moments experienced on either side of the Pier 3 in the Model 1, 2 and 3 for the earthquake loading case, higher bending moments are observed in the Model 3. Correspondingly, higher bending moments are observed in the floor beams of the Model 3 as shown in Figure 4.18. The comparison results show that the main influence of the floor slabs on the strain distributions in the MRF is attracting higher seismic loading, which in turn leads to higher strain values in the structure.

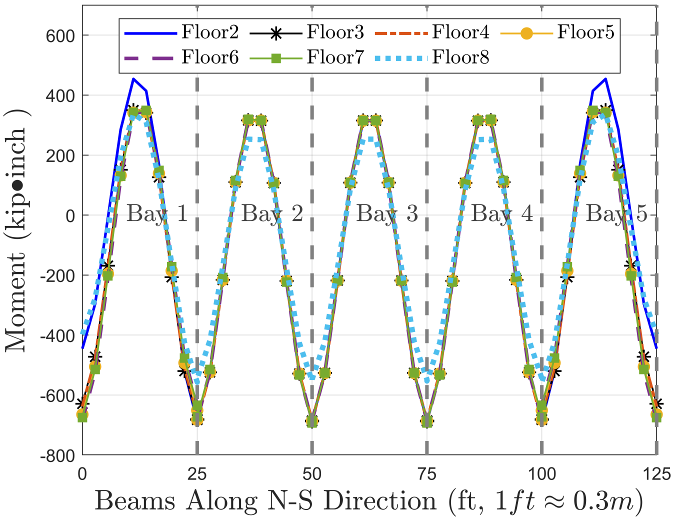

(a) Model 1

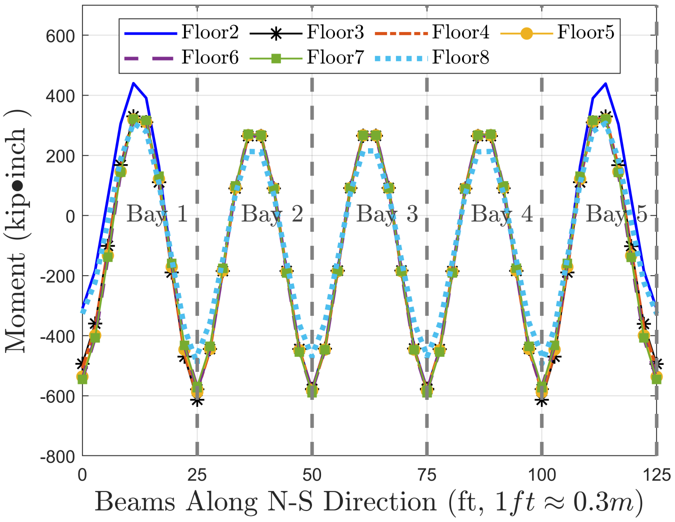

(b) Model 2

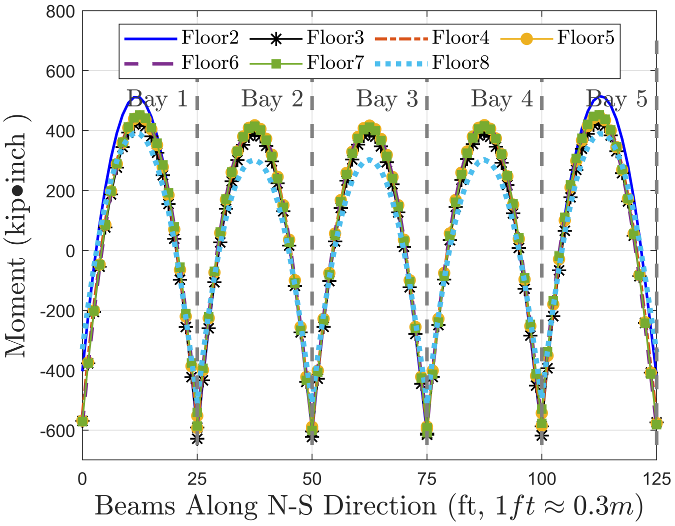

(c) Model 3

Figure 4.15: Bending moment diagram of floor beams, Gravity load

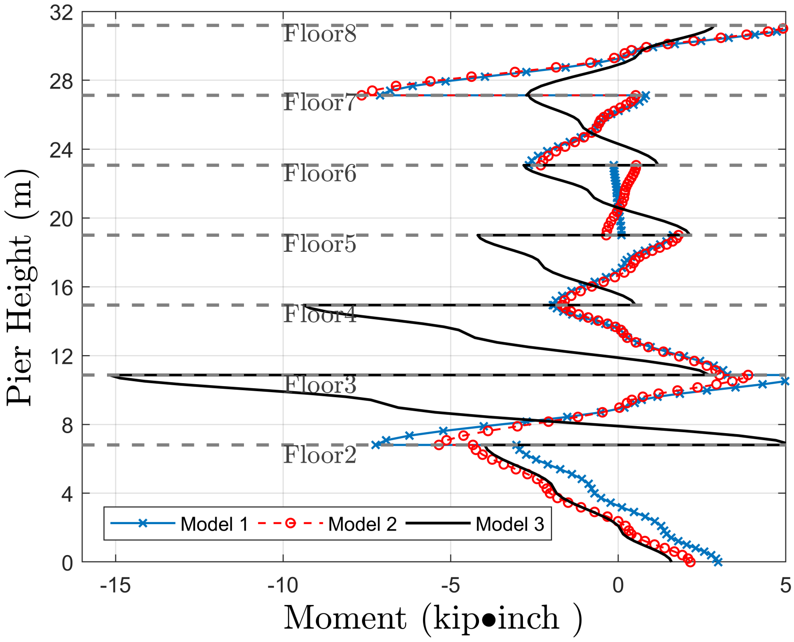

Figure 4.16: Pier 3 moment diagram, Gravity load

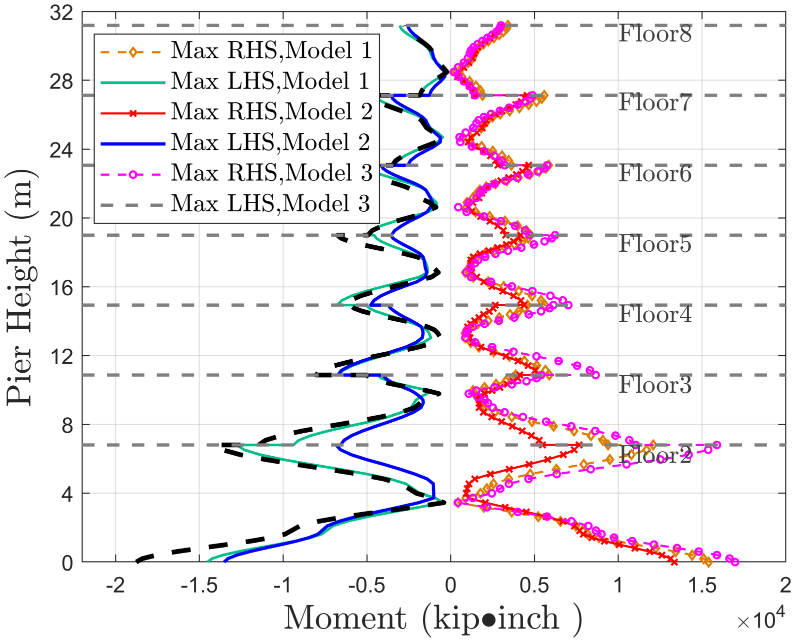

Figure 4.17: Pier 3 Max. moment diagram, Seismic load

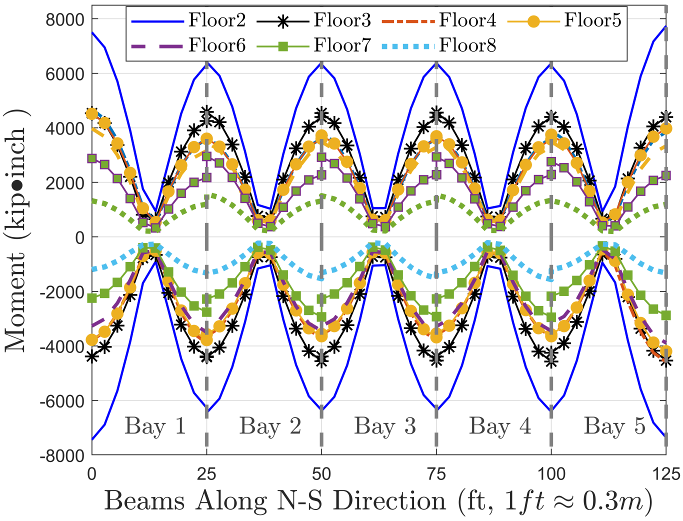

(a) Model 2

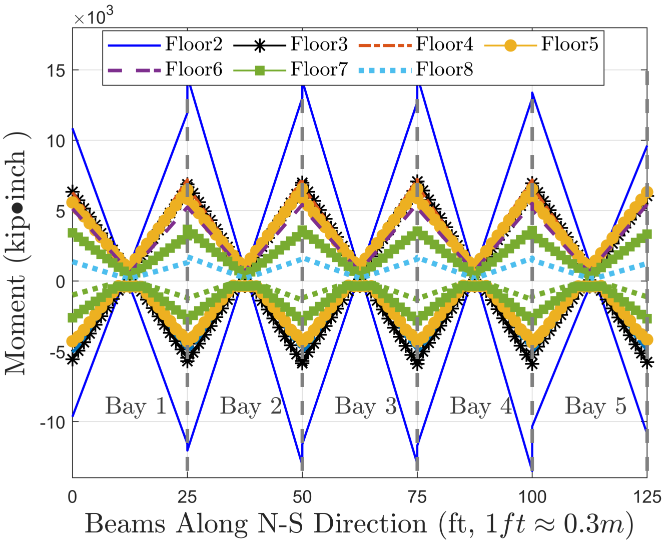

(b) Model 3

Figure 4.18: Max. negative &positive moments in floor beams, Seismic load

4.3.9 Conclusions of sensitivity study

The sensitivity study investigated the strain distributions within the MRF structure using different models with varying structural details. It was discovered that neglecting the stiffness of column-beam connections, i.e., panel zones would cause higher predictions of strains in the floor beams, overestimating the potential PFP damage area.

The impact of the stiffness contribution of floor slabs is complicated. The sensitivity study found higher seismic loading was attracted to the structure when including the floor slabs in the model, resulting in higher strain levels in the overall structure.

The response of the five models, ranging from the basic centreline model to models that incorporate the strength and stiffness of the panel zones and the contribution from gravity columns and floor slabs, is evaluated. It is evident that the prediction of the scale of the PFP damage is strongly influenced by the model selected. In order to achieve higher accuracy at the element level, a more sophisticated model is generally required. However, a compromise between accuracy, efficiency and practicality is usually necessary in the context of the problem being solved, especially for practical engineering problems. The sensitivity study forms the basis for the selection of representative models for assessing the potential PFP damage in MRFs.

Despite of the differences observed in the strain distributions from different models, the analysis results of the five models agreed that the most vulnerable locations for cementitious PFP damage are near the column-beam connections at the floor levels of high IDRs, particularly in the floor beams near the beam-column connections.

4.4 Remaining fire resistance assessment of MRF

4.4.1 PFP damage area identification

The seismic analysis results of Model 4 is adopted for the PFP damage assessment of the MRF because it captures the most structural details. Figure 4.19 schematically shows the damaged area identified using the ε_{cyclic} as the damage indicator. The size of the damaged area was quantified based the assumption that the PFP is deemed completely lost its function wherever the strain at the outmost surface of the flange exceeded the ε_{cyclic}. Based on the strain results in Figure 4.13c (Pier 3 strain distributions of Model 4), a damage length of approximately 400mm is identified at the base and at the floor 7 of the Pier 3. Figure 4.20 presents the strain results in Pier 1 &2 of the Model 4. A damage length of 250 mm is identified at the base and at the floor 7 of Pier 2. Similar damage patterns to Pier 3 and 2 is adopted in Pier 4 and Pier 5 respectively in light of structural symmetry. Based on the strain results in Figure 4.14c, damage in floor beams are identified at the floor 5 and 6. A damage length of approximately 2625 mm is observed at the exterior end of the beams in the two end bays. A damage length of about 1875 mm is found for the rest of the beam ends.

It is worthwhile noting that the PFP damage within the beam-column connections are considered have little impact on the remaining fire resistance. The connections are commonly designed of high steel volume and are not directly exposed to radiation and convection of a fire. Moreover, their high $\frac{Volume}{Exposed\ \ Area}$ ratios, make them difficult for being heated.

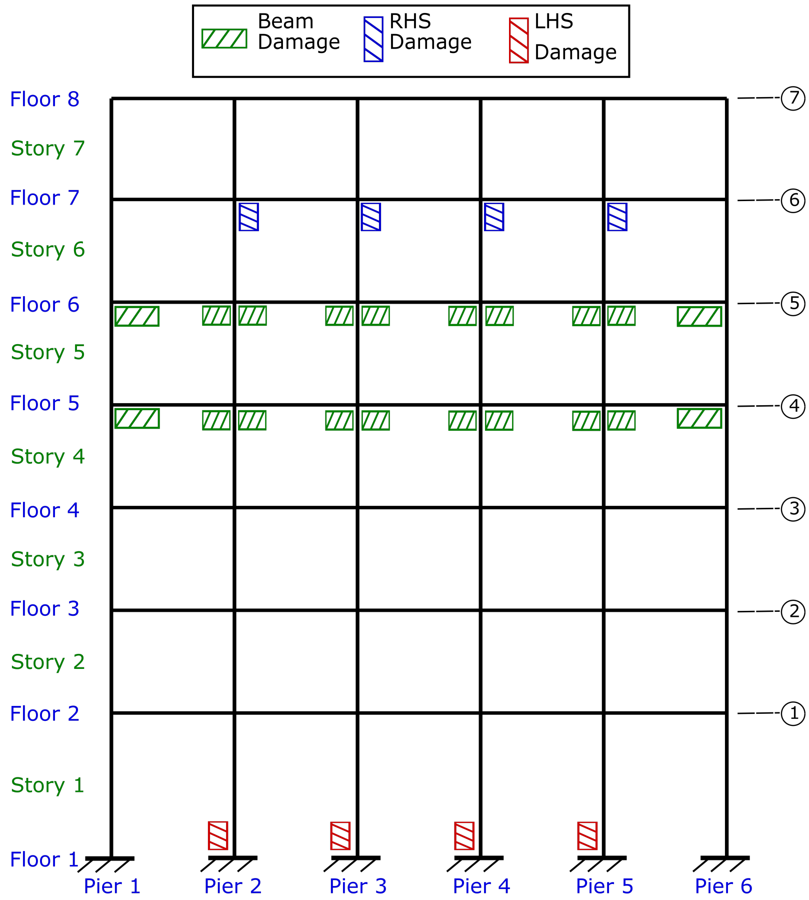

Figure 4.19: Schematic view of the cementitious PFP damage identified in MRF, Model 4

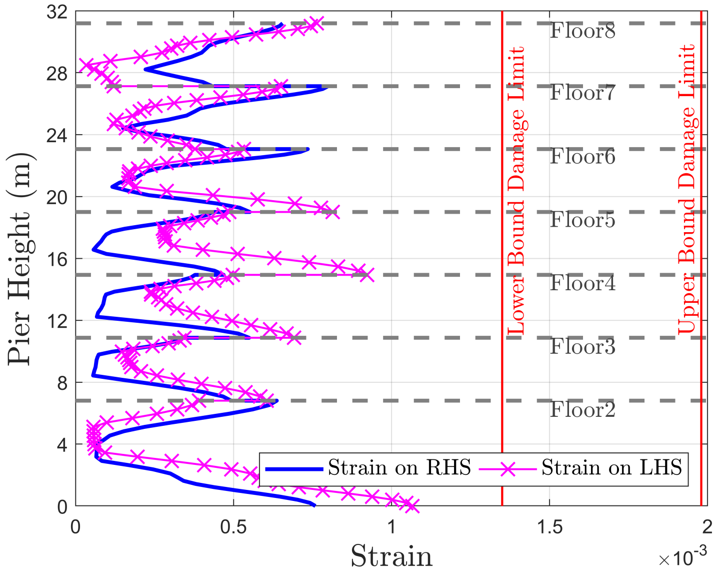

(a) Pier 1

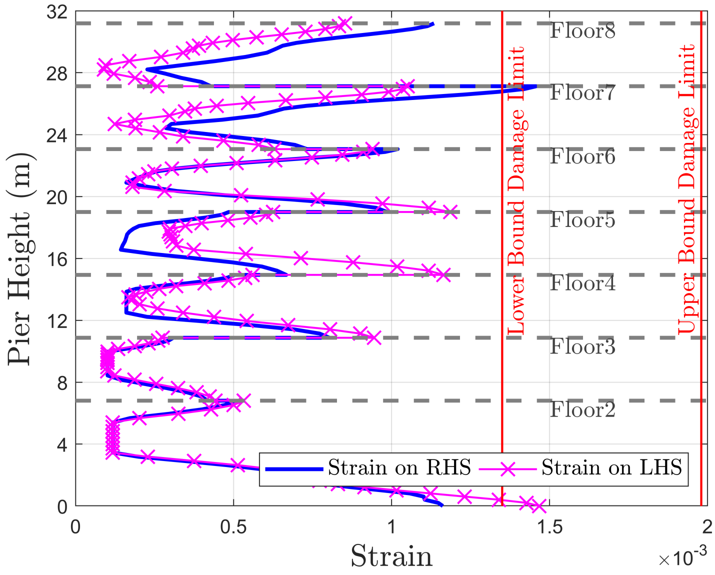

(b) Pier 2

Figure 4.20: Strain distribution in Pier 1 & 2, Model 4

The existence of potential damage in PFP can significantly jeopardise the survivability of the structure in an event of fire. In the following sections, the possible perilous consequences are analysed using a thermo-mechanical analysis of the MRF.

4.4.2 Heat transfer analysis

For structural fire analysis, it's considered that the temperature evolution in the structures are resulted from the external fire source, hence can be determined using a heat transfer analysis decoupled from the thermo-mechanical analysis.

4.4.2.1 Fire loading

The Standard Fire Curve (ISO 834) [26] was adopted to represent the temperature development of a uniform compartment fire for this office building. The fire location was selected at the compartment framed by the Pier 2 and Pier 3 at floor 1. This was considered the most onerous fire scenarios since within this compartment the PFP damage was identified at the base of the column (Pier 3). It's worth mentioning that the PFP damage identified at the base of Pier 2 was at the LHS (exterior of the compartment) hence the Pier 2 was still considered protected for the selected fire scenario.

4.4.2.2 Fire protection required

According to Table 25 of BS9999:2008 [197], a two hour fire resistance for structural components of office buildings over 30m tall is required. The PFP thickness of the beams and columns have been determined based on BSI PD7974-3:2011, Part 3 Table 9 [35]. The coating thickness required to satisfy the 2 hrs fire resistance requirement are summarised in Table 4.7. The columns were considered to be protected for 4 sides and the beams were considered to be protected for 3 sides with the top flange shielded by floor slabs.

Table 4.7: Cementitious PFP thickness

Section	Structural Type	Thickness (mm)
W24x146	Story 1 Column	23
W24x207	Floor 2 Beam	18

4.4.2.3 Coefficients for heat transfer analysis

The material properties specified in the heat transfer model include conductivity, specific heat and density. The HTMaterial –CarbonSteelEC3 developed in OpenSEES for heat transfer analysis was used. The default thermal properties of the cementitious coating in OpenSEES were adopted (thermal conductivity $\lambda = 0.05W/m/K$, density $\rho = 350kg/m3$, and specific heat $c_p = 1100J/kgK$).

The boundary conditions for the heat transfer analyses include convection and radiation. The structural cross-section was subjected to the 2 hrs fire exposure (temperature-time history), defined by the Standard Fire Curve [26] on the exposed sides. According to EC 3 [1], the convection coefficient for the unexposed and exposed surfaces were applied as 4 W/m^2K and 25 W/m^2K, the emissivity for radiation was adopted as 0.7 for steel and 0.9 for the cementitious coating.

4.4.2.4 Heat transfer analysis results

The wide flange beam W24x146 is used for the columns and the W24x207 is for the beam of this compartment. For the heat transfer analysis, the LHS flange of the Pier 3 and the RHS flange of the Pier 2 were considered subjected to the compartment fire while the beam is subjected to the fire from three sides with the top being shielded by the slab. The heat transfer analysis was performed for the unprotected and the protected column cross-section, and for the protected beam cross-section as no PFP damage was identified in the floor beam of this compartment. The temperature evolution at 12 thermal points across the I-section were obtained. Figure 4.21 shows the temperature evolution at the flange surface of the unprotected and protected columns (W24x146), and at the bottom flange surface of the protected W24x207 beam.

Albeit the longitudinal conduction within a structural member is neglected by a 2D cross-sectional heat transfer analysis, through parametric study, Jiang [198] concluded that a transitional length of 1.0 metre can be prescribed to represent the temperature gradient between the unprotected segment and the protected segment of a steel member as illustrated in Figure 4.22. Thus 2D heat transfer analysis can be used for a three dimensional frame structure subjected to a compartment fire.

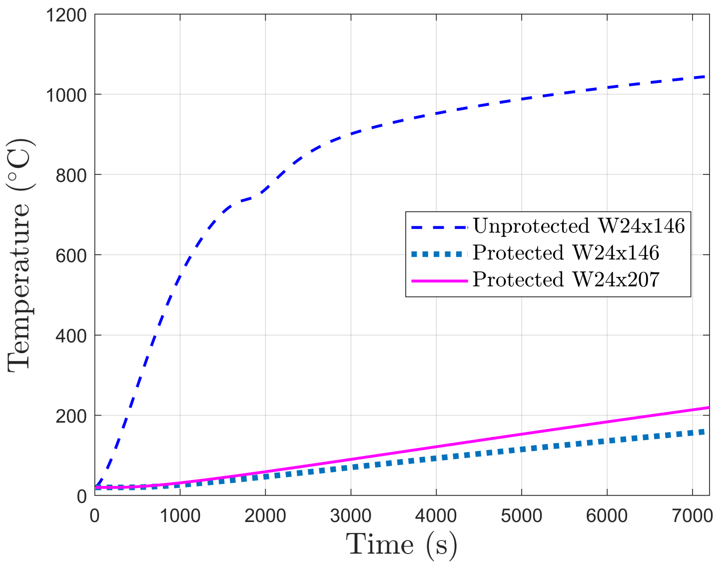

Figure 4.21: Temperature history results

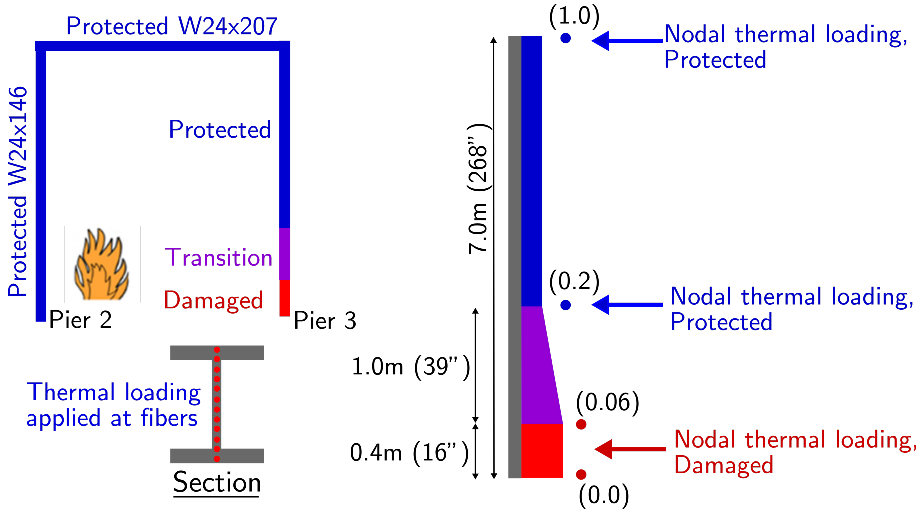

Figure 4.22: Schematic illustration of thermal loading application

4.4.3 Thermo-mechanical analysis

4.4.3.1 FE model

The same finite element model developed for the seismic analysis was used for the thermo-mechanical analysis, with appropriate modifications implemented. The uniaxial material model SteelEC02Thermal was adopted, which is the new material model proposed from Chapter 3 implemented in OpenSEES. The Voce hardening law [114] was used to model the Eurocode 3 [1] non-linear stress-strain relationships for carbon steel at elevated temperatures. The model parameters applied in the SteelEC02Thermal are presented in Table D.1. The 2D Euler-Bernoulli Displacement based element “DispBeamColumn2dThermal” was used for all structural members. Thermal Action Wrapper function was employed for thermal loading application. The cross-sectional temperature histories obtained from the heat transfer analysis were adopted as the thermal loading, and applied to the 12 fibre points across the I-section of the structural members as illustrated in Figure 4.22. For the damaged column, the heat transfer results of the unprotected W24x146 was applied to the damaged segment (shown in red in Figure 4.22) while that of the protected W24x146 was applied to the protected segments (shown in blue in Figure 4.22). The 1.0 *m* transitional segment (shown in purple in Figure 4.22) between the damaged and the protected was adopted to include the temperature gradient along the length of the damaged column. The Thermal Action Wrapper function applies a temperature distribution to the transitional segment by using a mixed order interpretation between the high temperature of the damaged segment and the low temperature of the protected segment. The heat transfer results of the W24x207 was adopted as the thermal loading for the floor beam. Longitudinal temperature gradient was not considered for the beam as uniform temperature development was assumed for the compartment fire. A static thermo-mechanical analysis was carried out to determine the remaining fire resistance of the steel frame.

4.4.3.2 Thermo-mechanical analysis results

The displacement evolution of the Pier 3 at the floor 2 and at the top floor during the fire are presented in Figure 4.23. At $t = 0\ s$, the deformation is due to the gravity loads. During the heating up to $t = 1200\ s$, the Pier 3 shows clear upward expansion, dragging its connected floor beams upwards, inducing tension into the adjacent Pier 2 &4. This phenomenon is reflected in the evolution of the vertical reactions at the column bases, as plotted in Figure 4.24, where axial load decreases in the Pier 2 &4 while increases in the Pier 3. The Pier 3 still retains its stiffness at this stage. At about $t = 1700\ s$, as the Pier 3 displacements start to drop quickly, substantial deformation and curvature were observed in the Pier 3 during the anal-

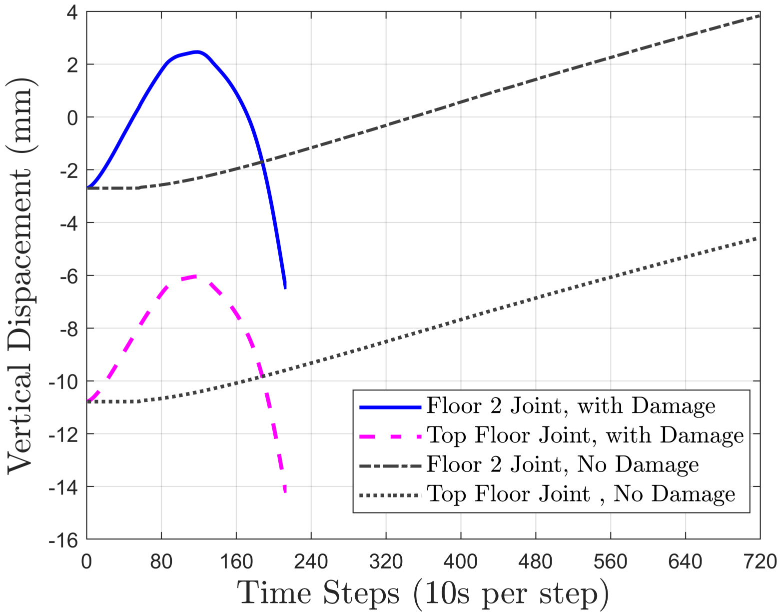

Figure 4.23: Pier 3 joint displacement comparison

ysis. This progression manifests in the base reactions as axial loads start rising in Pier 2 &4 while dropping dramatically in the Pier 3. At $t = 2150\ \ s$, the large deformation mechanism starts to form in the Pier 3. The results demonstrated that collapse failure started to show in the Pier 3 at $t = 2150\ \ s$ with the PFP damage properly taken into account.

In comparison, a thermo-mechanical analysis was carried out considering no PFP damage in the structure. The temperature history for the protected I-sections obtained from the heat transfer analysis presented in Figure 4.21 were adopted as the thermal loadings. As shown in Figure 4.23, at the end of the 2 hrs heating, the Pier 3 experienced an approximately 6mm upward movement due to thermal expansion. In contrast to the Pier 3 displacement evolution in the case of considering damaged PFP, no large deflection mechanism was observed.

The thermo-mechanical analysis results demonstrate that the structure is no longer 2 hrs fire resistant due to the damage of PFP. Whereas intact PFP system can protect the structure sufficiently from the 2 hrs Standard Fire. The safety hazard associated with the undetected and unrepaired PFP damage has therefore been highlighted.

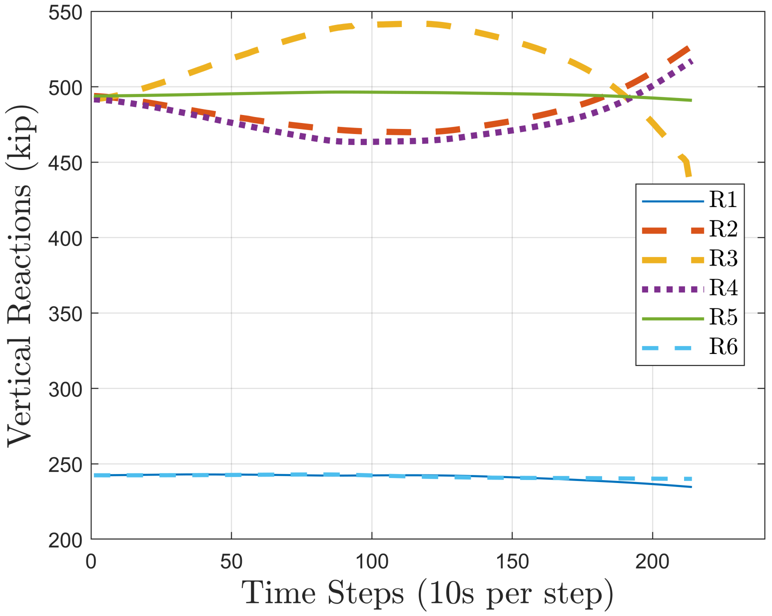

Figure 4.24: Vertical reaction development, with PFP damage

4.5 Discussion and conclusions

In this chapter, the new material model [192] from Chapter 3 was implemented in a framework for assessing the remaining fire resistance of steel frames using the cementitious PFP system subjected to moderate earthquakes. The proposed framework is implemented in the OpenSEES and demonstrated by a case study of a multi-story steel frame subjected to a moderate earthquake loading, using two equivalent seismic steel frame designs: a steel MRF and a steel CBF.

In this framework, the strain level in the beams and columns is adopted as the PFP damage indicator. Experimental results revealed that cementitious PFP coatings experience damage at a substantially lower strain level under cyclic loading (ε_{cyclic}) than that under monotonic loading ($\varepsilon_{monotonic}$). A power law based formula is proposed as an attempt to correlate the two bounding strain values using the number of cycles in the loading. Because of the large number of cycles commonly experienced under earthquake loading, it is believed conservative to adopt the lower bound ε_{cyclic} as the damage indicator for the cementitious PFP damage assessment, until a better estimate could be found trough future research. Given the damage strain limit is highly influenced by the material properties and the application techniques, e.g., spay-applied or plastered, it is the authors' opinion that the manufacturers/suppliers should be required in the future to provide the $\varepsilon_{monotonic}$ and ε_{cyclic} value to facilitate the assessment of remaining structural fire resistant post-earthquakes.

The PFP damage in the frame structure was identified based on the strain results of the seismic analysis. The comparison study shows that the PFP in the MRF structure is more susceptible to earthquake induced damage than that in the CBF structure. The sensitivity study of the various modelling assumptions of the MRFs concludes that the PFP damage assessment is highly influenced by the structural details included in the finite element model. The panel zone and reduced beam section detailing that ensure the strong column weak beam seismic design approach lead to larger PFP damage in the floor beams. The stiffness contribution from floor slabs attracts higher seismic loading to the frame, bringing about an overall higher strain level in the structure, resulting in greater PFP damage in both columns and beams. In conclusion, for the damage assessment it is recommended that the panel zone and reduced beam section detailing should be included in the finite element model. The commonly adopted centreline to centreline model is found underestimated the damage scale.

The thermo-mechanical analysis results for the selected fire scenario demonstrate that the post-earthquake PFP damage could result in significant reductions in structural fire resistance, which, in the worst case scenario may lead to structural collapse due to column failure at around 36 mins. In comparison, the structure with an intact PFP system can withstand the full 2 hrs Standard Fire as designed.

The step by step procedure of using the framework can be summarised as follows:

1. Determine the ε_{cyclic} of the cementitious material used in the PFP system.
2. Perform seismic structural analysis, by selecting suitable ground motions as the earthquake load input.
3. Establish PFP damage map.

4. Perform heat transfer analysis.
    (a) Select a fire location within the frame.
    (b) Define a fire scenario, e.g. the Standard Fire.
    (c) Determine the required fire insulation thickness according to the building regulations.
    (d) Analyse the cross-sectional and longitudinal temperature evolution for the PFP damaged and protected structural components respectively.
5. Perform thermo-mechanical analysis.

The integrated multi-hazard framework as presented herein offers a practical solution for assessing remaining fire resistance of PFP protected structures subjected to fire following moderate earthquakes.

Chapter 5

A Thermo-mechanical Analysis of Stainless Steel Structures in Fire

Adapted from M. Zhou, R. Cardoso, H. Bahai, and A. Usmani, “A thermo-mechanical analysis of stainless steel structures in fire”, *Engineering Structures*, under review, 2019

5.1 Introduction

The development of structural design codes, standards and specifications for stainless steel has been a research focus since early 1960s. The first American specification dealing with the design of structural stainless steel members was published in 1968 by the AISI [199]. In Europe, the first edition of the design manual for structural stainless steel was published in 1994. Since then, several European research projects have been carried out to analyse the performance of structural stainless steel, resulting in the publication of the Design Manual for Structural Stainless Steel (DMSSS) fourth edition [2] in 2017.

Large scale fire tests of carbon steel structures, such as Cardington tests [106], have revealed significant difference between global structural behaviour in fire and individual structural component tested in the furnace. However, testing steel sub-assemblies and frame structures in a fire is extremely expensive and one single test provides only a limited amount of data. The current research gap in understanding stainless steel structural systems in fire can be approached economically and efficiently using FEA; by taking advantage of existing experimental observations and experience using FEA on large carbon steel structures in fire.

This chapter investigates stainless steel structural behaviour in fire using finite element modelling, focusing on comparisons between carbon steel and stainless steel structures, with the aim of exploring potential advantages offered by the stainless steel materials. Using the new material model developed by Zhou et al. [192], also presented in Chapter 3, the influence of stainless steel's highly non-linear material behaviour on its structural performance in fire is investigated, the impact of its higher thermal expansion is also discussed. Due to limited available testing data for stainless steel structures at elevated temperatures, structural models used in the FEA were validated against existing testing data of carbon steel structures in fire.

5.2 Temperature development in stainless steel I sections

In this section, the temperature development within structural stainless steel I-sections is investigated using heat transfer analysis carried out in OpenSEES [24]. The impact of section factors (A/V), defined as the heated perimeter of the exposed cross-section divided by the total sectional area, is examined. A comparison study between structural stainless steels and structural carbon steel is performed.

5.2.1 Heat transfer model validation

Gardner and Ng [20] conducted a series of furnace tests of stainless steel beams tp investigate the temperature development within the sections over the time. The I section steel beams were subjected to four sides heating during the test as illustrated in Figure 5.1. Validations of the FE model is performed by comparing the OpenSEES heat transfer results with the testing data and the Abaqus finite element results obtained by Gardner and Ng [20]. The I cross sections were modelled using the heat transfer element in the OpenSEES. The boundary conditions for the heat transfer analyses include convection and radiation. The recordings of the furnace temperature were adopted as the fire loading for the validation study. In accordance with Eurocode 3 [1], the convection coefficient of $25W/m^2K$ was adopted for both carbon steel and stainless steel sections; the emissivity for radiation is adopted as 0.7 for the carbon steel and 0.4 for the stainless steel. The comparison results are presented in Figure 5.2, where a good agreement is observed. The sharp increase in the furnace temperature at around 850 °C for I120x64 and I160x82 has been well captured by the FE model.

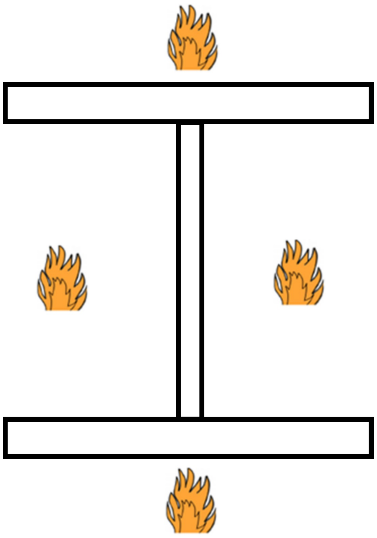

Figure 5.1: I section subjected to 4 sides heating

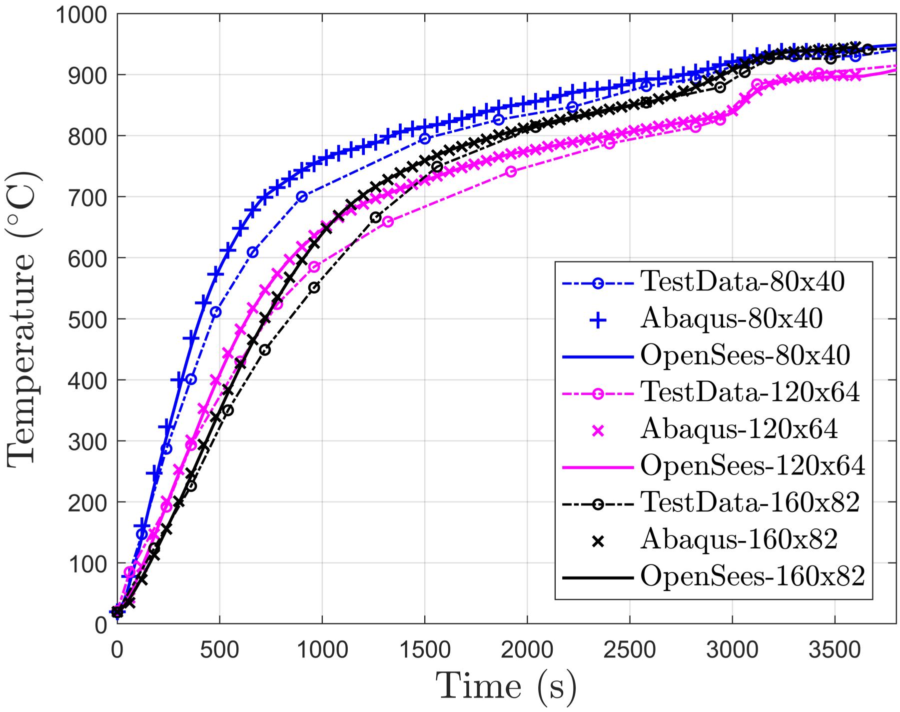

Figure 5.2: Temperature development within sections

5.2.2 Heat transfer parametric study

Temperature development within stainless steel I-sections is studied through a parametric study using the heat transfer model validated in the previous section. For steel I-sections subjected to high temperatures, radiation is the predominant heat transfer mode and conduction within the cross-section is almost instantaneous due to the high thermal conductivity. A comparison study of the temperature development within the carbon steel and the stainless steel I-sections was carried out for 9 typical I-sections subjected to 4 sides heating. A summary of the dimensions of the 9 I-sections and their section factors (A/V) is presented in Table 5.1.

Table 5.1: Section dimensions and Section factors

Section	Depth (mm)	Width (mm)	Web t (mm)	Flange t (mm)	A/V (m^{-1})
UB914x305x289	926.6	307.7	19.5	32.0	83
UB762x267x197	769.8	268.0	15.6	25.4	104
UB914x419x388	921.0	420.5	21.4	36.6	71
UB610x305x238	635.8	311.4	18.4	31.4	82
UC305x305x198	339.9	314.5	19.1	31.4	76
UC254x254x73	254.1	254.6	8.6	14.2	166
UC356x406x634	474.6	424.0	47.6	77.0	32
UC356x406x393	419.0	407.0	30.6	49.2	48
UC356x406x235	381.0	394.8	18.4	30.2	78

The boundary conditions for the heat transfer analyses include convection and radiation. The I-sections were subjected to a 1 hr fire exposure defined by the Standard Fire Curve [26] on all 4 sides. In accordance with Eurocode 3 [1], the convection coefficient of $25W/m^2K$ was adopted for both carbon steel and stainless steel sections; the emissivity for radiation is adopted as 0.7 for the carbon steel and 0.4 for the stainless steel.

Figure 5.3 shows the temperature difference vs.time relationships at the bottom flange for each I-section. The temperature difference is determined as $Temp_{carbon} - Temp_{stainless}$ through the duration of the heating. $Temp_{carbon}$ is the temperature of the carbon steel while $Temp_{stainless}$ is the temperature of the stainless steel.

At the same time step, carbon steel I-sections experienced higher temperatures than stainless steel ones since only positive temperature differences were observed. A maximum temperature difference of 122 °C was observed at the bottom flange of section UC356x406x634, which is of the lowest A/V of 32 m^{-1}, at around 2400 s. The section of the highest A/V of 166 m^{-1} (UC254x254x73) experienced the lowest maximum temperature difference of 80 °C at about 600s. In general, it has been observed that higher A/V leads to a smaller magnitude and an earlier occurrence of the maximum temperature difference.

The same trend has also been observed at the mid-web of the I-sections, as shown in Figure 5.4. The slower temperature rise experienced in the stainless steel is believed mainly attributed to its lower emissivity.

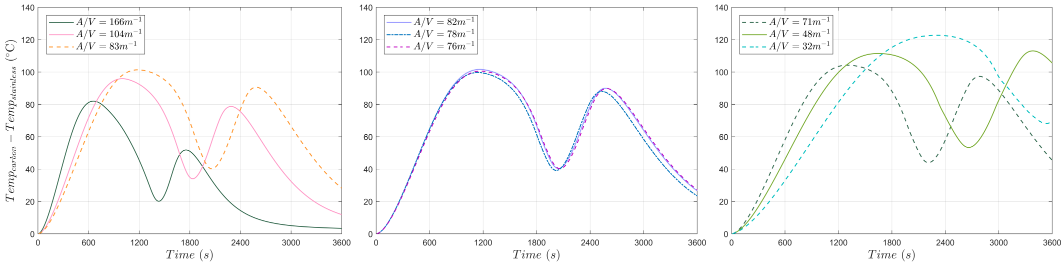

Figure 5.3: Temperature difference in bottom flange, 4 sides heated

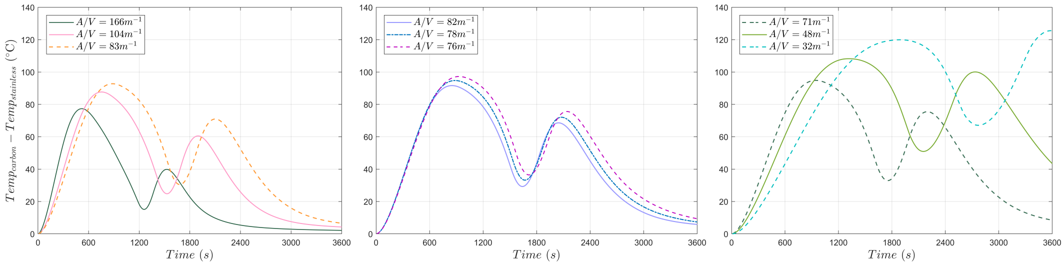

Figure 5.4: Temperature difference in web, 4 sides heated

5.3 Stainless steel structural behaviour in fire

For this study, the multi-dimensional material model presented in Chapter 3 was developed to a one-dimensional plasticity model, and implemented as uniaxial material models in OpenSEES [24]. The uniaxial material "SteelEC02Thermal" has been implemented for the carbon steel, "Stainless01Thermal" for the duplex stainless steel and "Stainless02Thermal" for the austenitic stainless steel. These three material models were adopted for the comparison studies in the section. Due to little available testing data for stainless steel structures at elevated temperatures, the FE models used in this study were validated against existing testing data of carbon steel structures in fire.

5.3.1 Simply supported beams in fire

5.3.1.1 FE model validation

The simply supported beam was modelled in OpenSEES [24] using the Euler-Bernoulli beam theory based "DispBeamColumn2DThermal" element. The FE beam model is pinned at one end and is free to move in the horizontal direction at the other end. The FE analysis accounted for both material and geometric non-linearities. A static thermo-mechanical analysis was performed to investigate the behaviour of stainless steel beams in fire.

Rubert and Schaumann [6] carried out a series of tests on simply supported beams subjected to 4 sides heating, with varying initial load ratios (L.R.) ranging from 0.2 to 0.85. The tested beams were of a length (L) $= 1140$ *mm*, with cross-section size IPE 80/ IPE 120, and made of St 37.2 Grade carbon steel. A point load was applied at the mid-span of the beams. The L.R. was calculated as the the maximum bending moment applied on the simply supported beam over the plastic bending moment capacity of the beam at ambient temperature. The uniaxial material model SteelEC02Thermal was used for the St 37.2 grade carbon steel. The material parameters of the hardening functions applied in the SteelEC02Thermal for the validation were determined by least square fitting the stress-strain curves of the tested St 37.2 carbon steel in [6], and are summarised in Table D.7.

The FE model was validated by comparing model predictions of the midspan deflection of the 4 sides heated beams with that of testing data. As shown in Figure 5.5a, a general good agreement has been observed between the testing data and the OpenSEES simulations.

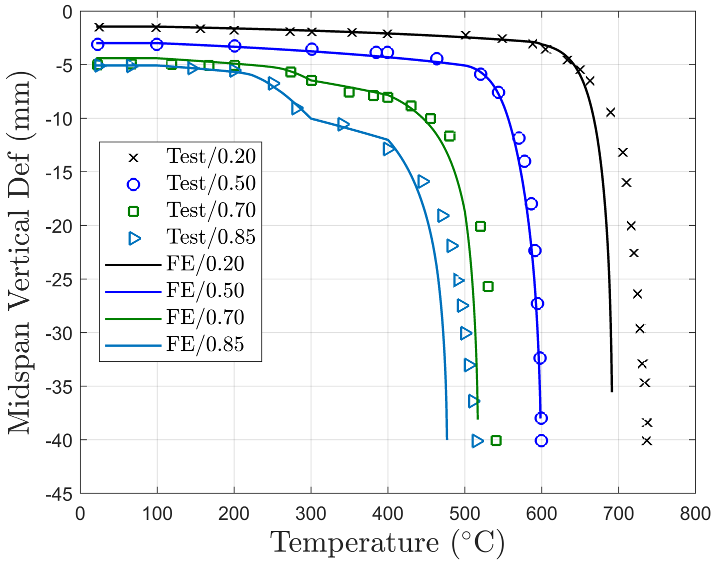

(a) Four sides heating

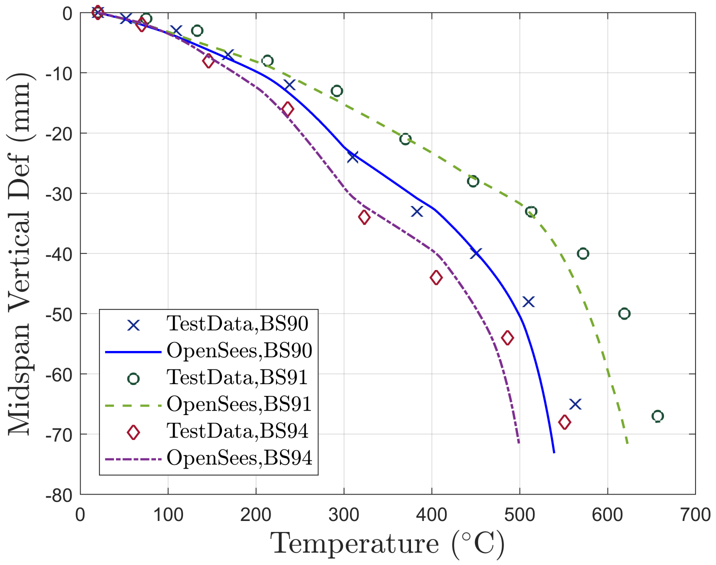

(b) Three sides heating

Figure 5.5: Validation of simply supported beam model

A series tests of simply supported beams in fire were also carried out by the British Steel and documented in the Compendium of UK Standard Fire Test Data [200]. The testing data of three beams, BS90 (UB356x171x67), BS91 (356x171x67) and BS94 (IPE 360) were also adopted for validation in this study. The beams were heated from three sides with the top being protected by a concrete slab. There were no composite actions between the steel beam and the slab. The

FE model was further validated by comparing model predictions of the midspan deflection of the three sides heated beams with the testing results. As shown in Figure 5.5b, a good agreement has been generally observed between the test data and the OpenSEES results.

5.3.1.2 Comparison study

Using the validated structural FE model, a comparison study was carried out to analyse the structural behaviour of simply supported stainless steel beams in fire. For this study, carbon steel S235, Austenitic 1.4571 (group III) and Duplex 1.4162 (group II) stainless steels have been selected. As discussed in Section 2.2.3.1, the Austenitic III shows the most promising stiffness and strength retention capability while the Duplex II shows an overall better stiffness and strength retention capability than the Duplex I. The lean duplex grade (Duplex 1.4162) was included in this study also because there has been a significant increase in its application in onshore building construction [22].

The room temperature values of the Young's modulus and the 0.2% proof strength ($\sigma_{0.2}$) for the three selected steels are summarised in Table 5.2. It is worth noting that DMSSS [2] proposes an identical Young's modulus value for the austenitic and duplex stainless steels, which is nearly the same to the value of carbon steel. The $\sigma_{0.2}$ of the austenitic steel is close to that of carbon steel, whereas the $\sigma_{0.2}$ of the duplex stainless steel is almost double the $\sigma_{0.2}$ of the carbon steel. The uniaxial material model Stainless01Thermal and Stainless02Thermal were adopted for the Duplex 1.4162 and Austenitic 1.4571 stainless steel respectively. The material model parameters applied were obtained based on the nominal stress-strain relationships of stainless steels at elevated temperatures in DMSSS [2], and are presented in Table D.2 and Table D.3. For the S235, the material model parameters determined using the EC 3 [1] stress-strain curves for carbon steel at elevated temperatures were applied in the SteelEC02Thermal, and are summarised in Table D.1. For better understanding the influence of stainless steel's highly material non-linearity and high thermal expansion on its structural fire behaviour, and the difference to carbon steel structural fire behaviour, the Bauschinger effect is therefore not included in this study. A Bauschinger ratio of 1.0 was adopted for all the materials.

Table 5.2: Material properties

Material Property	S235	Austenitic	Duplex
Young's modulus (GPa)	210	200	200
$\sigma_{0.2\%}$ (MPa)	235	220	450

In this study, four series of comparison analyses were performed. The applied load, initial deflection and initial L.R. of each beam for each series are summarised in Table 5.3. In each series, the magnitude of the applied load was kept constant for the three beams of different steel materials. Comparable initial midspan deflections were attained due to the similar Young's modulus of the carbon steel and the stainless steels, with slightly higher deflection observed in stainless steels. In each series, the initial L.R.s of the duplex steel beam was almost half of the carbon steel and austenitic stainless steel beams because of its higher $\sigma_{0.2}$ value. In the Series 3 &4, a notably higher initial deflection is observed for the austenitic stainless steel beam, indicating the tangent modulus is already considerably lower than the initial elastic modulus at higher L.R.s.

Table 5.3: Comparison study series, Simply supported beams

Series	Applied Load	Initial Deflection (mm)			L.R.		
No.	(kN)	S235	Austenitic	Duplex	S235	Austenitic	Duplex
1	3.71	0.70	0.75	0.75	0.20	0.21	0.10
2	9.27	1.8	1.9	1.9	0.50	0.53	0.26
3	12.98	2.5	3.1	2.6	0.70	0.75	0.37
4	15.77	3.0	4.9	3.2	0.85	0.95	0.44

The midspan deflection vs. temperature curves are presented in Figure 5.6. In the first series, the deflection of the carbon steel beam started to increase rapidly at around 650 °C and the run-away mechanism occurred at about 750 °C. Identical deflections were observed for the austenitic and duplex beams until near the occurrence of the run-away mechanism, which was at around 800 °C for the duplex and at around 900 °C for the austenitic steel. Based on the deflection results of the first series, the two stainless steels exhibit superior behaviour to that of carbon steel with the run-away mechanism occurring at the highest temperature for the

Austenitic 1.4571 beam. The mechanical stress-strain results of the Series 1 are presented in Figure 5.7a. The carbon steel showed a linear stress-strain relationship in their results, whereas noticeable strain hardening was observed in the stainless steel beams. It's worth noting that thermal strain does not contribute to material yielding in simply supported beams.

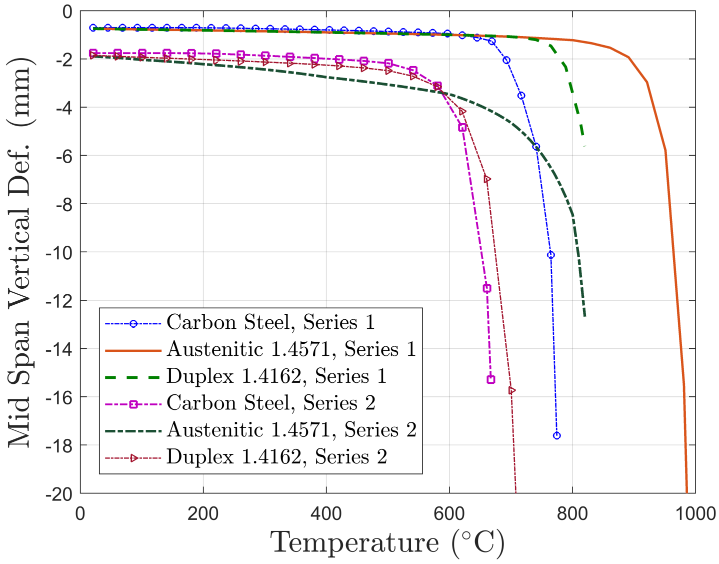

(a) Series 1 and 2

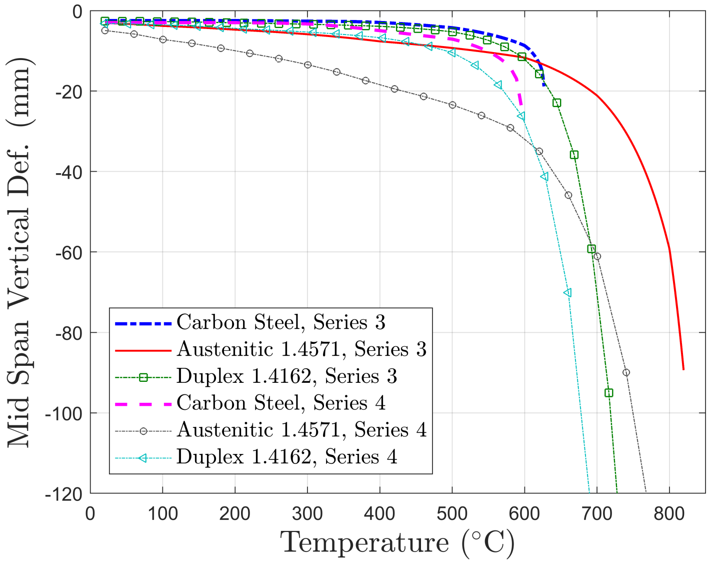

(b) Series 3 and 4

Figure 5.6: Deflection comparisons, Simply supported beam

Figure 5.6a shows that for the second series, the deflection of austenitic beam develops faster than the other two beams because the Austenitic 1.4571 steel approaches the non-linear region faster. The deflection vs. temperature curve suggests that with the initial L.R. =0.53, the Austenitic 1.4571 experienced a faster and greater reduction in its tangent modulus. The run-away mechanism was still evident at the highest temperature for the austenitic beam, at around 800 °C. The run-away mechanism for the carbon steel beam and for the Duplex 1.4162 beam initiated at a similar temperature, around 600 °C. As shown in Figure 5.7b, substantial amount of strain hardening was observed for the stainless steel beams.

For the third series, Figure 5.6b shows that with L.R. =0.75, higher initial deflection and faster deflection development is observed for the austenitic beam. This is due to faster reduction in the tangent modulus as the material approaches plastic state. The run-away mechanism occurred at about 610 °for the carbon steel beam, at around 700 °C for the duplex beam and at around 800 °C for the austenitic beam.

For the fourth series, starting with similar initial deflections, the carbon steel beam displayed a slower deflection development than the duplex beam until the run-away occurred at around 550 °C. The deflection of the Duplex 1.4162 started to increase quickly at around 500 °C and reached 114 *mm* (L/10) at about 690 °C. Due to the high initial L.R., austenitic beam was already in the plastic state at the start of the heating, resulting in significant reduction in the tangent modulus. This was manifested as higher initial deflection and notably faster deflection rate in the austenitic beam than the other two steel beams. However, due to its superior stiffness retention, the austenitic beam reached the large deflection of 114 *mm* (L/10) later at about 750 °C. Figure 5.7c and 5.7d show that in Series 3 and 4, substantial strain hardening was able to develop in the simply supported stainless steel beams while none was observed for the simply supported carbon steel beams.

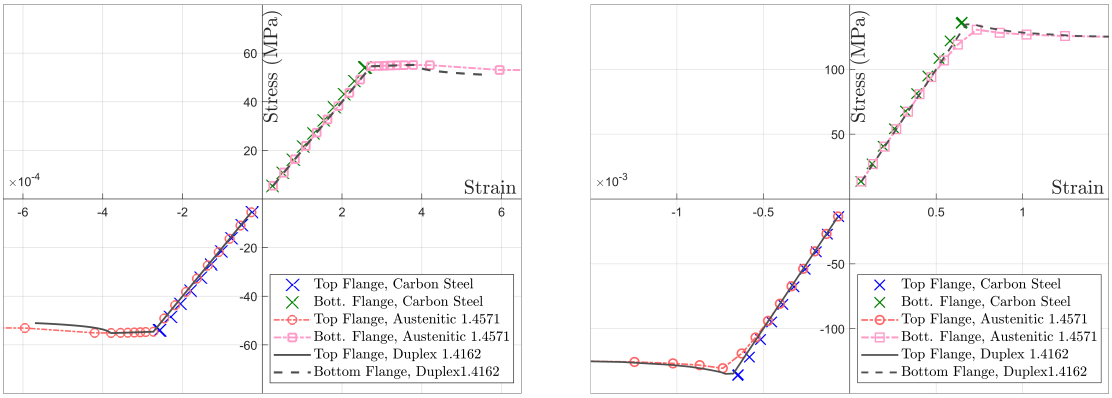

(a) Series 1 **(b)** Series 2

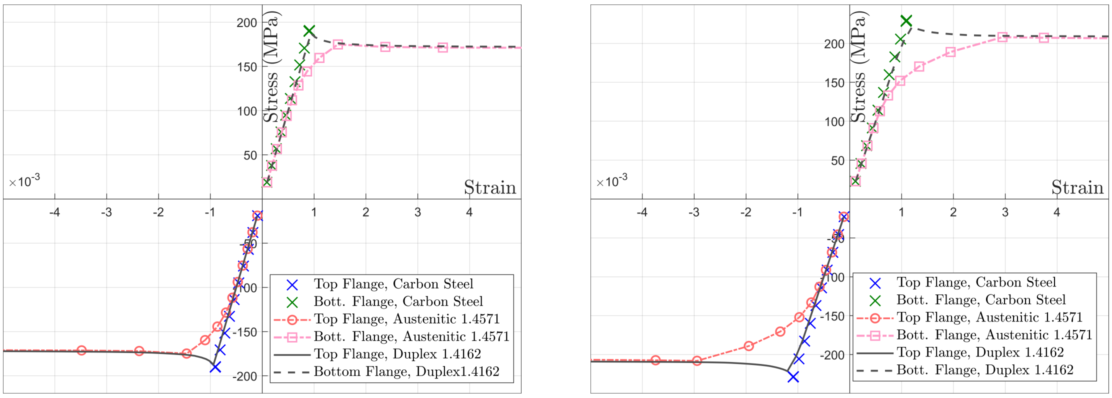

(c) Series 3 **(d)** Series 4

Figure 5.7: Stress strain development, simply supported beam

5.3.1.3 Discussion

The deflection results suggest that the initiation of the run-away mechanism for simply supported beams in fire is primarily determined by the material's stiffness degradation and the initial load ratio. At the lowest L.R., the run-away mechanism occurs when the stiffness of the material starts to deteriorate rapidly, at around 500 °C for the carbon steel and 800 °C for the stainless steel. For carbon steel, the elastic modulus retention capability at elevated temperatures is a good indication to the occurrence of the run-away mechanism in simply supported beams. For simply supported stainless steel beams with higher initial L.R., the retention factor ($k_{E,\theta}$) cannot consistently indicate well the occurrence of the run-away mechanism, because the early plastic state achieved in the material gives rise to significant reduction in the tangent modulus.

The comparison study between the simply supported stainless steel and the carbon steel beams shows that the Austenitic 1.4571 beam exhibits the best behaviour based on the judgement of midspan deflection development. This is as expected because of its overall superior stiffness and strength retention capability, as shown in Figure 2.1 and Figure 2.2. However, at higher L.R.s, the early reduction in the tangent modulus of the stainless steel results in faster deflection development rate.

The stress-strain plots show similar behaviour for the four different L.R.s, as seen in Figure 5.7. The most significant difference observed between the simply supported carbon steel and stainless steel beams is that the plastic state occurred at a lower strain level, hence lower L.R.s, in the austenitic stainless steel beams. This is caused by the significantly shorter linear elastic stress-strain range of the stainless steels.

The FE results of the carbon steel stress strain response did not observe any plastic strain development. However, it should be noted that the FE analysis terminated in the carbon steel beams quickly after its deflection vs. temperature curve started approaching vertical, as the static analysis could not cope with the sudden substantial loss of the structural stiffness. The elastic modulus of carbon steel rapidly reduces from 60% of its room temperature value at 500 °C to about only 30% at 600 °C. The deflection results were still in the small deflection regime when the FE analysis terminated hence plastic hardening was not experienced in the numerical model. Plastic strain would be experienced in real life beams during the development of large deflections following the occurrence of the run-away mechanism.

5.3.2 Plane frame structures in fire

5.3.2.1 FE model validation

Unlike simply supported beams, thermal expansion induced compression dominates beam behaviour in real structures where there exist end restraints provided by the surrounding structure. Consequently, the performance of stainless steel frame structures in fire will be determined by two competing factors: superior stiffness retention and high thermal expansion.

The study of stainless steel frames was carried out using finite element analysis with the FE model validated against the testing data of the EHR3 carbon steel frame tests performed by Rubert and Schaumann [6]. The configuration of the EHR3 frame is illustrated in Figure 5.8. All members were uniformly heated during the test. The frame beam was pinned at right end while the column was pinned at the bottom. The lateral torsional displacement and the out-of-plane deformation were prevented by using stiffeners during testing, hence a 2D plane frame model was considered suitable for this study. The frame was modelled in in OpenSEES [24] using the Euler-Bernoulli beam theory based "DispBeamColumn2DThermal" element. A static thermo-mechanical analysis was performed to investigate the behaviour of stainless steel beams in fire. The FE analysis accounted for both material and geometric non-linearities.

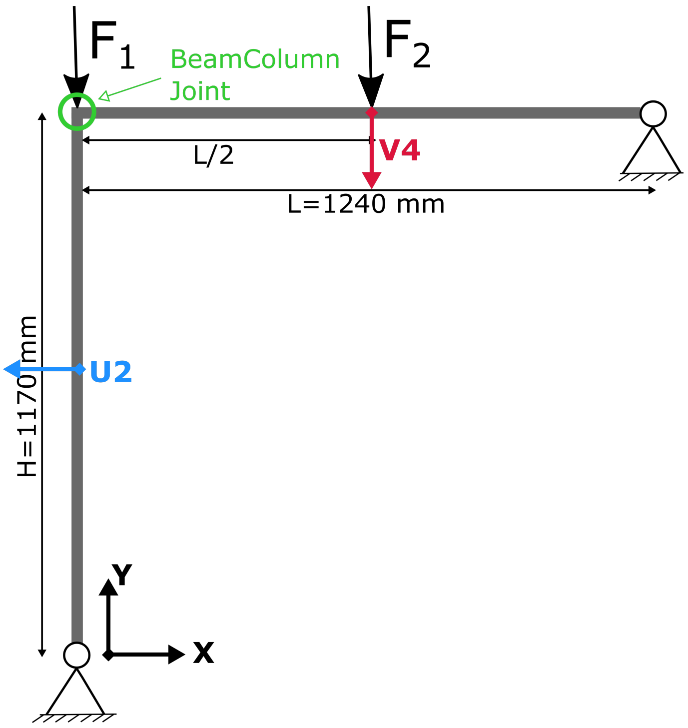

Figure 5.8: EHR3 frame configuration

Validation of the FE model was carried out by comparing the deformation vs. temperature history (deflection U2 and V4 as illustrated in Figure 5.8), predicted by the FE model with that from experimental results. The material model parameters in Table D.7 for the St37 carbon steel were used. A general good agreement can be observed for the results presented in Figure 5.9.

The predicted critical temperatures, defined as the maximum temperature anywhere on the frame at which deformations increased in an uncontrollable fashion and corresponding to the last converged solution from the FE simulation are also provided in Table 5.4. These compare very well with those reported from tests [6].

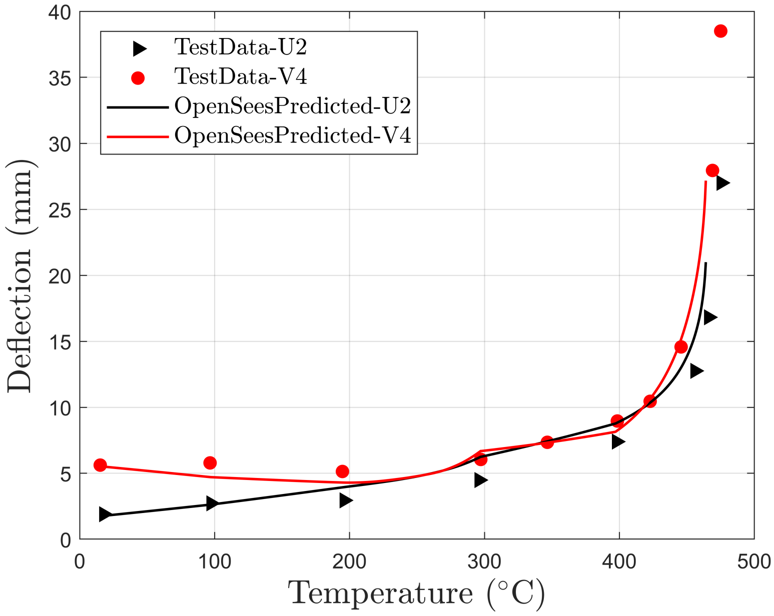

Figure 5.9: EHR3 frame deflection comparison

Table 5.4: Test parameters used in Validation

Type	L (mm)	H (mm)	σ_y (N/mm^2)	F1 (kN)	F2 (kN)	Critical Temp Tested (°C)	Critical Temp Predicted (°C)
EHR3	1240	1170	382	112	28	475	467

5.3.2.2 Comparison study

Using the validated FE model, the structural behaviour of stainless steel frames in fire was investigated and compared with that of EC 3 carbon steel frame. Similar to the comparison study of the simply supported beams, the carbon steel S235, Austenitic 1.4571 (group III) and Duplex 1.4162 (group II) have been adopted for this frame comparison study. The same material models used for the study of the simply supported beam in Section 5.3.1.2, namely Stainless01Thermal, Stainless02Thermal, SteelEC02Thermal were also adopted for this frame structure analysis. A Bauschinger ratio of 1.0 was adopted for all the steel material models.

Three series of load ratios (L.R.s) of the frames were investigated, as summarised in Table 5.5. The L.R. for the beam was calculated as the maximum bending moment applied on the beam to the plastic bending moment capacity of the beam at ambient temperature. The L.R. for the column was calculated as the maximum axial force on the column over the axial capacity of the column at ambient temperature.

Table 5.5: Comparison study series, EHR3 frame

Series No.	L.R. in Beam	L.R. in Column
1	0.15	0.075
2	0.30	0.15
3	0.60	0.30

Since there were no restraints at the beam-column joint, the beam could expand to the left whilst the column could expand upwards during heating. As a result, the V4 deflection of the beam moved upwards in the positive direction of the global Y axis in the beginning, whereas the U2 displacement of the column moved leftwards in the negative direction of the global X axis.

Figure 5.10 compares the midspan deflection results of the frame beam (V4) of the three series. During heating, the V4 increased initially as a result of the thermal expansion in the column. As the stiffness of the column reduced at increasing temperatures, a rapid drop in the V4 was observed, indicating the collapse of the column.

In the Series 1 to 3, the V4 of the Austenitic 1.4571 steel showed the highest upward movement since the austenitic stainless steel possesses the highest thermal elongation. In the Series 3, the upward behaviour was not observed in the V4 deflection of the Duplex 1.4162 steel, suggesting the duplex column was already in the plastic state when L.R. reached the value of 0.30.

The column collapse occurred at the highest temperature for the Austenitic 1.4571 frame, however the degree of this advantage diminished as the L.R. increased. When the column achieved L.R. =0.075, the Austenitic 1.4571 steel postponed the collapse by approximately 240 °C in comparison to the carbon steel. This value dropped to 180 °C when the column L.R. increased to 0.30.

With similar initial deflection (Duplex 1.4162 in the Series 1 compared with carbon steel and Austenitic 1.4571 in the Series 2; Series 2 Duplex 1.4162 compared with the other two materials in the Series 3), the frame collapse occurred at higher temperatures for the Duplex 1.4162 than for the carbon S235, but the temperatures were still lower than that of the Austenitic 1.4571 steel. Within each series, the same initial L.R.s were shared by the frame beams and columns of the three different steel materials. For the Series 1, the Duplex 1.4162 frame collapsed at a temperature about 10 °C higher than that of the carbon S235 and 210 °C lower than that of the Austenitic 1.4571 steel. For the Series 2 and 3, the Duplex 1.4162 frame collapsed at the lowest temperature among the three materials.

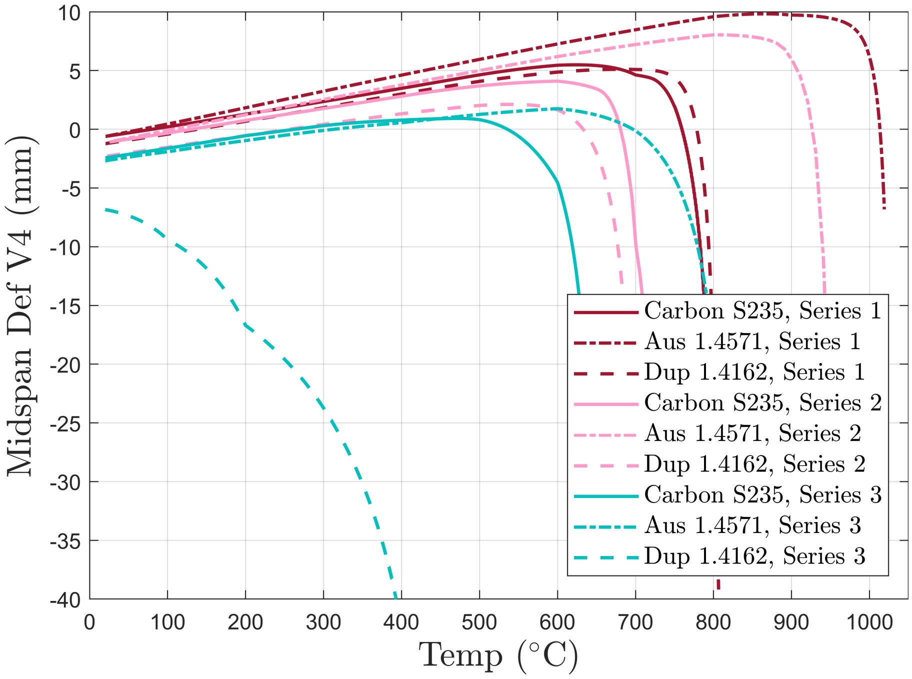

Figure 5.10: Beam midspan deflection V4

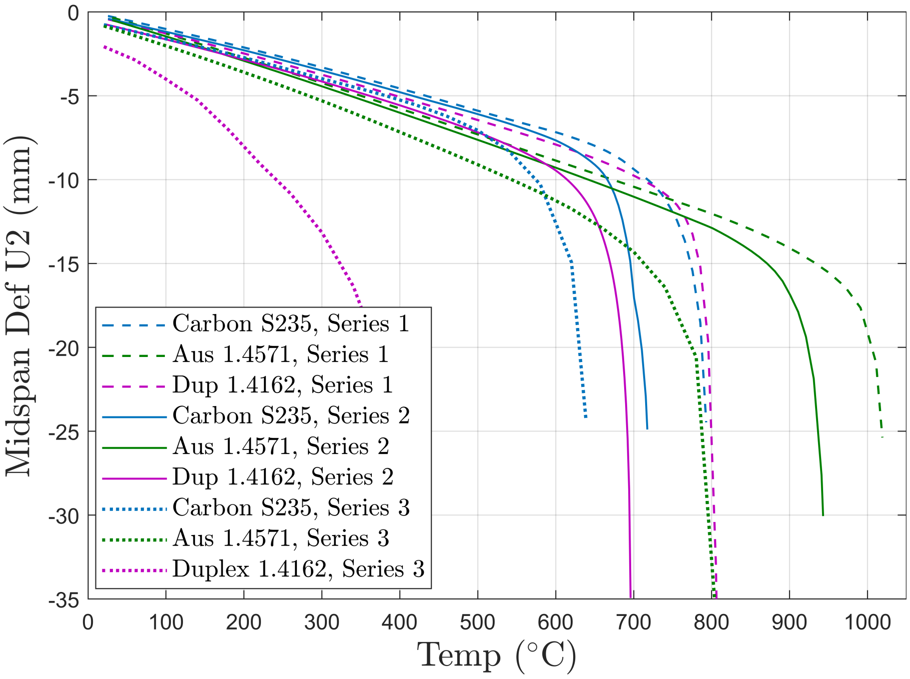

Figure 5.11: Column midspan deflection U2

The midspan deflection results of the frame column (U2) are plotted and compared in Figure 5.11. During heating, the U2 displayed a linear increase along the negative direction of the global X axis because of the beam expansion in that direction, until the large deflection mechanism occurred as a result of the column collapse.

The deflection results of the frame beam (V4) and the frame column (U2) showed a clear advantage of the Austenitic 1.4571 steel in delaying the collapse of the frame structure. For the duplex 1.4162, the superior behaviour when compared with the carbon steel was only evident in the Series 1. The degree of the advantage offered by the two stainless steel grades generally diminishes as the L.R. increases. As seen from the previous comparison study of simply supported beams, stainless steels enter the plastic domain at lower strains than carbon steel because of their shorter elasticity range. The results of the Series 3 showed that the Duplex 1.4162 frame rapidly developed into the collapse mode since the column, with an initial L.R.=0.30, was already in the plastic state at the start of the fire. The comparison results demonstrate that the initial plasticity of stainless steel columns are detrimental to the structural fire performance of stainless steel frames.

Figure 5.12 presents the stress strain development at the beam-column joint of the Series 1 during the heating, in the beam and in the column respectively. The imposed vertical and horizontal displacements due to temperature effects at the joint are inducing bending moments in the left extreme of the beam and in the upper cross-section of the column. Hence the stress at the bottom of the joint cross-section is in negative while at the top is in positive as seen in the figure. The stress strain results of the Series 1 (which is of the lowest L.R.s) showed that substantial plastic hardening was developed during the fire. The austenitic beam-column joint experienced the highest plastic hardening for this case. The strain reversals occurred at the lowest strain value for the duplex at the beam-column joint.

5.3.2.3 Effect of axial restraints

The EHR3 frame represents a single frame structure where the beam-column joint is free to move without any external axial restraints during fire. In reality, during a fire, there exist axial restraints on the beam-column joints provided by the surrounding cooler structure. The effect of external axial restraints are of particular research interest for stainless steel structural fire performance because stainless steels exhibit higher thermal elongations when compared to carbon steel, as seen in Figure 2.3.

In this section, the effect of external axial restraints on the structural fire behaviour of the frame column and beam was studied by applying varying degrees of axial restraints to them at the beam-column joint, as illustrated in Figure 5.13. The axial restraints were modelled using elastic spring elements. Three levels of axial restraints were investigated, which are $0.05K_\beta$, $0.15K_\beta$ and $0.30K_\beta$, where K_β is the axial stiffness of the structural component (frame column or beam) at the room temperature. The restraint stiffness was considered constant during the fire. The L.R.s of the Series 2 and 3 from the previous comparison study was selected for this parametric study. For the Series 2, the L.R. of beam =0.30 and L.R. of column =0.15; for the Series 3, the L.R. of beam =0.60 and L.R. of column =0.30.

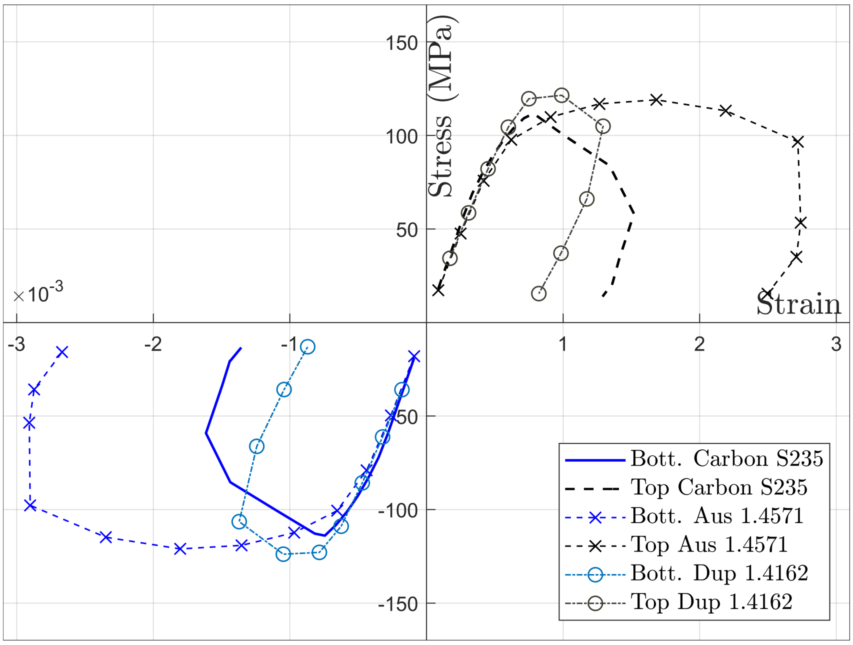

(a) Stress strain in the beam

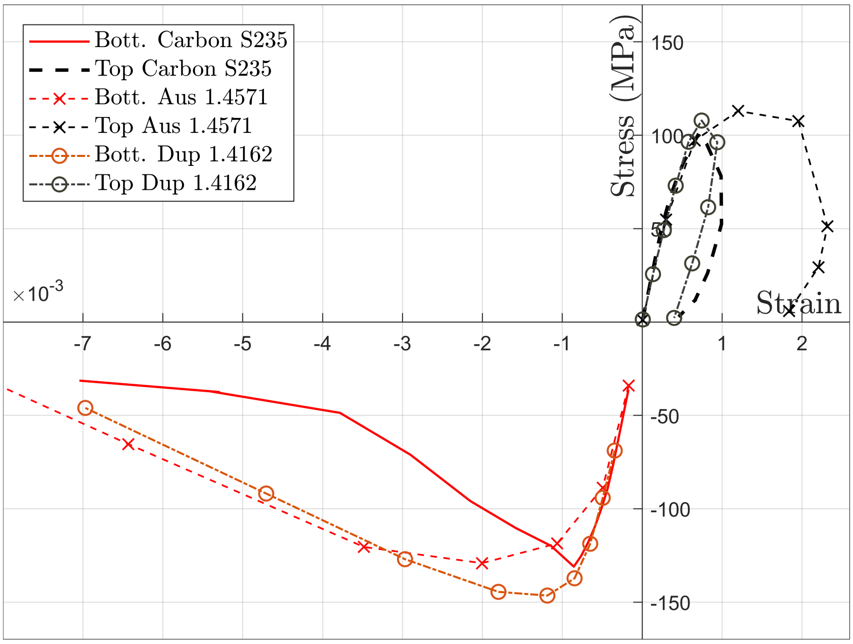

(b) Stress strain in the Column

Figure 5.12: Stress strain at the beam-column joint

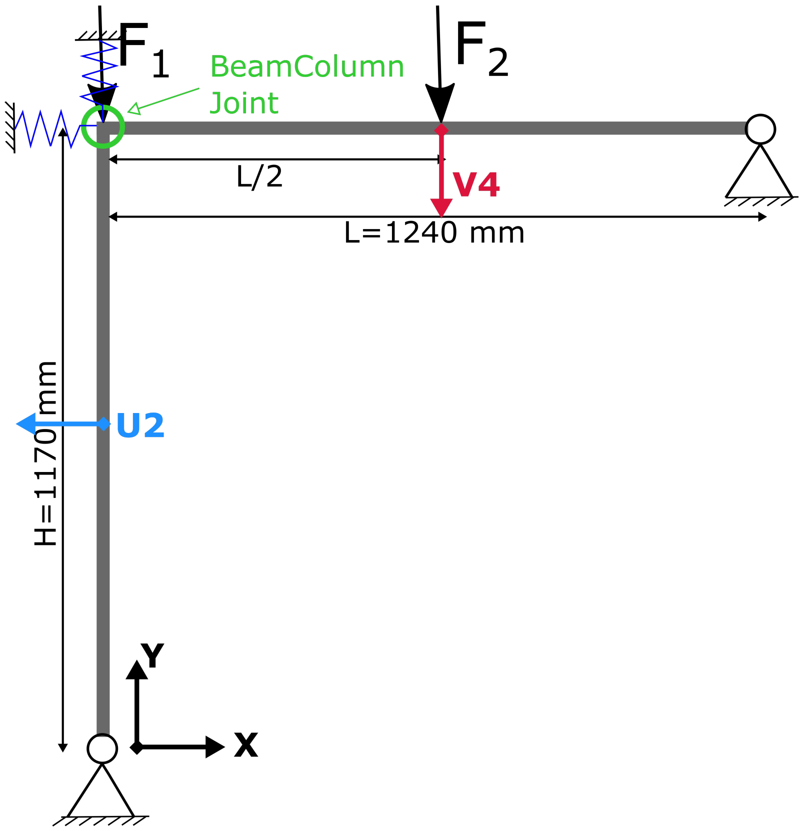

Figure 5.13: EHR3 frame with external axial restraints applied

Figure 5.14 compares the midspan deflection (V4) development of the frame beam (L.R.=0.30) without/with varying degrees of external restraints at the beam-column joint. It shows that as the restraint stiffness increases, the magnitude of the initial upward movement resulting from column expansion reduces. Also, the temperature at which the beam begins to displace downward lowers. When there were no external restraints ($k_\beta = 0.0$), the run-away mechanism was observed at around 910 °C for the austenitic steel beam, at about 700 °C for the carbon steel beam and at about 680 °C for the duplex steel beam. These temperature values correspond to the collapse temperatures of the columns (L.R.=0.15), as presented in Figure 5.15. The initiation of the column collapse is considered to coincide with the reversal of the direction of vertical displacement from positive to negative when plotted against temperature.

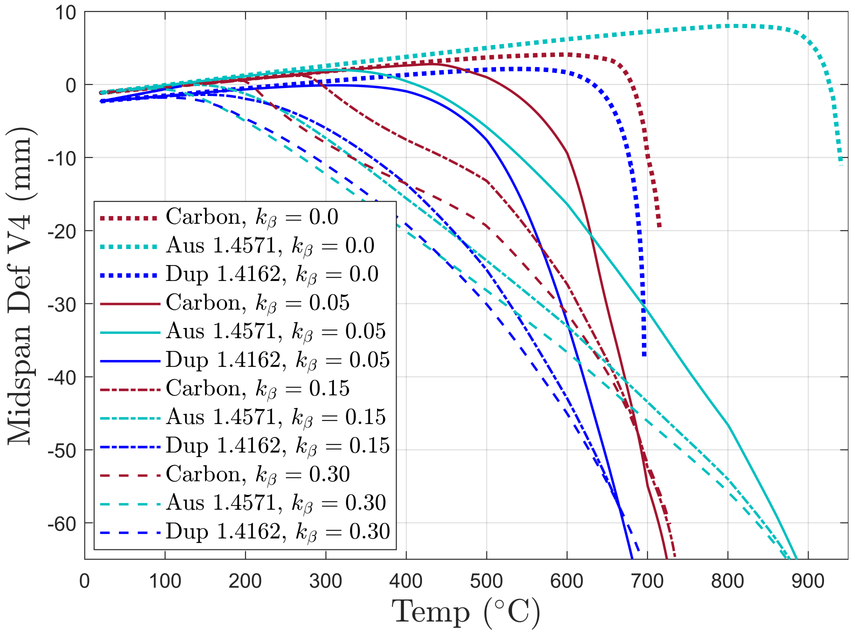

Figure 5.14: Beam midspan def (V4), Beam L.R.=0.30

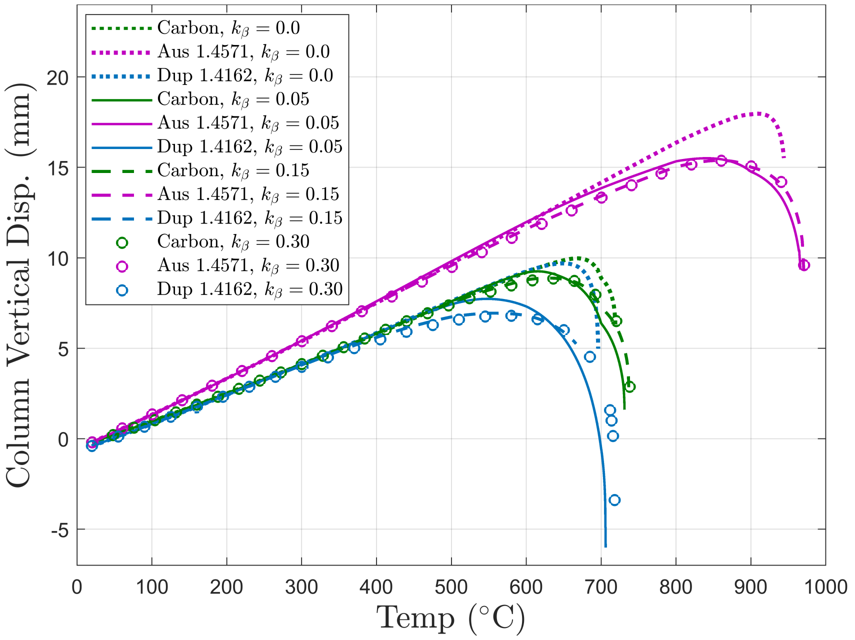

Figure 5.15: Column vertical disp, Column L.R.=0.15

Figure 5.15 shows that the introduction of external restraints of $k_\beta = 0.05$ decreases the collapse temperature of the columns: the turning point of the disp vs. temp curve of the austenitic stainless steel column reduced from around 910 °C to about 870 °C, from 680 °C to around 640 °C for the carbon steel and from 660 °C to around 560 °C for the duplex steel. This behaviour is expected as the restrained thermal expansion increases the load on the columns. The inclusion of external restraints also induces gradual development of V4 into the large displacement regime, in contrast to the abrupt run-away point observed in the unrestrained beams. Due to the external restraints, instead of running away, the beam goes into catenary action in the large displacement regime.

The increase of restraint stiffness level has little impact on the turning point of the column vertical disp vs. temp curve. The same behaviour is seen in the results of beam midspan deflection (V4), presented in Figure 5.14, as the beams of the same material with varying levels of restraint stiffness entered large deflection regime at similar temperatures. The three restrained austenitic steel beams reached a large deflection of 70 *mm* (L/18) at around 900 °C; the restrained carbon steel beams reached 60 *mm* (L/21) at about 720 °C and the restrained duplex steel beams reached 60 *mm* (L/21) at about 680 °C.

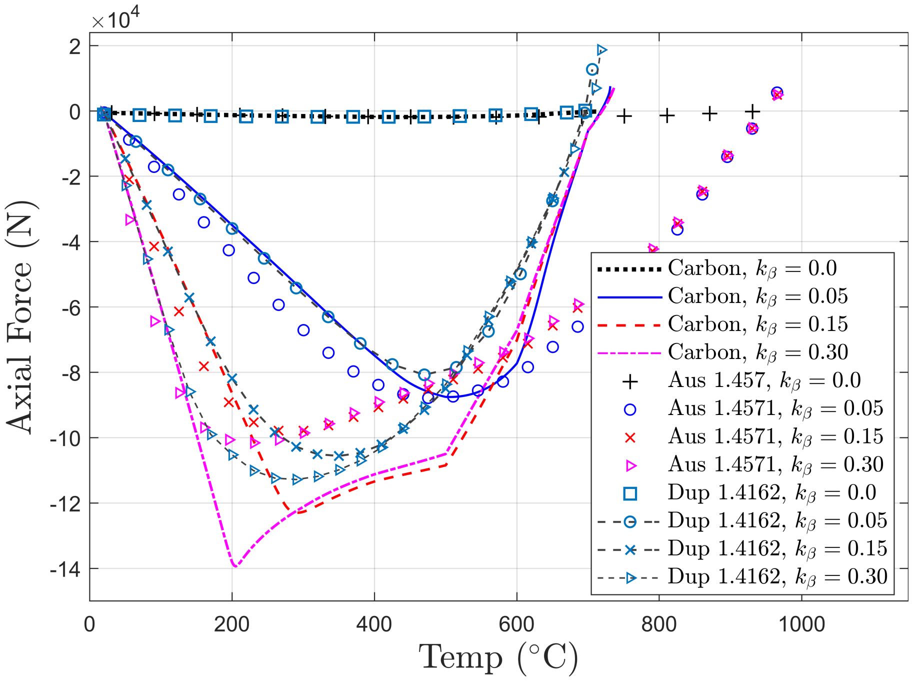

Figure 5.16: Beam axial force vs. temp., Beam L.R.=0.30

Figure 5.16 compares the axial force in the frame beam without/with varying degrees of axial restraints. The higher axial restraint stiffness is the higher the maximum compressive force will be. With the same degree of axial restraint stiffness, the compression resulted from the restrained thermal expansion increased at the fastest rate for the Austenitic 1.4571 beam due to its highest thermal elongation.

The maxima of the axial force vs. temp curve occurs when the beam cross-section reaches its axial capacity. At the stiffness level of $0.15K_\beta$ and $0.30K_\beta$, the carbon steel beam showed significantly higher maximum compression than the other two stainless steel beams, because the carbon steel beam possesses higher bending capacity in the lower temperature range. When compared with the stainless steels, carbon steel exhibits superior stiffness retention capability at temperatures lower than 200 °C, as seen in Figure 2.1.

The catenary action in the restrained beams starts as the axial force changes from negative to positive. This occurs at around 920 °C for the austenitic beams, about 720 °C for the carbon steel beams, and around 690 °C for the duplex beams. These values generally correspond to the temperature levels at which large deflection was observed in the beams as identified previously based on the V4 results plotted in Figure 5.14.

The displacement and axial force results suggest that the structural fire performance of the frames was dominated by the column behaviour. The catenary action in the frame beam occurred when the large deflection was induced because of thermal expansion against the restraints.

Figure 5.17 presents the midspan deflection (V4) of the beams under the L.R.=0.6 without/with varying degrees of external restraints. The corresponding vertical displacements of the columns under the L.R.=0.3 are plotted in Figure 5.18. Similar results to the Figure 5.14 and Figure 5.15 were observed.

As the K_β increased from 0.0 to 0.05, the collapse temperature for the restrained columns reduced from 780 °C to around 650 °C for the austenitic, from 620 °C to 520°C for the carbon steel, and from 390 °C to about 350 °C for the duplex stainless steel. The larger reduction in the collapse temperatures observed for the stainless steel columns are caused by the significant reduction in the tangent modulus at higher L.R.s.

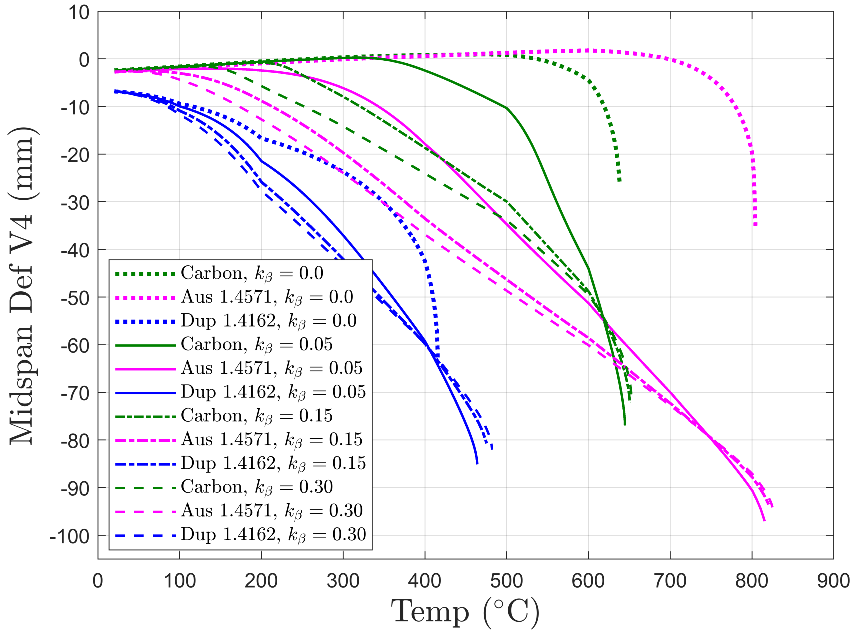

Figure 5.17: Beam midspan def vs. temp,
Beam L.R.=0.60

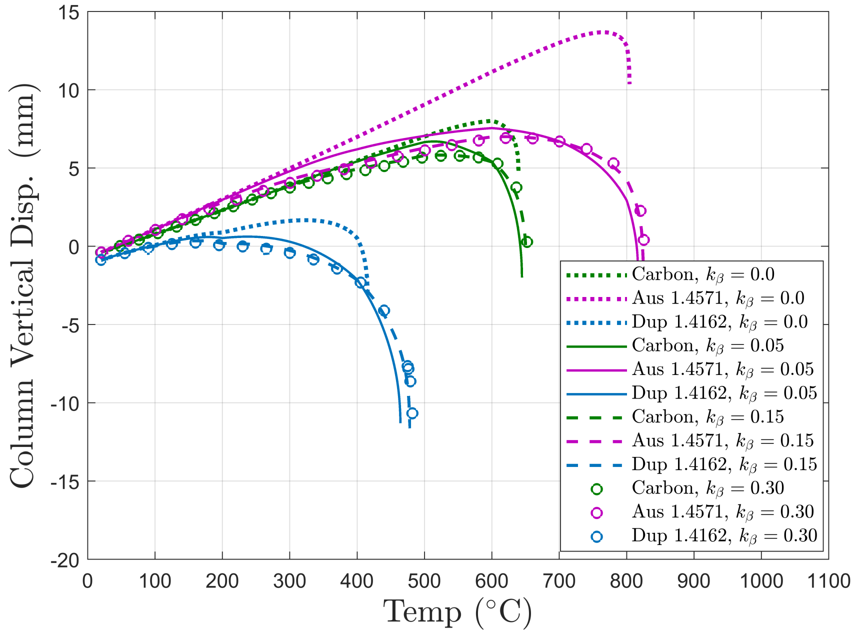

Figure 5.18: Column vertical disp vs. temp,
Column L.R.=0.30

Figure 5.19 presents the stress-strain developments at the beam-column joint during the fire , in the cross-section of the beam and the column respectively. An negative bending moment —bottom flange in compression while top flange in tension is observed in the beginning of the fire due to the $P-\delta$ effect of the initial beam deflection. During heating, compressive stresses developed across the entire cross-section, manifested as the tensile stress at the top shifted to the compressive side and the compressive stress at the bottom increased until the occurrence of the collapse. Higher peak stresses were observed for the case of $0.15K_\beta$ restraint when compared to the $0.05K_\beta$ restraint case.

Figure 5.19 show that the strain reversals were clearly experienced at the beam-column joint, in both beams and columns. This occurrence demonstrated that the strain reversals would occur with the presence of axial restraints within the structure.

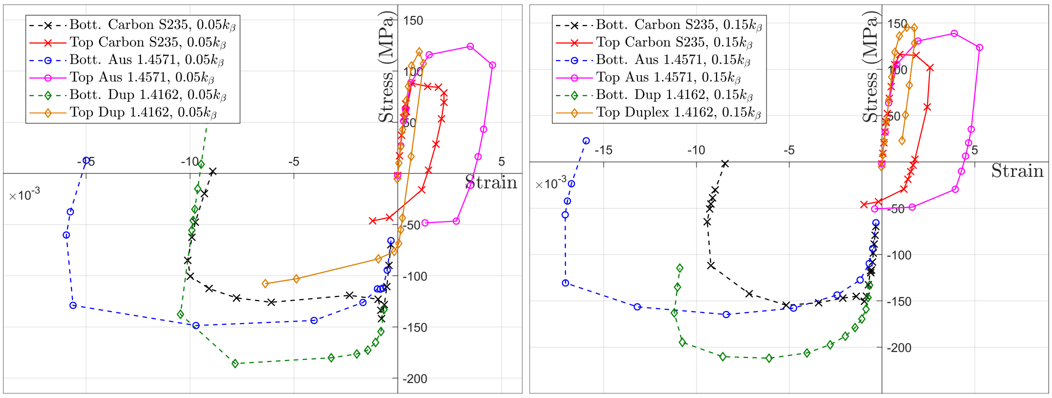

(a) Stress strain in the column, $0.05K_\beta$ **(b)** Stress strain in the column, $0.15K_\beta$

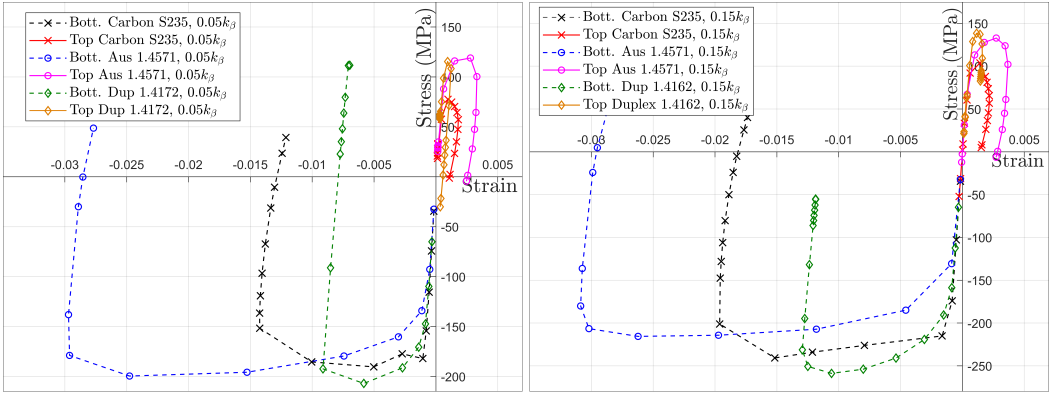

(c) Stress strain in the beam, $0.05K_\beta$ **(d)** Stress strain in the beam, $0.15K_\beta$

Figure 5.19: Stress strain developments at beam-column joint

The comparison study showed that for structural fire performance, the inclusion of external restraints is detrimental to the columns because it accelerates the initiation of the column collapse; meanwhile beneficial to the beams since it enables the catenary action. The stress redistributions due to the catenary action subsequently result in strain reversals in the structure. Increasing the stiffness level of restraints showed little impact on the column collapse temperature, however it induced higher stresses in the frame.

5.4 Conclusions

In this chapter, the new material model from Chapter 3 has been implemented in OpenSEES as uniaxial material models for the Austenitic 1.4571 and Duplex 1.4612 stainless steel in order to study their structural behaviour in fire.

The comparison study of temperature development between carbon steel and stainless steel I-sections subjected to four sides heating using the Standard Fire Curve [26], demonstrated a slower temperature rise for the stainless steel sections. For thin-walled structures, lower emissivity is the main beneficial factor that stainless steel offers. The comparison study results showed that sections with a smaller section factor (A/V) benefit more from using stainless steels in terms of achieving a slower temperature development.

The comparison study of simply supported beams suggest that the Austenitic 1.4571 stainless steel can generally postpone the onset of run-away mechanism in the beam to a temperature more than 200 °C higher than that of the carbon steel. At higher L.R.s (L.R.>0.75), the deflection rate of austenitic stainless steel beams are significantly faster than that of carbon steel beams due to the reduction in its tangent modulus, which can quickly reduce to about 50% of the material's initial value when stress approaches 50% of its strength capacity.

Similarly, the Duplex 1.4612 stainless steel showed the capability of delaying the run-away mechanism of the simply supported beams during the heating at lower L.R.. The Duplex 1.4612 steel experiences substantial reduction in the tangent modulus when L.R. exceeds 0.37, which accelerates the onset of run-away mechanism.

The comparison of EHR3 frames have shown that the Austenitic 1.4571 steel offers a clear advantage in delaying the occurrence of frame collapse, and the degree of advantage diminishes as the L.R. increases. The Duplex 1.4612 steel only showed benefits of postponing the collapse of the EHR3 frame in the Series 1 study where the L.R. is 0.15 in the beam and 0.075 in the column. The advantage offered by the Duplex 1.4612 steel is believed probably uneconomic because of the low level of L.R.s that has to be maintained.

The comparison study results show that the introduction of axial restraints at the beam-column joint of the EHR3 frame causes earlier column collapse, where the stainless steels suffer greater reduction in the collapse temperature when compared to the carbon steel.

The study showed that evident strain reversals were experienced in the frame beam and column when external restraints were included. The catenary action is beneficial for structural fire performance of frames. However the strain reversals experienced during the catenary action can cause reduction in the material tensile strength due to the Bauschinger effect. Future investigation of the Bauschinger effect on the structural behaviour of steel structures in fire using the new material model is of great research interest.

Chapter 6

Bauschinger Effect in Steel Beams Subjected to Realistic Building Fire

6.1 Introduction

One prominent feature of modern architectural design is its pursuit of large open-plan space where sufficient ventilation inevitably turns fire growth into a fuel-controlled regime. Consequently, the likelihood of an early flash-over phenomenon of a ventilation-controlled fire that is commonly observed in traditional building fires, has been substantially reduced. It has been observed in real life fire events, for instance in the World Trade Centre Towers [201] and in the Windsor Tower in Madrid [202], that fires in large compartments/open spaces, burn locally and have the tendency to move across the entire floor over a period of time. The concept of a travelling fire model [10–12,58,203] has been introduced to describe the movement and spreading behaviour of fires observed in large and/or complex spaces, where traditional concepts of compartment fire behaviour becomes inappropriate. The "travelling nature" of fire has been of growing research interest to fire scientists and engineers. Recently in 2017, a joint research project TRAFIR (characterisation of travelling fires in large compartments), in collaboration with ArcelorMittal Belval & Differdange, Liege University, the University of Edinburgh, RISE Research Institute of Sweden and the University of Ulster, has set out to investigate what are the conditions that cause the development of a travelling fire. The TRAFIR project focuses on studying the influence of compartment geometry and the interaction with representative fuel loads through fire tests and CFD simulation using the FDS software. While, the research has focused on better understanding fire demand estimation, the mechanical response of composite steel structures under travelling fire scenarios has been little explored [13]. Using FEA, Rackauskaite et al. [204] investigated the structural response a 2D steel frame subjected to multiple floor horizontal and vertical travelling fire load computed using the Stern-Gottfried & Rein's travelling fire model [10, 11], where significantly different structural behaviour compared to a single compartment fire was observed.

Various travelling fire models [10–12, 58, 203] have been proposed to describe the moving behaviour of a fire commonly observed in a large open compartment space, where the Standard Fire Curve [9] is no longer applicable. In this chapter, the recently proposed travelling fire model — extended travelling fire methodology (ETFM) framework [12] was adopted to obtain the structural thermal loading. The ETFM enables temperature development in a realistic large and/or complex compartment space, capturing both spatial and temporal changes of the thermal field, based on energy and mass conservation with smoke accumulation. With the ETFM framework implemented in the SIFBuilder [205] of OpenSEES software [24], the OpenSEES framework provides the facility to perform a streamlined heat transfer and thermo-mechanical analysis for large structures in one software environment.

In this chapter, a case study was carried out to investigate the structural fire performance of a single steel beam (UB 305x127x42) located in an idealised structural layout, shown in Figure 6.1a, representing a 630 m^2 floor area of a generic modern office building with a central core structure of 162 m^2. The structural behaviour of the beam subjected to complex travelling fire loadings was investigated using the new material model developed by Zhou et al. [192], also presented in Chapter 3.

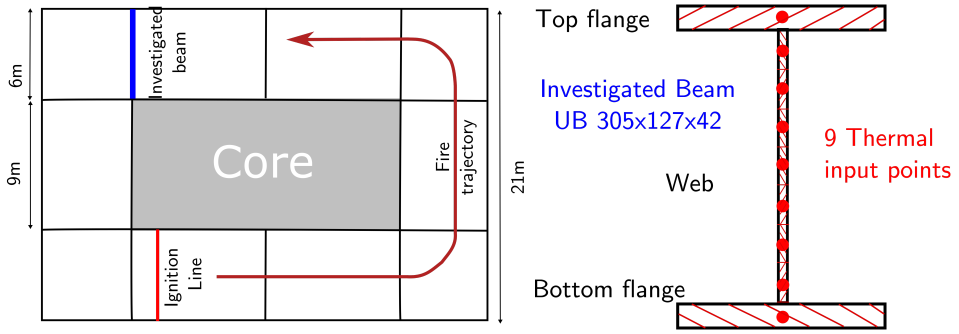

(a) Case study structural plan view with predefined travelling fire trajectory

(b) Schematic view of the investigated beam cross-section

Figure 6.1: Structural model geometries

In Section 6.3, the steel beam is investigated in Abaqus, modelled using shell elements and the proposed multi-axial material model, implemented in Abaqus Umat subroutine. The structural behaviour, predicted using the proposed material model, is also compared with that using the Abaqus FEA software with the isotropic hardening material model only.

In Section 6.4, the structural behaviour of the steel beam is studied in OpenSEES, using the Euler-Bernoulli beam theory based “DispBeamColumn2DThermal” element, and the uniaxial material model “SteelEC02Thermal” which is a one-dimensional plasticity model developed from the new material model, as presented in Chapter 3.

For both the 3D and the 2D analysis, the EC3 [1] stress-strain curves of carbon steel at elevated temperatures were adopted. The temperature-dependent thermal expansion coefficients (α) were defined in accordance with EC 3 [1]. A Poisson’s ratio of 0.3 was adopted for all temperatures. The Bauschinger ratio evolution function determined for the carbon steel material from Section 3.5 has been applied for this study. A static thermo-mechanical analysis was performed for both the 3D and 2D thermo-mechanical analysis.

6.2 Thermal loading

A series of parametric studies have been conducted by Dai et al. [13] to investigate the temperature development within the cross-section of the investigated beam subjected to travelling fire following the defined trajectory. Various combinations of the fire spread rate, v (mm/s) and the characteristic fuel load density, $q_{f,k}$ (MJ/m^2) were studied. During the heat transfer analysis, Dai et al. [13] considered the beam was exposed from three sides with top flange being shielded by the floor slab. Hence they adopted the heat transfer coefficients of convection and radiation associated with the ambient temperature as the boundary condition for the top flange surface.

Two temperature history results from [13] were selected for the study, Case 1 ($v = 1.6$ mm/s; $q_{f,k} = 780$ MJ/m^2), representing a slow but dense fire; Case 2 ($v = 10.0$ mm/s; $q_{f,k} = 100$ MJ/m^2), representing a rapid but light fire. Figure 6.2a presents the temperature history of Case 1, a nearly uniform cross-sectional temperature development is observed and the maximum temperature reached was about 700 °C. A more complex cross-sectional temperature distribution history is observed in Case 2, as shown in Figure 6.2b, where different cooling rates were experienced at the bottom, middle and top of the cross-section, giving rise to the thermal gradient reversal phenomenon i.e., the change of sign in the thermal gradient ratio. The thermal gradient ratio was computed as the temperature ratio between the mid-web and the bottom flange, and between the mid-web and the top flange respectively. A lower maximum temperature of 580 °C was reached in the Case 2.

For better understanding the structural implications of a complex thermal loading encompassing varying stages of heating and cooling; cross-sectional thermal gradients as well as reverse thermal gradients, the case study hence focused on examining the structural behaviour of the single steel beam with the composite stiffness contribution from the slab not considered.

6.3 Numerical analysis in 3D

6.3.1 FE model

A finite element model of the steel beam (UB305x127x42) was built in Abaqus/CAE, as shown in Figure 6.3. The UB consists a bottom and top flange plate of 6000 *mm* x 124.3 *mm* x 12.1 *mm* and a web plate of 6000 *mm* x 282.4 *mm* x 8 *mm*. The element type of shell S4 was selected. The transverse shear stiffness (K) of the shell section had to be defined when using the Umat subroutine and it was

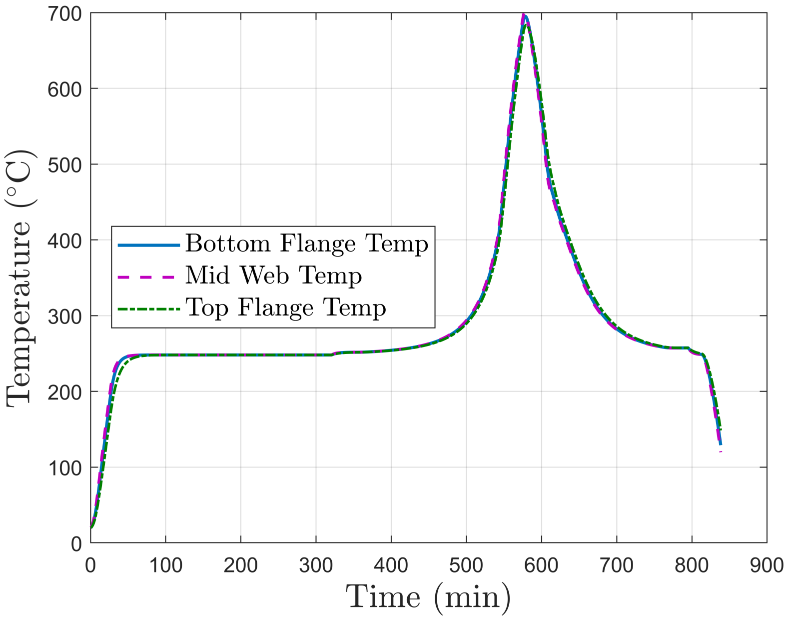

(a) Case 1

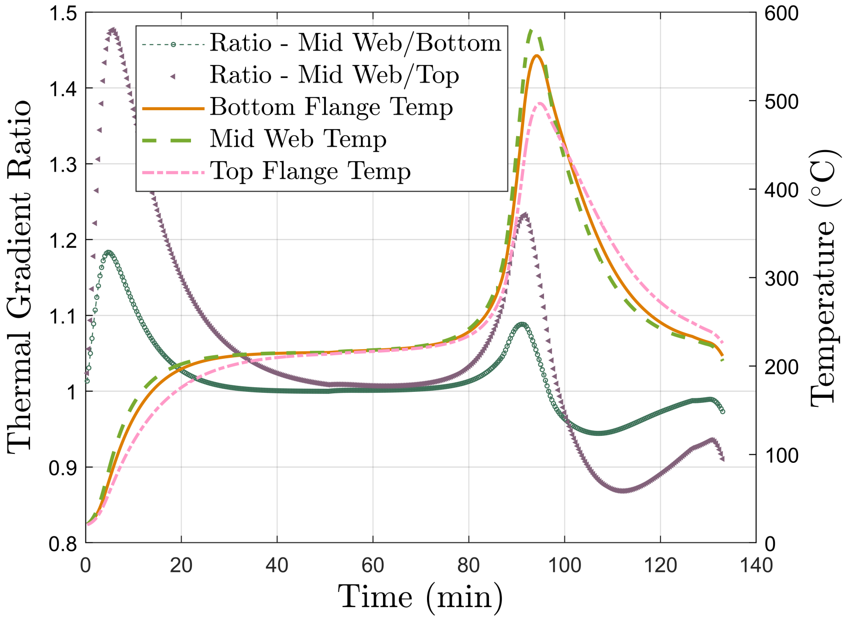

(b) Case 2

Figure 6.2: Temperature history

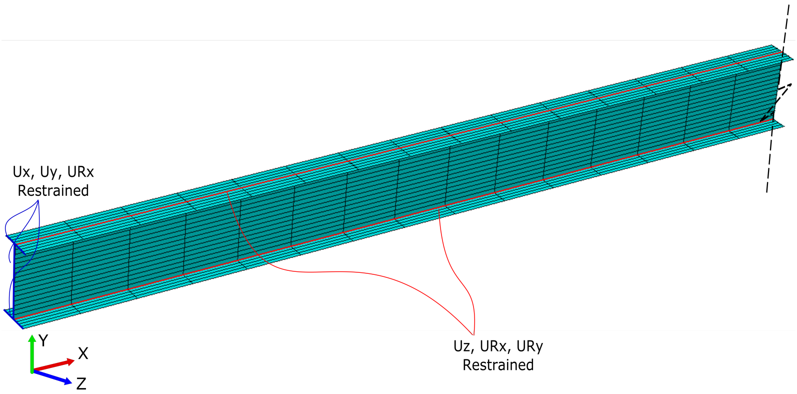

Figure 6.3: Single steel beam modelled, half of the model length shown

determined using Equation 6.1 as recommended by the Abaqus Analysis User's manual [206]:

$$K_{11} = \frac{5}{6}G_{13}t; \qquad K_{22} = \frac{5}{6}G_{23}t; \qquad K_{12} = 0.0 \tag{6.1}$$

Where G_{13} and G_{23} are the material's shear moduli in the out-of-plane direction and t is the thickness of the shell.

The translational and rotational restraints at both ends of the beam were realised by constraining the horizontal (U1), the vertical (U2) displacement, and the torsion (UR1) on the nodes at the ends of the beam. The out-of-plane failure of the beam was prevented by restraining the bending about the global Y axis (UR2) and the out-plane-displacement (U3) on the intersection nodes between the web and the flange as highlighted in red in Figure 6.3. A mesh with 8 elements for the flanges, 16 elements for the web and 30 elements along the length was adopted based on a sensitivity analysis.

An initial vertical perturbation of 6 mm $(L/1000)$ was introduced by imposing a point load at the midspan of the beam, representing the initial displacement of the structural component. The point load was applied to the model by means of nodal forces at the midspan cross-section to prevent local instabilities due to load application.

The temperature time histories at 9 thermal points across the I-section obtained using the ETFM in [13] were adopted as the thermal loading for the model. The thermal loading of each point was applied to its corresponding area of the cross-section, as depicted as the hatched area in Figure 6.1b.

6.3.2 Stress/Deformation analysis —Case 1

The evolution of the deflection and the accumulated plastic strain at the midspan cross-section during the fire are presented in Figure 6.4a. The deflection started to increase at around 100 °C, corresponding to the initiation temperature of the elastic modulus degradation. The slight kink observed at around 250 °C was believed to be caused by the small thermal gradient experienced in the temperature history. At around 550 °C a distinctive change in the curvature of the temperature deflection curve was observed, indicating large deflection mode has occurred. The beam has become too weak to support the load as a result of material degradation. During the cooling stage, the midspan deflection experienced a recovery as the steel material regained its stiffness. The development of accumulated plastic strain ($\overline{\varepsilon^p}$) correlated to that of the deflection during the heating stage. While under cooling, the $\overline{\varepsilon^p}$ still experienced growth due to the continuous stress development.

The development of the axial stress (S11) at midspan during the fire is plotted in Figure 6.4b. At the start of the fire, the section is in sagging bending moment —the bottom cross-section in positive S11 while the top in negative S11. As temperature rises, compressive stresses started to develop due to restrained thermal expansion, manifested as the growth of compressive S11 until the whole cross-section (bottom, mid and top) descended into compression at around 90 °C. Thereafter, due to the increasing midspan deflection as observed in Figure 6.4a, thermal expansion induced compression started to exert bending in the beam hence the S11 at the bottom of the cross-section started shifting to tension. This is the P-delta effect of the axial force. Furthermore, the difference of S11 between the top and the bottom started to increase, indicating an increasing bending moment.

The plastic state was first observed at the top half of the cross-section at around 120 °C, when the mid and top S11 plateaued at its yield strength value. At around 300 °C, the entire midspan cross-section has reached the plastic state, indicating the formation of a plastic hinge. Under heating, the tensile and compressive stresses

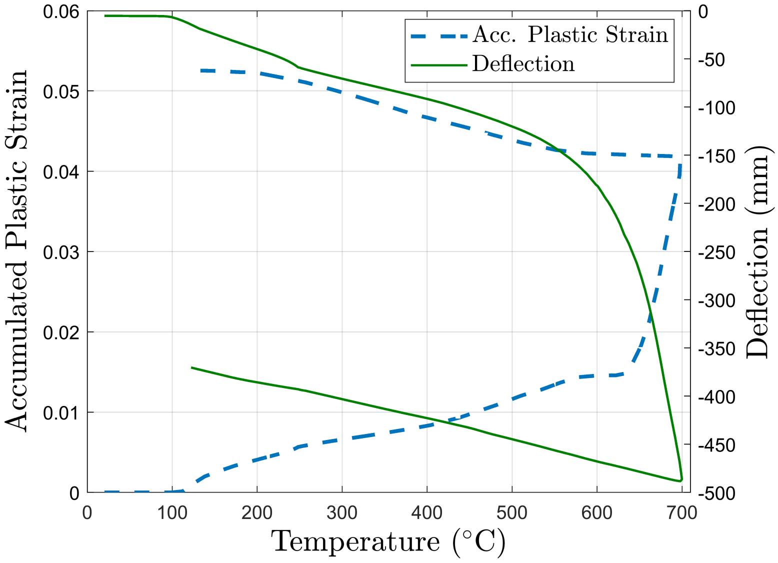

(a) Deflection, $\overline{\varepsilon^p}$ vs. temp

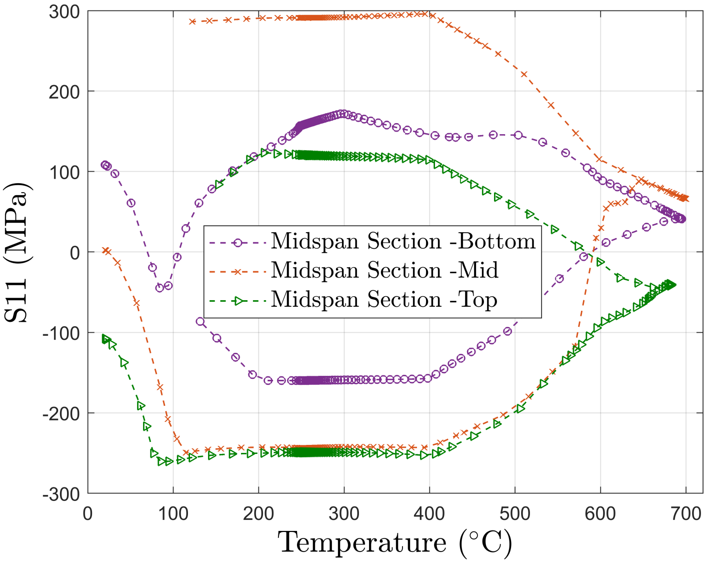

(b) Axial stress (S11) vs. temp

Figure 6.4: Midspan cross-section results, Case 1

started to decrease at 400 °C due to the reduction in the yield strength of the steel material. During cooling, the bending moment at the midspan cross reversed from sagging to hogging —negative S11 at the bottom while positive at the top.

The modelled structure behaved as expected under the Case 1 thermal loading. The analysis results showed that the plastic deformation due to heating and cooling has been successfully captured.

6.3.3 Stress/Deformation analysis —Case 2

Figure 6.5a presents the evolution of the deflection and the accumulated plastic strain ($\overline{\varepsilon^p}$) at the midspan cross-section throughout the fire. The deflection also started to increase at around 100 °C. The growth of deflection developed at a faster rate when compared to the Case 1 as a result of the thermal bowing —the hotter surface expands more than the cooler surface inducing the bending in the structure, caused by the cross-sectional thermal gradient. At around 550 °C the curvature of the temperature deflection curve started to increase significantly indicating substantial stiffness reduction in the beam due to the material degradation. The midspan deflection showed a recovery as the steel material regained its stiffness during cooling. The $\overline{\varepsilon^p}$ grew throughout the heating and cooling as a result of continuous stress development.

The axial stress (S11) vs. temperature curves at midspan cross-section during the fire are plotted in the Figure 6.5b. Similar S11 developments to the Case 1 have been observed for the Case 2. The main difference is the entire midspan cross-section remained in tension at the end of fire. It is interesting to note that the bottom S11 did not show yielding until later during the cooling. This suggests that the midspan cross-section did not reach the plastic state until much later at the cooling stage, in contrast to what observed for the Case 1 where it became plastic at as early as 300 °C.

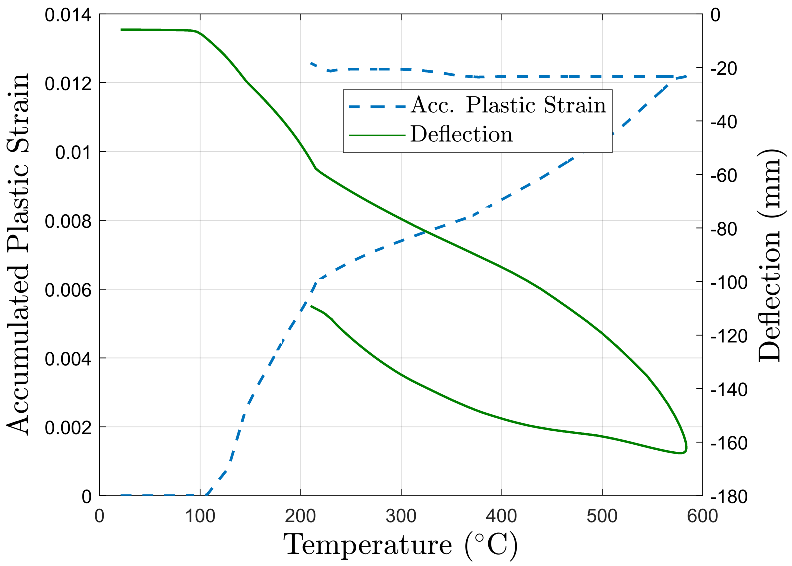

(a) Deflection, $\overline{\varepsilon^p}$ vs. temp

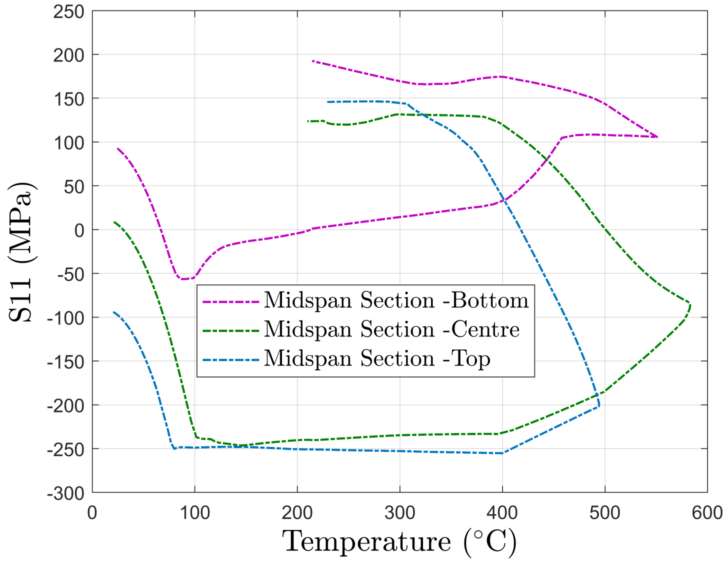

(b) Axial stress (S11) vs. temp

Figure 6.5: Midspan cross-section results, Case 2

6.3.4 Comparison study

A comparison study between the proposed material model and the Abaqus isotropic hardening model was performed. Figure 6.6 compares the stress development during the fire at the end and at the midspan cross-section produced using the two material models respectively.

Identical monotonic stress increase and evident stress reversals were observed.

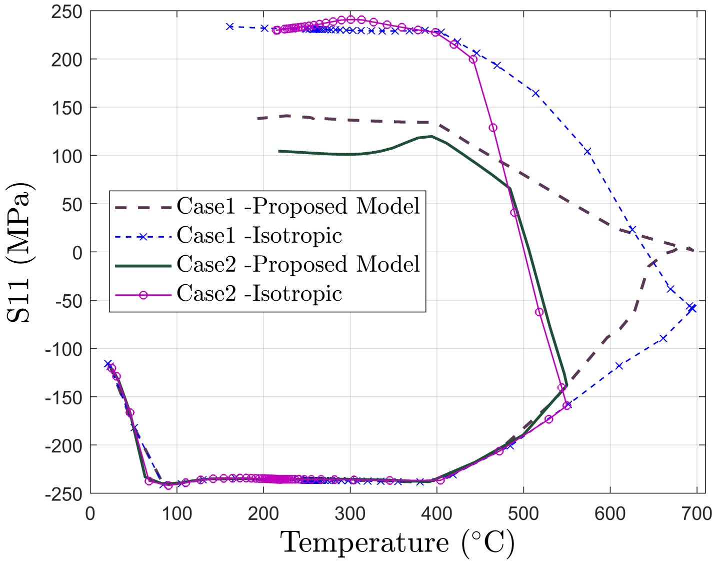

(a) Endspan S11 vs. Temp

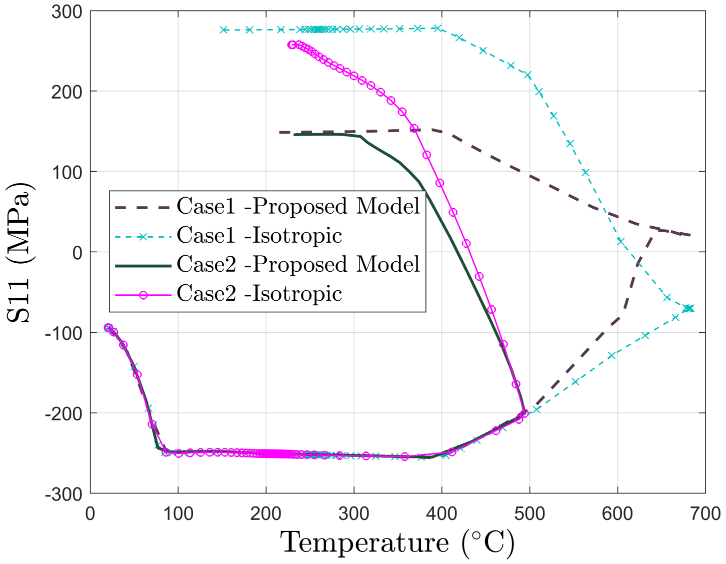

(b) Midspan S11 vs. Temp

Figure 6.6: Proposed material model vs. Isotropic hardening model

The key difference was the yielding during the reversal, where a lower yield stress was observed in the results of the proposed material model. Thus the reduction in the tensile strength due to the Bauschinger effect has been successfully captured by the new model. Therefore, in cases where strain reversals exist, more accurate evaluation of structural fire capacity can be achieved by adopting the new material model proposed in Chapter 3.

6.4 Numerical analysis in 2D

The FE model of the investigated beam was also analysed in OpenSEES using the 2D BeamColumnElement. The composite stiffness contribution from the slab was not included in this model. The beam was translationally and rotationally restrained at both ends. The I-section was modelled using the fibre element [207], where the cross-section was subdivided into fibres. The study model adopted 8 fibres along the web, and 8 fibres along the flange. A mesh of 30 elements along the length was adopted after performing a sensitivity study. The thermal loading was applied at 9 thermal points along the I-section, seen as in Figure 6.1b. Linear interpolation was used to compute the thermal loading on the section fibres that are between the application points.

Similarly to the 3D model, an initial vertical perturbation of 6 mm (L/1000) was introduced by imposing a point load at the midspan, representing the initial displacement of the structural component.

6.4.1 Stress deformation analysis

The evolution of the midspan deflection during the Case 1 and Case 2 fire are presented in Figure 6.7, and compared with that of the 3D analysis results. For the Case 1, similar deflection development to that of the 3D analysis was observed in the 2D results until the deflection reached around 180 *mm* (L/33). Thereafter, the deflection developed at a slower rate in the 2D model and reached a significant lower maximum deflection when compared to the 3D model. This is believed to be due to the fact that the 2D beam model is stiffer because of the adoption of 2D Euler-Bernoulli BeamColumn element, which disregards the shear deformation. When the beam enters the large deflection regime, the shear deformation becomes significant in the 3D shell model.

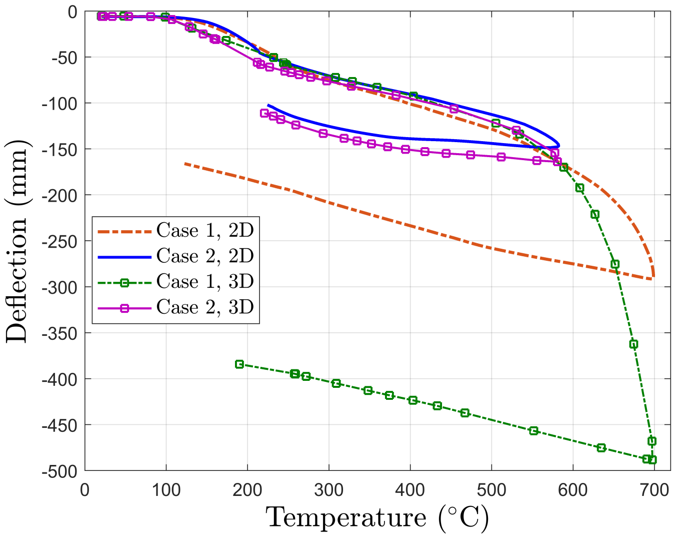

Figure 6.7: Midspan deflection, 2D compared with 3D

Because of the lower maximum temperature in the Case 2, lower maximum midspan deflections were observed in comparison to that of the Case 1. The maximum midspan deflection obtained is 164.1 *mm* (L/36) for the 3D model and 148.8 *mm* (L/40) for the 2D model, both are lower than the L/33 observed in the Case 1. This suggested that the deflections in the Case 2 fire did not develop into the large deflection regime. Therefore the deflection vs. temperature curve predicted by the 2D model is very similar to that by the 3D shell model in this case. The 2D analysis results show an overall lower deflection because of the stiffer Euler-Bernoulli beam element adopted.

Significant shear deflections could be expected in deep carbon steel members under temperatures higher than 550 °C as the stiffness decreases very rapidly beyond this value (from about 40% at 550 °C to about 10% at 700 °C). Since the maximum temperature experienced in the Case 2 was about 580 °C, the shear deflection was still insignificant hence the 2D model could produce similar results to the 3D model. In contrast, the higher maximum temperature of 700 °C in the Case 1 led to notable shear deflection in the beam which was been able to be captured by the 3D shell model but not the 2D Euler-Bernoulli beam model, as seen in Figure

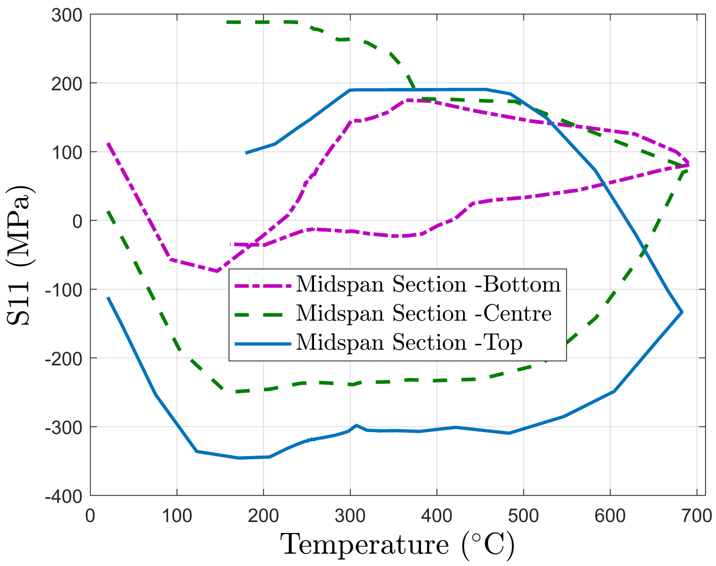

(a) Case 1

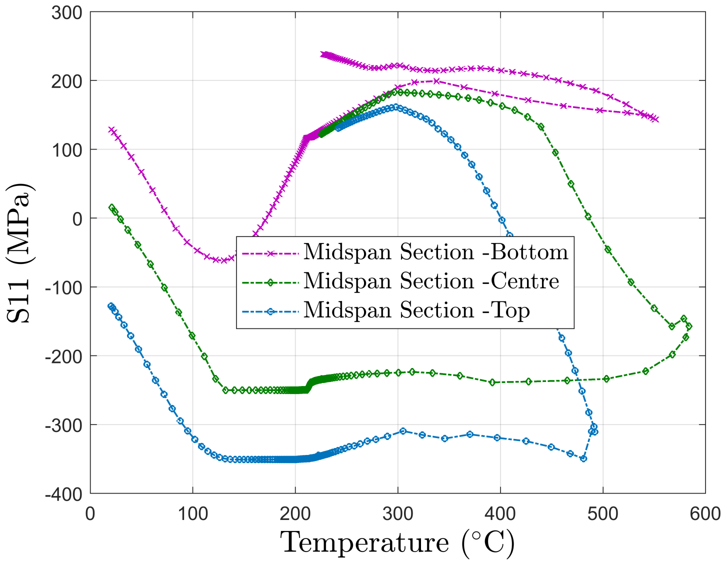

(b) Case 2

Figure 6.8: Midspan S11 vs. Temperature, 2D

6.7.

The 2D analysis results of the axial stress (S11) vs. temperature curves at midspan cross-section during the fire of Case 1 and Case 2 are plotted in Figure 6.8. Similar results to the 3D model have been observed. At the end of Case 1 fire, the bending moment at the midspan cross reversed from sagging to hogging —negative S11 at bottom while positive at top. While the midspan cross-section ended in tension for the Case 2 fire.

The deflection and stress results showed that the steel beam modelled using 2D BeamColumn element in OpenSEES behaved as expected under the thermal loading, the plastic deformation due to heating and cooling has been successfully captured using the new material model.

6.5 Summary

In this chapter, the new material model proposed in Chapter 3 was utilised to investigate the structural behaviour of a single steel beam subjected to travelling fires. The proposed material model in multi-axial state was used to study the steel beam modelled using shell elements in Abaqus, while the proposed material model in uniaxial state was used for the 2D beam analysis conducted in OpenSEES. Reasonable and comparable results of deformation and stress have been observed for the 3D and 2D analysis.

The comparsion study between the proposed material model and the isotropic hardening model from Abqus demonstrated that the reduction in the structural capacity due to the Bauschinger effect has been successfully captured by the new model.

Therefore it is believed that the proposed material model has been successfully implemented in the Abaqus Umat subroutine and in the OpenSEES uniaxial material model and was able to analyse the structural behaviour of steel structures under complex realistic building fires.

Chapter 7

Conclusions and Future Work

7.1 Summary and conclusions

A new rate-independent combined isotropic-kinematic hardening material model was developed for the thermo-mechanical analysis of steel materials in fire. In order to demonstrate the different aspects of its capability under various loading conditions, five validations, as presented in Chapter 3, have been carried out:

1. Validation of the evolution of isotropic and kinematic hardening variables during monotonic loading at elevated temperatures.

2. Validation of the Bauschinger effect and the transient hardening under isothermal loading conditions at elevated temperatures.

3. Validation of the thermal unloading algorithm.

4. Validation for multi-axial loading conditions at elevated temperatures.

5. Validation of the Bauschinger effect and the transient hardening under transient loading conditions during both heating and cooling.

The validations demonstrated that the new material model is capable of: handling strain reversals, capturing the Bauschinger effect and transient hardening behaviour and modelling material non-linearity at elevated temperatures. As such, the three objectives that were identified in the Introduction (Chapter 1) have been successfully accomplished by the proposed material model.

The goal of the proposed material model was to improve the FEA tools for performance-based structural fire design. More accurate determination of structural fire resistance can be achieved by adopting the new material model, with the reduction in the material strength due to strain reversals being properly calculated. In this research, the new material model proposed in Chapter 3 was applied in three different studies, each has provided valuable engineering insights into the behaviour of steel structural systems subjected to fire. Additionally, the model's capability of describing steel material behaviour for thermo-mechanical analysis, its applicability in structural fire analysis and its integrability into the performance-based engineering framework have been demonstrated through the studies.

7.1.1 Application to remaining structural fire resistance

The application of the new material model in a multi-hazard analysis, fire following earthquake, was showcased in Chapter 4. Rather than investigating the structural behaviour in a fire immediately following a severe earthquake, which is a loading scenario commonly considered to be of low likelihood, Chapter 4 focused on the reduction in the fire resistance of steel structures resulting from undetected PFP damage, which is a serious fire safety concern that has been largely neglected. Being specifically designed to be lightweight, cementitious PFP is prone to damage under deformation even caused by moderate earthquakes. Higher likelihood of this fire safety concern is expected for the cementitious PFP that experienced multiple small/moderate earthquakes during its service.

Chapter 4 implemented the new material model in a novel multi-hazard framework for evaluating the remaining fire resistance of steel structures protected by cementitious PFP, subjected to moderate earthquakes. A case study carried out using the proposed framework found that post-earthquake PFP damage could result in significant reductions in the structural fire resistance, which, in the worst case scenario, may lead to structural collapse due to column failure, reducing the fire resistance from the designed 2 hrs to about 36 mins.

The proposed multi-hazard framework is implemented in the OpenSEES environment, and offers structural engineers a practical solution to access the fire safety concern associated with the PFP damage. A step-by-step procedure of using the multi-hazard framework is provided at the end of Chapter 4.

7.1.2 Application for novel construction materials

A comprehensive understanding of the fire performance of structures using novel construction materials can be obtained economically and efficiently by utilising the computational based engineering framework. However, the accuracy of FEA-based study is strongly depended on the material model adopted. With its sophistication demonstrated in Chapter 3, Chapter 5 used the new material model to investigate the structural fire behaviour of stainless steel structures. The stainless steel grade Austenitic 1.4571 and Duplex 1.4612 were studied in comparison to the carbon steel S235.

The investigation of simply supported beams showed that the Austenitic 1.4571 stainless steel can generally postpone the onset of the run-away mechanism in the beam to a temperature more than 200 °C higher than that of the carbon steel. The Duplex 1.4612 stainless steel only showed limited advantage over the carbon steel in terms of delaying the run-away when its L.R. is low (<0.37). The investigation of EHR3 frames showed that the Austenitic 1.4571 steel offers a clear advantage in delaying the occurrence of frame collapse, although the degree of advantage diminishes as the L.R. increases. The Duplex 1.4612 steel only showed benefits of postponing the frame collapse in the case where the frame beam L.R. $=0.15$ and the frame column L.R. $=0.075$. The high thermal expansion of stainless steels accelerates the displacement development of the structural components when external restrains are applied.

The investigations carried out in Chapter 5 showed that Austenitic 1.4571 stainless steel in general offers superior structural fire performance when compared to the carbon steel, while the advantage offered by the Duplex 1.4612 steel is believed overall uneconomic because of the low L.R.s that have to be maintained. Additionally, the comparison study of temperature development within I-sections subjected to four sides heating using the Standard Fire Curve [26] showed a slower temperature development for the stainless steel sections when compared to the carbon steel ones, and the sections of a smaller section factor (A/V) benefited more from using stainless steels in terms of achieving a slower temperature development.

7.1.3 Application for advanced structural design

One motivation to develop a sophisticated plastic model for thermo-mechanical analysis of steels was the desire to accurately analyse the steel structures subjected to complex realistic building fires, simulated using the newly developed extended travelling fire framework model. This enables the analysis of structural fire resistance of modern architectural designs where travelling fire behaviour is expected to occur.

The proposed material model was applied in Chapter 6 to study the structural behaviour of a single carbon steel beam (UB 305x127x42) subjected to two different travelling fire scenarios. One is a slow, but dense fire, and the other is a rapid, but light fire. The structural fire behaviour of the beam was successfully captured by a 3D and a 2D model. The 3D analysis used the new material model in multi-axial state while the 2D analysis used the the uniaxial model. Reasonable and comparable structural behaviour were observed in the two analyses. An evident reduction in the strength capacity using the new material model was observed when compared to the results obtained using the isotropic hardening model of Abaqus.

7.2 Limitations and future work

The new material model adopted the von Mises yield criterion, which has been shown, in the literature, able to provide satisfactory results for steel materials at elevated temperatures. However, the distortion of the yield surface due to plastic deformation could not be captured by the von Mises yield function. The yield function proposed by Barlat et al. [208] has become a popular approach to model the distortion of yield surface shape due to anisotropic plastic hardening. Adopting this yield function in the proposed material model will improve its accuracy and greatly expand its applicability for thermo-mechanical analysis of other metals, e.g., aluminium.

The effect of the varying hardening and evolution function parameters on the stability of the proposed model was not investigated in this work due to limited available testing data. A sensitivity study dedicated to this subject in the future can better demonstrate the applicability of the new material model to a wide range of steel materials.

It has been observed that catenary action is beneficial for the structural fire performance of frames. However, the strain reversals experienced during catenary action can cause reduction in the material tensile strength due to the Bauschinger effect and was not investigated in this research. Future investigation into the impact of the Bauschinger effect on the catenary action of steel beam structures in fire using the new material model can help to achieve a more accurate method for taking advantages of the catenary action in structural fire design.

Appendix A

Numerical Algorithm for Combined Isotropic and Kinematic Hardening Model

The numerical algorithm of the proposed combined isotropic and kinematic hardening model for thermo-mechanical analysis of structures in fire described in the preceding section is summarised in the Table below. The proposed model is implemented into the commercial finite element code Abaqus/Standard, using the user subroutine —Umat [23].

Table A.1: Numerical algorithm for the proposed combined isotropic- kinematic hardening model

Last Converged Step n
If Temperature change $\Delta T \neq 0$, Go to Thermal Step, Else Go to Mechanical Step
Thermal Step, Current Temperature T_{n+1}
1. Update Temperature-dependent parameters
Young's modulus E_{Tn+1}, Initial yield stress $\sigma_{p,Tn+1}$
Hardening function parameters v_{Tn+1} and δ_{Tn+1}
Bauschinger ratio evolution equation parameters a_{Tn+1}, b_{Tn+1} and c_{Tn+1}
Material model parameter Vh_{Tn+1}
2. Update Bauschinger ratio

$\vartheta_{Tn+1} = a_{Tn+1} * exp(-b_{Tn+1} * \overline{\varepsilon^p}_n) + c_{Tn+1}$

3. Update the size of bounding surface

$$Y = \sqrt{\tfrac{2}{3}} Y_{1D,Tn+1}(\overline{\varepsilon_n^p})$$

4. Update the position of the yield surface centre, $\boldsymbol{\beta_1}$ term

$$\boldsymbol{\beta_1}_n = (1.0 - \vartheta_{Tn+1}) Y \frac{\boldsymbol{\varepsilon_n^p}}{\|\boldsymbol{\varepsilon_n^p}\|}$$

Mechanical Step, Strain Increment $\Delta\boldsymbol{\varepsilon}$

---

1. Elastic predictor

$\boldsymbol{\sigma}_{n+1}^{trial} = \boldsymbol{C}_{n+1} \cdot (\boldsymbol{\varepsilon}_n + \Delta\boldsymbol{\varepsilon} - \boldsymbol{\varepsilon^p}_n), \quad \boldsymbol{\beta_1}_{n+1}^{trial} = \boldsymbol{\beta_1}_n, \quad \boldsymbol{\beta_2}_{n+1}^{trial} = \boldsymbol{\beta_2}_n$

$\boldsymbol{s}_{n+1}^{trial} = \boldsymbol{I_{dev}} : \boldsymbol{\sigma}_{n+1}^{trial}, \quad \boldsymbol{I_{dev}} = \boldsymbol{I} - \tfrac{1}{3}\mathbf{1} \otimes \mathbf{1}$

$\boldsymbol{\eta}_{n+1}^{trial} = \boldsymbol{s}_{n+1}^{trial} - \boldsymbol{\beta_1}_{n+1}^{trial} - \boldsymbol{\beta_2}_{n+1}^{trial}, \quad \boldsymbol{N_{n+1}} = \frac{\boldsymbol{\eta_{n+1}^{trial}}}{\|\boldsymbol{\eta_{n+1}^{trial}}\|}$

$\vartheta_{n+1} = a_{n+1} * exp(-b_{n+1} * \overline{\varepsilon^p}_n) + c_{n+1}$

$\nu_{n+1} = 1.0 - exp(-b_{n+1} * \overline{\varepsilon_l^p}_n)$

Reverse loading index :$l_{n+1}^{trial} = l_n$

$\overline{\beta}_{l_{n+1}}^{trial} = \overline{\beta}_{l_n}$

- Check the reverse loading criterion according to Equation 3.21

If $cos(\theta) < 0.0$ then

$l_{n+1}^{trial} = l_n + 1$

$\overline{\varepsilon^p}_{l\ n+1}^{trial} = 0.0$

$\overline{\beta}_{l_{n+1}}^{trial} = Vh_{Tn+1}\sqrt{\tfrac{3}{2}(\boldsymbol{\beta_1}_n + \boldsymbol{\beta_2}_n) : (\boldsymbol{\beta_1}_n + \boldsymbol{\beta_2}_n)}$

$\boldsymbol{\beta_2}_{n+1}^{trial} = 0.0$

Else, Do nothing

- Check the yield condition

If $f(\boldsymbol{\eta_{n+1}^{trial}}) - \vartheta_{n+1} Y_{1D,n+1}(\overline{\varepsilon^p}) < Tolerance$, then Set $(\bullet)_{n+1} = (\bullet)^{Trial}$ Exit

Else Go to Plastic corrector

2. Plastic corrector

- Newton-Raphson iteration is employed to determine plastic multiplier $\Delta\gamma$. Initialise $\Delta\gamma = 0.0$

Iterate until $|g(\Delta\gamma)| < Tolerance$

$g(\Delta\gamma) = \| \boldsymbol{\eta}_{n+1}^{trial} \| - 2 * \mu_{n+1} * \Delta\gamma - \vartheta_{n+1}\sqrt{\tfrac{2}{3}} * Y_{1D,n+1}(\overline{\varepsilon_n^p} + \sqrt{\tfrac{2}{3}}\Delta\gamma)$

$dg(\Delta\gamma) = -2 * \mu_{n+1} - \tfrac{2}{3} * [Y'_{1D,(n+1)}(\overline{\varepsilon_n^p} + \sqrt{\tfrac{2}{3}}\Delta\gamma)] * \vartheta_{n+1}$

Y' is the first derivative of Y with regard to $\Delta\gamma$

$\Delta\gamma = \Delta\gamma - g/dg$

- ϑ_{n+1} is considered a constant during the Newton-Raphson iteration for small step of $\Delta\gamma$.

The consequent 'residual stress' of this simplification will be solved in the next iteration.

3. Update stress state

$\boldsymbol{\varepsilon^p}_{n+1} = \boldsymbol{\varepsilon^p}_n + \Delta\gamma \boldsymbol{N}_{n+1}$; $\overline{\varepsilon^p_{n+1}} = \overline{\varepsilon^p_n} + \sqrt{\frac{2}{3}}\Delta\gamma$; $\overline{\varepsilon^p_{l(n+1)}} = \overline{\varepsilon^p_{l\ n+1}}^{trial} + \sqrt{\frac{2}{3}}\Delta\gamma$

$l_{n+1} = l^{trial}_{n+1}$

$\vartheta_n = c + a * exp(-b * \overline{\varepsilon^p_n})$; $\vartheta_{n+1} = c + a * exp(-b * \overline{\varepsilon^p_{n+1}})$

If $l_{n+1} \neq 0$ then

$\nu_n = 1 - exp(-b * \overline{\varepsilon^p_{l\ (n)}})$; $\nu_{n+1} = 1 - exp(-b * \overline{\varepsilon^p_{l\ (n+1)}})$

$\overline{\beta_2} = (\nu_{n+1} - \nu_n) * \overline{\beta_{l n+1}}^{trial}$; $\boldsymbol{\beta_2}_{n+1} = \boldsymbol{\beta_2}^{trial}_{n+1} + \overline{\beta_2}\boldsymbol{N}_{n+1}$

Endif

$\boldsymbol{\beta_1}_{n+1} = \boldsymbol{\beta_1}^{trial}_{n+1} + \sqrt{\frac{2}{3}} * [(1 - \vartheta_{n+1})Y_{(n+1)}(\overline{\varepsilon^p}_{n+1}) - (1 - \vartheta_n)Y_{(n+1)}(\overline{\varepsilon^p}_n)]\boldsymbol{N}_{n+1}$

$\boldsymbol{\sigma}_{n+1} = \boldsymbol{\sigma}^{trial}_{n+1} - 2 * \mu_{(n+1)} * \Delta\gamma \boldsymbol{N}_{n+1}$

Appendix B

Implementation for Plane Stress Material Model

The algorithms developed in the previous section are based on elastoplastic three-dimensional constitutive equations. To implement the three-dimensional plasticity algorithm to plane stress elements, a global Newton-Raphson iteration loop has been used to enforce the plane stress constraint $\sigma_{33} = 0$ at the Gauss point level, following the approach introduced by Dodds [209].

The overall algorithm implemented is summarised in Table B.1, where D_{22} is the component of the axisymmetric consistent tangent matrix:

$$\left[\begin{array}{c} d\sigma_{11} \\ d\sigma_{22} \\ d\sigma_{12} \\ \hline d\sigma_{33} \end{array}\right] = \left[\begin{array}{c|c} & \\ \boldsymbol{D_{11}} & \boldsymbol{D_{12}} \\ & \\ \hline \boldsymbol{D_{21}} & D_{22} \end{array}\right] \left[\begin{array}{c} d\varepsilon_{11}^{e\ trial} \\ d\varepsilon_{22}^{e\ trial} \\ 2d\varepsilon_{12}^{e\ trial} \\ \hline d\varepsilon_{33}^{e\ trial} \end{array}\right] \tag{B.1}$$

Table B.1: Numerical algorithm for plane stress material

```
1. Set initial guess for the elastic trial thickness strain to the converged value from last step
   $\varepsilon_{33}^{e\ trial} = (\varepsilon_{33}^{e})_n$
2. Call the stress integration algorithm in Table A.1
3. For the obtained trial $\sigma_{33}$, if $|\sigma_{33}| <$ Tolerance, Then Exit loop
4. Compute component D22 of the consistent tangent matrix
5. Apply Newton-Raphon correction to the thickness trial strain
   $\varepsilon_{33}^{e\ trial} := \varepsilon_{33}^{e\ trial} - \frac{\sigma_{33}}{D_{22}}$
6. Go to Step 2
```

It is noted that for the above methodology a number of iterations will be required in each Gauss point to ensure that the plane stress condition. Consequently, the present procedure can be computational expensive. However the cost of the calculations carried out at Gauss point level increases linearly with the problem size, whereas the cost of the solution of the global linearised problem increases at a much higher nonlinear rate [153].

The elastoplastic consistent tangent modulus obtained in Section 3.3.4 for three dimensional plasticity was modified for the plane stress plasticity to ensure the tangent operator remain consistent with the above nested iteration algorithm. The elastoplastic consistent tangent modulus is derived by first differentiating the residual equation of the plane stress enforcement loop : $\sigma_{33} = 0$. Together with Equation B.1, it gives:

$$\begin{aligned} d\sigma_{33} &= \boldsymbol{D_{21}} d\boldsymbol{\varepsilon}_{n+1}^{e\ trial} + D_{22} d\varepsilon_{33}^{e\ trial} = 0 \\ \Rightarrow \qquad d\varepsilon_{33}^{e\ trial} &= \frac{-1}{D_{22}} \boldsymbol{D_{21}} d\boldsymbol{\varepsilon}^{e\ trial} \end{aligned} \tag{B.2}$$

Replacing Equation B.2 into Equation B.1 results in the following consistent tangent relation between in-plane stress and strain components:

$$\frac{d\boldsymbol{\sigma}_{n+1}}{d\boldsymbol{\varepsilon}_{n+1}^{e\ trial}} = \boldsymbol{D_{11}} - \frac{1}{D_{22}} \boldsymbol{D_{12}} \boldsymbol{D_{21}} \tag{B.3}$$

For the von Mises model, the above Equation B.3 relates the elastoplastic consistent tangent modulus to generic three dimensional expression as follows:

$$D_{ijkl}^{ep,PlaneStress} = D_{ijkl}^{ep,3D} - D_{ij33}^{ep,3D} \frac{D_{33kl}^{ep,3D}}{D_{3333}^{ep,3D}} \tag{B.4}$$

The above Equation B.4 has been implemented in the Abaqus subroutine Umat [23] for performing plane stress analysis using shell elements.

Appendix C

Derivation of Elastoplastic Consistent Tangent Modulus $\boldsymbol{D^{ep}}$

When the material is subjected to monotonic loading, the yield condition function can be reduced to the Equation C.1 below, which then becomes differentiable:

$$\Phi(\Delta\gamma) \equiv \|\boldsymbol{\eta}^{trial}_{n+1}\| - 2\mu\Delta\gamma - (\overline{\beta_1}_{n+1} - \overline{\beta_1}_{n}) - \sigma_{y,iso} = 0 \qquad \text{(C.1)}$$

During reverse loading, the elastoplastic consistent tangent modulus shall be derived using the equation C.2:

$$\Phi(\Delta\gamma) \equiv \|\boldsymbol{\eta}^{trial}_{n+1}\| - 2\mu\Delta\gamma - (\overline{\beta_1}_{n+1} - \overline{\beta_1}_{n}) - (\overline{\beta_2}_{n+1} - \overline{\beta_2}_{n}) - \sigma_{y,iso} = 0 \qquad \text{(C.2)}$$

The following section focuses on presenting in details the derivation of the elastoplastic consistent tangent modulus for the proposed material model under monotonic loading case. The derived elastoplastic consistent tangent operator for the reverse loading case will be provided at the end of this section.

Substituting Equation 3.16 and 3.17 into Equation C.1 gives:

$$\begin{aligned}\Phi(\Delta\gamma) \equiv \|\boldsymbol{\eta}^{trial}_{n+1}\| - 2\mu\Delta\gamma - [(1-\vartheta_n)\sqrt{\frac{2}{3}}Y_{1D}(\overline{\varepsilon^p}_n + \sqrt{\frac{2}{3}}\Delta\gamma) - \overline{\beta}_n]\\ - \vartheta_n\sqrt{\frac{2}{3}}Y_{1D}(\overline{\varepsilon^p}_n + \sqrt{\frac{2}{3}}\Delta\gamma) = 0\end{aligned}$$

Re-arranging and combining the terms related to Y_{1D} gives:

$$\Phi(\Delta\gamma) \equiv \|\boldsymbol{\eta}_{n+1}^{trial}\| - 2\mu\Delta\gamma - \overline{\beta}_n - \sqrt{\frac{2}{3}} Y_{1D}(\overline{\varepsilon^p}_n + \sqrt{\frac{2}{3}}\Delta\gamma) = 0 \tag{C.3}$$

where the Bauschinger ratio (ϑ) is considered of constant value of ϑ_n during the Newton-Raphson iteration for increment (n+1).

The m^{th} Newton-Raphson iterative correction to $\Delta\gamma$ for the solution of Equation C.3 reads:

$$\Delta\gamma^{(m)} := \Delta\gamma^{(m-1)} - \frac{\Phi(\Delta\gamma^{(m-1)})}{d} \tag{C.4}$$

where

$$d = -2\mu - \frac{2}{3} H_{1D}(\overline{\varepsilon^p}_n + \sqrt{\frac{2}{3}}\Delta\gamma) \tag{C.5}$$

where $H_{1D} \equiv Y'_{1D}$ is the slope of the uniaxial tensile stress—plastic strain curve.

The incremental algorithmic constitutive update function for $\boldsymbol{\sigma_{n+1}}$ for the von Mises model with nonlinear combined hardening using back-Euler return mapping is:

$$\Delta\boldsymbol{\sigma} = \boldsymbol{D^e} : \Delta\boldsymbol{\varepsilon} - 2\mu\Delta\gamma\boldsymbol{N} \tag{C.6}$$

where $\Delta\boldsymbol{\varepsilon}$ is the deviatoric strain increment, γ is the plastic multiplier, $\boldsymbol{D^e}$ is the constant isotropic elasticity tensor

$$\begin{aligned} \boldsymbol{D^e} &= \kappa\mathbf{1} \otimes \mathbf{1} + 2\mu\boldsymbol{I_{dev}} \\ \boldsymbol{I_{dev}} &= \boldsymbol{I} - \frac{1}{3}\mathbf{1} \otimes \mathbf{1} \end{aligned} \tag{C.7}$$

where κ is the bulk modulus, μ is the shear modulus, $\boldsymbol{I}$ is the fourth-order symmetric unit tensor, and $\mathbf{1}$ is the second-order symmetric unit tensor.

The deviatoric unit flow vector ($\boldsymbol{N}$) is:

$$\boldsymbol{N} = \frac{\boldsymbol{\eta}_{n+1}}{\|\boldsymbol{\eta}_{n+1}\|} = \frac{\boldsymbol{\eta}_{n+1}^{trial}}{\|\boldsymbol{\eta}_{n+1}^{trial}\|} \tag{C.8}$$

Differentiate the stress update Equation C.6 gives:

$$\frac{\partial \Delta \boldsymbol{\sigma}}{\partial \Delta \boldsymbol{\varepsilon}} = \boldsymbol{D}^e - 2\mu \boldsymbol{N} \otimes \frac{\partial \Delta \gamma}{\partial \Delta \boldsymbol{\varepsilon}} - 2\mu \Delta \gamma \frac{\partial \boldsymbol{N}}{\partial \Delta \boldsymbol{\varepsilon}} \tag{C.9}$$

The incremental plastic multiplier derivation ($\frac{\partial \Delta \gamma}{\partial \Delta \boldsymbol{\varepsilon}}$) is obtained by differentiating the yield condition Equation C.3 with respect to deviatoric trial strain $\boldsymbol{\varepsilon}$

$$\begin{aligned}
\Phi(\boldsymbol{\eta}_{n+1}, \boldsymbol{\varepsilon^p}_{n+1}) &= \Phi(\boldsymbol{\eta}_n, \boldsymbol{\varepsilon^p}_n) = 0 \\
\Rightarrow \qquad & \frac{\partial \Phi}{\partial \Delta \boldsymbol{\varepsilon}} = 0 \\
\frac{\partial \Phi}{\partial \Delta \boldsymbol{\varepsilon}} &= \frac{\partial}{\partial \Delta \boldsymbol{\varepsilon}} [\|\boldsymbol{\eta}^{trial}_{n+1}\| - 2\mu \Delta \gamma - \overline{\beta}_n - \sqrt{\frac{2}{3}} Y_{1D}(\overline{\varepsilon^p}_n + \sqrt{\frac{2}{3}} \Delta \gamma)] = 0 \\
\Rightarrow \qquad & \frac{\partial \|\boldsymbol{\eta}^{trial}_{n+1}\|}{\partial \Delta \boldsymbol{\varepsilon}} - 2\mu \frac{\partial \Delta \gamma}{\partial \Delta \boldsymbol{\varepsilon}} - \frac{2}{3} H_{1D}(\overline{\varepsilon^p}_n + \sqrt{\frac{2}{3}} \Delta \gamma) \frac{\partial \Delta \gamma}{\partial \Delta \boldsymbol{\varepsilon}} = 0
\end{aligned} \tag{C.10}$$

The derivative of relative stress tenor ($\frac{\partial \boldsymbol{\eta}^{trial}_{n+1}}{\partial \Delta \boldsymbol{\varepsilon}}$) can be obtained by following:

$$\frac{\partial \boldsymbol{\eta}^{trial}_{n+1}}{\partial \Delta \boldsymbol{\varepsilon}} = \frac{\partial (\boldsymbol{s}^{trial}_{n+1} - \boldsymbol{\beta}_n)}{\partial \Delta \boldsymbol{\varepsilon}} = 2\mu \boldsymbol{I_{dev}} \tag{C.11}$$

Subsequently we have:

$$\begin{aligned}
& \|\boldsymbol{\eta}^{trial}_{n+1}\| = (\boldsymbol{\eta}^{trial}_{n+1} : \boldsymbol{\eta}^{trial}_{n+1})^{1/2} \\
\Rightarrow \qquad & \frac{\partial \|\boldsymbol{\eta}^{trial}_{n+1}\|}{\partial \Delta \boldsymbol{\varepsilon}} = \frac{1}{2} (\boldsymbol{\eta}^{trial}_{n+1} : \boldsymbol{\eta}^{trial}_{n+1})^{-1/2} 2 \boldsymbol{\eta}^{trial}_{n+1} : \frac{\partial \boldsymbol{\eta}^{trial}_{n+1}}{\partial \Delta \boldsymbol{\varepsilon}} = \frac{\boldsymbol{\eta}^{trial}_{n+1}}{\|\boldsymbol{\eta}_{n+1}\|} : 2\mu \boldsymbol{I_{dev}} = 2\mu \boldsymbol{N}
\end{aligned} \tag{C.12}$$

After substitution of Equation C.12 into Equation C.10 we can therefore obtain $\frac{\partial \boldsymbol{\eta}^{trial}_{n+1}}{\partial \Delta \boldsymbol{\varepsilon}}$:

$$\begin{aligned}
& 2\mu \boldsymbol{N} - \big(2\mu + \frac{2}{3} H_{1D}(\overline{\varepsilon^p}_n + \sqrt{\frac{2}{3}} \Delta \gamma)\big) \frac{\partial \Delta \gamma}{\partial \Delta \boldsymbol{\varepsilon}} = 0 \\
\Rightarrow \qquad & \frac{\partial \Delta \gamma}{\partial \Delta \boldsymbol{\varepsilon}} = 2\mu \boldsymbol{N} \frac{1}{\Theta} \\
& \Theta = 2\mu + \frac{2}{3} H_{1D}(\overline{\varepsilon^p}_n + \sqrt{\frac{2}{3}} \Delta \gamma)
\end{aligned} \tag{C.13}$$

The derivative of the deviatoric unit flow vector ($\frac{\partial \boldsymbol{N}}{\partial \Delta \boldsymbol{\varepsilon}}$) is obtained as follows:

$$\frac{\partial \boldsymbol{N}}{\partial \Delta \boldsymbol{\varepsilon}} = \frac{\partial \boldsymbol{N}}{\partial \Delta \boldsymbol{\eta}_{n+1}^{trial}} : \frac{\partial \boldsymbol{\eta}_{n+1}^{trial}}{\partial \Delta \boldsymbol{\varepsilon}} \tag{C.14}$$

We have

$$\begin{aligned} \frac{\partial \boldsymbol{N}}{\partial \Delta \boldsymbol{\eta}_{n+1}^{trial}} &= \frac{\partial}{\partial \boldsymbol{\eta}_{n+1}^{trial}} \left(\frac{\boldsymbol{\eta}_{n+1}^{trial}}{\|\boldsymbol{\eta}_{n+1}^{trial}\|} \right) = \frac{\boldsymbol{I}}{\|\boldsymbol{\eta}_{n+1}^{trial}\|} - \frac{\boldsymbol{\eta}_{n+1}^{trial} \otimes \boldsymbol{\eta}_{n+1}^{trial}}{\|\boldsymbol{\eta}_{n+1}^{trial}\|^3} \\ &= \frac{1}{\|\boldsymbol{\eta}_{n+1}^{trial}\|} [\boldsymbol{I} - \boldsymbol{N} \otimes \boldsymbol{N}] \end{aligned} \tag{C.15}$$

Substituting Equation C.15 and C.11 into Equation C.14 gives:

$$\frac{\partial \boldsymbol{N}}{\partial \Delta \boldsymbol{\varepsilon}} = \frac{1}{\|\boldsymbol{\eta}_{n+1}^{trial}\|} [\boldsymbol{I} - \boldsymbol{N} \otimes \boldsymbol{N}] : 2\mu \boldsymbol{I_{dev}} = \frac{2\mu}{\|\boldsymbol{\eta}_{n+1}^{trial}\|} [\boldsymbol{I_{dev}} - \boldsymbol{N} \otimes \boldsymbol{N}] \tag{C.16}$$

Finally, substituting Equation C.13 and C.16 into Equation C.9, the elastoplastic consistent tangent can be obtained:

$$\boldsymbol{D^{ep}} = \boldsymbol{D^e} - 4\mu^2 \frac{1}{\Theta} \boldsymbol{N} \otimes \boldsymbol{N} - \frac{4\mu^2}{\|\boldsymbol{\eta}_{n+1}^{trial}\|} [\boldsymbol{I_{dev}} - \boldsymbol{N} \otimes \boldsymbol{N}] \tag{C.17}$$

During reverse loading, the elastoplastic consistent tangent can still be computed following Equation C.17, with the term Θ modified to include the $\boldsymbol{\beta_2}$ term as follows:

$$\Theta = 2\mu + \frac{2}{3} H_{1D}(\overline{\varepsilon^p}_n + \sqrt{\frac{2}{3}} \Delta\gamma) - \frac{2}{3} \overline{\beta_l} exp\big(-V_b(\overline{\varepsilon_l^p}_n + \sqrt{\frac{2}{3}} \Delta\gamma)\big)(-V_b) \tag{C.18}$$

where V_b is the material coefficient as adopted in the reverse loading evolution Equation 3.23. $\overline{\beta_l}$ is the backstress from the last branch of loading as defined in Equation 3.25.

The above elastoplastic consistent tangent operators have been implemented in the Abaqus Umat subroutine [23].

Appendix D

Tables of Parameters

Table D.1 presents the curve fitting results of v_T and δ_T for every 100 °C. Linear interpolation will be used to obtain the intermediate values.

Table D.1: Least square fitting results for hardening law, EC3 carbon steel

Temperature (°C)	v_T	δ_T	Adj-R-sq
100	0.0	-	-
200	48.1	168.5	0.996
300	90.9	187.8	0.996
400	133.6	198.5	0.996
500	114.6	197.8	0.996
600	87.8	206.2	0.995
700	48.3	213.9	0.995
800	23.7	202.5	0.995
900	13.1	195.9	0.995
1000	8.9	196.1	0.995
1100	0.9	196.3	0.995

Table D.2: Least square fitting results for hardening law, Austenitic III

Temperature (°C)	σ_{0_T}	k_T	n_T	Adj-R-sq	$\sigma_{0_T}/\sigma_{0.2\%,T}$
20	50.61	551.65	0.2003	0.99	0.23
100	43.08	484.22	0.1962	0.99	0.22
200	39.70	446.63	0.1964	0.99	0.22
300	37.27	426.00	0.1988	0.99	0.22
400	34.85	406.35	0.2021	0.99	0.22
500	33.40	389.78	0.2024	0.99	0.22
600	31.47	366.31	0.1995	0.99	0.22
700	28.56	311.30	0.1921	0.98	0.22
800	24.69	238.75	0.1734	0.97	0.22
900	13.40	153.97	0.1877	0.98	0.21
1000	7.26	91.26	0.2123	0.97	0.22

Table D.3: Least square fitting results for hardening law, Duplex II

Temperature (°C)	σ_{0_T}	k_T	n_T	Adj-R-sq	$\sigma_{0_T}/\sigma_{0.2\%,T}$
20	171.16	1494.3	0.3673	0.98	0.38
100	140.30	1170.8	0.3544	0.98	0.38
200	116.60	951.3	0.3446	0.98	0.37
300	108.30	883.5	0.3446	0.98	0.37
400	99.96	808.7	0.3435	0.98	0.37
500	85.91	682.0	0.3343	0.98	0.36
600	66.18	514.1	0.3247	0.98	0.34
700	41.32	316.1	0.3029	0.98	0.31
800	2.93	22.5	0.2837	0.98	0.30
900	9.45	75.3	0.2756	0.98	0.25
1000	1.12	11.1	0.2631	0.98	0.25

Table D.4: Least square fitting results, 304L stainless steel in Section 3.4

Temperature	Hardening Function			Bauschinger Ratio Evolution Function			
°C	v_T	δ_T	Adj-R-sq	a_T	b_T	c_T	Adj-R-sq
200	448.9	6.31	0.993	0.8504	184.5	0.1495	0.998
600	312.7	9.941	0.999	0.6996	189.3	0.3004	0.980
800	38.34	26.45	0.952	0.6786	267.2	0.3214	0.987
1000	1000.0	0.1003	0.977	0.9050	500.0	0.0943	0.974

Table D.5: Least square fitting results, Low carbon steel in Section 3.5

Temperature	Hardening Function			Bauschinger Ratio Evolution Function				Material parameter
°C	v_T	δ_T	Adj-R-sq	a_T	b_T	c_T	Adj-R-sq	Vh_T
300	138.1	741.9	0.918	0.2212	5000.0	0.7781	0.996	1.45
700	19.22	1331.0	0.957	0.2801	4274.0	0.7100	1.0	1.45

Table D.6: Least square fitting results, 316 stainless steel in Section 3.7

Temperature	Hardening Function			Bauschinger Ratio Evolution Function			
°C	v_T	δ_T	Adj-R-sq	a_T	b_T	c_T	Adj-R-sq
650	13.5	1533.0	0.854	0.3078	800.0	0.70	1.0

Table D.7: Least square fitting results for hardening law, St 37.2 carbon steel in [6]

Temperature (°C)	σ_{0_T}	v_T	δ_T	Adj-R-sq
100	250.0	0.0	-	-
200	226.4	23.61	22.84	0.980
300	158.5	90.58	23.62	0.988
400	143.6	105.5	24.42	0.982
500	129.5	56.57	25.03	0.991
600	56.58	67.48	24.27	0.990
700	22.1	39.67	23.97	0.991

Table D.8: Least square fitting results, 304 Stainless Steel

Temperature	Hardening Function			Bauschinger Ratio Evolution Function			
°C	v_T	δ_T	Adj-R-sq	a_T	b_T	c_T	Adj-R-sq
150	302.1	0.1675	0.977	0.38	1143	0.62	1.0
350	237.4	0.1729	0.984	0.28	1098	0.72	1.0
600	208.2	0.2144	0.998	0.25	1055	0.75	1.0
850	26.37	0.0748	0.975	0.26	974	0.74	1.0
1000	31.34	0.2569	0.939	0.37	1069	0.63	1.0

Table D.9: Bauschinger ratio calibration results, based on Fig.8 in [5]

Temperature	Bauschinger ratio	$\overline{\varepsilon^p}$
150 °C	0.3756	0.0039
350 °C	0.2766	0.0040
600 °C	0.2463	0.0040
850 °C	0.2797	0.0043
1000 °C	0.3675	0.0047

Bibliography

[1] *Eurocode 3 : Design of steel structures - Part 1-2: General rules -Structural fire design*, vol. 3. British Standards Instituion, 2005.

[2] *Design manual for structural stainless steel.* The Steel Construction Institute, 4^{th} ed., 2017.

[3] C. Bailey, I. Burgess, and R. Plank, "Analyses of the effects of cooling and fire spread on steel-framed buildings," *Fire Safety Journal*, vol. 26, no. 4, pp. 273–293, 1996.

[4] M. Miller, E. Harley, and D. Bammann, "Reverse yield experiments and internal variable evolution in polycrystalline metals," *International Journal of Plasticity*, vol. 15, pp. 93–117, mar 1999.

[5] N. Ohno, R. Yamamoto, and D. Okumura, "Thermo-mechanical cyclic hardening behavior of 304 stainless steel at large temperature ranges: Experiments and simulations," *International Journal of Mechanical Sciences*, vol. 146-147, pp. 517 – 526, 2018.

[6] A. Rubert and P. Schaumann, "Structural steel and plane frame assemblies under fire action," *Fire Safety Journal*, vol. 10, pp. 173–184, may 1986.

[7] Y. Wang, I. Burgess, F. Wald, and M. Gillie, *Performance Based Fire Engineering of Structures.* CRC Press LLC, Baton Rouge, 2012.

[8] A. Jonsdottir and G. Rein, "Out of range," pp. 14–17, 2009.

[9] *Eurocode 1 : Actions on structures -Part 1-2: Gerneral actions -Actions on structures exposed to fire*. British Standards Institution, 2013.

[10] J. Stern-Gottfried and G. Rein, “Travelling fires for structural design-Part I: Literature review,” *Fire Safety Journal*, vol. 54, pp. 74–85, nov 2012.

[11] J. Stern-Gottfried and G. Rein, “Travelling fires for structural design - Part II: Design methodology,” *Fire Safety Journal*, vol. 54, pp. 96–112, nov 2012.

[12] X. Dai, S. Welch, and A. Usmani, “A critical review of travelling fire scenarios for performance-based structural engineering,” *Fire Safety Journal*, vol. 91, pp. 568–578, jul 2017.

[13] X. Dai, S. Welch, and A. Usmani, “Structural Implications due to an extended travelling fire methodology (ETFM) framework using SIFBUILDER,” in *The* 10^{th} *International Conference on Structures in Fire*, 2018.

[14] G. M. Newman, “Structural fire engineering investigation of Broadgate phase 8 fire,” *The Steel Construction Institute, Ascot*, 1991.

[15] FEMA, “World Trade Center Building Performance Study,” Tech. Rep. 403, FEMA, 2002.

[16] J. Quintiere, M. di Marzo, and R. Becker, “A suggested cause of the fire-induced collapse of the world trade towers,” *Fire Safety Journal*, vol. 37, no. 7, pp. 707 – 716, 2002.

[17] A. Usmani, “Stability of the world trade center twin towers structural frame in multiple floor fires,” *Journal of Engineering Mechanics*, vol. 131, no. 6, pp. 654–657, 2005.

[18] G. Flint, A. Usmani, S. Lamont, B. Lane, and J. Torero, “Structural response of tall buildings to multiple floor fires,” *Journal of Structural Engineering*, vol. 133, no. 12, pp. 1719–1732, 2007.

[19] P. Kotsovinos and A. Usmani, “The world trade center 9/11 disaster and progressive collapse of tall buildings,” *Fire Technology*, vol. 49, pp. 741–765, jul 2013.

[20] L. Gardner and K. Ng, “Temperature development in structural stainless steel sections exposed to fire,” *Fire Safety Journal*, vol. 41, no. 3, pp. 185–203, 2006.

[21] L. Gardner and N. Baddoo, “Fire testing and design of stainless steel structures,” *Journal of Constructional Steel Research*, vol. 62, no. 6, pp. 532–543, 2006.

[22] N. Baddoo, “Stainless steel in construction: A review of research, applications, challenges and opportunities,” *Journal of Constructional Steel Research*, vol. 64, no. 11, pp. 1199–1206, 2008.

[23] *Abaqus 6.14 User subroutine reference guide*. SIMULIA.

[24] F. McKenna, “Opensees: A framework for earthquake engineering simulation,” *Computing in Science Engineering*, vol. 13, pp. 58–66, jul 2011.

[25] V. Babrauskas and R. B. Williamson, “The historical basis of fire resistance testing - Part II,” *Fire Technology*, vol. 14, no. 4, pp. 304–316, 1978.

[26] *ISO 834-1:1999, Fire-resistance tests - Elements of building construction - Part 1: General requirements*. International Organization for Standardisation, 1999.

[27] *ASTM E119-18ce1,Standard test methods for fire tests of building construction and materials*. ASTM International, 2018.

[28] C. Maluk and L. Bisby, “120 years of structural fire testing: Moving away from the status quo,” in *The Second Fire engineering conference*, 2012.

[29] S. Ingberg, “Tests of the severity of building fires,” *NFPA Quarterly*, 1928.

[30] D. Drysdale, *An Introduction to Fire Dynamics: Third Edition*. Wiley Blackwell, 2011.

[31] G. Thomas, A. Buchanan, and C. Fleischmann, “Structural fire design: The role of time equivalence,” *Fire Safety Science*, vol. 5, pp. 607–618, 1997.

[32] C. Maluk, “Motivation, drivers and barriers for a knowledge-based test environment in structural fire safety engineering science,” *Fire Safety Journal*, vol. 91, pp. 103–111, jul 2017.

[33] T. Z. Harmathy, “The fire resistance test and its relation to real-world fires,” *Fire and Materials*, vol. 5, no. 3, pp. 112–122, 1981.

[34] *Fire protection for structural steel in buildings*. The Association for Specialist Fire Protection, 2004.

[35] *PD 7974-3: Application of fire safety engineering principles to the design of buildings. Structural response to fire and fire spread beyond the enclosure of origin (Sub-system 3)*. British Standards Institution, 2011.

[36] *BS-476-20: Fire tests on building materials and structures. Method for determination of the fire resistance of elements of construction (general principles)*. British Standards Institution, 1987.

[37] C. Bailey, D. Moore, and T. Lennon, “The structural behaviour of steel columns during a compartment fire in a multi-storey braced steel-frame,” *Journal of Constructional Steel Research*, vol. 52, pp. 137–157, Nov 1999.

[38] “The behaviour of multi-storey steel-framed buildings in a fire: A european joint research programme,” tech. rep., Swinden Technology Centre, 1999.

[39] A. Usmani, J. M. Rotter, S. Lamont, A. Sanad, and M. Gillie, “Fundamental principles of structural behaviour under thermal effects,” *Fire Safety Journal*, vol. 36, no. 8, pp. 721–744, 2001.

[40] A. Buchanan, “The challenges of predicting structural performance in fires,” *Fire Safety Science*, no. 9, pp. 79–90, 2008.

[41] V. Babrauskas, “Performance-Based Fire Safety Engineering Design: The Role of Fire Models and Fire Tests,” in *Interflam*, pp. 799–807, 1999.

[42] *ISO 16733:2015, Fire safety engineering - Selection of design fire scenarios and design fires. Part 1: Selection of design fire scenarios.* International Organisation for Standardisation.

[43] P. H. Thomas, “Modelling of compartment fires,” *Fire Safety Journal*, vol. 5, pp. 181–190, jan 1983.

[44] K.Kawagoe, “Fire Behaviour in Rooms,” tech. rep., Building Research Institute, Ministry of Construction, Tokyo, 1958.

[45] T. T. Lie, “Characteristic temperature curves for various fire severities,” *Fire Technology*, vol. 10, no. 4, pp. 315–326, 1974.

[46] O. Pettersson, S. E. Magnusson, and J. Thor, “Fire Engineering Design of Steel Structures,” tech. rep., Swedish institute of steel construction, 1976.

[47] Z. Ma and P. Mäkeläinen, “Parametric temperature-time curves of medium compartment fires for structural design,” *Fire Safety Journal*, vol. 34, no. 4, pp. 361–375, 2000.

[48] C. R. Barnett, “BFD curve: A new empirical model for fire compartment temperatures,” *Fire Safety Journal*, vol. 37, pp. 437–463, jul 2002.

[49] C. R. Barnett, “Replacing international temperature-time curves with BFD curve,” *Fire Safety Journal*, vol. 42, pp. 321–327, jun 2007.

[50] B. Zhao and J. Kruppa, “Structural behaviour of an open car park under real fire scenarios,” *Fire and Materials*, vol. 28, no. 2-4, pp. 269–280, 2004.

[51] M. Garlock, I. Paya-Zaforteza, V. Kodur, and L. Gu, “Fire hazard in bridges: Review, assessment and repair strategies,” *Engineering Structures*, vol. 35, no. Supplement C, pp. 89 – 98, 2012.

[52] A. Pchelintsev, Y. Hasemi, T. Wakamatsu, and Y. Yokobayashi, “Experimental and numerical study on the behaviour of a steel beam under ceiling exposed to a localized fire,” *Fire Safety Science*, vol. 5, pp. 1153–1164, 1997.

[53] T. Wakamatsu, Y. Hasemi, K. Kagiya, and D. Kamikawa, “Heating mechanism of unprotected steel beam installed beneath ceiling and exposed to a localized fire: Verification using the real-scale experiment and effects of the smoke layer,” *Fire Safety Science*, pp. 1099–1110, 2003.

[54] G. Heskestad, “Peak gas velocities and flame heights of buoyancy-controlled turbulent diffusion flames,” *Symposium (International) on Combustion*, vol. 18, no. 1, pp. 951–960, 1981.

[55] K. Horová, T. Jána, and F. Wald, “Temperature heterogeneity during travelling fire on experimental building,” *Advances in Engineering Software*, vol. 62-63, pp. 119–130, aug 2013.

[56] J. L. Torero, A. H. Majdalani, A. E. Cecilia, and A. Cowlard, “Revisiting the compartment fire,” *Fire Safety Science*, vol. 11, pp. 28–45, 2014.

[57] D. R. J. Degler, A. Eliasson, J. Anderson, D. Lange, “A-priori modelling of the Tisova Fire Test as input to the experimental work,” in *Proceedings of the First International Conference on Structural Safety under Fire & Blast*, pp. 429–438, 2015.

[58] G. Rein, X. Zhang, P. Williams, B. Hume, and A. Heise, “Multi-storey fire analysis for high-rise buildings,” in *Interflam: The* 11^{th} *international conference on fire science and engineering*, pp. 605–616, 2007.

[59] R.L.Alpert, “Turbulent ceiling-jet induced by large-scale fires,” *Combustion Science and Technology*, vol. 11, no. 5-6, pp. 197–213, 1975.

[60] G. Rein, W. Jahn, and J. Torero, “Modelling of the growth phase of dalmarnock fire test one,” pp. 245–256, 2011.

[61] W. Jahn, G. Rein, and J. Torero, “A posteriori modelling of the growth phase of dalmarnock fire test one,” *Building and Environment*, vol. 46, no. 5, pp. 1065–1073, 2011.

[62] B. Merci, J. L. Torero, and A. Trouvé, “Iafss working group on measurement and computation of fire phenomena,” *Fire Technology*, vol. 52, pp. 607–610, may 2016.

[63] G. Baker, C. Wade, M. Spearpoint, and C. Fleischmann, “Developing probabilistic design fires for performance-based fire safety engineering,” *Procedia Engineering*, vol. 62, pp. 639–647, 2013.

[64] G. Cooke, “An introduction to the mechanical properties of structural steel at elevated temperatures,” *Fire Safety Journal*, vol. 13, no. 1, pp. 45–54, 1988.

[65] L. Twilt, “Strength and deformation properties of steel at elevated temperatures: Some practical implications,” *Fire Safety Journal*, vol. 13, no. 1, pp. 9 – 15, 1988.

[66] Y. Wang, “An analysis of the global structural behaviour of the Cardington steel-framed building during the two BRE fire tests,” *Engineering Structures*, vol. 22, pp. 401–412, may 2000.

[67] G. Q. Li and S. X. Guo, “Experiment on restrained steel beams subjected to heating and cooling,” *Journal of Constructional Steel Research*, vol. 64, pp. 268–274, mar 2008.

[68] T. Liu, M. Fahad, and J. Davies, “Experimental investigation of behaviour of axially restrained steel beams in fire,” *Journal of Constructional Steel Research*, vol. 58, pp. 1211–1230, sep 2002.

[69] S. Lamont, B. Lane, A. Usmani, and D. Drysdale, “Assessment of the fire resistance test with respect to beams in real structures,” *Engineering Journal*, vol. 40, no. 2, pp. 63–75, 2003.

[70] V. Kodur and M. Dwaikat, “Response of steel beam - columns exposed to fire,” *Engineering Structures*, vol. 31, pp. 369–379, feb 2009.

[71] M. Dwaikat and V. Kodur, “A performance based methodology for fire design of restrained steel beams,” *Journal of Constructional Steel Research*, vol. 67, pp. 510–524, mar 2011.

[72] Y. Yin and Y. Wang, “Analysis of catenary action in steel beams using a simplified hand calculation method, Part 1: Theory and validation for uniform temperature distribution,” *Journal of Constructional Steel Research*, vol. 61, pp. 183–211, feb 2005.

[73] Y. Yin and Y. Wang, “Analysis of catenary action in steel beams using a simplified hand calculation method, part 2: Validation for non-uniform temperature distribution,” *Journal of Constructional Steel Research*, vol. 61, pp. 213–234, feb 2005.

[74] A. Sanad, J. Rotter, A. Usmani, and M. O’Connor, “Composite beams in large buildings under fire - numerical modelling and structural behaviour,” *Fire Safety Journal*, vol. 35, no. 3, pp. 165–188, 2000.

[75] V. Kodur and A. Shakya, “Effect of temperature on thermal properties of spray applied fire resistive materials,” *Fire Safety Journal*, vol. 61, pp. 314 – 323, 2013.

[76] S. Chen, L. Jiang, A. Usmani, G. Q. Li, and C. Jin, “Damage mechanisms in cementitious coatings on steel members under axial loading,” *Construction and Building Materials*, vol. 90, pp. 18–35, 2015.

[77] N. L. Braxtan and S. Pessiki, “Bond performance of SFRM on steel plates subjected to tensile yielding,” *Journal of Fire Protection Engineering*, vol. 21, no. 1, pp. 37–55, 2011.

[78] A. Arablouei and V. Kodur, “Dynamic delamination of fire insulation applied on steel structures under impact loading,” *International Journal of Impact Engineering*, vol. 83, pp. 11–27, 2015.

[79] K. T. Tan, C. C. White, and D. L. Hunston, “An adhesion test method for spray-applied fire-resistive materials,” *Fire and Materials*, vol. 35, no. 4, pp. 245–259, 2011.

[80] A. Arablouei and V. Kodur, “Cohesive zone model properties for evaluating delamination of spray-applied fire-resistive materials from steel structures,” *Engineering Fracture Mechanics*, 2015.

[81] N. L. Braxtan and S. Pessiki, “Seismic performance of sprayed fire resistive material (sfrm) on steel moment frame buildings,” Tech. Rep. ATLSS report number 10-03, ATLSS Reports, 2010.

[82] N. L. Braxtan and S. P. Pessiki, “Postearthquake fire performance of sprayed fire-resistive material on steel moment frames,” *Journal of Structural Engineering*, vol. 137, no. 9, pp. 946–953, 2011.

[83] W. J. Keller and S. Pessiki, “Effect of earthquake-induced damage to spray-applied fire-resistive insulation on the response of steel moment-frame beam-column connections during fire exposure,” *Journal of Fire Protection Engineering*, vol. 22, no. 4, pp. 271–299, 2012.

[84] W. J. Keller and S. Pessiki, “Cyclic load tests of SFRM-insulated steel gravity frame beam-column connection assemblies,” *Journal of Structural Engineering*, vol. 141, oct 2015.

[85] S. Chen and L. Jiang, "Damage mechanisms in cementitious coatings on steel members in bending," *Proceedings of the ICE - Structures and Buildings*, vol. 168, no. Volume 168, Issue 5, pp. 351–369, 2015.

[86] S. Chen, L. Jiang, L. Wu, Y. Wang, and A. Usmani, "Damage investigation of cementitious fire resistive coatings under complex loading," *Construction and Building Materials*, vol. 204, pp. 659 – 674, 2019.

[87] Y. Wang, "Experimental studies on damage mechanisms in cementitious coatings on structural members under complex loadings," Master's thesis, Tongji University, 2016.

[88] M. Dwaikat, V. Kodur, and F. Asce, "Modeling fracture and delamination of spray-applied fire-resisting materials under static and impact loads," *Journal of Engineering Mechanics*, vol. 137, no. 12, pp. 901–910, 2011.

[89] A. Arablouei and V. Kodur, "A fracture mechanics-based approach for quantifying delamination of spray-applied fire-resistive insulation from steel moment-resisting frame subjected to seismic loading," *Engineering Fracture Mechanics*, vol. 121-122, pp. 67–86, 2014.

[90] V. Kodur, P. Eng, F. Asce, and A. Arablouei, "Mechanics-based approach for modeling delamination of fire insulation from steel structures," *Journal of Engineering Mechanics*, vol. 140, no. 6, 2014.

[91] V. Kodur and A. Arablouei, "Effective properties of spray-applied fire-resistive material for resistance to cracking and delamination from steel structures," *Construction and Building Materials*, vol. 84, pp. 367–376, 2015.

[92] Huang, Hou-cheng; Usmani, Asif, *Finite element analysis for heat transfer:Theory and software*. Springer London Ltd, United Kingdom, 2010.

[93] Y. Jiang, *Development and application of a thermal analysis framework in OpenSees for structures in fire*. PhD thesis, The university of Edinburgh, 2012.

[94] L. Gardner and D. Nethercot, “Experiments on stainless steel hollow sections Part 1: Material and cross-sectional behaviour,” *Journal of Constructional Steel Research*, vol. 60, no. 9, pp. 1291–1318, 2004.

[95] J. Chen and B. Young, “Stress strain curves for stainless steel at elevated temperatures,” *Engineering Structures*, vol. 28, pp. 229–239, jan 2006.

[96] R. K. Desu, H. Nitin Krishnamurthy, A. Balu, A. K. Gupta, and S. K. Singh, “Mechanical properties of Austenitic Stainless Steel 304L and 316L at elevated temperatures,” *Journal of Materials Research and Technology*, vol. 5, pp. 13–20, jan 2016.

[97] L. Gardner, A. Insausti, K. Ng, and M. Ashraf, “Elevated temperature material properties of stainless steel alloys,” *Journal of Constructional Steel Research*, vol. 66, no. 5, pp. 634–647, 2010.

[98] J. Sahu, U. Krupp, R. Ghosh, and H.-J. Christ, “Effect of 475 $^\circ$ C embrittlement on the mechanical properties of duplex stainless steel,” *Materials Science and Engineering: A*, vol. 508, pp. 1–14, may 2009.

[99] E. Mirambell and E. Real, “On the calculation of deflections in structural stainless steel beams: an experimental and numerical investigation,” *Journal of Constructional Steel Research*, vol. 54, pp. 109–133, apr 2000.

[100] B. Young, “Experimental and numerical investigation of high strength stainless steel structures,” *Journal of Constructional Steel Research*, vol. 64, pp. 1225–1230, nov 2008.

[101] N. Lopes, P. Vila Real, L. Simões da Silva, and J.-M. Franssen, “Numerical analysis of stainless steel beam-columns in case of fire,” *Fire Safety Journal*, vol. 50, pp. 35–50, 2012.

[102] L. Gardner and D. Nethercot, “Experiments on stainless steel hollow sections Part 2: Member behaviour of columns and beams,” *Journal of Constructional Steel Research*, vol. 60, no. 9, pp. 1319–1332, 2004.

[103] M. Ashraf, L. Gardner, and D. Nethercot, "Compression strength of stainless steel cross-sections," *Journal of Constructional Steel Research*, vol. 62, no. 1, pp. 105–115, 2006.

[104] S. Fan, L. Zhang, W. Sun, X. Ding, and M. Liu, "Numerical investigation on fire resistance of stainless steel columns with square hollow section under axial compression," *Thin-Walled Structures*, vol. 98, pp. 185–195, 2016.

[105] P. M. M. Vila Real, N. Lopes, L. Simões da Silva, and J. M. Franssen, "Lateral-torsional buckling of stainless steel I-beams in case of fire," *Journal of Constructional Steel Research*, vol. 64, no. 11, pp. 1302–1309, 2008.

[106] "Results and observations from full-scale fire test at BRE Cardington," Tech. Rep. 215, BRE Centre, 2003.

[107] W. Ramberg and W. R. Osgood, "Description of stress-strain curves by three parameters," tech. rep., National Advisory Committee for Aeronautics, 1943.

[108] H. Saab and D. Nethercot, "Modelling steel frame behaviour under fire conditions," *Engineering Structures*, vol. 13, pp. 371–382, oct 1991.

[109] N. Mostaghel and R. Byrd, "Inversion of Ramberg-Osgood equation and description of hysteresis loops," *International Journal of Non-Linear Mechanics*, vol. 37, pp. 1319–1335, dec 2002.

[110] K. Abdella, "Inversion of a full-range stress-strain relation for stainless steel alloys," *International Journal of Non-Linear Mechanics*, vol. 41, no. 3, pp. 456–463, 2006.

[111] J. Hollomon, "Tensile deformation," *Transactions of the Metallurgical Society of AIME*, vol. 162, pp. 268–290, 1945.

[112] P. Ludwik, *Elemente der Technologischen Mechanik.* Springer, 1909.

[113] H. Swift, "Plastic instability under plane stress," *Journal of the Mechanics and Physics of Solids*, vol. 1, no. 1, pp. 1–18, 1952.

[114] E. Voce, “A practical strain hardening function,” *Metallurgia*, vol. 51, pp. 219–226, 1955.

[115] J. Franssen, “The unloading of building materials submitted to fire,” *Fire Safety Journal*, vol. 16, no. 3, pp. 213–227, 1990.

[116] G. Masing, “Internal stresses and hardening of brass,” in *Proceedings of* 2^{nd} *International Congress for Applied Mechanics, Zurich*, sep 1926.

[117] J.-M. Franssen and T. Gernay, “Modeling structures in fire with SAFIR: theoretical background and capabilities,” *Journal of Structural Fire Engineering*, no. 07, 2017.

[118] J.-M. Franssen, “Safir: A thermal/structural program for modeling structures under fire,” *Engineering Journal*, vol. 42, no. 3, pp. 143–150, 2005.

[119] N. Elhami Khorasani, M. E. M. Garlock, and S. E. Quiel, “Modeling steel structures in OpenSees: Enhancements for fire and multi-hazard probabilistic analyses,” *Computers and Structures*, vol. 157, pp. 218–231, 2015.

[120] C. Bailey, “Development of computer software to simulate the structural behaviour of steel-framed buildings in fire,” *Computers & Structures*, vol. 67, no. 6, pp. 421–438, 1998.

[121] C. K. Iu, S. L. Chan, and X. X. Zha, “Nonlinear pre-fire and post-fire analysis of steel frames,” *Engineering Structures*, vol. 27, no. 11, pp. 1689–1702, 2005.

[122] K. Lien, Y. Chiou, R. Wang, and P. Hsiao, “Nonlinear behavior of steel structures considering the cooling phase of a fire,” *Journal of Constructional Steel Research*, vol. 65, pp. 1776–1786, aug 2009.

[123] H. Armen, “Assumptions, models, and computational methods for plasticity,” *Computers & Structures*, vol. 10, no. 1, pp. 161–174, 1979.

[124] E. Silvestre, J. Mendiguren, L. Galdos, and E. S. de Argandona, "Comparison of the hardening behaviour of different steel families: From mild and stainless steel to advanced high strength steels," *International Journal of Mechanical Sciences*, vol. 101-102, pp. 10 – 20, 2015.

[125] A. Olsson, *Stainless steel plasticity - Material modelling and structural applications*. PhD thesis, Lulea University of Technology, 2001.

[126] J.Gozzi, *Plastic behaviour of steel: Experimental invesitgation and modelling*. PhD thesis, Lulea University of Technology, 2004.

[127] A. Phillips, C. S. Liu, and J. W. Justusson, "An experimental investigation of yield surfaces at elevated temperatures," *Acta Mechanica*, vol. 14, pp. 119–146, jun 1972.

[128] Harley, E.J and Miller, M.P and Bammann, D.J, "Experimental study of internal variable evolution in SS304L, at multiple rates and temperatures," *Journal of Engineering Materials and Technology*, vol. 121, no. 2, pp. 162–171, 1999.

[129] K. Maciejewski, Y. Sun, O. Gregory, and H. Ghonem, "Time-dependent deformation of low carbon steel at elevated temperatures," *Materials Science and Engineering: A*, vol. 534, pp. 147 – 156, feb 2012.

[130] *BS EN ISO 6892-1 Metallic materials - Tensile testing Part 1: Method of test at room temperature*. British Standards Institution, jul 2016.

[131] U. Lindholm and R. Bessey, "A survey of rate dependent strength properties of metals," Tech. Rep. AFRL-TR-69-119, Southwest research institue, jun 1969.

[132] Seif, Mina S. and Luecke,William E. and Choe, Lisa Y. and Main,Joseph A. and McColskey, Joseph D. and Zhang, Chao and Weigand, Jonathan M. and Gross, John L.and Sadek, Fahim, "Temperature-dependent material modeling for structural steels: Formulation and application," Tech. Rep. NIST

Technical Note 1907, National Institute of Standards and Technology, U.S. Department of Commerce, 2016.

[133] L. M. Lindholm, U. S.and Yeakley, "High strain-rate testing: Tension and compression," *Experimental Mechanics*, vol. 8, pp. 1–9, jan 1968.

[134] N. Torić and I. W. Burgess, "A unified rheological model for modelling steel behaviour in fire conditions," *Journal of Constructional Steel Research*, vol. 127, pp. 221 – 230, 2016.

[135] E. Stoddart, M. Byfield, J. Davison, and A. Tyas, "Strain rate dependent component based connection modelling for use in non-linear dynamic progressive collapse analysis," *Engineering Structures*, vol. 55, pp. 35 – 43, 2013.

[136] B. Jiang, G. Q. Li, and A. Usmani, "Progressive collapse mechanisms investigation of planar steel moment frames under localized fire," *Journal of Constructional Steel Research*, vol. 115, pp. 160 – 168, 2015.

[137] H. Nguyen, A. Jeffers, and V. Kodur, "Computational simulation of steel moment frame to resist progressive collapse in fire," *Journal of Structural Fire Engineering*, vol. 7, no. 4, pp. 286–305, 2016.

[138] V. Kodur, M. Dwaikat, and R. Fike, "High-temperature properties of steel for fire resistance modeling of structures," *Journal of Materials in Civil Engineering*, vol. 22, no. 5, pp. 423–434, 2010.

[139] I. Boko, N. Torić, and B. Peroš, "Structural fire design parameters and procedures – analysis of the potential of eurocode 3," *Materialwissenschaft und Werkstofftechnik*, vol. 43, no. 12, pp. 1036–1052, 2012.

[140] L. Twilt, "Stress-strain relationships of structural steel at elevated temperatures: Analysis of various options and european proposal -part f: mechanical properties," Tech. Rep. TNO Rep No. BI-91-015, Delft, The Netherlands, 1991.

[141] *Structural fire protection*. American Society of Civil Engineers, 1992.

[142] Z. Mroz, “On the description of anisotropic workhardening,” *Journal of the Mechanics and Physics of Solids*, vol. 15, no. 3, pp. 163 – 175, 1967.

[143] R. D. Krieg, “A practical two surface plasticity theory,” *Journal of Applied Mechanics*, vol. 42, no. 3, p. 641, 1975.

[144] Y. F. Dafalias and E. P. Popov, “Plastic internal variables formalism of cyclic plasticity,” *Mechanics Research Communications*, vol. 3, no. 1, pp. 33–38, 1976.

[145] M. G. Lee, D. Kim, C. Kim, M. Wenner, R. Wagoner, and K. Chung, “A practical two-surface plasticity model and its application to spring-back prediction,” *International Journal of Plasticity*, vol. 23, no. 7, pp. 1189 – 1212, 2007.

[146] R. P. Cardoso and J. W. Yoon, “Stress integration method for a nonlinear kinematic/isotropic hardening model and its characterization based on polycrystal plasticity,” *International Journal of Plasticity*, vol. 25, no. 9, pp. 1684 – 1710, 2009. Exploring New Horizons of Metal Forming Research.

[147] D. W. Prager, “The theory of plasticity: A survey of recent achievements,” *Proceedings of the Institution of Mechanical Engineers*, vol. 169, no. 1, pp. 41–57, 1955.

[148] H. Ziegler, “A modification of prager’s hardening rule,” *Quarterly of Applied Mathematics*, vol. 17, no. 1, pp. 55–65, 1959.

[149] J. L. Chaboche and G. Rousselier, “On the Plastic and Viscoplastic Constitutive Equations - Part I: Rules Developed With Internal Variable Concept,” *Journal of Pressure Vessel Technology*, vol. 105, no. 2, p. 153, 1983.

[150] J. Chaboche, “Time-independent constitutive theories for cyclic plasticity,” *International Journal of Plasticity*, vol. 2, no. 2, pp. 149–188, 1986.

[151] J. Chaboche, “A review of some plasticity and viscoplasticity constitutive theories,” *International Journal of Plasticity*, vol. 24, no. 10, pp. 1642 – 1693, 2008. Special Issue in Honor of Jean-Louis Chaboche.

[152] C. Frederick and P. Armstrong, “A mathematical representation of the multiaxial Bauschinger effect,” tech. rep., 1966.

[153] E. A. de Souza Neto, D. Peri, and D. R. J. Owen, *Computational Methods for Plasticity : Theory and Applications*. Wiley-Blackwell, 2008.

[154] A. Khan and S. Huang, *Continuum Theory of Plasticity*. Wiley-Interscience publication, Wiley, 1995.

[155] N. Rebelo and S. Kobayashi, “A coupled analysis of viscoplastic deformation and heat transfer - i: Theoretical considerations,” *International Journal of Mechanical Sciences*, vol. 22, no. 11, pp. 699 – 705, 1980.

[156] N. Rebelo and S. Kobayashi, “A coupled analysis of viscoplastic deformation and heat transfer - ii: Applications,” *International Journal of Mechanical Sciences*, vol. 22, no. 11, pp. 707 – 718, 1980.

[157] J. H. Kim, S. K. Kim, C. S. Lee, M. H. Kim, and J. M. Lee, “A constitutive equation for predicting the material nonlinear behavior of aisi 316l, 321, and 347 stainless steel under low-temperature conditions,” *International Journal of Mechanical Sciences*, vol. 87, pp. 218 – 225, 2014.

[158] C. J. Lissenden, B. A. Lerch, J. R. Ellis, and D. N. Robinson, “Verification of experimental techniques for flow surface determination,” tech. rep., National Aeronautics and Space Administration, feb 1996.

[159] Y. Sun, K. MacIejewski, and H. Ghonem, “Simulation of viscoplastic deformation of low carbon steel structures at elevated temperatures,” *Journal of Materials Engineering and Performance*, vol. 21, no. 7, pp. 1151–1159, 2012.

[160] D. Bushnell, “A strategy for the solution of problems involving large deflections, plasticity and creep,” *International Journal for Numerical Methods in Engineering*, vol. 11, no. 4, pp. 683–708, 1977.

[161] C. Nyssen, “An efficient and accurate iterative method, allowing large incremental steps, to solve elasto-plastic problems,” *Computers & Structures*, vol. 13, no. 1, pp. 63 – 71, 1981.

[162] S. Sloan, “Substepping schemes for numerical integration of elastoplastic stress strain relations,” *International Journal for Numerical Methods in Engineering*, vol. 24, pp. 893 – 911, 05 1987.

[163] J. Marques, “Stress computation in elastoplasticity,” *Engineering Computations*, vol. 1, no. 1, pp. 42–51, 1984.

[164] J. Rice and D. Tracey, “Computational fracture mechanics,” *Numerical and Computer Methods in Structure Mechanics*, pp. 585–623, feb 1973.

[165] M. Ortiz and E. P. Popov, “Accuracy and stability of integration algorithms for elastoplastic constitutive relations,” *International Journal for Numerical Methods in Engineering*, vol. 21, no. 9, pp. 1561–1576, 1985.

[166] M. Wilkins, L. L. Laboratory, and B. L. R. L. University of California, *Calculation of elastic-plastic flow*. University of California Lawrence Radiation Laboratory, 1963.

[167] R. D. Krieg and D. B. Krieg, “Accuracies of numerical solution methods for the elastic-perfectly plastic model,” *Journal of Pressure Vessel Technology*, vol. 99, no. 4, p. 510, 1977.

[168] J. Simo and S. Govindjee, “Exact closed-form solution of the return mapping algorithm in plane stress elasto-viscoplasticity,” *Engineering Computations*, vol. 5, no. 3, pp. 254–258, 1988.

[169] M. Ortiz and J. C. Simo, "An analysis of a new class of integration algorithms for elastoplastic constitutive relations," *International Journal for Numerical Methods in Engineering*, vol. 23, no. 3, pp. 353–366, 1986.

[170] A. Lush, G. Weber, and L. Anand, "An implicit time-integration procedure for a set of internal variable constitutive equations for isotropic elasto-viscoplasticity," *International Journal of Plasticity*, vol. 5, no. 5, pp. 521 – 549, 1989.

[171] J. Yoon, D. Yang, and K. Chung, "Elasto-plastic finite element method based on incremental deformation theory and continuum based shell elements for planar anisotropic sheet materials," *Computer Methods in Applied Mechanics and Engineering*, vol. 174, no. 1, pp. 23 – 56, 1999.

[172] R. Hill, *The mathematical theory of plasticity.* Oxford University Press, 1998.

[173] T. Inoue and K. Tanaka, "Subsequent yield conditions of metal under cyclic loading at elevated temperature," *Ingenieur-Archiv*, vol. 44, no. 2, pp. 53–62, 1975.

[174] J. C. Nagtegaal, "On the implementation of inelastic constitutive equations with special reference to large deformation problems," *Computer Methods in Applied Mechanics and Engineering*, vol. 33, no. 1, pp. 469 – 484, 1982.

[175] J. Simo and R. Taylor, "Consistent tangent operators for rate-independent elastoplasticity," *Computer Methods in Applied Mechanics and Engineering*, vol. 48, no. 1, pp. 101 – 118, 1985.

[176] J. R. Ellis, D. N. Robinson, and C. E. Pugh, "Time dependence in biaxial yield of type 316 stainless steel at room temperature," *Journal of Engineering Materials and Technology*, vol. 105, no. 4, pp. 250–256, 1983.

[177] *Abaqus 6.14 Benchmarks manual.* SIMULIA.

[178] W. W. Yu and R. A. LaBoube, *Cold-formed steel design*. John Wiley & Sons, Inc., 2010.

[179] X. Qiang, F. S. Bijlaard, and H. Kolstein, “Post-fire mechanical properties of high strength structural steels s460 and s690,” *Engineering Structures*, vol. 35, pp. 1 – 10, 2012.

[180] X. Qiang, F. S. Bijlaard, and H. Kolstein, “Post-fire performance of very high strength steel s960,” *Journal of Constructional Steel Research*, vol. 80, pp. 235 – 242, 2013.

[181] W. Wang, T. Liu, and J. Liu, “Experimental study on post-fire mechanical properties of high strength q460 steel,” *Journal of Constructional Steel Research*, vol. 114, pp. 100 – 109, 2015.

[182] F. Azhari, A. Heidarpour, X. L. Zhao, and C. R. Hutchinson, “Mechanical properties of ultra-high strength (grade 1200) steel tubes under cooling phase of a fire: An experimental investigation,” *Construction and Building Materials*, vol. 93, pp. 841 – 850, 2015.

[183] X. Q. Wang, Z. Tao, T. Y. Song, and L. H. Han, “Stress strain model of austenitic stainless steel after exposure to elevated temperatures,” *Journal of Constructional Steel Research*, vol. 99, pp. 129 – 139, 2014.

[184] Z. Tao, X. Q. Wang, M. K. Hassan, T. Y. Song, and L. A. Xie, “Behaviour of three types of stainless steel after exposure to elevated temperatures,” *Journal of Constructional Steel Research*, vol. 152, pp. 296 – 311, 2019.

[185] Y. Huang and B. Young, “Post-fire behaviour of ferritic stainless steel material,” *Construction and Building Materials*, vol. 157, pp. 654 – 667, 2017.

[186] Y. Huang and B. Young, “Mechanical properties of lean duplex stainless steel at post-fire condition,” *Thin-Walled Structures*, vol. 130, pp. 564 – 576, 2018.

[187] F. Azhari, A. Heidarpour, X.-L. Zhao, and C. R. Hutchinson, “Post-fire mechanical response of ultra-high strength (grade 1200) steel under high temperatures: Linking thermal stability and microstructure,” *Thin-Walled Structures*, vol. 119, pp. 114 – 125, 2017.

[188] E. Silvestre, J. Mendiguren, L. Galdos, and E. S. de Argandona, “Comparison of the hardening behaviour of different steel families: From mild and stainless steel to advanced high strength steels,” *International Journal of Mechanical Sciences*, vol. 101-102, pp. 10 – 20, 2015.

[189] D. Booth, Edmund; Key, *Earthquake Design Practice for Buildings*. Thomas Telford Publishing, Thomas Telford Ltd, 2^{nd} ed., 2006.

[190] M. Design and O. Structures, *Minimum Design Loads for Buildings and Other Structures*. American Society of Civil Engineers, 2013.

[191] B. S. S. C. of the National Institute of Building Sciences National Institute of Building Sciences, *NEHRP Recommended Seismic Provisions for New Buildings and Other Structures (FEMA P-750)*. Federal Emergency Management Agency of the U.S. Department of Homeland Security, 2009.

[192] M. Zhou, R. P. Cardoso, and H. Bahai, “A new material model for thermo-mechanical analysis of steels in fire,” *International Journal of Mechanical Sciences*, vol. 159, pp. 467 – 486, 2019.

[193] B. S. S. C. of the National Institute of Building Sciences, *FEMA P-751: 2009 NEHRP Recommended Seismic Provisions: Design Examples*. Federal Emergency Management Agency of the U.S. Department of Homeland Security, 2012.

[194] E. B. V. Filippou, F.C.and Popov, “Effects of bond deterioration on hysteretic behavior of reinforced concrete joints,” tech. rep., Earthquake engineering research center, University of California, Berkeley, 1983.

[195] P. Uriz and S. Mahin, “Toward earthquake-resistant design of concentrically braced steel-frame structures,” Tech. Rep. November, Pacific Earthquake Engineering Research Center, College of Engineering University of California, Berkeley, 2008.

[196] A. Gupta and H. Krawinkler, “Seismic demands for performance evaluation of steel moment resisting frame structures,” Tech. Rep. 132, The John A. Blume Earthquake Engineering Centre, 1999.

[197] *BS9999: Code of practice for fire safety in the design, management and use of buildings*, vol. 3. British Standards Institution, 2008.

[198] L. Jiang, *Development of an integrated computational tool for modelling structural frames in fire considering local effects*. PhD thesis, The University of Edinburgh, 2015.

[199] *Specification for the design of light gauge cold-formed stainless steel structural members*. American Iron and Steel Institute, 1968.

[200] “Compendium of UK standard fire test data - Unprotected structural steel -1,” tech. rep., UK Department of the Environment Fire Research Station; British Steel Corporation, 1988.

[201] R. G. Gann, A. Hamins, K. McGrattan, H. E. Nelson, T. J. Ohlemiller, K. R. Prasad, and W. M. Pitts, “Reconstruction of the fires and thermal environment in world trade center buildings 1, 2, and 7,” *Fire Technology*, vol. 49, pp. 679–707, jul 2013.

[202] I. A. Fletcher, A. Borg, N. Hitchen, and S. Welch, “Performance of concrete in fire: A review of the state of the art, with a case study of the windsor tower fire,” in *Proceeding of 4th international workshop in Structures in Fire*, pp. 779–790, sep 2007.

[203] C. Clifton, “Fire models for large firecells,” tech. rep., HERA, 1996.

[204] E. Rackauskaite, P. Kotsovinos, and G. Rein, “Structural response of a steel-frame building to horizontal and vertical travelling fires in multiple floors,” *Fire Safety Journal*, vol. 91, pp. 542–552, 2017.

[205] X. Dai, L. Jiang, J. Maclean, S. Welch, and A. Usmani, “Implementation of a new design travelling fire model for global structural analysis,” in *9th International Conference on Structures in Fire*, pp. 959–966, 2016.

[206] *Abaqus 6.14 Analysis user’s manual.* SIMULIA.

[207] E. Spacone, F. Filippou, and F. Taucer, “Fibre beam–column model for non-linear analysis of r/c frames: Part i. formulation,” *Earthquake Engineering & Structural Dynamics*, vol. 25, no. 7, pp. 711–725, 1996.

[208] F. Barlat, H. Aretz, J. Yoon, M. Karabin, J. Brem, and R. Dick, “Linear transfomation-based anisotropic yield functions,” *International Journal of Plasticity*, vol. 21, no. 5, pp. 1009 – 1039, 2005.

[209] R. H. Dodds, “Numerical techniques for plasticity computations in finite element analysis,” *Computers & Structures*, vol. 26, no. 5, pp. 767 – 779, 1987.